



**CHARACTERIZATION AND DISCRIMINATION OF
LARGE CALIBER GUN BLAST AND FLASH SIGNATURES**

DISSERTATION

Bryan J. Steward, Civilian

AFIT/DS/ENP/11-D01

**DEPARTMENT OF THE AIR FORCE
AIR UNIVERSITY**

AIR FORCE INSTITUTE OF TECHNOLOGY

Wright-Patterson Air Force Base, Ohio

DISTRIBUTION STATEMENT A.
APPROVED FOR PUBLIC RELEASE; DISTRIBUTION IS UNLIMITED.

The views expressed in this thesis are those of the author and do not reflect the official policy or position of the United States Air Force, Department of Defense, or the United States Government. This material is declared a work of the U.S. Government and is not subject to copyright protection in the United States.

AFIT/DS/ENP/11-D01

**CHARACTERIZATION AND DISCRIMINATION OF
LARGE CALIBER GUN BLAST AND FLASH SIGNATURES**

DISSERTATION

Presented to the Faculty

Graduate School of Engineering and Management

Air Force Institute of Technology

Air University

Air Education and Training Command

in Partial Fulfillment of the Requirements for the

Degree of Doctor of Philosophy

Bryan J. Steward, BS, MS

Civilian


October 2011

DISTRIBUTION STATEMENT A.
APPROVED FOR PUBLIC RELEASE; DISTRIBUTION IS UNLIMITED.

CHARACTERIZATION AND DISCRIMINATION OF
LARGE CALIBER GUN BLAST AND FLASH SIGNATURES

Bryan J. Steward, BS, MS
Civilian

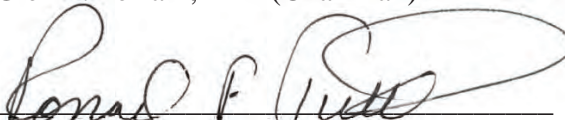
Approved:



Glen P. Perram, PhD (Chairman)

26 OCT 11


Date



Ronald F. Tuttle, PhD (Member)

25 OCT 2011

Date



Kenneth W. Bauer, PhD (Member)

25 OCT 11

Date




Korin M. Elder (Member)

25 OCT 11

Date

Accepted:



M. U. Thomas
Dean, Graduate School of Engineering
and Management

22 Nov 11

Date

Abstract

Muzzle blast and flash signatures are an important source of battlefield information because they can reveal the location of weapons fire. While this has been performed by the human eye since the advent of guns, detection of weapon signatures has recently become more technologically sophisticated, and the content of firing signatures can reveal far more information than just the gun's location. Prior to this work, several aspects of gun firing signatures were largely uncharacterized. The results of this research include a description of blast properties and visible through infrared spectral emissions of a large caliber gun, and a demonstration of their potential for battlespace classification.

Two hundred and one firings of three 152 mm howitzer munitions were observed. Muzzle flow expanded into three plumes of 2 – 3 m radius and side-on projected area of $35 \sim 40 \text{ m}^2$, estimated from 1600 Hz imagery. Initial Mach 3 – 4 expansion of the flow produced a blast that detached at $\sim 1 \text{ ms}$ and approached acoustic velocities within $4 \sim 5 \text{ ms}$. The trajectory of the blast front was well approximated by a modified point-blast model described by constant rate of energy deposition (2300 – 2600 MJ/s). A constant breech pressure (CBP) gun model was used to estimate propellant heat release, and determined that 18 – 24% of the energy was transferred to the blast. Plume temperatures of 980 – 1210 K were estimated from energy remaining in the plume, and averages trend with class likelihood of secondary combustion.

Visible and near-infrared (450 – 850 nm) spectra of secondary combustion were acquired at $\sim 0.75 \text{ nm}$ spectral resolution and depict strong contaminant emissions including Li, Na, K, Cu, and Ca. Non-equilibrium potassium excitation concentrations

are characterized by Boltzmann temperatures in the range 7,921 – 8,945 K. The potassium D1 and D2 lines are sufficiently broad that the O₂ (X→b) absorption band is evident in the blue wing. An empirical model reproduces potassium emissions to within 3% in the wings and was used for monocular passive ranging. Range was estimated to within 4 – 9% for individual firings and ~0.5% with multiple observations.

Infrared (1800 – 6000 cm⁻¹) spectra were collected at 100 Hz and 32 cm⁻¹ resolution. A low dimensional radiative transfer was used to characterize plume emissions in terms of area, temperature, soot emissivity, and species concentrations. Secondary combustion emissions have ~100 ms duration, 1200 – 1600 K temperature, and are dominated by H₂O and CO₂. Non-combusting plume emissions last ~20 ms, are 850 – 1050 K, and show significant continuum (emissivity ~0.36) and CO structure. Combusting plume temperatures are sustained by ~5 MJ/kg additional heat released in combustion, estimated from temperature rate of change using an empirical model. CBP heat of combustion assumes stoichiometric conditions and is within 50% agreement (~2.5 MJ/kg).

Classification accuracy of 96% required only 2 – 3 firing signature features to discriminate 152 mm howitzer munitions. The most salient features identified were atomic potassium to sodium intensity ratio (18.6 between-class to within-class variance ratio) and band-integrated MWIR intensities near 4500 cm⁻¹ (25.3 variance ratio, cumulative) and 3300 cm⁻¹ (39.6 variance ratio, cumulative). Physics-based features were less effective classifiers, likely because model interpretations do not capture pertinent firing signature phenomenology. Discrimination of the howitzer from a 120 mm cannon (15.7 variance ratio) was demonstrated using real-world bandpass filters, suggesting significant potential for use in battlefield classification.

To My Wife and Children

Acknowledgments

My sincerest gratefulness is to my beautiful wife for her patience, understanding, and much encouragement during the many trials encountered along the way. I could not have done it without her. Thank you to my daughter for still playing with me even after so many nights busy with school. To my parents I am particularly grateful for always believing in me. Without their love and encouragement I would not be who I am today.

I wish to express my deep appreciation to my advisor and source of much inspiration, Dr. Glen Perram. I am always amazed at his keen grasp of a range of scientific fields, and I fully believe that his insights and guidance have made this work the success it is. Likewise, I am grateful to committee members Ms. Kori Elder, Dr. Ken Bauer, and Dr. Ron Tuttle for supporting me in this research and helping to separate the wheat from the chaff. I owe a debt of gratitude to Dr. Kevin Gross for the significant amount of time and effort he has devoted to helping me throughout all stages of this research, and for his friendship. The many friends I've made (Chris, Joe, Christina, and Randy to name a few) also deserve thanks for their friendship and encouragement.

Many thanks goes to Greg Smith, Jeremy Pitz, Matt Bollinger, Douglas Wertepny, LtCol Mike Hawks, Raj Sinha, and Dr. Anthony Kotlar for all their technical assistance; teams and individuals (who are too numerous to name) with AFIT, NASIC, NGIC, ATC, DRDC, and ARL for hard work and fun during data collection; all those who advocated for the time I needed to finish this work (Mr. Rowland, Ms. Rivera, Col Brenner, Ms. Elder, and likely many others I am not even aware of); and especially Julie, Cliff, Jody, and my Flight for taking on additional burdens in my absence. Thank you all!

Bryan J. Steward

Table of Contents

	Page
Abstract	iv
Acknowledgments.....	vii
Table of Contents	viii
List of Figures	xi
List of Tables	xx
I. Introduction	1
Document Overview	7
II. Background	9
Gun Firing Phenomenology	9
Muzzle Flash Spectra Research	18
Battlespace Classification	23
Linear Classification	26
III. Reduction of Optically Observed Artillery Blast Wave Trajectories using Low Dimensionality Models	29
Introduction	29
<i>Phenomenology</i>	30
Experimental	31
<i>Test Articles</i>	32
<i>Instrumentation</i>	34
Data	36
<i>Blast Wave Trajectories</i>	36
<i>Flow Regions</i>	40
Results	43
<i>Point Blast</i>	43
<i>Drag</i>	44
<i>Asymptotic</i>	46
<i>Inverse Power Series</i>	47
<i>Fit Results</i>	48
Conclusions	51

	Page
IV. Optical Characterization of Large Caliber Muzzle Blast Waves.....	55
Introduction	55
Experimental	57
Results	60
<i>Blast Wave Imagery</i>	60
<i>Point Blast Model</i>	63
<i>Muzzle Plume</i>	70
Discussion	71
<i>Constant Breech Pressure Gun</i>	71
<i>Blast Wave Energy</i>	74
<i>Muzzle Flash</i>	78
<i>Classification Potential</i>	82
Conclusions	84
V. Visible and Near-Infrared Spectra of the Secondary Combustion of a 152 mm Howitzer	86
Introduction	86
Experimental	88
Results and Discussion.....	90
<i>Observed Spectra</i>	90
<i>Instrument Spectral Response and Lineshape</i>	94
<i>Optically Thick Conditions</i>	97
<i>Passive Ranging</i>	100
<i>Relative Line Intensity Ratios</i>	105
<i>Munitions Discrimination</i>	107
Conclusions	110
VI. Modeling Midwave Infrared Muzzle Flash Spectra from Unsuppressed and Flash-Suppressed Large Caliber Munitions	113
Introduction	113
Experimental	114
Results	118
<i>Observed Spectra</i>	118
<i>Spectral Model</i>	121
<i>Plume Dynamics</i>	123
Discussion	129
<i>Spectral Model with Spatial Variations</i>	129
<i>Multiple Spatially Varying Regions</i>	133
<i>Temperature Dynamics</i>	134
Summary	138

	Page
VII. Remote Discrimination of Large Caliber Gun Firing Signatures.....	142
Introduction	142
Feature Data	144
Results	150
<i>Feature Sets</i>	150
<i>Feature Correlations</i>	154
Discussion	158
<i>Feature Selection</i>	158
<i>Classification</i>	161
<i>Munitions Discrimination</i>	162
<i>Weapons Discrimination</i>	166
Summary	169
VIII. Conclusion	172
Muzzle Flash	173
Muzzle Blast	175
Battlespace Classification	177
Future Efforts	179
Appendix A. Propellant, Muzzle Gas, and Plume Thermochemistry	181
Appendix B. Constant Breech Pressure Gun	186
Model Overview	186
Example Calculation	192
Appendix C. Calibration of VNIR Spectra	195
Wavelength Calibration	195
Relative Spectral Response Calibration	198
Appendix D. Feature Tables	204
Appendix E. Selected Data	209
Bibliography	219
Vita.....	231

List of Figures

Figure	Page
1. Breech pressure (—) and projectile velocity (---) as a function of distance the projectile has traveled down the barrel. Curves are digital reproductions of those determined by Steifel for a 155 mm howitzer [43]. CBP simulation of pressure (—) and velocity (---) are estimates of the maximum performance of the gun.....	11
2. Schematic depiction of quasi-steady supersonic flow that develops after shot exit.....	13
3. Double-baffle muzzle brake. <i>Upper left</i> : schematic depiction of a typical brake. <i>Lower left</i> : 152 mm howitzer brake. <i>Right</i> : Computational fluid dynamics simulation of flow shows the existence of strong shocks in the muzzle [52]. Color scale indicates pressure in Pascals.....	14
4. Primary flash, intermediate flash, and secondary combustion muzzle flash regions are separated temporally and spatially.....	15
5. Notional internal energy potential for combustion of propellant during gun firing. Propellant and oxygen reactants (R) release energy ΔH_d when converted to intermediaries (I). Re-ignition allows the intermediaries to combust to product species (P) with the additional release of combustion energy ΔH_c	17
6. Comparison of visible spectral distribution of intermediate and secondary flash [30:2-3].	20
7. Spectral distribution of infrared radiation from secondary flash [30:2-9].....	21
8. Oscilloscope traces of suppressed flash from 155 mm gun [30:3-11].....	22
9. Spectral emittance of unsuppressed flash from 155 mm gun [30:3-8].....	22
10. MDA separation of three classes (●, ■, ▲). <i>Left-to-right, top-to-bottom</i> : $\Lambda = 0.7$, $\Lambda = 2.8$, $\Lambda = 7.5$, and $\Lambda = 35.1$	28
11. The test layout is shown. Site A and Site B (■) were located on small hills (---) overlooking the gun (▲) at the R&A Site (····). Due to the gun's firing elevation of approximately 45°, Site A had a side-on view of all the lateral plumes and an oblique rear view of the forward plume. Site B's location provided for a side-on view of the forward plume and a front-on view of the left lateral plume. Co-located at the R&A site was a radar unit for tracking the projectile.....	32

Figure	Page
12. Projectile trajectories for each munitions configuration. From top to bottom: Full Charge, Charge 1, and Charge 2. <i>Left Axis</i> : velocity versus down-range distance (—). <i>Right Axis</i> : height versus down-range distance (···).	36
13. The blast first six frames captured by the Phantom v7 imager operating at 25 kHz are shown for a Charge 2 firing. The blast wave is visible due to the index gradient induced by the high density shock front. The progression shows that lateral muzzle plumes begin to form as the projectile clears the first muzzle brake at 0.32 ms. The shock front is indistinguishable from the muzzle flow until 0.64 – 0.96 ms, at which point it is still in contact with the plume but begins to appear distinct. By 1.28 – 1.60 ms the leading edge of the blast wave has detached from the plume. The final still in the series shows major and minor axes lengths of the blast wave relative to the axis of the barrel.	37
14. <i>Left</i> : blast wave radius (•), median plume radius (—), and the ± 2 standard deviations of the plume radius (···) are shown as a function of time for the aggregate of all Charge 1 firings data. The inset plot shows the log of early-time data, where it is apparent that the early-time blast wave trajectory can be represented by a line (—). <i>Right</i> : residuals between all radius data for each configuration and the Charge 1 best-fit 6 th degree polynomial are shown. Full Charge is positively biased, indicating greater blast wave velocity. Similarly, Charge 2 is negatively biased, indicating a lesser blast wave velocity than Charge 1. The strong curvature at early times results because the polynomial is not an adequate fit to the data, and it is only used to emphasize variance in the data from event-to-event and amongst configurations.....	39
15. Characteristic curves are shown for each model. <i>Upper left</i> : point blast model with $A = 50 \text{ m s}^{-b}$ and $R_f = \infty$. <i>Upper right</i> : drag model with $R_m = 4 \text{ m}$, $a_0 = 0$, and κ in Hz. <i>Lower left</i> : asymptotic model with $R_0 = 10^{-3} \text{ m}$, $a_0 = 341 \text{ m/s}$, and k in seconds. <i>Lower right</i> : inverse power series with $a_0 = 341 \text{ m/s}$ and λ in meters.	45
16. Firing signatures are shown for the 152 mm howitzer. (a) Image processing improves contrast so that the blast wave is visible in all directions around the muzzle. (b) Each feature of interest in the processed image is identified in the sketch.	62

17. Aggregate of observed gun firing data as a function of time. (a) Radius-time data points (×) for all Full Charge firings. The point blast model with $b' = 0.6$ (—) is overlaid and correlates well with the data. A single observation (◆) obtained at the instrumentation site was not included in the fit data and demonstrates that the model accurately predicts the blast wave trajectory very far from the gun. Muzzle plume expansion for a sampling of firings (•) and drag model fit (—) show that detachment of the shock from the plume occurs in the near-field. (b) Residual (×) between constrained Full Charge point blast model and (from top to bottom) Full Charge, Charge 1, and Charge 2 radius-time data. At equivalent times the blast waves from lower charge masses propagate a shorter distance on average. Spread in the data represents the variance in firings for similar configurations, and curvature is evidence of systematic error. 64
18. Distributions of (a) A , (b) b , and (c) A' fit parameters are shown for Full Charge (■), Charge 1 (■), and Charge 2 (■). Parameters of similar magnitude are grouped into bins and the number of events per bin is shown. Bars for each class are slightly offset for visibility but correspond to the same bin values. The mean value of each fit parameter increases with increasing propellant mass..... 69
19. The rate of energy deposition into the blast is shown on the right axis for the Full Charge point blast model with b unconstrained (—) and constrained to a value of $b' = 3/5$ (---). The constrained rate is constant and the unconstrained case is initially large but drops quickly. The total energy deposited into the blast as a function of time is shown on the left axis. The unconstrained case is nearly parallel to the constrained case excepting that it has deposited more energy into the blast at very early times. Both sets of curves stop at $\tau = 0.95$ ms where the blast wave detaches from the plume and is no longer influenced by muzzle flow..... 76
20. The number of plumes combusting is shown for each event as a function of estimated plume temperature and measured muzzle velocity of the projectile. Circles (○) indicate no flash; and diamonds (◇), squares (□), and triangles (△) represent 1, 2, and 3 plumes flashing. Configurations containing flash suppressant are shown with solid symbols and rarely flash. Three distinct groupings are observed corresponding to Full Charge, Charge 1, and Charge 2, from right to left..... 80
21. Mean and variance in projectile muzzle velocity is shown as a function of the number of plumes flashing for each configuration, from top to bottom: Full Charge, Charge 1, and Charge 2. The data indicate a weak correlation in which lower muzzle velocity increases the likelihood of flash. 82

Figure	Page
22. Distributions of the time-independent rate of energy deposition, corresponding to $b' = 3/5$, is shown for Full Charge (—), Charge 1 (---), and Charge 2 (—) munitions configurations. The configurations are clearly separated despite overlap due to variation from event to event.....	84
23. View of the gun, plumes, and flash from the instrumentation site. (a) The axial extent of the plumes is approximately 8 m at 27 ms after shot exit. The circle shows the approximate field of view of the spectrometer. Flash scenarios include (b) all plumes combusting and (c) one or more plumes do not combust. (d) When the left lateral plume does not combust the flash may be partially obscured by cooler, unburned soot and propellant gases.	88
24. Uncalibrated response from the Ocean Optics grating spectrometer is shown for a single gun firing. The instrument collected 200 – 1100 nm spectral intensity data at 10 Hz.....	91
25. Atomic lines and molecular bands labeled are identified in Table 1. Relative source spectra (—) at (a) shorter wavelengths show that most emission features are due to species containing contaminants. (b) All atomic and molecular features are superimposed on a continuum baseline (····) from hot particulate emissions and plume-scattered solar radiation.	92
26. The potassium $4^2P - 4^2S$ doublet is significantly broader than the instrument lineshape (—) as a result of self-absorption. A simple radiative transfer model (—) approximates the phenomena, but an empirical function (---) provided a better fit to the data (\square). $O_2 X \rightarrow b$ absorption is evident in the shortwave wing of the broadened potassium profile due to atmospheric oxygen along the observation path.....	99
27. Intensity collected by the spectrometer varied significantly from event to event depending on the fraction of emissive plume in the instrument's field of view. An empirically determined potassium $4^2P - 4^2S$ profile (—) was scaled to the unsaturated data (\bullet) for each firing in order to extrapolate what the intensity should be in the saturated (x) region of each spectrum. Residuals between the model and unsaturated data are shown, and in all cases average less than 3% error.....	102
28. Spectral transmittance in the $O_2 X \rightarrow b$ absorption band is shown for observed data (\square) and as computed with the LBLRTM code (—) for a 429 m path with standard atmospheric constituents. Band-integrated absorption was calculated from $\lambda_1 = 758$ nm to $\lambda_2 = 763.5$ nm. Line reversal is observed near the potassium $4^2P - 4^2S$ doublet linecenters, likely due to a cooler outer layer at the surface of the plume.....	104

29. Relative concentrations of excited levels in potassium are shown for Full Charge (\circ), Charge 1 (\square), and Charge 2 (Δ) munitions configurations. The slopes of the best-fit lines ($\bullet\bullet\bullet$) for each configuration can be interpreted to provide temperature if a Boltzmann distribution is assumed. A 2,000 K line (—) is shown for reference. 107
30. Cumulative between-class to within-class variance (class separation) is shown as a function of the number of features used in MDA. The features are sorted to show order of importance and indicate that the ratios of species (a) $\text{K } 6^2\text{S} - 4^2\text{P} / \text{Na } 3^2\text{D} - 3^2\text{P}$, (b) $\text{K } 4^2\text{P} - 4^2\text{S} / \text{Na } 3^2\text{D} - 3^2\text{P}$, (c) $\text{K } 6^2\text{S} - 4^2\text{P} / \text{Li } 2^2\text{P} - 2^2\text{S}$, and (d) $\text{K } 6^2\text{S} - 4^2\text{P} / \text{K } 13^2\text{F} - 3^2\text{D}$ are better discriminators than temperatures (e) $\text{K } 6^2\text{S} - 4^2\text{P} / \text{K } 4^2\text{P} - 4^2\text{S}$, (f) $\text{Na } 3^2\text{P} - 3^2\text{S} / \text{Na } 3^2\text{D} - 3^2\text{P}$, (g) $\text{K } 7^2\text{S} - 4^2\text{P} / \text{K } 4^2\text{P} - 4^2\text{S}$, and (h) $\text{K } 7^2\text{S} - 4^2\text{P} / \text{K } 6^2\text{S} - 4^2\text{P}$ 109
31. Features are projected into subspaces that maximize the between-class to within-class variance amongst the class. The gray-scale gradients indicate the relative probability of a particular configuration being present, and white gradients between distributions indicate overlap approaching equal probabilities. (a) Four line intensity ratios are projected to two subspace dimensions that completely separate the distributions of Full Charge (\circ), Charge 1 (\square), and Charge 2 (Δ). (b) Two potassium to sodium line ratios discriminate the three configurations in two dimensions. Projection shows that the probability distributions for Full Charge and Charge 1 significantly overlap in a 1-dimensional subspace. 111
32. Spectral data cube of irradiance observed for an unsuppressed Full Charge firing. Spectra were collected at 100 Hz with 32 cm^{-1} resolution and show strong emissions until nearly 100 ms. 117
33. Peak observed spectra for combusting (—) and non-combusting (—) firings are shown. The left ordinate and image correspond to a combusting (unsuppressed) plume and show significant spectral structure. The right ordinate and image correspond to a non-combusting (suppressed), optically thick plume. Combustion results in band-integrated MWIR intensities a factor of ten greater than non-combusting. A near-local noon background spectrum ($\bullet\bullet\bullet$) is also shown on the right ordinate. Atmospheric transmittance is shown in the lower panel. 120
34. HE model (—) and observed (\bullet) spectral intensities are shown for the peak band-integrated intensity of a combusting (left) and non-combusting (right) plume. Planckian emissions ($\bullet\bullet\bullet$) at equivalent temperatures are shown for reference. Residuals between the model and data as a fraction of RMS intensity are indicated in the bottom panels. 124

35. Temporal dependence of HE model parameters when fit to combusting (—) and non-combusting (—) plumes. The values corresponding to peak intensity are indicated (\circ) and $t = 0$ occurs at gun firing. *Left, top to bottom*: band-integrated intensity, area, temperature, and soot emissivity. *Right, top to bottom*: column densities of H_2O , CO_2 , and CO ; and H:C ratio. Theoretical H:C ratios for combusting (---) and non-combusting (---) plumes are shown. For depiction on the same scale, non-combusting column densities and uncertainties are multiplied as following: $\text{H}_2\text{O} \times 50$, $\text{CO}_2 \times 50$, and $\text{CO} \times 1/5$. Error bars are excluded when off the scale of the plots..... 127
36. HE and distribution model fits to a combusting plume. *Upper panel*: distributions of temperature (—) and H_2O column density (—) centered at $T_0 = 1472 \text{ K}$ and $\mu_0 = \mu_{\text{H}_2\text{O}} = 4.7 \times 10^{20} \text{ cm}^{-2}$. CO_2 and CO have the same column density distribution centered at $\mu_{\text{CO}_2} = 1.6 \times 10^{21} \text{ cm}^{-2}$ and $\mu_{\text{CO}} = 8.9 \times 10^{19} \text{ cm}^{-2}$. *Lower panel*: Residuals between observed spectral intensity and distribution (—) and HE (—) models. RMS error is reduced from $e = 21.5\%$ to $e = 16.9\%$ when temperature and concentrations vary spatially..... 131
37. Distributions of a two-region model fit to the peak spectrum of a combusting muzzle plume. a) H_2O , b) CO_2 , and c) CO compose an optically thick core of temperature near $T \approx 1500 \text{ K}$ and thin flame-front near $T \approx 2550 \text{ K}$. Contours indicate relative area-weighting of emissions for the range of temperatures and concentrations. d) Soot emissivity distribution shows that most Planckian-like emissions are near 1500 K . Parameters of the HE model (\otimes) are located within the core region's distributions. 135
38. Temperatures extracted from a combusting muzzle plume using the HE model (\bullet), one region distribution (\blacksquare), and two region distribution (\blacktriangle). The temperature of a suppressed, non-combusting plume (\circ) was estimated using the HE model. Curves through the data (—) represent empirically modeled temperature as a function of time. 135
39. Observed 152 mm howitzer blast wave expansion (\square) and trajectory model $R = At^b$ (—) at early times. The model is linear on a log-log plot where its slope is the temporal exponent b , and A is determined from the ordinate intercept at $\log_{10} t = 0$ 146
40. Peak intensity spectrum representative of combusting 152 mm howitzer visible and near-infrared flash signatures. The strongest ($\text{SNR} > 1$) identified lines emissions are labeled. 147

41. *Left ordinate:* Apparent midwave infrared spectra are shown for a combusting 152 mm howitzer plume (—) and a 120 mm tank cannon plume (•). Also shown is the Planckian distribution (---) for the howitzer's model-estimated temperature $T = 1389$ K. *Right ordinate:* Source spectral emissivity of H_2O (—), CO_2 (—), and CO (---) as estimated from fit of the model to the howitzer data..... 149
42. *Upper panel:* Normalized 152 mm howitzer (—) and 120 mm cannon (---) midwave infrared spectra are superimposed on the relative response curves for the F1 – F7 band filters. The howitzer spectrum is the mean of all normalized firing spectra. *Lower panel:* Residuals between the mean normalized howitzer spectrum and the mean normalized Full Charge (—), Charge 1 (—), and Charge 2 (—) spectra are shown on the left ordinate. Residuals between the mean normalized howitzer and normalized cannon spectra (---) are an order of magnitude larger, indicated on the right ordinate. Band edges are shown for E1 – E10 and, except for the near-zero atmospheric transmission region from $3560 - 3900\text{ cm}^{-1}$, span the spectrum. Each band defines a region where spectral residuals show distinct differences between configurations. 153
43. *Upper right:* Correlation matrix containing the twelve empirical features with the largest r^2 values. Strong correlations are evident for features within and across instrument data sets. *Lower left:* Correlation matrix for all phenomenological features. Very few strong correlations are observed, with the exception of blast parameters. 155
44. Correlation matrix of all phenomenological and empirical features. 157
45. Class-conditional probability densities are shown for a discriminant subspace composed of the four most salient phenomenological features (T_{34} , E , T_{eq} , and μ_{CO}). Class probabilities are indicated by shading from gray (100%) through white (probabilities approach zero or equal values for two or more classes). Observations of Full Charge (○), Charge 1 (□), and Charge 2 (Δ) projected into the subspace have class separation $\Lambda = 10.9$ 163
46. Class-conditional probability densities are shown for a discriminant subspace composed of the four most salient empirical features (R_{35} , F6, E6, and A'). Class probabilities are indicated by shading from gray (100%) through white (probabilities approach zero or equal values for two or more classes). Observations of Full Charge (○), Charge 1 (□), and Charge 2 (Δ) projected into the subspace have class separation $\Lambda = 48.3$ 163

47. The most salient phenomenological features are indicated. Shading depicts stability (left ordinate) and shows the fraction of times each feature has the indicated saliency or better. Classification accuracy (—) for each number of discrimination features is also shown on the left ordinate. Class separation (***) is shown on the right ordinate and increases as dimensionality increases. 164
48. The most salient empirical features are indicated. Shading depicts stability (left ordinate) and shows the fraction of times each feature has the indicated saliency or better. Classification accuracy (—) for each number of discrimination features is also shown on the left ordinate. Class separation (***) is shown on the right ordinate and increases as dimensionality increases. 164
49. Class-conditional probability densities are indicated by shading from gray (100%) through white (probabilities approach zero or equal values for two or more classes). Observations of 152 mm howitzer Full Charge (\circ), Charge 1 (\square), Charge 2 (Δ), and 120 mm cannon (\diamond) are overlaid. Y_1 and Y_2 are the dimensions of a subspace composed of all MWIR band features, characterized by $\Lambda = 76.4$ and $D^2 = 46.6$. *Inset*: Feature space of filter bands F5 and F1. 168
50. Pressure as a function of projectile travel. Gases generated during burning of the propellant expand to fill the chamber. Upon reaching maximum pressure, the projectile accelerates at a constant rate from its initial position, x_c , to where the propellant burns out, x_b . Propellant gases continue to expand isentropically, providing continued acceleration until the projectile has reached the muzzle exit, x_m 188
51. Relationship between pixel number and wavelength over the 550 – 850 nm spectral range. The 3rd order polynomial conversion function (—) was obtained by fitting to alkali lines (\diamond) present in the muzzle flash spectra. 197
52. Residual difference between NIST reported wavelengths and those obtained with the 3rd order polynomial conversion function. 197
53. *Upper panel*: instrument response (—) to a 1200 °C blackbody distribution (***). Curves are normalized for depiction on the same scale. *Lower panel*: estimated blackbody-based RSR (—). 199
54. *Upper panel*: original (—) and smoothed (—) instrument responses from Event #32 background spectra are shown relative to simulated skyshine (***) at solar noon. Curves are normalized for depiction on the same scale. *Lower panel*: estimated skyshine-based RSR (—). 201

Figure	Page
55. <i>Upper panel:</i> estimated system RSR (—) is shown relative to response curves derived from blackbody (—) and skyshine (•) spectra. <i>Lower panel:</i> muzzle flash instrument response (—) and relatively calibrated intensity spectrum (—).....	203
56. Event 44, unsuppressed Full Charge peak intensity VNIR and MWIR muzzle flash spectra.....	209
57. Event 44, unsuppressed Full Charge flow imagery and blast trajectory.	210
58. Event 158, unsuppressed Charge 1 peak intensity VNIR and MWIR muzzle flash spectra.....	211
59. Event 158, unsuppressed Charge 1 flow imagery and blast trajectory.....	212
60. Event 68, unsuppressed Charge 2 peak intensity VNIR and MWIR muzzle flash spectra.	213
61. Event 68, unsuppressed Charge 2 flow imagery and blast trajectory.....	214
62. Event 98, suppressed Full Charge VNIR and MWIR muzzle plume spectra. Flash did not occur and the VNIR spectrum is representative of background.	215
63. Event 98, suppressed Full Charge flow imagery and blast trajectory.	216
64. Event 127, suppressed Charge 1 VNIR and MWIR muzzle plume spectra. Flash did not occur and the VNIR spectrum is representative of background.	217
65. Event 127, suppressed Charge 1 flow imagery and blast trajectory.....	218

List of Tables

Table	Page
1. Average ballistic and thermodynamic properties for the three munitions configurations.	34
2. Theoretical near and far-field ranges for the three munitions configurations.	43
3. Forms of the models, constraints, and resultant mean and standard deviation fit parameters for each configuration.	50
4. Goodness of fit measures, numbers of free parameters, and constraints for each model and munitions configuration.	52
5. Average ballistic, propellant, and blast properties for three munitions configurations.	59
6. Average values of the fit parameters for each munitions configuration.	67
7. Properties of the muzzle gas at shot exit.	72
8. Muzzle blast and flash quantities for spherical dimensionality ($n = 2$).	75
9. Potassium and sodium level and transition properties [100].	91
10. Potassium profile line, scale, and continuum parameters.	101
11. Excitation temperatures (Kelvin) for potassium and sodium transition ratios.	106
12. Propellant and observation details for each munition configuration. Stoichiometry is relative to carbon. R_d is the incomplete combustion H:C ratio. The numbers for each instrument resolution indicate the useable data out of the total observed.	116
13. Model parameters for optimized fit to peak spectra from combusting and non-combusting plume. Derived quantities are indicated by italics. Gas mixing fraction indicates the percentage of each species relative to the concentrations of H_2O , CO_2 , and CO	126
14. Model parameters and relative RMS error for the peak intensity spectrum of a combusting muzzle plume.	132
15. Temperature rate parameters	137

Table	Page
16. Numbers of firings, successful collection of each signature type, and firings for which all signatures were available are indicated for each munitions configuration.....	145
17. Mean phenomenological blast, VNIR, and MWIR features for each munitions configuration. Variability is indicated by the standard deviation of each feature, expressed as a percent of the mean value, per configuration.....	151
18. Mean empirical blast, VNIR, and MWIR features for each munitions configuration. Variability is indicated by the standard deviation of each feature, expressed as a percent of the mean value, per configuration.	152
19. Propellant properties.....	181
20. Properties of ideal propellant deflagration interior to the gun.....	183
21. Equilibrium muzzle gas properties from BLAKE.....	184
22. Plume properties for stoichiometric mixing and complete combustion	185
23. Thermodynamic and interior ballistic properties at well-defined CBP states.	194
24. Location of alkali lines present in muzzle flash spectra.	196
25. Blast features	204
26. VNIR features.....	205
27. MWIR filter features.....	206
28. MWIR square-band features.....	207
29. MWIR phenomenological features.....	208

CHARACTERIZATION AND DISCRIMINATION OF LARGE CALIBER GUN BLAST AND FLASH SIGNATURES

I. Introduction

Remote detection and exploitation of gun firing signatures is an important, underdeveloped asset to the warfighter, both tactically and strategically. This assertion is the motivation of the work presented here and is taken as axiomatic, and is easily justified. Consider:

It is late at night and two American F-16s are returning from a ten hour patrol over Afghanistan. As they transit through the Kandahar region, one pilot notices flashes from what appears to be triple-A (anti-aircraft artillery) and small arms. The weapons are being fired from a site known to the pilot as one of Al-Queda's main training facilities, and invoking the right to self-defense, he releases a 500 lb Mark 82 Guided Bomb Unit (GBU-12) Laser-Guided Bomb (LGB) on the position. Weapons fire from the site ceases and both pilots return to base.

Tragically, the engagement was "blue on blue" and four Canadian soldiers lost their lives. The incident occurred on April 17, 2002 at Tarnak Farm Multi-Purpose Range Complex [1]. The former Al-Queda installation had been converted to a multi-purpose Coalition firing range where a section from "A" Company, 3rd Battalion, Princess Patricia's Canadian Light Infantry BG (3 PPCLI BG) were conducting live-fire exercises. Mistakenly perceiving the weapons fire as a threat and lacking critical information, the

pilots responded, resulting in the fourth reported case of fratricide during Operation Enduring Freedom [1]. Combat Identification (CID) should be sufficient to prevent these “blue on blue” engagements; however, despite considerable effort since Operation Desert Storm, the rate of friendly-fire incidents has increased [2].

Automated detection, characterization, and identification of weapon signatures – if merged with a real-time battlespace awareness system – has the potential to reduce such incidents. The current battlespace awareness systems did not (and perhaps could not) provide the necessary real-time information; however, with modern technological advances in remote sensing and pattern recognition, such a system is conceivable. Indeed, the U.S. Navy has recently awarded a Small Business Innovation Research (SBIR) award for the explicit purpose of characterizing muzzle flash signatures such that friend or foe can be identified [3]. Consider how a hypothetical future scenario may transpire. Weapons fire is observed by both the pilot of a fighter jet and onboard sensors. Before the pilot even has the opportunity to inquire about the presence of hostile forces in the region, the jet’s onboard target recognition system analyzes the signatures and identifies their source as allied artillery. The pilot confirms with his airborne controller that friendly forces are conducting live-fire exercises and continues his patrol. An alternative outcome could be the identification of hostile weapon signatures from an insurgency training site, providing valuable intelligence and enabling preemptive interdiction operations.

Sufficient knowledge and understanding of gun firing signatures – such that friend or foe can be classified – is only one component of a battlespace awareness system, but it is obviously an important component. If characterization of signatures is improved to the point that a weapon can be further identified, the effectiveness of the warfighter’s

response can also be improved; e.g. the counter-fire necessary to eliminate hostile tanks is different than would be employed against mobile artillery, and knowledge of which counter-measures to employ (by identifying the weapon system from its signature) may save valuable resources, or even lives. To the strategic warfighter, identification of weapons or even general classes of systems can reveal an adversary's level of sophistication and the extent of foreign proliferation; both influence the diplomatic and military response.

Beyond the ideality of warfighters utilizing weapons signatures, not much more will be said on the topic – this is not an exposition on strategy, policy, or doctrine – rather the point is to indicate that a thorough understanding of weapon signatures is necessary for practical application. Recognizing this fact, over the past decade the remote sensing group (RSG) at the Air Force Institute of Technology (AFIT) has endeavored to describe signatures of various transient combustion events that occur in the battlespace. Aircraft engines, rocket exhaust, and missile plumes have been investigated [4 – 6]. Much study has focused on the infrared spectra of various types of high explosives [7 – 14]. Fruits have included the development of phenomenological and empirical models that describe several aspects of combustion fireball thermochemistry and temporal dynamics [15, 16] and techniques to discriminate between classes of explosives [17, 18]. Gun firing signature has previously received only limited study by the RSG [19, 20], a point which this research addresses.

Many properties of gun firing signatures are already understood. Muzzle blasts from small-arms have been thoroughly investigated in laboratory environments [21 – 27], and relationships for scaling the phenomena to larger caliber weapons have been developed

[23:169-174; 28, 29]. Similarly, spatial and temporal aspects of muzzle flash have been well-characterized [21, 28, 30 – 32]. Indeed, the understanding of both blast and flash signatures have enabled the recent development of several technologies that localize the source of weapons fire using acoustic [33 – 35] or broadband flash [36 – 38] signature characteristics. However, further battlefield characterization – such as weapon classification, not merely location – is hindered because details of firing signature's spectral content and assessment of variability in the signatures are strangely absent in the published literature. Whether these topics are being researched and not reported (unlikely) or the research focuses on aspects other than these signatures (more likely) is not known. Circumstantial confirmation of the need for characterization of these signatures is evident in that results of this research have already been requested by members of academic and professional communities for the precise reason that they are one of few that have been available.

Motivated by the preceding discussion, the objectives of this research are: (1) provide a characterization of remotely observable optical and infrared gun firing signatures; and (2) identify features that may be extracted from firing signatures and used for classification of weapon configuration. The objectives do not imply an exhaustive study of gun firing signatures was attempted. Indeed, such an undertaking would require investigating the full range of gun weapons (such as small-arms, howitzers, cannons, etc.) as well as all remotely observable firing phenomena. Considering that the latter includes the electromagnetic spectrum spanning the ultraviolet through very high frequency (VHF) radio waves and complex shock structure consisting of precursor, compression and rarefaction waves whose power spectra evolve in time [23:3-14], such an undertaking

is beyond the scope of research performed in a single doctoral dissertation. Rather, this work addresses two chief deficiencies in a description of gun firing signatures in order to enable further characterization of the battlespace.

First, characterization of signatures from a statistically significant number of large-caliber gun firings has been unavailable. This is principally because of the logistical difficulty associated with collecting high-fidelity gun firing signatures outside of a laboratory environment [23:13]. The results of this work include collection of signatures from 201 firings of a 152 mm howitzer, allowing for a direct characterization of large caliber gun muzzle blasts rather than relying on simulation or scaling relationships. The number of observations permits firing-to-firing variation to be assessed, which is critical to identifying signature features that may be used for classification.

The second, principal deficiency is that spectral characterization has been limited to a handful of investigations from the 1940s – 1970s whose quality are inferior to those available with modern instrumentation [23:397-412; 30, 31, 39, 40]. This research presents visible through near infrared (VNIR) and midwave infrared (MWIR) muzzle flash spectra of the 152 mm howitzer. Besides alleviating the dearth of available spectral data, the results are significant because collection fidelity represents significant improvement over previous results. Sensitivity and spectral resolutions are sufficient to discern fine structure of several emitters in the VNIR, and time-resolved MWIR spectra enable characterization of the temporal behavior of muzzle flash.

Collection and characterization of a statistically significant number of blast and flash firing signatures from a large caliber, 152 mm howitzer addresses the first objective and facilitates the second. Observable firing signatures are reduced to a set of features that

may be used to discriminate between weapon configurations. Reduction of signatures to features is advantageous because the correct choice of features can convey most (if not all) information about a signature in a considerably smaller parameter space. This is necessary to optimally apply pattern recognition techniques which often suffer if dimensionality is too high [41]. Features are obtained from the remotely observable gun firing signatures comprised of high-speed imagery of muzzle blast propagation, spectral content of VNIR muzzle flash, and time-resolved spectra of MWIR plume emissions. Phenomenological and empirical features extracted from these components are assessed for their ability to differentiate amongst three munitions configurations (essentially propellant configurations) fired from a 152 mm howitzer. Limited data on a 120 mm tank cannon were obtained, and the most salient features are used to demonstrate an improved ability to discriminate between different gun weapons.

This research advances the understanding of gun firing signature content and its phenomenological development. In particular, investigation of a large caliber gun provides data on signature variability on a weapon that is unlikely to be measured in a laboratory environment and difficult to measure outside of one. Just as an understanding of gun firing acoustics and flash has enabled localization of weapon fire, characterization of spectral content enables improved battlespace awareness (via classification) and has the potential to give rise to new applications advantageous to the warfighter.

Document Overview

Chapters III – VII of this document were written as independent articles for publication to update and supplement the academic literature. As a consequence, there is a level of redundancy that was unavoidable in order to ensure that each chapter is a complete text detailing its subject matter. However, the redundant information (primarily discussions of motivation, background, and experimentation) are presented in a context unique to the focus of each chapter and should not be considered immaterial. An overview of the remainder of this document follows.

Chapter II provides the background material necessary for understanding this work. This includes a description of gun firing phenomenology, from which subsequent chapters further provide selected details and summaries as necessary. Summaries of prior research on muzzle flash spectra and classification of battlespace events are also provided, and a brief discussion of linear discrimination is presented.

Chapters III and IV examine the muzzle blast wave. Characterization is performed using observations from a high-speed, optical imager. The fidelity with which the blast wave can be represented by various low-dimensionality models is presented, and flow regions are described. Stability of blast features is assessed in context of munitions discrimination, and possible physical interpretations of the features are offered.

Chapters V and VI present time-resolved visible and infrared spectra of plume emissions. Several physical properties of the munitions and plume thermochemistry are estimated through a combination of modeling and direct characterization. Monocular passive ranging using oxygen absorption in the near infrared is demonstrated as an

unanticipated practical application. A technique for discrimination of classes of munitions is identified and potential of features for classification is demonstrated.

Chapter VII is a capstone that quantifies classification of different weapon configurations. The results of Chapters III – VI are used to define sets of empirical and phenomenological features, and additional band-integrated intensity features are obtained from MWIR spectra using several ideal and real-world spectral filters. A technique for feature selection and class discrimination is presented in detail. The most salient firing signature features are identified, and the resulting stabilities and classification accuracies are reported.

Conclusions are presented in Chapter VIII along with recommendations for future study. Following the conclusions are several appendices that provide additional data and details important to this research but whose length precluded inclusion in the stand-alone chapters.

II. Background

Gun firing blast and flash signatures are a result of complex flow and thermodynamic processes occurring interior and external to a gun weapon. Because characteristics of the signatures are directly dependent on these processes, it is instructive to review the phenomena that give rise to them. Firing phenomenology has been extensively studied and the current authority, Klingenberg and Heimerl's *Gun Muzzle Blast and Flash*, is a compilation of more than 60 years of research on the topic [23]. The bulk of this chapter provides a summary of firing phenomena that is drawn from the work of Klingenberg and Heimerl as well as the broader body of literature.

The remainder of this chapter is devoted to a review of historical muzzle flash spectra research, a summary of battlespace classification efforts by the AFIT RSG, and a very brief discussion of two linear classifiers. These provide the context necessary for the work presented in Chapters III – VII.

Gun Firing Phenomenology

A gun may be defined as any weapon that ejects a projectile from one end of a barrel (the *muzzle*) by the application of force at the other end. In conventional guns, force is provided by the combustion of a solid propellant in a contained volume (the chamber or *breech*). Propellant composition, mass, and projectile type (such as high explosive, armor piercing, etc.) are often packaged together as a particular munitions configuration for an intended application.

The firing of a gun begins with initiation of the propellant's igniter charge, followed immediately by combustion of the propellant itself. As the propellant burns in the fixed

volume of the gun chamber, it is converted to a gaseous state, increasing chamber pressure and driving the gases to higher temperatures. This rise in temperature results in higher burn rates, creating increasingly more gaseous propellant, and the cycle of escalating pressure and temperature continues [42]. When the chamber pressure increases sufficiently, frictional forces between the projectile and munition's casing are overcome, and the projectile begins to accelerate down the barrel; this is known as *shot start*. As the projectile traverses the gun barrel and additional volume becomes available, the propellant gases expand into it.

Initially, the rate of propellant burning is such that chamber pressure rises despite expansion of the propellant gases. When all available oxygen is consumed, propellant burning ceases. This, combined with the continuing increase in volume as the projectile travels down the barrel, results in a decrease in chamber pressure as the propellant gases further expand and cool [43]. Pressure as a function of time (or more appropriately, as a function of distance the projectile has traveled down the barrel) is dependent on the burn rate and geometry of the propellant; the more quickly the propellant is consumed, the more rapidly the chamber pressure increases. The projectile's acceleration, velocity, and travel are dependent on the entire pressure-distance history [44]. Pressure history affects more than the kinetics of the projectile – it also defines the thermodynamic state of the propellant gases leaving the barrel, and thus defines the conditions that lead to weapon signature.

A wide range of gun systems have very similar pressure-time profiles and a relative scaling of the curves' magnitudes allows for a representation of many systems [43]. The relationship between breech pressure and projectile velocity versus in-barrel distance for

a 155 mm howitzer* fired in its full charge configuration is demonstrated in Figure 1. The curves are digitized versions of those generated by Stiefel using the Interior Ballistic Interactive Simulation (IBIS) code for profiling large caliber munitions [43]. Also shown are the curves for a constant breech pressure (CBP) gun model often used by ballisticians to estimate the maximum efficiency of a gun system (i.e. projectile muzzle velocity) and thermodynamic state of gaseous propellant flow [45]. The CBP model is presented in detail with an example calculation in Appendix B.

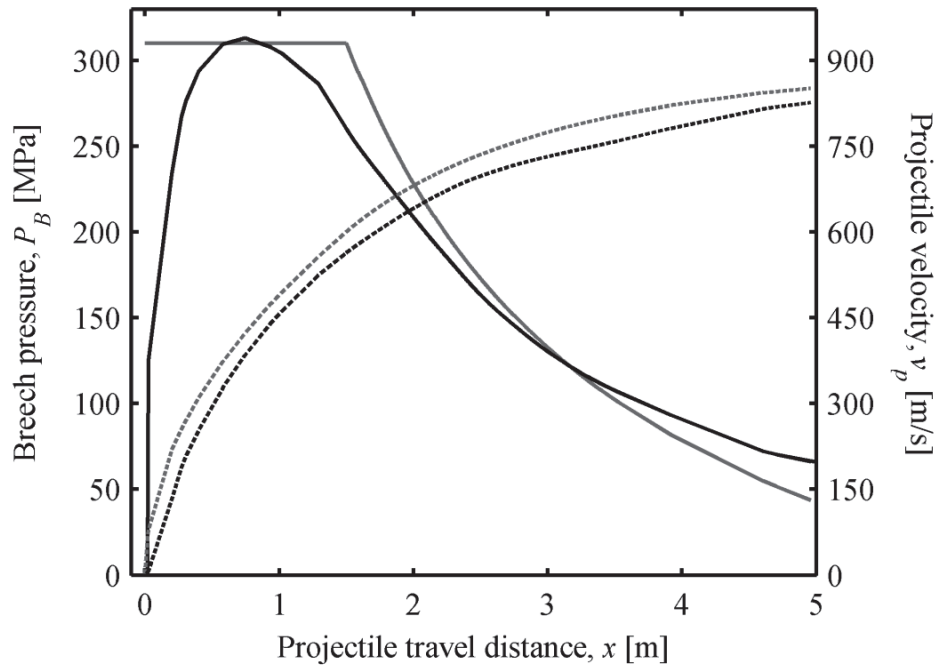


Figure 1. Breech pressure (—) and projectile velocity (···) as a function of distance the projectile has traveled down the barrel. Curves are digital reproductions of those determined by Stiefel for a 155 mm howitzer [43]. CBP simulation of pressure (—) and velocity (···) are estimates of the maximum performance of the gun.

* Interior ballistics data are shown for a 155 mm howitzer because it is similar to the 152 mm howitzer studied in this research. The data are calibrated with experimental measurement and serve as a reference point for typical large caliber interior ballistics [43].

The projectile is accelerated by mechanical work performed by expanding propellant gases until it exits the barrel (*shot exit*). After shot exit, the high pressure propellant gases are no longer confined to the barrel and flow from the muzzle at supersonic velocity. A shock discontinuity is formed as the muzzle flow impinges upon and compresses atmosphere [27:161-165]. The shock is characterized by strong discontinuities in pressure and density and expands coincidentally with the gases that drive it. Eventually, drag exerted by the atmosphere decelerates the flow sufficiently such that the pressure discontinuity detaches and propagates as a blast wave. The blast propagates as a supersonic pressure wave whose amplitude and velocity decrease as it expands. It is useful as a firing signature because its strength and propagation are directly related to weapon configuration through the thermodynamic state of the muzzle flow and geometry of the gun muzzle [46:186]. Propagation of the blast and its potential to provide classification features are examined in Chapters III – IV.

Despite the transient nature of the muzzle flow, it quickly develops into a highly under-expanded, supersonic region at the exit plane of the muzzle and may be treated as a quasi-steady jet [23:87-90; 47]. The region is depicted schematically in Figure 2. It is characterized by an upstream Mach cone that separates the high pressure in-bore flow from the under-expanded supersonic flow; a barrel shock that allows flow to expand laterally but also constrains it to a curved region that expands downstream of the muzzle; and a Mach disk that acts as a boundary between supersonic and subsonic flow regions. The flow field is initially limited in its expansion until the blast wave detaches and propagates beyond the range of the flow [48].

The contact surface is a discontinuity that plays an important role in the flow-field. It is an interface between ambient air trapped against the blast wave downstream and gaseous propellant passing through the Mach disk upstream. Eventually the contact surface dissolves due to shear between the largely different velocities on its lateral boundaries, causing the two regions to turbulently mix. Because most propellants are fuel rich, combustion can only continue to completion after entrainment of ambient air and if temperatures in the flow are high enough to support ignition [23:200-202; 27:166; 49]. The Mach disk is especially important in this regard because it is a shock front normal to the axial flow and causes propellant gases to be heated as they pass through it and decelerate to subsonic velocities [50, 51].

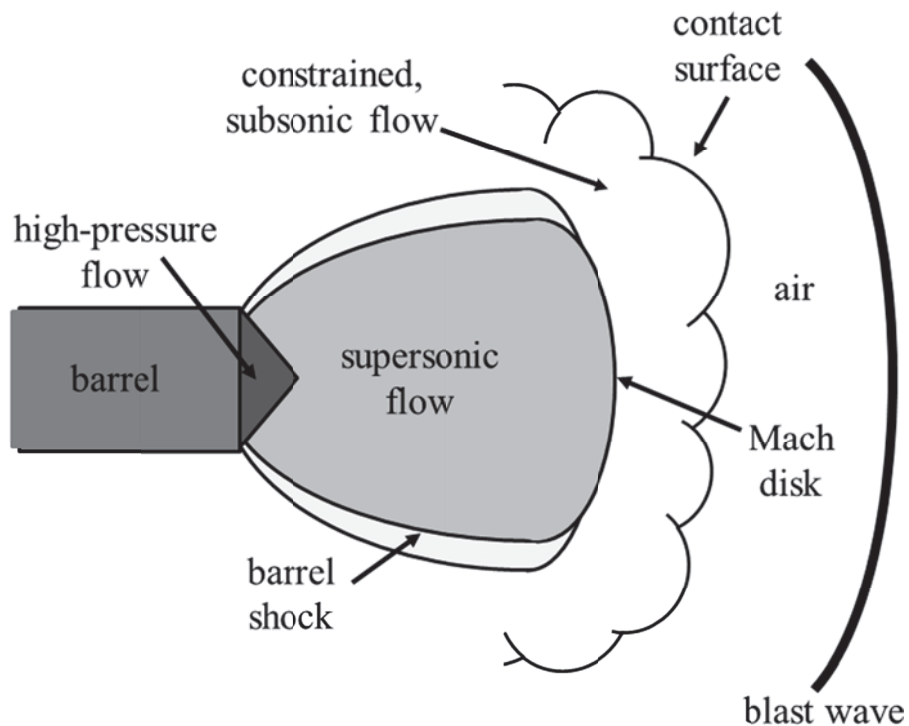


Figure 2. Schematic depiction of quasi-steady supersonic flow that develops after shot exit.

An additional source of shock heating is introduced by muzzle brakes that are often equipped on large caliber guns [23:177-179]. Due to the significant stress self-imposed on large caliber guns by their recoil, muzzle brakes are used to redirect the flow field and recover momentum. The double-baffle muzzle brake shown in Figure 3 is a common design owing to its high efficiency. In the double brake design, flow is deflected laterally, thereby reducing efflux through the central bore and inducing a force on the muzzle in a direction opposite to the recoil. A consequence is the formation of multiple flow regions, each with the characteristics shown in Figure 2. One of the significant drawbacks of muzzle brakes is that additional shock fronts are formed; these choke the flow and contribute to additional heating of the propellant gases at the muzzle [28, 52].

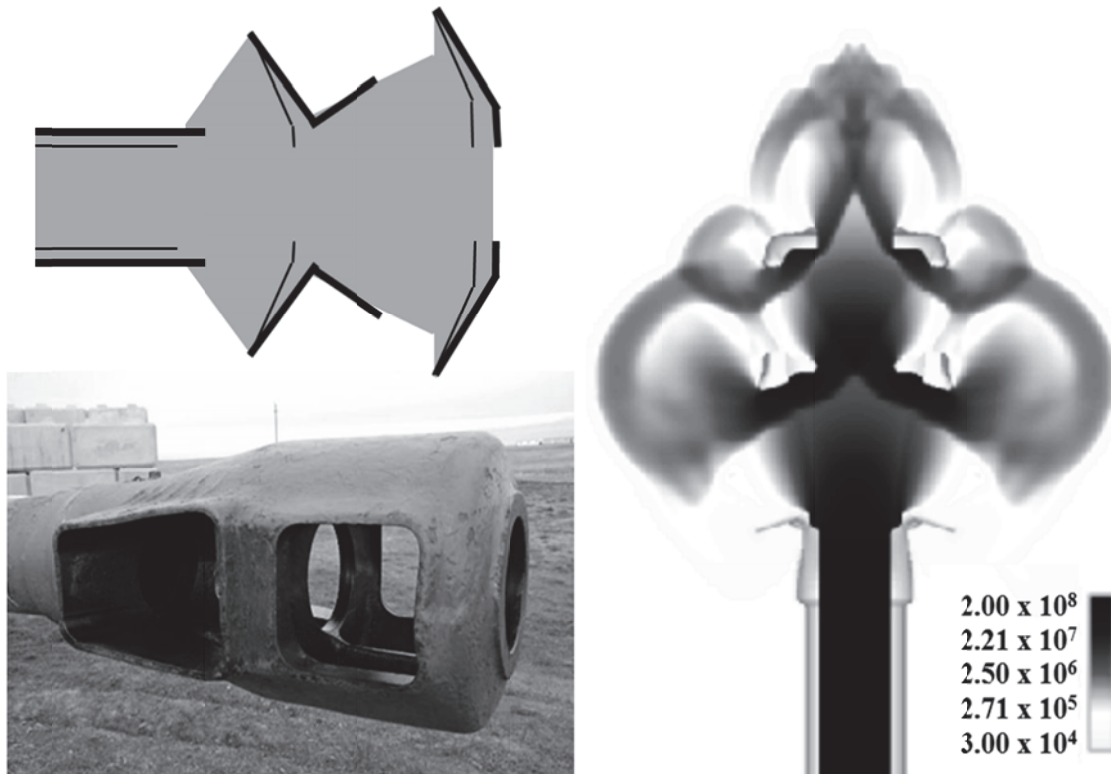


Figure 3. Double-baffle muzzle brake. *Upper left:* schematic depiction of a typical brake. *Lower left:* 152 mm howitzer brake. *Right:* Computational fluid dynamics simulation of flow shows the existence of strong shocks in the muzzle [52]. Color scale indicates pressure in Pascals.

Line, band, and continuum radiation are the result of the high temperatures of the gases escaping a gun's muzzle. Figure 4 depicts several temporally and spatially distinct regions in which these emissions occur [28, 30, 31, 39]. Emissions from hot, non-combusting propellant gases that exit the muzzle immediately after ejection of the projectile are the *primary flash*. The region is spatially very small and is located in the high-pressure flow. *Intermediate flash* is also due to hot, non-combusting gases, but it is located further downstream from the barrel. It is the result of thermal self-luminescence of expansion-cooled propellant gases that are reheated after pass through shocks (primarily the Mach disk). The third region is *secondary combustion* (or secondary flash) and is characterized by re-ignition of propellant gases after turbulent entrainment of atmospheric oxygen into the downstream plume. The term *muzzle flash* typically refers to secondary combustion (and does hereafter as well) because it is the greatest source of radiation in size, intensity, and duration [28].

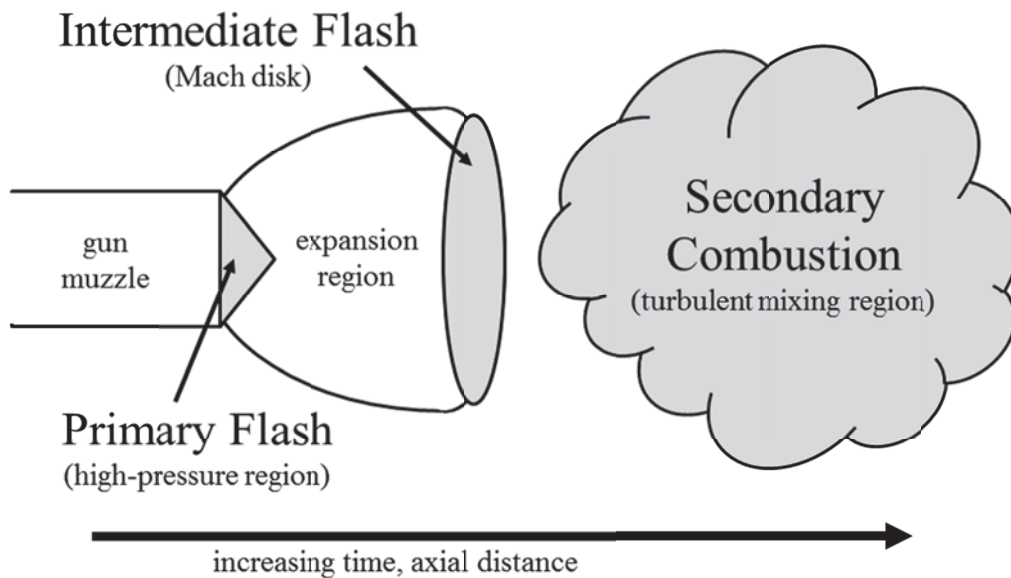


Figure 4. Primary flash, intermediate flash, and secondary combustion muzzle flash regions are separated temporally and spatially.

Only the occurrence of secondary combustion is not assured. Re-ignition requires that certain conditions be satisfied. These principally include sufficiently high temperatures and fuel-to-oxygen mixing ratios that can sustain combustion. For most propellants, muzzle gases are fuel-rich and contain large concentrations of combustion intermediaries, soot, and propellant particulates. The turbulent entrainment of atmospheric oxygen provides a range of mixing ratios that will support combustion [32, 49, 53]. Plume temperature is often the critical factor for re-ignition, and several studies have found that a minimum temperature of 900 – 1,000 K is required, independent of propellant [23:263-264; 28, 49]. After re-ignition, the flame front quickly envelops the entire muzzle plume, resulting in combustion emissions throughout the visible and infrared.

Figure 5 depicts a notional propellant energy potential curve during gun firing. Detonation of the propellant's igniter at shot start provides the activation energy, E_a , necessary to set the propellant burning (at $\xi \sim 0.2$ in the figure). Intermediaries – such as H_2 , CO, soot, and propellant particulates – are formed and heat, ΔH_d , is released ($\xi = 0.2 \sim 0.4$) [27]. This supplies the energy needed to accelerate the projectile. Burning continues as the projectile travels but ceases when available oxygen is consumed ($\xi \sim 0.4$), prior to shot exit. Combustion can resume downstream of the muzzle if the temperature is sufficient to re-ignite the plume (denoted in the figure as equivalent thermal energy E_T). When this occurs, intermediaries react with atmospheric oxygen to form H_2O , CO_2 , and N_2 (for ideal, complete combustion, $\xi = 0.5 \sim 1.0$) and releases additional combustion energy, ΔH_c [54]. This further raises the temperature of the plume and has been correlated with higher sustained temperatures [12]. The plume radiates strongly during combustion and continues to emit as it cools.

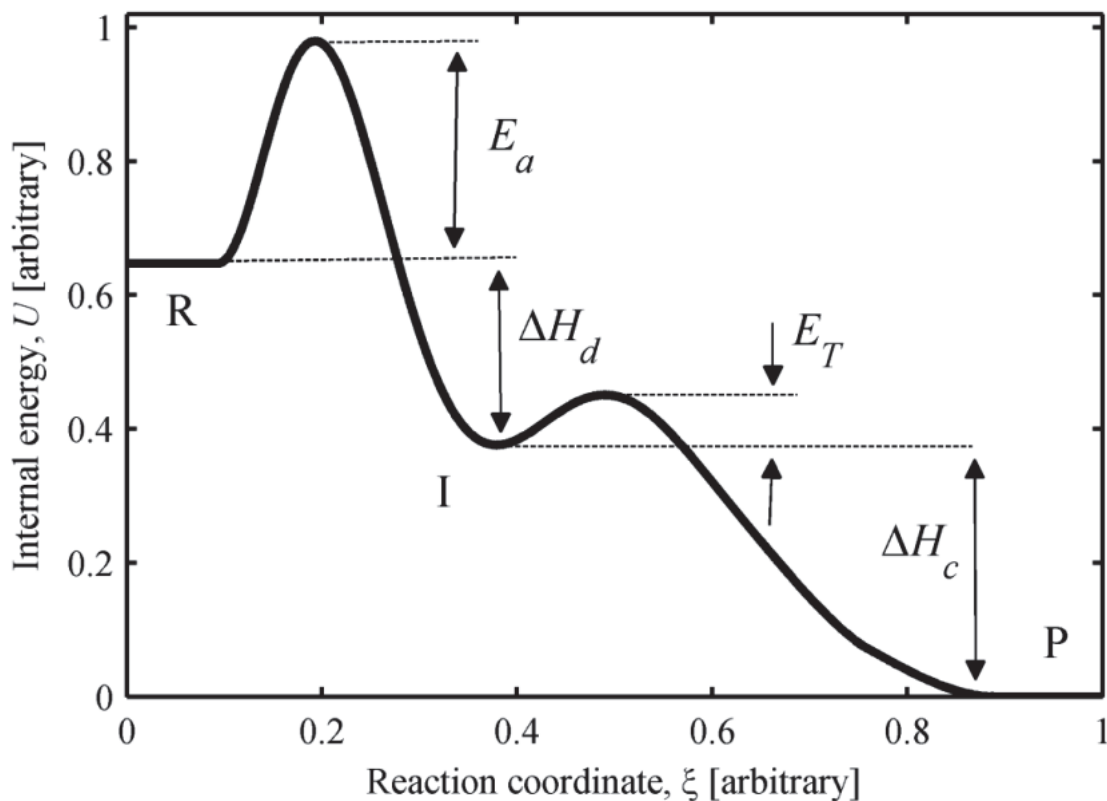


Figure 5. Notional internal energy potential for combustion of propellant during gun firing. Propellant and oxygen reactants (R) release energy ΔH_d when converted to intermediaries (I). Re-ignition allows the intermediaries to combust to product species (P) with the additional release of combustion energy ΔH_c .

If re-ignition does not occur, ΔH_c remains as internal energy of the propellant and does not contribute to weapon firing signature. Chemical flash suppressants are often added to propellants for this precise purpose. Temperature can be increased to greater than 1,200 K without re-ignition with the addition of certain alkali-containing compounds that consume radicals needed to sustain combustion, e.g. O, H, and OH [49, 55 – 57]. In this case the muzzle plume remains composed of hot, unreacted intermediary species, particulates, and air. However, even when secondary combustion is inhibited and flash does not occur, the large concentrations of particulate matter emit Planckian radiation that contributes to gun firing signature in the infrared.

Muzzle Flash Spectra Research

Although spatial and temporal aspects of the muzzle flash are understood [28, 30, 31, 39], spectral characterization is lacking and there are only a handful of published studies that have assessed the spectral content of firing signatures. The limited amount of research in this area is summarized below in context of its historical development. To convey the relative fidelity of previously collected muzzle flash spectra, examples are reproduced when permitted.

The Franklin Institute Research Laboratories, on contract with the Army, completed the first in-depth program to “study the physical properties of gun flash” in 1949 [31]. The institute’s work was foundational in identifying the aforementioned temporally and spatially separated muzzle flash regions. Indeed, much of the terminology describing muzzle flash that is used today resulted from this program’s report. Visible and ultraviolet (UV) spectra of 20 mm and .50 caliber machine gun firings were collected, but only the findings were reported. These include identifying that the principal emissions in the visible and UV portions of the spectrum are due to atomic K, Na, and Cu; molecular OH, CuO, CuOH, CuH, CuCl, CaO, CaOH, and CO₂; and particulate matter.

In 1967 the Army Materiel Command, in an effort to provide the Armed Forces with an authoritative reference on the subject of muzzle flash, published the *Engineering Design Handbook: Spectral Characteristics of Muzzle Flash* [30]. It was a consolidation of the research of several laboratories, but is primarily composed of the results from over 75 progress reports of The Franklin Institute’s research on muzzle flash from the preceding two decades. The institute’s objective was suppression of the visible muzzle flash signature by shifting emissions to the infrared. While the method of suppression

was not successful, its investigation revealed that greater than 99% of the radiated energy is contained in the infrared, and infrared emissions are primarily due to continuum, CO₂, H₂O and to a lesser extent OH and NH₃.

The handbook reported spectra of a 20 mm gun that were collected using a combination of visible and infrared spectrographs with photographic plates. Plate sensitivity typically required 20 – 2000 firings to obtain a single primary or intermediate flash spectrum, and only 1 – 5 firings for secondary combustion because of its significantly greater intensity. Relative spectral intensity was estimated by the exposure level on each plate, and reproductions of reported visible and infrared results are shown in Figure 6 and Figure 7. Spectral resolution was limited by granularity of the plates and the fidelity with exposures could be interpreted.

Spectra for several large caliber guns were also collected using a spectrometer with multi-channel detectors coupled to an oscilloscope. Photographs of the oscilloscope traces (reproduced in Figure 8) provided the data necessary to plot the spectra reproduced in Figure 9. Spectral resolution was sufficiently limited by the use of a multi-channel detector, and only broad features can be identified. However, temporal resolution ($\Delta t \sim 10$ ms) was sufficient to identify and further characterize the aforementioned primary, intermediate, and secondary flash temporal regions. Secondary combustion emissions were found to be 10 – 100 times greater than emissions from non-combusting plumes, and 100 – 1000 greater than those from intermediate flash.

Gun Muzzle Blast and Flash includes a chapter on flash spectra that summarizes research from 1973 – 1974 originally published by Klingenberg in German [23:397-412]. Visible muzzle flash of 7.62 mm rifle firings were dispersed onto photographic film.

Lines from sodium, potassium and calcium; bands from CaO and CaOH; and significant continuum radiation were observed. Time-resolved recordings were also obtained with a drum camera. Only the unresolved sodium D lines, CaOH, and continuum were apparent due to reduced exposure time. Film exposures were converted to spectral intensity curves using a densitometer and the most prominent features were identified. The quality of the spectral curves represented a substantial improvement over previously reported results.

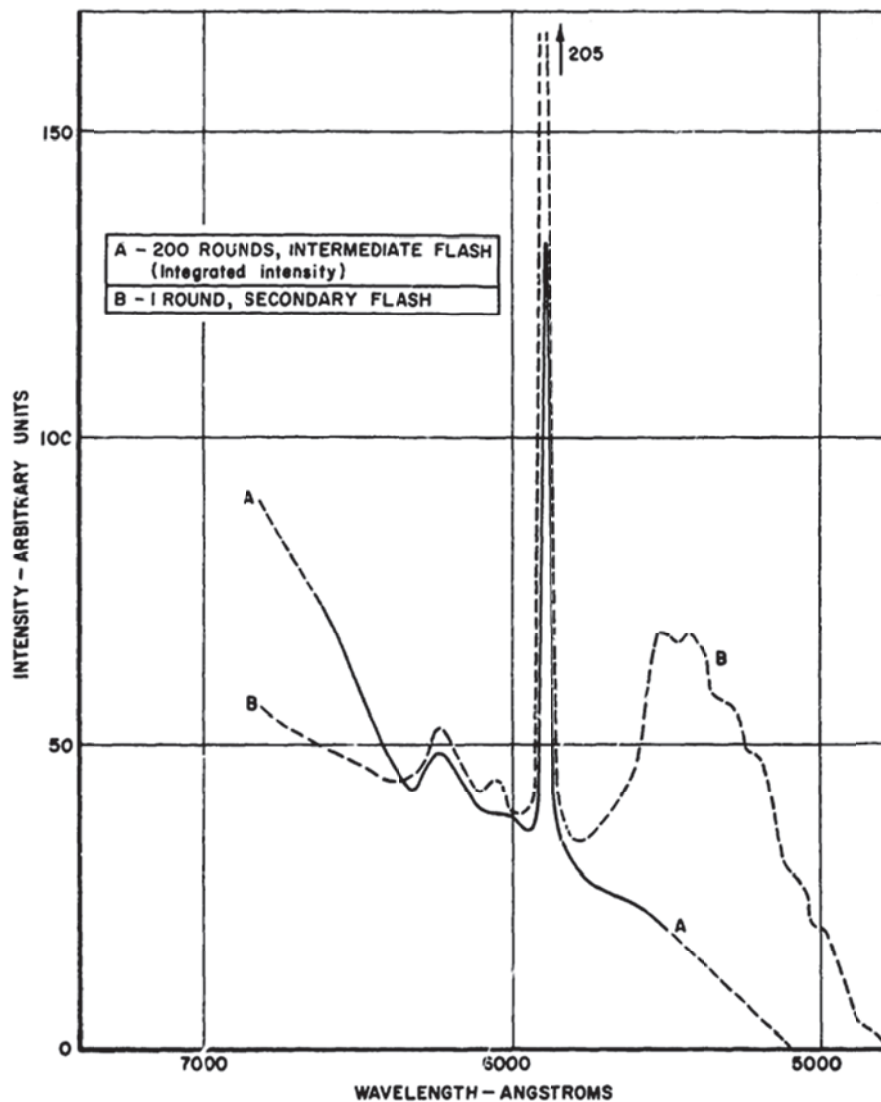


Figure 6. Comparison of visible spectral distribution of intermediate and secondary flash [30:2-3].

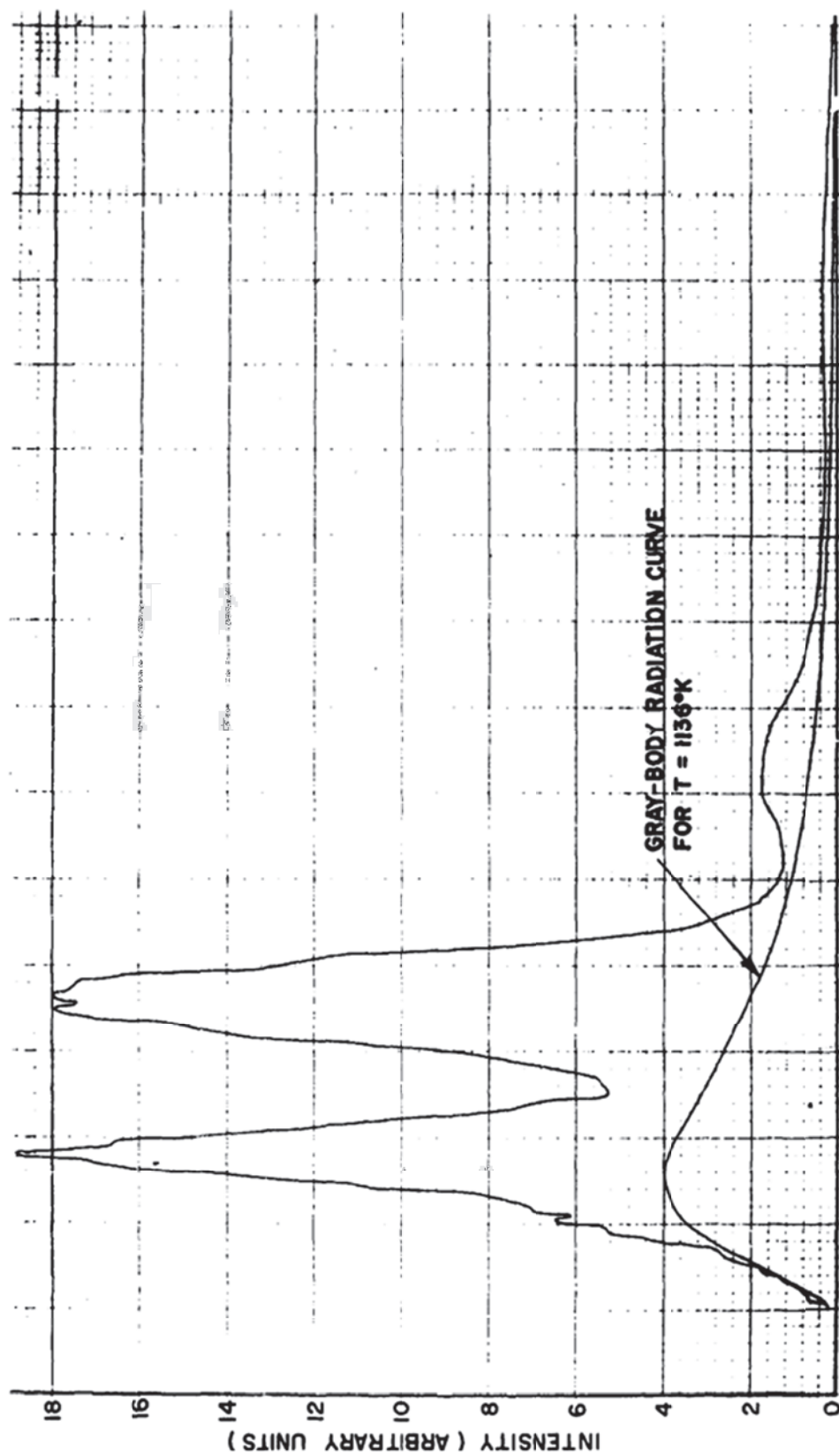


Figure 7. Spectral distribution of infrared radiation from secondary flash [30:2-9].

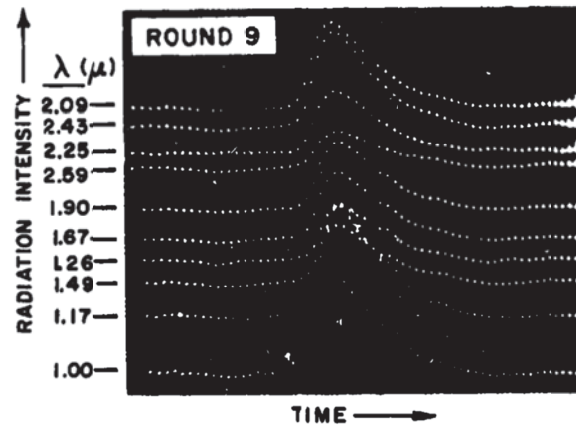


Figure 8. Oscilloscope traces of suppressed flash from 155 mm gun [30:3-11].

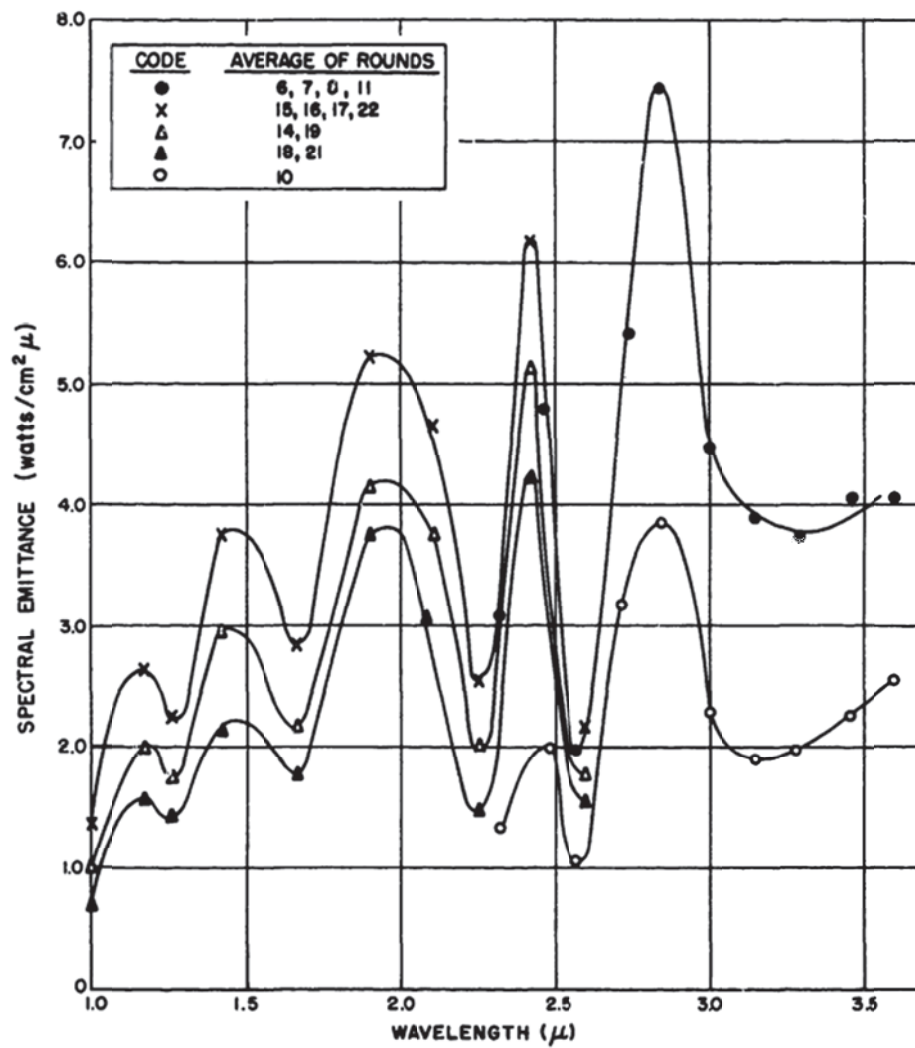


Figure 9. Spectral emittance of unsuppressed flash from 155 mm gun [30:3-8].

Investigation of spectroscopic temperature measurement by Klingenberg and Mach in 1976 included limited collection of additional time-resolved visible muzzle flash spectra [39]. Spectra of 7.62 mm firings were recorded to film with a drum camera and converted to spectral intensity plots. Temporal resolution of ~1 ms was possible in the most intense spectral regions and spectral resolution appears better than $\Delta\lambda \leq 25$ nm. CaOH, CO, and CN bands were identified and reported to account for nearly all non-particulate, visible, continuum radiation. Combustion was found to be caused by re-ignition of propellant burning byproducts, yielding an increase in plume temperature of up to 1,600 K.

Recently reported muzzle flash signatures have been limited to band-integrated radiances or spectra in very narrow bands ($\Delta\lambda \leq 10$ nm) centered near prominent emission lines [36 – 38, 58, 59]. No other muzzle flash spectra have been identified in the available literature since Klingenberg's work in the mid-1970s. Modern visible and infrared muzzle flash spectra collected during this research are characterized in Chapters V – VI.

Battlespace Classification

Battlespace awareness is defined by the *Department of Defense Dictionary of Military and Associated Terms* (Joint Publication 1-02) as [60]:

Knowledge and understanding of the operational area's environment, factors, and conditions, to include the status of friendly and adversary forces, neutrals and noncombatants, weather and terrain, that enables timely, relevant, comprehensive, and accurate assessments, in order to successfully apply combat power, protect the force, and/or complete the mission.

Characterization of the battlespace includes the use of remote sensing platforms to provide this awareness, specifically detection and identification of military assets [61]. Many battlespace events result in combustion phenomena that are easily detected by their intense radiative emissions throughout the visible and infrared. For example, explosive detonations, gun firings, aircraft afterburner, rockets, missiles, etc. all expel gases that are burning (or capable of burning), and even a rudimentary knowledge of physics reveals that combustion sources can be easily detected at great distances.

Identification of a particular battlespace event requires an understanding of its characteristics in order to distinguish it from other sources. Different classes of battlespace sources (e.g. rockets, explosives, muzzle flashes, etc.) can be differentiated based on their temporal characteristics [14]. Distinguishing between types within the same class (e.g. between two guns) is much more challenging. Over the past decade, the AFIT RSG has deployed on several field tests to investigate the use of remote sensing for battlespace characterization. Classification has primarily been applied to signatures from various types of high explosives. Despite the difference in timescales between muzzle flash and explosive fireballs (less than 10 – 100 ms compared to 1 – 5 seconds), a review of the results from explosives is warranted because of the similarity in many of their remotely observable features [12, 13, 15, 30, 31].

Orson and Bagby used temporal overlap of temperature, emissive area, and radiance profiles to discriminate between various static ground and aircraft delivered military ordnance [8, 11, 13]. They found that – despite signature variability introduced by aspect angle, environment, and inherent irreproducibility – distinct explosives could be discriminated from their mid wave infrared (MWIR) emissions. Their conclusion was

significant because it refuted the previously held notion that explosive detonations are too variable for classification.

Dills explored battlespace classification using statistical pattern recognition [17, 62, 63]. Visible, near infrared, and MWIR signatures were reduced to a set of features that characterize various spatial and temporal aspects of explosive fireballs. A robust classification methodology based on Fisher linear discrimination (FLD) and Bayesian decision boundaries was developed. A subset of several temporal features extracted from broadband imagery was shown to be the most effective in discriminating between two of five explosives types. Specifically, linear combinations of the most salient two features provided the best ability to discriminate between two classes in one dimension, but suffered when extended to multiple classes. Dills suggests that a multi-dimensional approach may perform better for multi-class problems.

Concurrently, Gross examined explosive signatures from a phenomenological perspective [9, 10, 15]. After examining a subset of the data of Orson and Bagby, he determined that classification could be improved by a better understanding of the non-Planckian nature of fireball emissions in the MWIR. A physics-based model was developed that characterizes emissions in terms of fireball size, temperature, soot, and gas concentrations of various emitting species. Gross significantly concluded that, in addition to effectively discriminating between classes of explosives, the hydrogen-to-carbon (H:C) ratios derived from the model provide forensic information on the composition of the explosive material.

Slagle drew on the work of Gross to select broad spectral bands which can provide the same phenomenological features (with moderately increased uncertainty) without the

need to acquire the entire MWIR spectrum [18]. Like Dills, he used the FLD statistical technique to identify features with potential to discriminate between two classes of explosives. Phenomenological features offered a better ability to classify than the raw band-integrated intensities upon which the features were based. However, when spectral bands were not constrained to those required to estimate phenomenological model parameters, the ability to discriminate doubled. Slagle concluded that band-integrated intensities and physics-based features can be used synergistically for classification. This concept is explored for muzzle flash signatures in Chapter VII.

Most recently, Gordon investigated the shock dynamics and fireball temperatures resulting from explosive detonation [12, 16]. He observed shock propagation using high speed imagery and modeled its expansion using point blast theory, from which detonation efficiency and shock velocity were estimated. More significantly, fireball temperature was empirically modeled and its rate of decay was found to be highly correlated with heat released in afterburning combustion, indicating its potential for use as a discriminator.

Linear Classification

A thorough search of the literature reveals a wide range of pattern recognition techniques available for classification; however there are a few standard references that can provide a good guided overview [64, 65]. In general, a classifier's effectiveness is reduced as its complexity is increased for a fixed number of observations [41]. The Fisher linear discrimination technique was chosen by Dills then Slagle because of the limited number of observations in their data, per class. FLD is a relatively robust technique that is effective even with small data sets. It linearly projects observations of several features

into a single dimension (i.e. onto a line) which maximizes the separation of classes [64:117-121; 65:360-372]. This in turn maximizes the ability to classify new observations that are projected onto the line. FLD is often used to discriminate between two classes. Dills performed a limited analysis of multiple classes with limited success; hence his suggestion that a multi-dimensional approach may yield better discrimination results.

Multiple discriminant analysis (MDA) is a multi-dimensional generalization of FLD in which signature features are projected into several dimensions that maximize separation of multiple classes. It was chosen as the technique to extend the discrimination of remotely observed battlespace events to large caliber gun firings. The metric that is used to quantify class separation is the between-class to within-class variance ratio, Λ . It is essentially a measure of the differences in class means relative to their spread. The calculation of Λ and mathematics of MDA are presented in Chapter VII, and a more detailed review of the technique is available in the literature [64:121-124; 65:400-407].

To provide a context for the values of Λ presented in Chapters V and VII, several examples are shown in Figure 10. In all cases, MDA was used to project mock features from three classes with different means but equal variance into two dimensions that maximize class separation. Substantial class overlap is indicated by $\Lambda = 0.7$ where there is greater variance within each class than difference between centroids. For $\Lambda = 2.8$ the classes are separated but overlap exists at the peripheries of their distributions. Classes are well separated with $\Lambda \geq 7.5$. For nearly equivalent separations between centroids, $\Lambda = 35.1$ represents a significant reduction in variation of projected feature values (relative to $\Lambda = 7.5$).

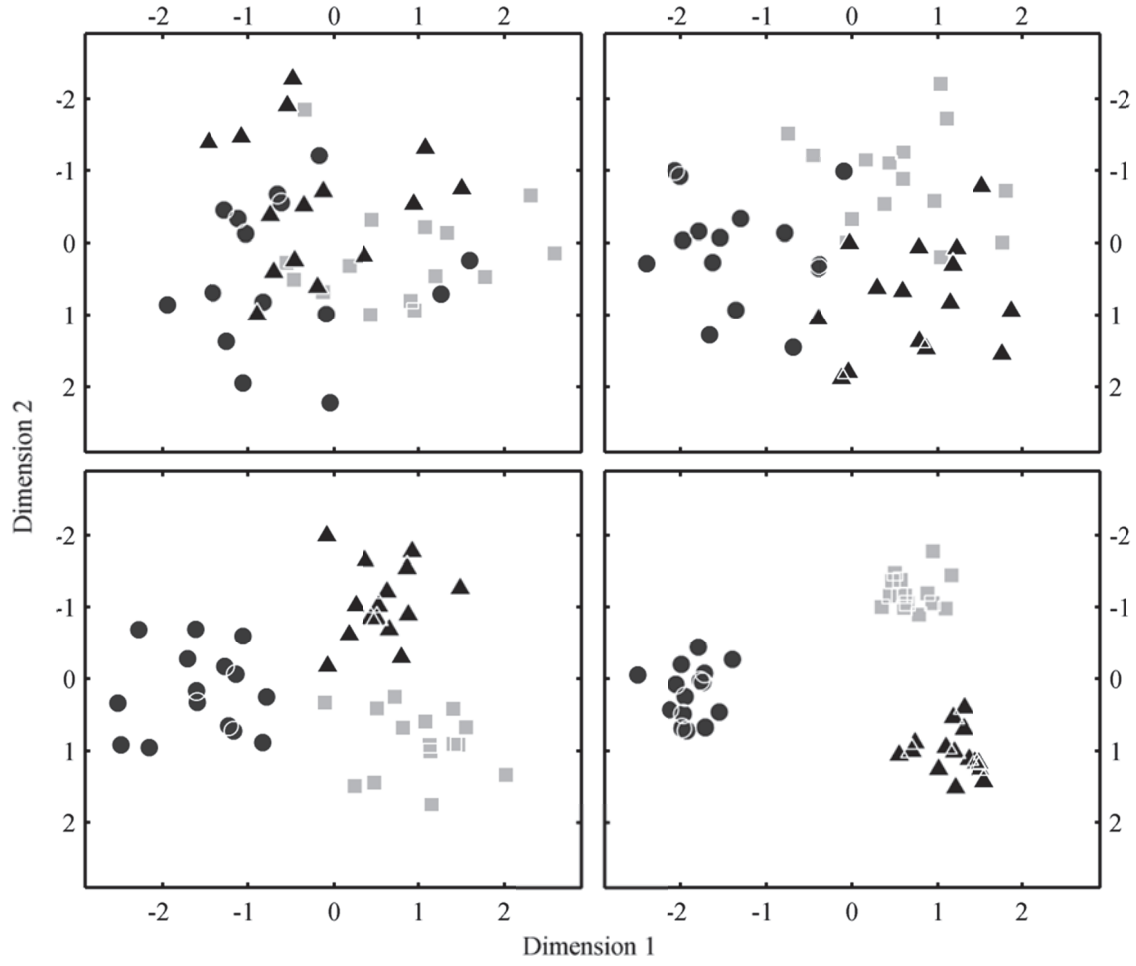


Figure 10. MDA separation of three classes (●, ■, ▲). *Left-to-right, top-to-bottom*: $\Lambda = 0.7$, $\Lambda = 2.8$, $\Lambda = 7.5$, and $\Lambda = 35.1$

III. Reduction of Optically Observed Artillery Blast Wave Trajectories using Low Dimensionality Models

Introduction

Muzzle blasts from laboratory-scale gun sources have previously been well characterized [21 – 25, 23:107-166; 27]. Large-caliber guns have also been studied, primarily to characterize the blast wave overpressure and its harmful effects on gun operators and surrounding structures [23:4; 25, 27 – 29], and a limited number of observations have also been used to verify that phenomena associated with laboratory measurements scale to large-caliber weapons systems [23:167-174, 28]. Blast signatures from a large number of large-caliber gun firings have not been well characterized due to the difficulty in performing a statistically significant number of measurements outside of the laboratory environment [23:13]. The work presented here represents a study of the blast wave trajectories resulting from a total of 201 firings in three similar munitions configurations of a 152 mm howitzer.

Data reduction is accomplished by fitting several blast propagation models to the time of arrival of the blast near to and far from the gun in order to identify the simplest description of muzzle blast wave propagation that represents the observed data. The primary reason for data reduction is the classification problem, which is to be able to differentiate weapon systems – or even multiple configurations of a single system – based on remote observation of its signature. Data reduction allows multiple signatures to be identified or distinguished based on a handful of parameters rather than requiring comparison of large data sets, and it allows for a straight-forward assessment of variance in firing signatures within a configuration and amongst different configurations.

The spatial and temporal ranges that describe different regions of the blast wave's propagation are examined to further refine understanding of the wave and models which may be applied to it. Because optical characterization of artillery blast waves is a non-traditional remote sensing technique, goodness of fit for each model is assessed and those parameters that provide a direct physical interpretation are compared to observation. The fit parameters with potential for discriminating between charge configurations are identified.

Phenomenology

The firing of a gun begins with combustion of the (typically solid) propellant, converting it to a high-temperature, high-pressure gaseous state which performs work to accelerate the projectile down the gun barrel. Shot exit occurs when the projectile departs the muzzle assembly and the supersonic propellant gases being expelled develop into a quasi-steady, under-expanded flow region at the exit plane of the muzzle [22, 32, 47, 51]. This efflux results in a small region at the gun muzzle occupied by a very hot, high pressure gas that begins to expand outward with its leading edge forming a shock as the atmosphere into which it expands is compressed. As the shock continues to develop, it leads a series of positive and negative pressure transients, the entire train of which forms a blast wave. The blast wave surrounds the entire flow-field and initially limits expansion until it detaches from the flow, allowing the jet plume to expand freely [23:157-162; 27]. Prior to detachment, the gas dynamics of the blast wave's development are complicated by the strong interaction with the muzzle flow, and simple models of the wave's motion do not apply [66].

The propagation of a blast wave resulting from an intense explosion has been well studied, and results are available in the literature [24, 66 – 70]. At times much greater than the formation time of the blast wave, the muzzle can be treated as a point source of mass and energy [24]. Although the cessation of mass and energy influx – combined with the geometrical expansion of the wave – results in a rapid decrease in overpressure, a long distance (relative to the caliber of the weapon) is still required for the blast wave to approach its acoustic limit [66 – 69]. A number of models have been proposed to describe the blast wave’s propagation while it is a strong shock in the mid-field and as it approaches its acoustic limit in the far-field, and they include approaches such as similarity and dimensionality arguments [66 – 72], empirical solutions [29, 71, 72], and theoretical derivations from gas dynamics equations [66, 68, 73, 74].

Experimental

A gun firing test was conducted during 10 – 19 October 2007 to develop an understanding of large-caliber gun weapon signatures. Figure 11 shows the layout of the test. A 152 mm howitzer was located at the Range & Accuracy (R&A) Site and fired at an azimuth of 54° True North towards three target impact sites designated by their ranges: 17.4 km, 16.0 km, and 13.4 km. The actual firing azimuth and impact ranges often deviated slightly from the nominal sites due to wind, ballistics performance, and occasionally to avoid hitting regions of wild-grass, which were susceptible to burning. Typical deviations were within a few hundred meters of the target impact sites. Gun elevation remained approximately 45 degrees in order to minimize ground interaction with the plume and blast wave.

A total of 201 rounds were fired, and firings were observed from two observation points. Site A was located 489 m behind the gun at 183.1° to the firing azimuth, and Site B was 429 m away at 265.4° to the firing azimuth. Both sites were chosen atop small hills for their visibility of the gun, and portable buildings were placed to provide shelter for the radiometric, spectroscopic, and imagery instruments located there.

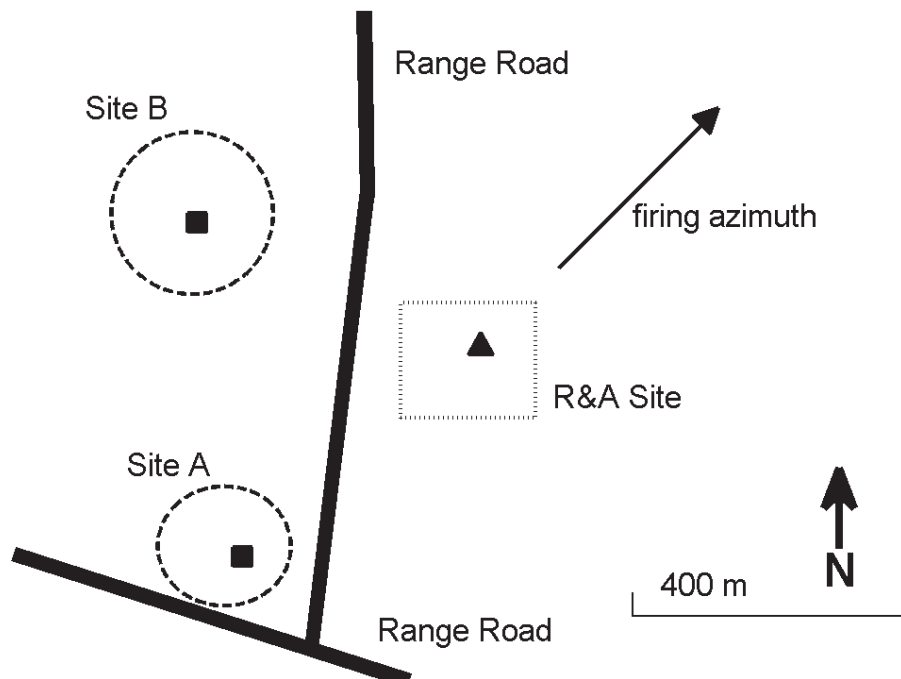


Figure 11. The test layout is shown. Site A and Site B (■) were located on small hills (***) overlooking the gun (▲) at the R&A Site (····). Due to the gun's firing elevation of approximately 45° , Site A had a side-on view of all the lateral plumes and an oblique rear view of the forward plume. Site B's location provided for a side-on view of the forward plume and a front-on view of the left lateral plume. Co-located at the R&A site was a radar unit for tracking the projectile.

Test Articles

The 152 mm gun-howitzer has a chamber diameter of 154.0 mm which tapers to a diameter of 152.4 mm over the first 15 cm of the 4.23 m barrel and chamber assembly. The barrel is equipped with a double-baffle muzzle brake that extends the total length of

the barrel assembly to 5.07 m. The brake acts to reduce recoil by redirecting propellant gases from the barrel so that they exert forward momentum on the gun. The result is a splitting of the muzzle effluent into a forward barrel plume and two lateral brake plumes.

All firings were of the same projectile which consisted of a forged steel shell, copper driving band, and high explosive warhead. The projectile was propelled by one of three propellant charge configurations. These correspond to total mass of the propellant – and thus also maximum impact range – in decreasing order: Full Charge, Charge 1, and Charge 2. Full Charge consists of a long and a short bundle of single perforated propellant sticks, two propellant bags of even shorter sticks, an igniter bag, and two flash suppressant bags. Charge 1 is obtained by removing the two additional bags of propellant sticks. Charge 2 is composed of six small bags of propellant, five of which are identical and the sixth which weighs more than twice as much as the smaller bags and contains the igniter.

Relevant ballistics properties of the test articles are shown in Table 1. Although the flash suppressant was removed from the Full Charge and Charge 1 configurations in a fraction of the firings, the suppressed and unsuppressed cases have similar thermodynamic and ballistic properties and are treated as a single class. The projectiles' muzzle velocities were measured experimentally using tracking radar. Propellant masses were obtained from documentation accompanying the munitions, and heats of formation were calculated using compositions of each state in conjunction with the JANAF thermochemical tables [75]. Suppressed and unsuppressed configurations for each charge are not distinguished, and the mean value is used where the propellant properties differ. The propellant composition is known for each of the munitions charges. Species of the

muzzle gases were estimated by assuming combustion of the propellant gas goes to completion using only internally available oxygen. Because the propellant is fuel rich, the rules developed by Kistiakowsky and Wilson were used to estimate which products are formed: oxygen is consumed to form CO, followed by H₂O, then CO₂ if any oxygen remains [76]. Excess hydrogen and nitrogen form H₂ and N₂, and carbon results in soot. Additional thermodynamic details of the propellants are located in Appendix A.

Table 1. Average ballistic and thermodynamic properties for the three munitions configurations.

Quantity	Full Charge	Charge 1	Charge 2	Method
Propellant charge mass, m_c [kg]	8.99	7.66	4.24	test article documentation
Propellant heat of formation, ΔH_f^0 [MJ]	-19.6	-16.6	-6.3	JANAF tables
Muzzle gas heat of formation, ΔH_f^g [MJ]	-43.8	-37.3	-20.6	JANAF tables
Projectile mass, m_p [kg]	43.5	43.5	43.5	test article documentation
Projectile muzzle velocity, u_p [m/s]	638 \pm 4	589 \pm 5	507 \pm 2	Weibel radar

Instrumentation

Weapon firing signatures were collected using a suite of spectrometers, radiometers, and imagers spanning the visible, near infrared, and mid-wave infrared. Ancillary instrumentation was deployed to collect acoustic data, meteorological conditions, and projectile trajectory. Only those instruments used in this analysis are described.

Visible imagery was collected primarily using high-speed Phantom cameras. A monochrome v5.1 Phantom camera with 1024 x 1024 pixel CMOS focal plane was located at Site B to view the gun side-on. A 3-color RGB v7.1 Phantom camera with 800

x 600 pixel CMOS focal plane (per color) was also located at Site B for the first half of the test, after which point it was moved to Site A. Both cameras are capable of collecting at greater than 100,000 frames per second (fps) by windowing the focal plane, but were used at lower rates to allow for larger fields of view. Typical configurations were 256 x 256 pixels at 25 kHz and 480 x 512 pixels at 6,400 Hz for the v7.1, and 1024 x 768 pixels at 1,600 Hz for the v5.1 camera. Nikon lenses having 400 mm focal length and f/# 2.8-32 were equipped on both instruments, resulting in instantaneous fields of view of 2.14 x 2.14 cm² and 1.71 x 1.71 cm² for the v7.1 and v5.1, respectively.

A Weibel MSL-60037 tracking radar was co-located with the gun and was used to monitor projectile trajectory at approximately 43 Hz. Typical trajectories for each munitions configuration are shown in Figure 12. The primary use of the radar system was to provide real-time feedback to the firing team, allowing them to make minor corrections to the gun azimuth and elevation to bring the actual impact area closer to the intended. In addition to trajectory, the muzzle velocity, impact location, and actual gun elevation were recorded.

Atmospheric meteorological conditions were monitored with a WeatherHawk weather station to collect air temperature, relative humidity, barometric pressure, wind speed and direction, and average solar irradiance at one minute intervals. Conditions were typically cool with temperatures ranging 8 – 21 °C. Relative humidity was 28 – 60% throughout the test, and barometric pressure ranged $P_0 = 83.4 - 96.8$ kPa. The collected weather data were used to estimate the local speed of sound for each firing, $a_0 = 341.0 \pm 4.2$ m/s, and an ambient air density $\rho_0 = 1.09 \pm 0.05$ kg/m³.

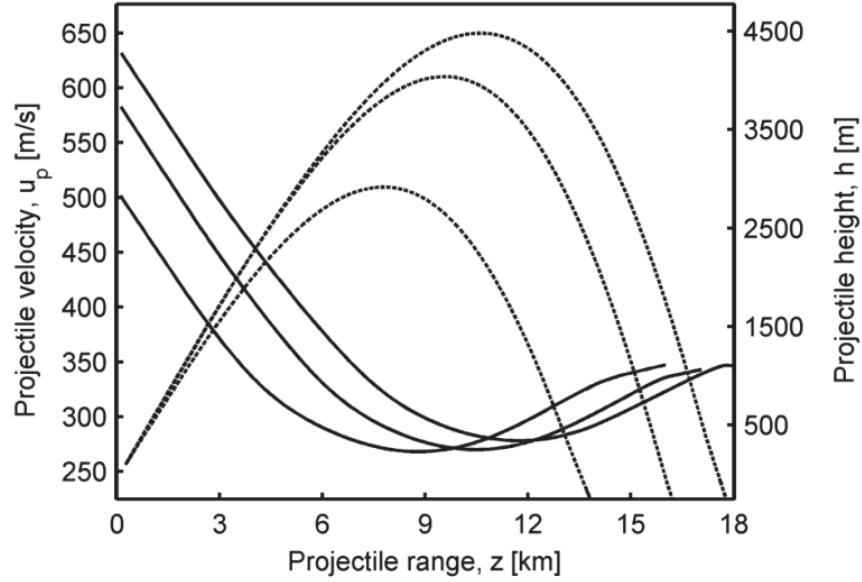


Figure 12. Projectile trajectories for each munitions configuration. From top to bottom: Full Charge, Charge 1, and Charge 2. *Left Axis*: velocity versus down-range distance (—). *Right Axis*: height versus down-range distance (···).

Data

Blast Wave Trajectories

Close to the gun where the shock is strong, the blast wave can easily be seen in high-speed imagery (Figure 13). This is due to the refractive index gradient induced by the large density discontinuity at the shock front. The position of the shock front was measured in all directions in the plane of the gun barrel for each frame of imagery, and the time-dependent shape history of the blast wave was precisely determined for firings of Full Charge, Charge 1, and Charge 2 configurations.

Good agreement was found by fitting the shock front's shape to an ellipse with major axis oriented along the gun barrel. The root mean squared difference between the ellipse and measured shape throughout the duration of the measurements was 6.2 cm, which is within the measurement uncertainty of approximately ± 10 cm. This uncertainty is based

on the blurring of the shock front over multiple pixels, not the approximately 1.7 cm instantaneous field of view of each pixel.

The minor axis length parameter can be eliminated with little loss of fidelity because the eccentricity of the ellipse is 0.316 ± 0.064 (i.e. minor axis length R_b equal to 94.9% of the major axis length R_a) which is low enough to suggest that a spherical model is sufficient. This is consistent with previous experiments in which muzzle shocks were initially found to be asymmetric (due to the geometry of the muzzle flow) but very quickly assumed spherical symmetry as they expanded into a free atmosphere [24, 27].

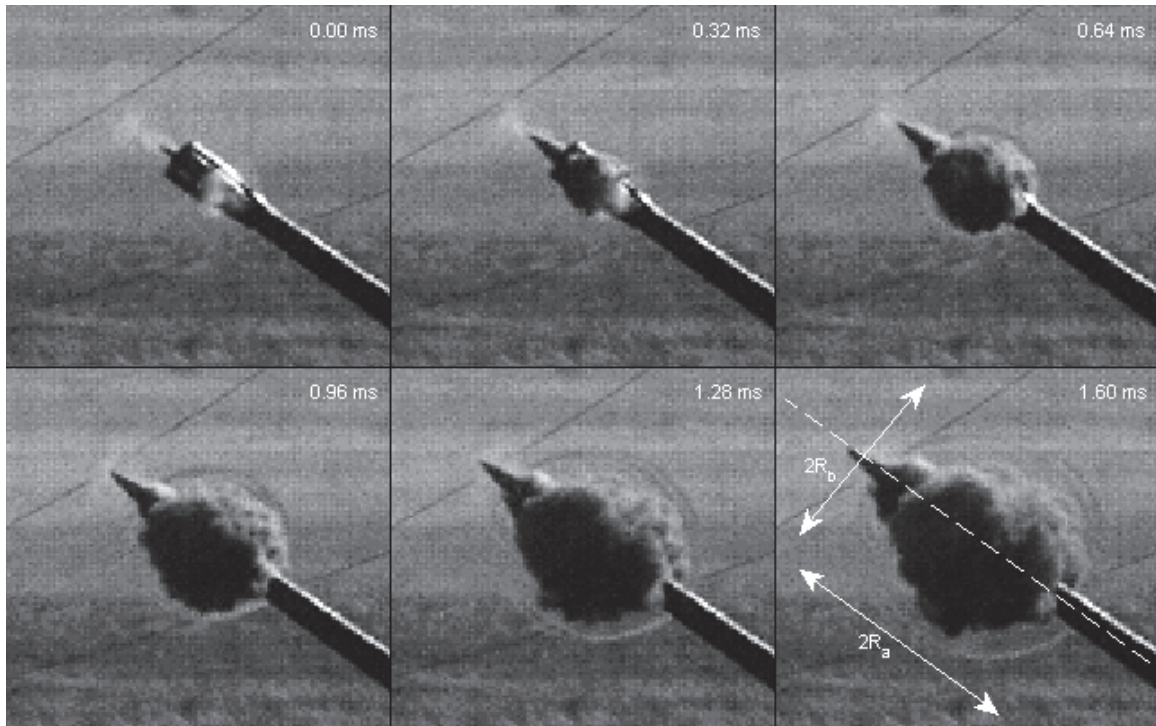


Figure 13. The blast first six frames captured by the Phantom v7 imager operating at 25 kHz are shown for a Charge 2 firing. The blast wave is visible due to the index gradient induced by the high density shock front. The progression shows that lateral muzzle plumes begin to form as the projectile clears the first muzzle brake at 0.32 ms. The shock front is indistinguishable from the muzzle flow until 0.64 – 0.96 ms, at which point it is still in contact with the plume but begins to appear distinct. By 1.28 – 1.60 ms the leading edge of the blast wave has detached from the plume. The final still in the series shows major and minor axes lengths of the blast wave relative to the axis of the barrel.

To very good approximation, the blast wave's shape can be treated as spherical after its formation time, and the position of the shock can be characterized solely in one spatial dimension by radius R as a function of time t . This is termed the blast wave's trajectory, and was measured for 49 Full Charge, 79 Charge 1, and 19 Charge 2 firings. The sampling interval was 0.625 ms corresponding to the 1,600 fps rate of the Phantom v5.1 imager used to extract all trajectories. This is the primary data set used here in the analysis. The remaining events could not be measured because of poor blast wave visibility due to night time conditions during which they were fired.

The left panel of Figure 14 shows the aggregate of all blast wave trajectories for the Charge 1 firings. Also shown are the median and ± 2 standard deviations of the muzzle plume radius. The latter was determined by measuring the maximum position of the edge of a single plume in the high speed imagery, as a function of time, for several firings. The plumes drifted during each event (due to a combination of wind and flow momentum), and to mitigate uncertainty in plume center, diameter was measured in several directions and used to calculate a mean plume radius in each frame of imagery. The Full Charge and Charge 2 configurations have very similar blast and plume profiles, distinguishable for the blast in curvature at times less than 4 ms and velocity throughout the range of measurement, and are not shown. At early times (in the near and mid-fields, to be defined below), the data are well represented by a line of slope 0.539 ± 0.006 in the log-log plane as shown in the inset plot.

Because the differences in each charge configuration's trajectories significantly overlap, plotting the trajectories for each configuration collectively is not clear. Rather, to show separation of the full trajectories, the Charge 1 data were least-square fit with a 6th

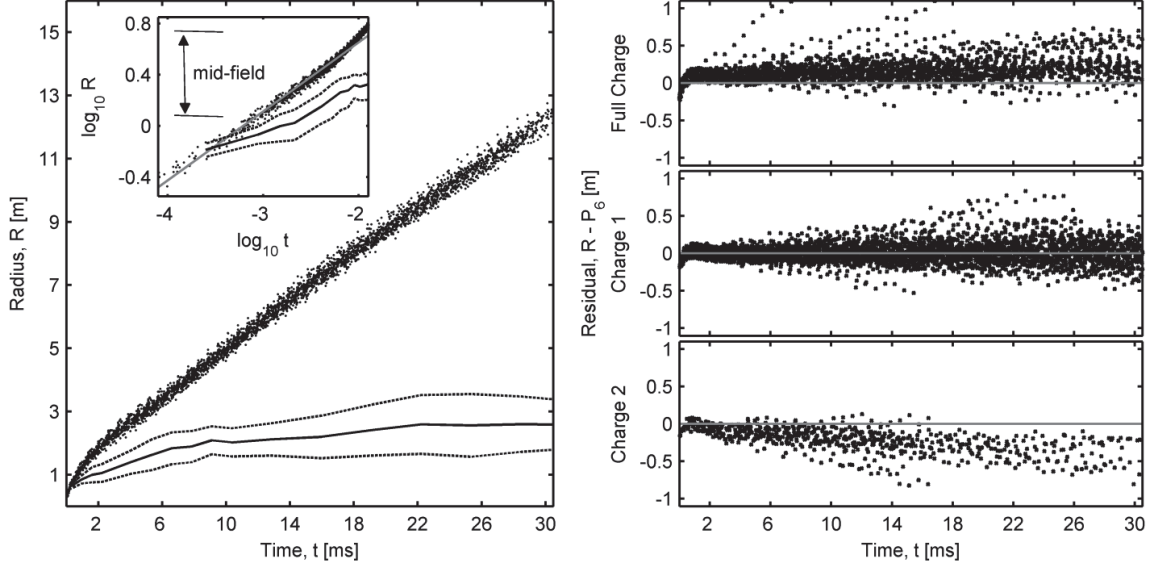


Figure 14. *Left:* blast wave radius (\bullet), median plume radius (—), and the ± 2 standard deviations of the plume radius (---) are shown as a function of time for the aggregate of all Charge 1 firings data. The inset plot shows the log of early-time data, where it is apparent that the early-time blast wave trajectory can be represented by a line (—). *Right:* residuals between all radius data for each configuration and the Charge 1 best-fit 6th degree polynomial are shown. Full Charge is positively biased, indicating greater blast wave velocity. Similarly, Charge 2 is negatively biased, indicating a lesser blast wave velocity than Charge 1. The strong curvature at early times results because the polynomial is not an adequate fit to the data, and it is only used to emphasize variance in the data from event-to-event and amongst configurations.

degree polynomial, P_6 . Characteristic quantities of the polynomial include offset (intercept) $R(t = 0) = 0.55$ m, median slope $dR/dt = 370$ m/s, and temporally separated mean accelerations $d^2R(t < 4 \text{ ms})/dt^2 = -74,000 \text{ m/s}^2$ and $d^2R(t > 4 \text{ ms})/dt^2 = -950 \text{ m/s}^2$. Differences amongst the charge configurations are apparent by examining the residual between each configuration's trajectory and P_6 , shown in the right panel of the figure. Full Charge can be seen to have a residual that is biased positively, and the Charge 2 residual is biased to the negative. This indicates that despite the overlap in the data, there is some separation in the trajectories amongst configurations. The curvature in the residuals at early times ($t < 4$ ms) results because the trajectories cannot be adequately represented by P_6 – it is only used in the figure to emphasize variance in the data of each

configuration and differences amongst configurations. The overlap of variance for each configuration's trajectories is the limiting factor in how well the configurations can be discriminated.

Flow Regions

Implicit to the description of blast wave propagation is defining three flow regions: the near, mid, and far-fields. The mid-field is of the most importance for characterizing – and consequently modeling – the blast wave trajectory because it is the region where the blast wave is easily represented by low-parameter models. Additionally, certain models are not valid in either the near or far-fields and defining the temporal and spatial extents of those regions is necessary.

The far-field is characterized as where the peak pressure of the blast wave is not much greater than ambient, and atmospheric pressure cannot be ignored in the treatment of the blast wave's gas dynamics [66, 69]. An estimate of the far-field limit can be obtained from atmospheric pressure P_0 and the energy released in the blast. The energy in the blast is the energy released by combustion of the propellant minus the work performed on the projectile. This is a theoretical maximum that neglects any heating of the gaseous propellant or friction loss to the gun. The energy released by the propellant is the difference in heat of formation of the muzzle gas ΔH_f^g and the propellant's initial state ΔH_f^0 . Work performed on the projectile is nearly equal to the projectile's translational kinetic energy. The far-field limit R_f is [69, 72]:

$$R_f > \left(\frac{\Delta H_f^0 - \Delta H_f^g - m_c u_p^2 / 2}{P_0} \right)^{1/3} \quad (1)$$

The near-field is the spatial region where high temperature, high pressure muzzle gas is expanding and forming a shock front as both propellant and atmospheric gases are compressed. Most simple models cannot be used in this region because the developing blast wave is influenced by local variations in the mass and energy flow, and the gas dynamics are highly complicated. Early work in treating blast waves (from explosives) has characterized this region as where neither the volume into which energy is released nor the energy source mass are negligible compared to the volume and mass of atmosphere encompassed by the blast wave [66, 69 – 71].

For explosives, the conversion of explosive charge to the gas that drives formation of the blast wave is treated as nearly instantaneous and initially equal to the volume of the charge [67 – 69]. Approximating a spherical shock front, this simplifies the extent of the near-field R_n to the region where source mass is less than the mass of atmosphere encompassed by the blast wave and depends only on charge mass m_c and atmospheric density ρ_0 :

$$R_n < \left(\frac{3}{4\pi} \frac{m_c}{\rho_0} \right)^{1/3} \quad (2)$$

In muzzle blasts neither energy nor mass are released instantaneously, and consequently the shock front has expanded by the time all energy and mass are exhausted from the gun. Because not all propellant charge mass is present in the initial volume in which the blast wave is formed, the range of interaction between the shock and plume may not correspond to the near-field limits given by Equation (2). In muzzle blasts, energy is deposited at a nearly constant rate during the period of coupling between the blast wave and exhaust plume [22, 78 – 80], which implies: (1) muzzle blasts continue to

be driven while in contact with the muzzle flow; and (2) energy is not added to the blasts after detachment from the muzzle flow. If these are assumed to be true, the near-field extent is limited to the timeframe during which the blast wave and muzzle plume are in contact; after the shock detaches from the plume any additions of mass or energy to the plume do not influence the shock front.

Detachment of the blast wave from the muzzle plume was shown in stills in Figure 13 and in the trajectories in Figure 14. Time zero is when the projectile passes beyond the first muzzle brake opening, allowing propellant gases to begin to escape. At 0.32 ms, the shock front and muzzle flow are indistinguishable, but by 0.64 – 0.96 ms they begin to appear distinct. After this time detachment occurs, and the blast wave has propagated beyond the range of interaction with the muzzle flow and the near-field is ended. The detachment timeframes were visually estimated for each munitions configurations and appear consistent with ranges calculated using Equation (2), suggesting that the shock-plume interaction time is nearly equal to the near-field limit. This provides confirmation for the 152 mm howitzer that Equation (2) can be used for explosions and muzzle blasts.

The near and far-field limits for Full Charge, Charge 1, and Charge 2 configurations are provided in Table 2. The times t_n and t_f were calculated as the average and ± 1 standard deviation of the aggregate of all data, per configuration, over which R_n and R_f occur. The mid-field is the region between the near and far-fields and ideally should be greatly separated from either. For the case of relatively weak shocks, e.g., from a muzzle blast, there is no truly isolated mid-field. Rather there is only a range over which the blast wave is markedly neither in its formation phase nor approaching its acoustic limit. This region is characterized by strong curvature in the trajectory of the blast wave.

Table 2. Theoretical near and far-field ranges for the three munitions configurations.

Limit	Full Charge	Charge 1	Charge 2
Near-field range, R_n (m)	1.25	1.19	0.98
Near-field time, t_n (ms)	0.91 ± 0.18	0.88 ± 0.15	0.77 ± 0.16
Far-field range, R_f (m)	5.52	5.25	4.57
Far-field time, t_f (ms)	10.85 ± 0.30	10.89 ± 0.33	9.68 ± 0.46

Results

A number of models may be used to represent an expanding blast wave's trajectory. Four of these models are presented with a discussion of their fit to the data, usefulness in data reduction, and potential for classification. Characteristic curves are shown in Figure 15 to illustrate the differences in each model and the effect of changes in the model parameters.

Point Blast

The point blast model is commonly used to describe the propagation of blast waves where treatment of the flow field is simplified by neglecting local source variations in the mass and energy flows, and where the effects of atmospheric pressure are ignored; i.e. in the mid-field. It is based on similarity in which the shape of the blast wave is assumed to be spherical and its radius scales with energy release [66, 69 – 73].

The classical form of the point blast model is the first term of the piecewise equation shown in Equation (3). R is the blast wave radius, A is a proportionality constant, t is time, and b is a rate exponent. The common form of the blast model is specific to spherical blasts formed by instantaneous energy release (in which case $b = 2/5$) and may be derived solely based on dimensionality arguments [69]. Theoretical derivations allow

for energy release to vary with time, with a special case being a constant rate of energy deposition into a spherical blast ($b = 3/5$) [66]. Because this model is only valid in the mid-field, and much of the blast wave trajectory data that have been observed extend into the far-field, the point blast model used here is a piecewise function:

$$R = \begin{cases} At^b & t_n < t < t_f \\ a_0 t + \Delta R & t > t_f \end{cases} \quad (3)$$

At times greater than the far-field limit t_f , the muzzle blast propagates near the local speed of sound a_0 with a notable difference being that the blast wave has propagated a greater distance ΔR than would a purely acoustic wave. The mid-field model is only valid at times greatly separated from the near and far-field limits, but because this doesn't occur for the relatively weak muzzle blasts, the restriction is relaxed here and it is simply used in between the limits. The piecewise function extends the range over which data can be represented, but characterization of the trajectory remains limited to either the mid-field where the blast is shock-like or the far-field where acoustic asymptotics are more realistic.

Drag

The drag model is useful when modeling the expansion of gases that experience drag by ambient atmosphere. It allows for an estimate of the initial velocity of the expansion and prediction of the decelerating particles' stopping distance due to drag effects [71, 72]. The preceding pertains to the expanding muzzle plume, but because the blast wave is formed by the inability of the pressure disturbance to propagate faster than the driving mass, the shock front is initially coincident with the muzzle flow. The coupling of plume and wave allows an alternate description of blast wave propagation at early times: the

trajectory of a spherically expanding blast wave may be estimated by treating the drag impeding mass flow:

$$R = R_m \left(1 - e^{-\kappa t}\right) + a_0 t \quad (4)$$

The classical form of the model is represented by setting $a_0 = 0$. The drag coefficient, κ , increases with increasing atmospheric pressure; and R_m is the particle stopping distance.

The drag model is only valid in the near-field where the shock front is inseparable from the mass flow driving the wave. Once the driving mass approaches its stopping distance (which may represent the maximum extent of the muzzle plume), the shock front detaches and the pressure disturbance propagates as a decaying blast wave. This is not represented by the drag model, but the additional of a linear velocity term may be used to

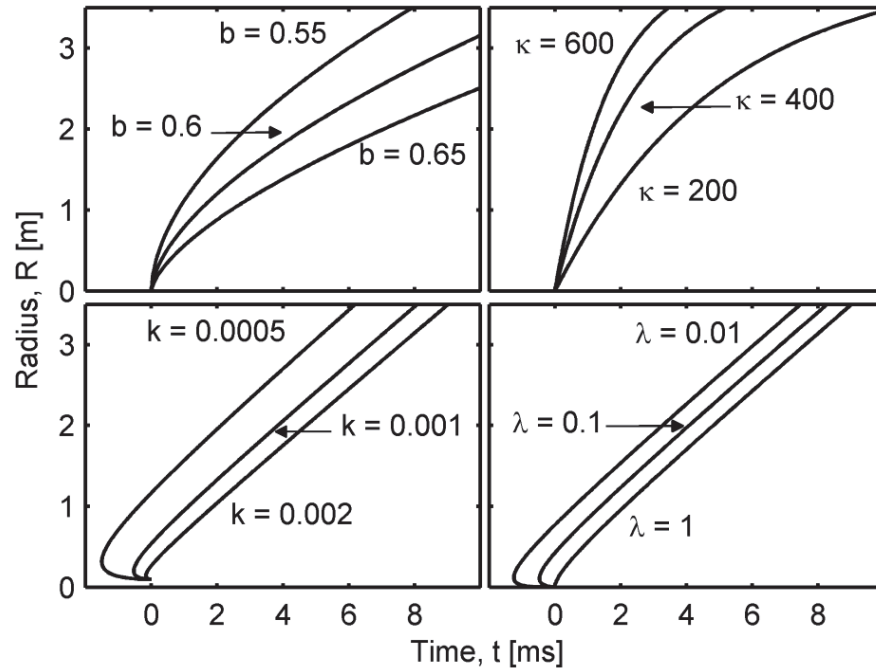


Figure 15. Characteristic curves are shown for each model. *Upper left*: point blast model with $A = 50 \text{ m s}^{-b}$ and $R_f = \infty$. *Upper right*: drag model with $R_m = 4 \text{ m}$, $a_0 = 0$, and κ in Hz. *Lower left*: asymptotic model with $R_0 = 10^{-3} \text{ m}$, $a_0 = 341 \text{ m/s}$, and k in seconds. *Lower right*: inverse power series with $a_0 = 341 \text{ m/s}$ and λ in meters.

extend the validity of the model – in a data fitting sense – to the far-field where the blast wave’s overpressure approaches ambient and it travels near the local speed of sound. Equation (4) is the modified drag model, where an $a_0 t$ term has been added to the classical drag model. The effect is that the meaning of R_m and κ are no longer clear apart from providing a relative assessment of the magnitude of the blast’s strength and atmospheric drag. Because only near and far-field terms are used, the meaning of the model fit to the mid-field is undefined.

Asymptotic

When the overpressure of the expanding blast wave becomes negligibly small, the wave travels at the local speed of sound and can be considered acoustic. Landau and Lifshitz developed gas dynamics equations for such a wave by treating the decay of a weak spherical shock as a disturbance that propagates as an acoustic wave, albeit with a more exact speed of sound [74]. Sedov, and later Korobeinikov, showed that a series expansion of these gas dynamics equations allows for the motion of the blast wave to be determined [68, 73]. Truncating after the second term allows the time versus radius to be derived in its asymptotic limit:

$$t = \frac{R}{a_0} - k \left(\ln \frac{R}{R_0} \right)^{1/2} + \delta t \quad (5)$$

where R_0 is the minimum distance at which the model may be applied and result in a real-valued time of arrival; physically it may be interpreted as the distance at which atmospheric pressure is no longer negligible. δt is an offset required to match the radial and temporal positions, and k is a constant with units of time. The model deviates from a characteristic line in the time-distance plane for small radii, the extent of which is

governed by k and is indicative of the strength of the shock, although a clear relationship to physical quantities is not known. This solution is only valid in the far-field where the peak blast wave pressure is small and higher order terms of the gas dynamics expansion can be neglected. Although the full range of motion of the blast wave is important, the time required for the shock to decelerate to near sonic velocities is short, and the asymptotic models are effective for much of the range of propagation.

Inverse Power Series

A similar asymptotic solution was obtained by Fansler using a semi-empirical method [72]. Blast wave peak pressure P is converted to a non-dimensional overpressure ΔP by removing and normalizing by atmospheric pressure, $\Delta P = (P - P_0)/P_0$. It is then assumed that this overpressure falls off in an inverse power series with range, and that because the strength of the blast wave is dependent on the properties of the flow behind it, overpressure can be matched to the standard Mach relation:

$$\Delta P = \frac{\alpha' \lambda}{R} + \frac{\beta' \lambda^2}{R^2} = \frac{2\gamma}{\gamma + 1} (M^2 - 1) \quad (6)$$

The Mach number of the flow behind the blast is equal to the differential of radius with time normalized by the local speed of sound: $M = (dR/dt)/a_0$. Substituting this into the relation allows the entire expression to be analytically integrated to an expression for time as a function of radius:

$$t = \frac{X}{a_0} - \frac{\alpha \lambda}{2a_0} \ln \left(\frac{2X + 2R}{\lambda} + \alpha \right) + \delta t \quad (7)$$

$$X^2 = R^2 + \alpha \lambda R + \beta \lambda^2 \quad (8)$$

δt is a time offset necessary for matching temporal and spatial positions, $\gamma = 1.4$ is the specific heat ratio for air, and λ is a length constant related to weapon properties. $\alpha = 2\gamma\alpha' / (\gamma + 1)$ and $\beta = 2\gamma\beta' / (\gamma + 1)$ where $\alpha' = 0.243$ and $\beta' = 0.022$ are empirically determined dimensionless coefficients that Fansler, et al. calculated using a range of guns systems. This formulation retains the acoustic limit in the far-field and approximates non-linear propagation in the mid-field.

Fit Results

Each model was fit to the radius versus time blast wave trajectories in one or more instances, with different constraints on the fit parameters in each instance, in order to examine various assumptions on the models. The fits were accomplished by minimizing an error function defined as the mean of squares residual between the data and model for N samplings of the trajectory. For the point blast and drag models, this is of the form:

$$Err(\mathbf{x}) = \frac{1}{N} \sum_i^N [R_i - f(t_i - t_0; \mathbf{x})]^2 \quad (9)$$

R_i is the i th radius corresponding to time t_i , and f is the model as a function of \mathbf{x} evaluated at time $t_i - t_0$, where \mathbf{x} is a vector of fit parameters. The time offset t_0 is allowed to vary to account for uncertainty in knowledge of the blast wave's temporal origin (and includes δt where applicable). The asymptotic and inverse power series represent time as an explicit function of radius, so the error function is similar but switches the positions of R_i and t_i and is a measure of the residual in time. In all cases those data in the near-field were excluded because local variations in flow conditions – and thus blast wave geometry – are significant and a radial trajectory model is not valid

The fits were all performed in Matlab with the *fminsearch* function used to minimize $Err(\mathbf{x})$. *fminsearch* performs an unconstrained non-linear optimization using the simplex search method of Lagarias, et al. [80]. Because this algorithm only solves for local minima, it was necessary to provide initial guesses for the fit parameters in the vicinity of the solution. The set of initial guesses used for individual events was obtained by manually applying the fit function to the aggregate of all data for each munitions configuration. The values of the free parameters resulting from the fits are shown in Table 3. The forms of the four models are shown, and all parameters are indicated as either constrained to specific values or as free parameters. The mean and standard deviation of fitting to all events per munitions configuration is shown for each fit parameter.

In the models where the local speed of sound a_0 is a parameter, it was replaced with an unspecified speed, a , that is allowed to vary to more accurately represent the far-field trajectory data. This caused the estimated value to be up to 10% greater than ambient because the blast wave has not yet fully transitioned to acoustic velocities within the range of measurements. A linear fit to the far-field data does not account for the trajectories' deceleration but was used due to both its low dimensionality and because measurement uncertainty does not allow significant resolution of far-field curvature.

When the far-field limit R_f was a free parameter, it was either allowed to vary to obtain an independent estimate of the far-field limit based on the data themselves, or it was set to infinity (resulting in $t_f = \infty$) to force the point blast model to its classical form by preventing it from switching to the linear term.

Table 3. Forms of the models, constraints, and resultant mean and standard deviation fit parameters for each configuration.

Model	Constraint		Par.	Full Charge	Charge 1	Charge 2
Point Blast $R = \begin{cases} At^b & t_n < t < t_f \\ a_0 t + \Delta R & t > t_f \end{cases}$ $\Delta R = R_f - a \left(R_f / A \right)^{1/b}$ $t_f = \left(R_f / A \right)^{1/b}$	none		A	70.6 ±3.0	64.2 ±1.9	56.5 ±1.5
			b	0.58 ±0.02	0.57 ±0.01	0.56 ±0.01
			R _f	3.31 ±0.35	2.90 ±0.28	2.61 ±0.28
			a	375 ±9	373 ±7	359 ±10
	b = 0.6		A	79.9 ±0.8	76.3 ±1.0	72.9 ±1.3
			R _f	3.65 ±0.39	3.32 ±0.33	3.37 ±0.41
			a	368 ±9	367 ±8	342 ±14
	b = 0.4		A	27.6 ±0.4	25.9 ±0.5	25.3 ±0.7
			R _f	2.68 ±0.17	2.42 ±0.20	2.44 ±0.27
			a	368 ±9	367 ±8	342 ±14
	R _f = ∞		A	213 ±2	203 ±1	189 ±3
			b	0.82 ±0.02	0.81 ±0.01	0.81 ±0.01
	R _f = ∞ t < 4 ms		A	57.5 ±2.4	51.7 ±2.7	42.3 ±0.5
			b	0.55 ±0.02	0.54 ±0.02	0.52 ±0.01
	t < 4 ms R _f = ∞	b = 0.6	A	77.1 ±1.1	73.0 ±1.3	68.6 ±2.0
		b = 0.4	A	25.6 ±0.3	23.6 ±0.3	21.6 ±0.4
Drag $R = R_m \left(1 - e^{-\kappa t} \right) + at$	none		R _m	2.29 ±0.08	1.96 ±0.07	1.51 ±0.01
			κ	2854 ±1793	3362 ±7658	3570 ±4248
			a	375 ±9	366 ±7	331 ±14
	t < 4 ms a = 0		R _m	1.97 ±0.08	1.73 ±0.05	1.48 ±0.02
			κ	602 ±27	612 ±87	668 ±48
Asymptotic $t = \frac{R}{a} - k \left(\ln \frac{R}{R_0} \right)^{1/2} + \delta t$	none		R ₀	0.45 ±0.03	0.33 ±0.02	0.31 ±0.02
			k x10 ³	2.00 ±0.04	1.47 ±0.03	1.20 ±0.01
			a	363 ±8	364 ±7	347 ±10
Inverse Power Series $t = \frac{X}{a} - \frac{\alpha}{2a} \ln(Z) + \delta t$ $Z = \frac{2X + 2R}{\lambda} + \alpha$ $X^2 = R^2 + \alpha \lambda R + \lambda^2 \beta$	A = 0.284 B = 0.0257		λ	4.37 ±0.38	3.42 ±0.44	2.80 ±0.67
			a	345 ±8	348 ±7	338 ±12
	A = 0.284 B = 0		λ	4.75 ±0.47	3.59 ±0.48	2.92 ±0.71
			a	346 ±8	349 ±7	339 ±12
	A = 0 B = 0.0257		λ	8.44 ±2.35	8.12 ±1.79	7.20 ±2.13
			a	367 ±8	365 ±7	345 ±13

Some instances of fitting to the point blast and drag models specify the constraint $t < 4$ ms. This was to examine the classical forms of the models which are not valid in the far-field. The constraint is less than half of the far-field limits specified in Table 2, but it is used because it ensures that far-field data are excluded (recall that the limits specified were the maximum theoretical and it is likely the far-field ends sooner). Four milliseconds was chosen as the limit because curvature is strongly apparent in the mid-field at earlier times (see Figure 14).

Two measures of the goodness of fit for each model are the root mean square (RMS) residual and the F-statistic. Both are represented for each munitions configuration in Table 4 for fits of all models and with each set of constraints. The number of fit parameters is also shown for reference, and in all cases t_0 is counted as one of the fit parameters. The RMS residual provides an estimate of the average radius error between the model and the data at equivalent times. The F-statistic normalizes goodness of fit based on the number of fit parameters and allows the different models to be compared on a relatively equal basis.

Conclusions

It has been shown that optical observation of large caliber muzzle blasts can provide a significant amount of information. The shock-plume interaction timescale is approximately equal to the near-field limit calculated from theory and indicates that the blast wave is driven only while it is in contact with the muzzle plume. Blast geometry was found to be spherical beyond the near-field, and the wave's propagation can be accurately represented by one of several radius versus time models in the mid and far-

fields. All models represent the data relatively well and can be used for data reduction – i.e. representing several dozen trajectory points per event with a significantly reduced set of fit parameters – and many have parameters that provide direct insight into the blast phenomena.

The drag model's maximum stopping distance may be equal to the maximum plume radius. This is a conclusion that is consistent with the phenomenology on which the

Table 4. Goodness of fit measures, numbers of free parameters, and constraints for each model and munitions configuration.

Constraint		# Par.	Full Charge		Charge 1		Charge 2	
			RMS (m)	F-stat	RMS (m)	F-stat	RMS (m)	F-stat
Point Blast								
none		5	0.092 ± 0.020	1628	0.094 ± 0.019	2171	0.082 ± 0.024	1037
$b = 0.6$		4	0.099 ± 0.022	2102	0.103 ± 0.020	2817	0.099 ± 0.022	1363
$b = 0.4$		4	0.128 ± 0.028	1907	0.123 ± 0.024	2554	0.134 ± 0.026	1302
$R_f = \infty$		3	0.115 ± 0.019	2887	0.119 ± 0.015	3781	0.092 ± 0.030	1553
$t < 4$ ms, $R_f = \infty$		3	0.021 ± 0.005	314	0.014 ± 0.004	493	0.013 ± 0.007	140
$t < 4$ ms $R_f = \infty$	$b = 0.6$	2	0.037 ± 0.010	436	0.029 ± 0.009	650	0.021 ± 0.010	182
	$b = 0.4$	2	0.104 ± 0.021	389	0.084 ± 0.028	589	0.070 ± 0.049	201
Drag								
none		4	0.375 ± 0.053	2169	0.259 ± 0.032	2190	0.127 ± 0.029	1254
$t < 4$ ms, $a = 0$		3	0.744 ± 0.064	330	0.620 ± 0.065	487	0.446 ± 0.065	124
Asymptotic								
none		4	0.088 ± 0.016	2165	0.088 ± 0.016	2901	0.081 ± 0.017	1384
Inverse Power Series								
$A = 0.284$	$B = 0.0257$	3	0.103 ± 0.018	2346	0.094 ± 0.014	2446	0.085 ± 0.019	1661
	$B = 0$	3	0.109 ± 0.020	2244	0.099 ± 0.016	2341	0.090 ± 0.021	1589
$A = 0, B = 0.0257$		3	0.121 ± 0.042	2346	0.098 ± 0.016	2446	0.110 ± 0.054	1661

model is based and is supported by the loose agreement between the fit values and the plume radius depicted in Figure 14. The product of the near-field fit's stopping distance and drag coefficient yields initial expansion velocities of Mach 3 – 4, which is also very reasonable for the weapon system considered. Yet both instances of the drag model show the largest residuals, and the modified version has highly significant fit uncertainties. Both of these suggest that although the model may be suited to represent the drag exhibited on mass flow in muzzle plume, it is not sufficient to precisely model the mid and far-field propagation of an expanding blast wave. The model should be further examined for representing the muzzle plume's expansion.

The piecewise form of the point blast model contains the far-field limit as a fit parameter. Accordingly, this fit parameter is an estimate of the far-field limit – based on the data themselves – where the trajectory is better represented by a linear, near-acoustic term than by a power law displaying strong curvature. The resulting values are 2.61 – 3.31 m (30 – 50% less than theory suggests) and support that the values in Table 2 are upper bounds: energy released by the propellant is much less than the theoretical maximum and the blast decays into the far-field flow region more quickly than estimated. The point blast model further confirms that the energy release into the blast is much closer to constant ($b \approx 3/5$) than instantaneous, which supports that energy and mass are deposited into the blast throughout the duration that the blast wave and muzzle flow are in contact. Constraining the models to $b = 0.6$ does not significantly increase residuals, yet it does improve data reduction via both retaining fewer parameters and reducing parameter uncertainties.

Those models whose observation derived fit parameters show the least within configuration variance and the greatest between configuration separation have the most potential for distinguishing amongst multiple configurations. Additionally, because curvature in the trajectory is directly related to energy released into the blast, it is expected that the fit parameters will be monotonically increasing or decreasing with the propellant mass. The residual plots in Figure 14 demonstrate that the blast trajectories are very similar (which limits how well even the best model can perform) yet examination of Table 3 reveals that most fit parameters are reasonably well separated. Certain parameters, such as the point blast models' A parameter, also have relatively low variance and trend with propellant mass, indicating good potential for classification. Likewise, the asymptotic model parameters are distinct (widely separated relative to their uncertainties). In both cases the goodness of the models are confirmed by low RMS residuals and excellent F-statistics.

In summary, a number of models have been examined for their suitability in reducing the blast wave trajectory of a large-caliber gun to a few parameters that retain the fidelity necessary to show potential to distinguish between even very similar munitions configurations. The work presented here is not an evaluation of the validity of the models themselves; rather it shows the results of these models applied to experimental data for a system of interest, and the potential use for classification. In general the models with fewer degrees of freedom have fit parameters that are more distinct, yet further study remains to be completed to provide a quantitative assessment of how well these models perform in distinguishing configurations solely on optical observation of the blast wave signature.

IV. Optical Characterization of Large Caliber Muzzle Blast Waves

Introduction

Characterization of blasts from a variety of laboratory-scale sources has been performed using both acoustical [82 – 85] and optical [21 – 23; 86 – 88] techniques. Acoustical methods may be viable to study large caliber guns in the field, but techniques such as Schlieren imaging and shadowgraphy are often impractical [87]. Under certain conditions, specifically the presence of optical inhomogeneities in the background of the field of view, standard imaging devices may be used to detect the presence of the blast waves from optical distortions caused by the lensing of the high-density shock front. This has been observed as early as the 17th century [88], and became prominent in the 20th century with its use in observing supersonic aircraft [89] and Taylor’s notable study of the blast wave from the atomic bomb [90].

There is little in the literature on the use of optical imaging for experimental characterization of large-caliber artillery. Optical investigations are typically of small arms in laboratory environments [21 – 23]. Many prior studies of large caliber guns report simulated, scaled, or representative results that do not establish the variation in firing properties of a particular weapon [25, 29, 43]. The current work observes a statistical sampling of firings of three different munitions configurations from a single gun. We seek to exploit passive optical signatures of blast wave propagation for event classification.

The firing of a gun begins with combustion of the (typically solid) propellant, converting it to a high-temperature, high-pressure gaseous state which performs work to

accelerate the projectile down the gun barrel. Shot exit occurs when the projectile departs the muzzle assembly and the supersonic propellant gases being expelled develop into a quasi-steady, under-expanded, supersonic flow region at the exit plane of the muzzle [28, 32]. For most propellants, the muzzle gases are fuel-rich combustion by-products that can re-ignite and sustain combustion after mixing with atmospheric oxygen [32, 49, 50, 53]. If this occurs, it results in the most visible muzzle signature often referred to as *muzzle flash*. A great deal of study has gone into predicting the occurrence of muzzle flash. These have relied on laboratory measurements of plume temperature [32] or modeling of external muzzle flow [49, 50, 53]. The latter requires treating the complexities of expansion and shock heating to estimate plume temperature. We present a method of estimating plume temperature based only on energy partitioning.

The efflux of high-pressure, supersonic gases at the muzzle also results in positive and negative pressure transients, the entire train of which forms a blast wave; this is differentiated from the shock wave, which is limited to the pressure discontinuity at the leading edge. The blast surrounds the entire flow-field and limits expansion until it detaches from the flow, allowing the plume to expand freely [28]. Prior to detachment, the gas dynamics of the blast wave's development are complicated by the strong interaction with the muzzle flow, and simple models of the wave's motion do not apply.

A number of models have been proposed to describe the blast wave's propagation for both a strong shock and a decaying shock approaching its acoustic limit. These include theoretical derivations from gas dynamics equations [66, 73, 91], similarity and dimensionality arguments [69:97-99; 70, 91], and empirical solutions [29, 92]. Several of these models have been previously examined for their suitability in representing the

muzzle blast trajectories of a large-caliber gun [93]; and these include point blast [66, 69:97-99; 70, 73, 91], drag [72], and those based on approximations to the gas dynamics equations governing flow behind the blast wave [29, 73]. While all models fit the data well where the blast is strong, many models are not valid close to or far from the gun. We apply the point blast model to extract key features from the 152 mm howitzer observations and characterize the potential for event classification.

Experimental

High-speed visible images were observed for 147 firings of a 152 mm howitzer during 10 – 19 October 2007. Signatures were collected from two sites – one located behind and one to the side of the gun – at ranges of approximately one half kilometer. Details of the test geometry have previously been reported [93]. The 152 mm howitzer was fired towards three impact sites at ranges of 17.4 km, 16.0 km, and 13.4 km, depending on the propellant charge. The gun elevation remained approximately 45 degrees to achieve maximum range and minimize interaction between the ground, muzzle plume and blast. The barrel was equipped with a double-baffle muzzle brake that split the muzzle effluent into one forward and two lateral plumes. The plumes did not appear to interact and were treated individually in our analysis. All firings were of a 43.5 kg projectile propelled by one of three propellant charge configurations characterized by decreasing propellant mass: Full Charge, Charge 1, or Charge 2.

Full Charge and Charge 1 propellants are a double-base consisting primarily of nitrocellulose and nitroglycerin, with minor amounts of dinitrotoluene, methylcentralite, and diethyl phthalate. There is a relatively high percentage of nitroglycerin in the

propellant composition which yields a higher than conventional force level at the cost of a higher flame temperature. Higher temperature promotes inducing muzzle flash, and the charges contain two chemical flash suppressant bags to reduce its likelihood. The flash suppressant accounts for less than 4% of the total propellant mass and is primarily composed of potassium sulfate and nitrocellulose, with trace amounts of nitroglycerine, diphenylamine, and diethyl phthalate. Charge 2 uses a single-base propellant composed primarily of a high-nitrogen content nitrocellulose with minor amounts of dinitrotoluene, diethyl phthalate, and black powder. Both charge types use a black powder igniter which accounts for less than 2% of the propellant charge mass.

Ballistic, propellant, and blast properties of the three munitions configurations are shown in Table 5. Although the flash suppressant was removed from the Full Charge and Charge 1 configurations in a fraction of the firings, the suppressed and unsuppressed cases have similar thermodynamic and ballistic properties and are treated as a single configuration for the purpose of blast analysis. Propellant heats of formation were calculated using the propellant compositions and the JANAF thermochemical tables [75]. The projectiles' muzzle velocities were measured experimentally using tracking radar.

Visible high-speed imagery was collected using a monochrome v5.1 Phantom imager with 1024 x 1024 pixel CMOS focal plane. It was located with a side-on view of the gun at a distance of 429 meters. The imager was capable of collecting at greater than 100,000 frames per second (fps) by windowing the focal plane, but it was used at a lower rate to allow for a larger field of view. The standard configuration throughout the test was 1024 x 768 pixels at 1,600 fps. A 400 mm focal length f/# 2.8-32 Nikon lens was equipped on the imager and provided an instantaneous field of view of $1.71 \times 1.71 \text{ cm}^2$ and a full field

Table 5. Average ballistic, propellant, and blast properties for three munitions configurations.

Quantity	Full Charge	Charge 1	Charge 2	Method
Propellant charge mass	9.0	7.7	4.2	test article documentation
Propellant heat of formation	-19.57	-16.56	-6.31	JANAF tables [75]
Projectile mass	43.5	43.5	43.5	test article documentation
Projectile muzzle velocity	638 \pm 4	589 \pm 5	507 \pm 2	Weibel radar
Projectile kinetic energy	8.86 \pm 0.11	7.55 \pm 0.13	5.59 \pm 0.04	$K_p = m_p u_p^2 / 2$
Theoretical near-field limit	1.25	1.19	0.98	Equation (15)
Theoretical maximum far-field limit	5.52	5.25	4.57	Equation (16)
Observed far-field limit	3.31 \pm 0.35	2.91 \pm 0.29	2.57 \pm 0.31	Steward, Gross, Perram [93]
Detachment time	0.95 \pm 0.24	0.92 \pm 0.12	0.69 \pm 0.10	Equations (14 – 15)

of view of $17.5 \times 13.1 \text{ m}^2$. Imagery and audio were also collected with a Canon XL1 camera. The camera was intended to document the test, but correlating its audio and video tracks provided additional data useful for analysis. It collected 48 kHz audio and 640 x 480 pixel, 30 fps imagery.

A Weibel MSL-60037 tracking radar unit was co-located with the gun and was used to monitor projectile trajectory at $\sim 23.5 \text{ ms}$ intervals. The primary use of the radar system was to provide real-time feedback to the firing team, allowing them to make minor corrections to the gun azimuth and elevation to adjust the actual impact area closer to the intended site. In addition to trajectory, the muzzle velocity, impact location, and actual gun elevation were recorded.

Atmospheric meteorological conditions were monitored using a number of instruments. These included a WeatherHawk weather station that collected air temperature, relative humidity, and barometric pressure at one minute intervals. Conditions were typically cool with temperatures ranging $8 - 21 \text{ }^\circ\text{C}$, relative humidity of $28 - 60\%$, and barometric pressure lower than the standard atmosphere at $P_0 = 83.4 - 96.8 \text{ kPa}$. The collected weather data were used to estimate the local speed of sound for each firing, $a_0 = 341.0 \pm 4.2 \text{ m/s}$, and an ambient air density $\rho_0 = 1.09 \pm 0.05 \text{ kg/m}^3$.

Results

Blast Wave Imagery

Figure 16 (a) shows a representative image used to determine the extent of the blast wave as a function of time and (b) displays pertinent features. Each frame of Phantom v5.1 camera data was image processed to enhance visibility of the blast wave. Processing

included subtracting consecutive frames to reveal frame-to-frame differences in the shock front's leading edge, applying a 3x3 median filter to reduce noise, and stretching the histogram to improve contrast of dim features. The leading edge of the shock was blurred across 5 – 10 pixels which limited measurement accuracy to approximately ± 0.1 meters. The position of the shock front was measured in the vertical plane containing the gun barrel in nearly all directions relative to the muzzle. The measurements were repeated for firings of Full Charge, Charge 1, and Charge 2 configurations for all frames from shot exit until the blast wave propagated out of the imager's field of view.

The shape of the blast wave was observed to be slightly elliptical with radial variation of less than 10% and major axis oriented along the barrel of the gun. Radial asymmetry was most pronounced in the near-field, but as the blast propagated into the far-field the minor axis length closed to within 95% of the major axis length. This is in agreement with prior experiments in which, due to the geometry of the muzzle flow, blast waves were initially found to be asymmetric but became spherical as they expanded against atmospheric counter-pressure [79].

Because the blast was nearly spherical in the plane of observation, the distance between the muzzle and the shock front in each frame was assumed to not vary as a function of angle. This distance was measured in multiple (5 – 10 samples) angular directions, and the mean value of the samples was used as the shock front's average radius for the frame. Uncertainty averaged less than ± 0.19 m and is due to both measurement error and minor ($< 5\%$) directional variation of the radius from semi-minor to semi-major axes. Radial measurements for consecutive frames are separated in time by 0.625 ms (corresponding to the 1,600 fps rate of the Phantom v5.1 imager) and the

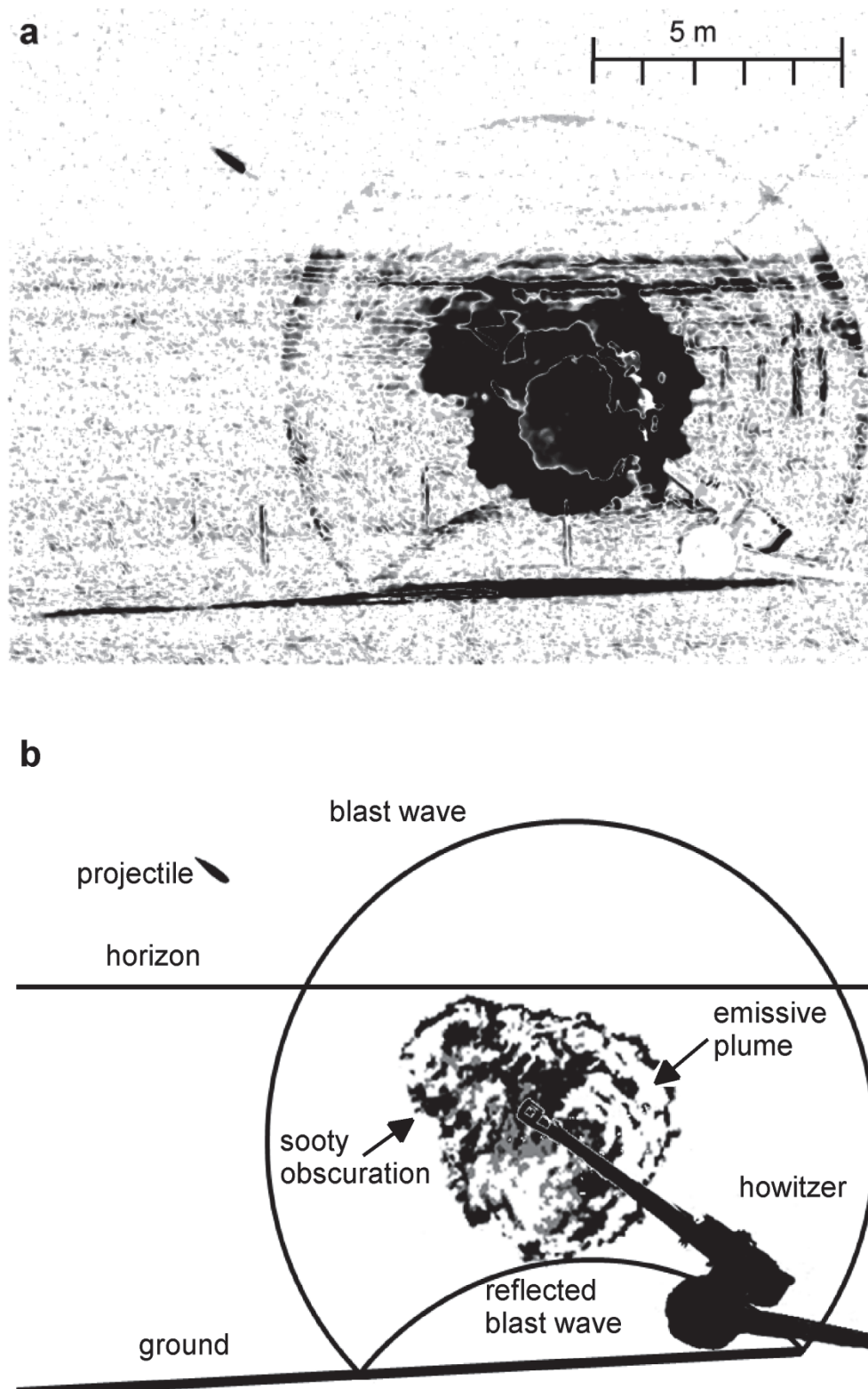


Figure 16. Firing signatures are shown for the 152 mm howitzer. (a) Image processing improves contrast so that the blast wave is visible in all directions around the muzzle. (b) Each feature of interest in the processed image is identified in the sketch.

collection of radius-time pairs for a single firing represents the blast's expansion trajectory for the firing. Trajectory was determined for 49 Full Charge, 79 Charge 1, and 19 Charge 2 firings. The aggregate of all Full Charge trajectories are shown in Figure 17 (a), and the temporal origins are aligned to the same relative time after shot exit. Charge 1 and Charge 2 data are very similar and are not shown. For times beyond the near-field, the variation in the aggregate blast wave radius is greater than measurement uncertainty and upwards of ± 0.5 meters from the configuration average. Early-time ($t \approx 1 - 3$ ms) data show less variance – on the order of measurement uncertainty – and indicate fairly uniform initial blast expansion velocities near Mach 3 – 4.

The Canon XL1 camera was used to obtain a single data point far (429 m) from the gun. The time of arrival of the blast wave was determined for each event by measuring the time delay between video of the gun firing and the audible boom recorded by the camera's microphone. Timing accuracy was limited by the 30 Hz frame rate of the camera, which corresponded to approximately 11.5 meter uncertainty.

Point Blast Model

A variety of models for the propagation of a blast wave, including similarity arguments, empirical solutions, and theoretical developments from gas dynamics have previously been developed [66, 69:97-106; 70, 73, 91]. A recent evaluation of these models revealed that the Taylor-Sedov point blast model extended to the acoustic, far-field limit adequately represented the data with two or three fit parameters [93]. This model has the additional benefit of interpreting fit parameters to derive propellant properties such as energy released, offering significant promise for event classification. We limited the present analysis to this blast model.

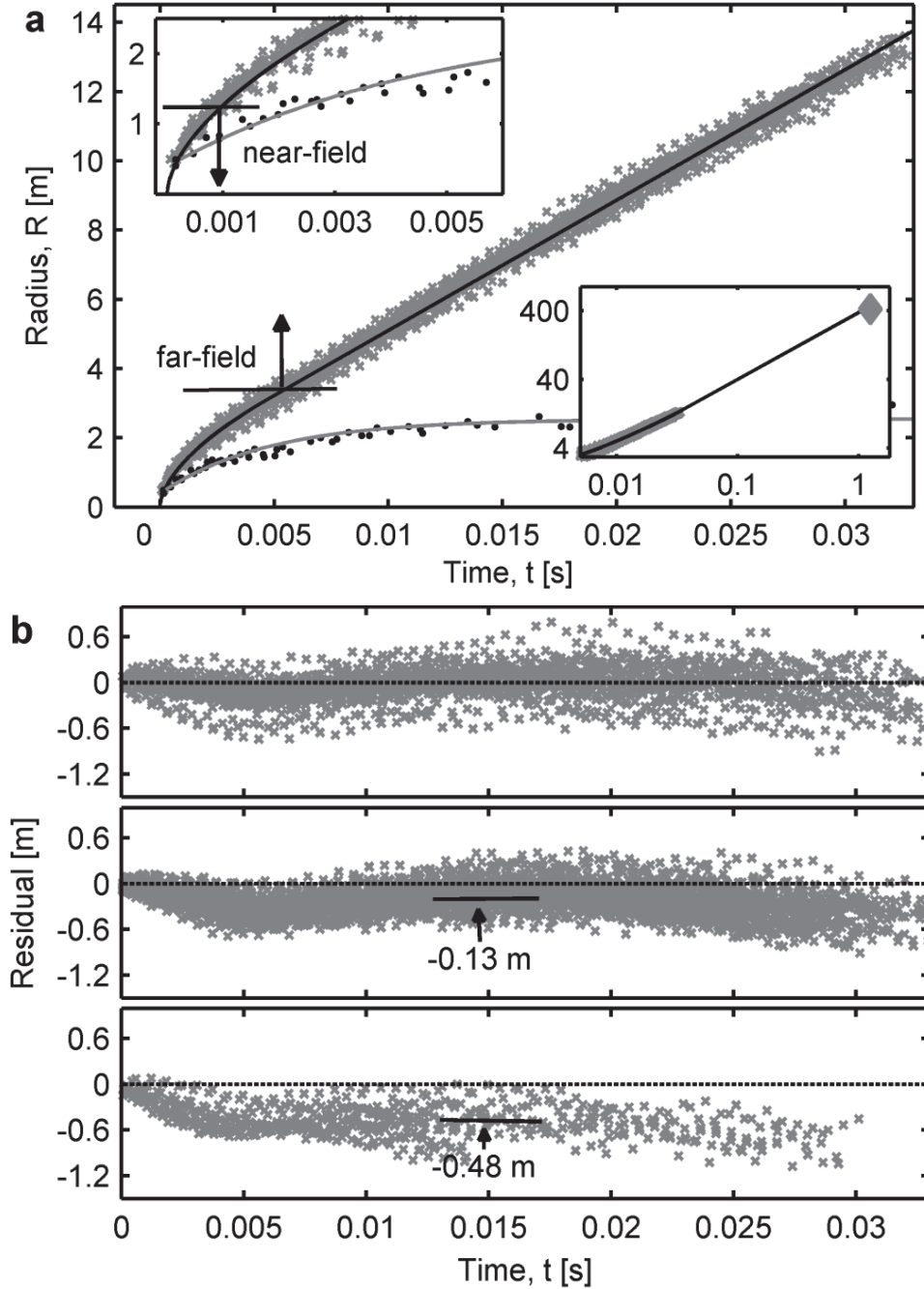


Figure 17. Aggregate of observed gun firing data as a function of time. (a) Radius-time data points (\times) for all Full Charge firings. The point blast model with $b' = 0.6$ (—) is overlaid and correlates well with the data. A single observation (\diamond) obtained at the instrumentation site was not included in the fit data and demonstrates that the model accurately predicts the blast wave trajectory very far from the gun. Muzzle plume expansion for a sampling of firings (\bullet) and drag model fit (—) show that detachment of the shock from the plume occurs in the near-field. (b) Residual (\times) between constrained Full Charge point blast model and (from top to bottom) Full Charge, Charge 1, and Charge 2 radius-time data. At equivalent times the blast waves from lower charge masses propagate a shorter distance on average. Spread in the data represents the variance in firings for similar configurations, and curvature is evidence of systematic error.

The point blast model was first put forth by Taylor [70], discovered independently by Sedov [73], and later generalized by Sakurai [66] and Rogers [91]. It was developed for intense explosions in which a large amount of energy is nearly instantaneously released and is based on a similarity solution in which the relationship between the radius and time are invariant to scaling. Modeling of the blast wave resulting from muzzle flows is less well established, but its treatment using the point blast model is not completely novel [21, 25, 79].

A piecewise function allows the point blast model to be extended to the far-field:

$$R(t) = \begin{cases} At^b & t_n < t < t_f \\ a_0 t + \Delta R & t \geq t_f \end{cases} \quad (10)$$

where the acoustic limit parameters are defined as:

a_0 = speed of sound in air

$\Delta R = At_f^b - a_0 t_f$ = radius off-set for the acoustic limit

The mid-field fit parameters:

$$A = \xi (E_0 / \rho_0)^{1/(n+3)} \quad (11)$$

$$b = (s + 2) / (n + 3) \quad (12)$$

are related to the blast dimensionality ($n = 0, 1$ and 2 correspond to planar, cylindrical and spherical expansions), the rate of energy release ($s = 0$ for instantaneous energy release and $s = 1$ for constant rate of energy release), and atmospheric density, ρ_0 . The energy released in the explosion is defined as:

$$E_b = E_0 t^s \quad (13)$$

The parameter, ξ , is a unitless constant that depends on the ratio of specific heats, the geometry of the blast, and the rate of energy release. Typically $0.9 < \xi < 1.1$ but is set $\xi = 1$ here; more exact values can be obtained with the derivations presented by Sedov [73]. The time to reach the end of the near-field, t_n , and beginning of the far-field, t_f , are related to the corresponding ranges [72]:

$$t_{n,f} = (R_{n,f} / A)^{1/b} \quad (14)$$

The range of the mid-field:

$$R_n = (3m_c / 4\pi\rho_0)^{1/3} \quad (15)$$

$$R_f = (E_b / P_0)^{1/3} \quad (16)$$

is defined by the requirements that sufficient air mass has been displaced to exceed the explosive mass, m_c , but the blast's peak overpressure still exceeds the atmospheric pressure, P_0 . Equation (16) is the radius at which the far-field begins and is a maximum if 100% of the explosive energy is converted to blast energy, E_b .

The model of Equation (10) was fit to the mid and far-field data for each event. An example of the fit to the aggregate of all Full Charge firings when dimensionality is constrained to spherical ($n = 2$) and energy release is constant ($s = 1$) is illustrated in Figure 17 (a). The radius at which the model switches from point blast to linear was set to the observed values of R_f in Table 5. The model is plotted using the average of the fit parameters for the configuration provided in Table 6. Residuals indicating the quality of the Full Charge fit are shown in the top panel of Figure 17 (b) and are primarily due to the variance in the data from event to event, although a small systematic error can be seen as a slow oscillation with time.

Table 6. Average values of the fit parameters for each munitions configuration.

Parameter	Full Charge	Charge 1	Charge 2
Unconstrained			
A	70.7 ± 3.0	64.2 ± 1.9	57.6 ± 1.8
b	0.58 ± 0.02	0.57 ± 0.01	0.56 ± 0.01
a_0	376 ± 9	373 ± 7	360 ± 11
Adjusted r^2	0.9951	0.9962	0.9944
RMS (m)	0.094 ± 0.020	0.095 ± 0.019	0.081 ± 0.024
Spherical constant energy release ($s = 1, n = 2$)			
A'	80.1 ± 0.8	76.8 ± 1.0	74.1 ± 1.4
b'	0.60 ± 0.00	0.60 ± 0.00	0.60 ± 0.00
a_0'	370 ± 9	366 ± 8	342 ± 13
Adjusted r^2	0.9952	0.9963	0.9946
RMS (m)	0.104 ± 0.022	0.106 ± 0.020	0.108 ± 0.022

The bottom two panels of Figure 17 depict differences in configurations' trajectories by showing the residual between the aggregate Charge 1 and Charge 2 data and the Full Charge model. The most noticeable difference is that the blast wave radius is greater for increased charge mass at equivalent times due to greater initial velocity (observed as curvature in the trajectory). For example, at 14 ms Charge 1 and Charge 2 have respectively propagated an average 0.13 m and 0.48 m less than Full charge. The systematic error observed in the Full Charge residual is also evident (even if the Charge 1 and Charge 2 models are used) and is a result of the linearity of the $a_0 t$ term that is not representative of deceleration of the blast wave in the far-field. Using a_0 as a fit parameter results in a value that is up to 10% larger than ambient speed of sound because the linear term is representing data that has not yet fully decelerated to sonic conditions.

Nonetheless, extrapolation to the far-field point obtained by the Canon XL1 camera at the instrumentation site, depicted in the Figure 17 (a) inset, indicates that the model predicts time of arrival to within 4.2 – 9.5% per event.

A range of best-fit parameters (A and b) were obtained for firings of similar munitions configurations, as is shown by the distributions of Figure 18 (a) and (b). The variation is due to a combination of uncertainty in measurement of the blast wave radius and variation in muzzle flow properties for each event. In general both A and b increase with increasing charge mass, but the variation from event to event causes overlap amongst configurations. The average values and standard deviations of the fit parameters for each munitions configuration are provided in Table 6. Adjusted r^2 statistic and root-mean-square (RMS) residual between the model and data indicate the quality of each fit. Non-adjusted r^2 values are larger for the unconstrained model by 0.002 – 0.003 because of the additional degree of freedom, and this is normalized by the adjusted statistic to show that there is a comparable fit quality between both models.

Also shown in Figure 18 (c) and Table 6 are the values of the fit parameters and distributions of A when b is constrained to a value of $3/5$. The fit results are denoted by a prime when b is constrained, i.e. A' and b' . The constraint corresponds to the case of spherical geometry ($n = 2$) and a constant rate of energy deposition ($s = 1$). The latter is often assumed because muzzle flow can be approximated – at least initially – as quasi-steady state [32], and previous studies have shown that energy deposition into the blast wave is much closer to continual than instantaneous [29, 79]. Fit residuals are not significantly increased by the constraint and the uncertainty in A' is reduced. Significant correlation $r^2 = 0.86$ exists between the fit parameters, A and b , without the constraint.

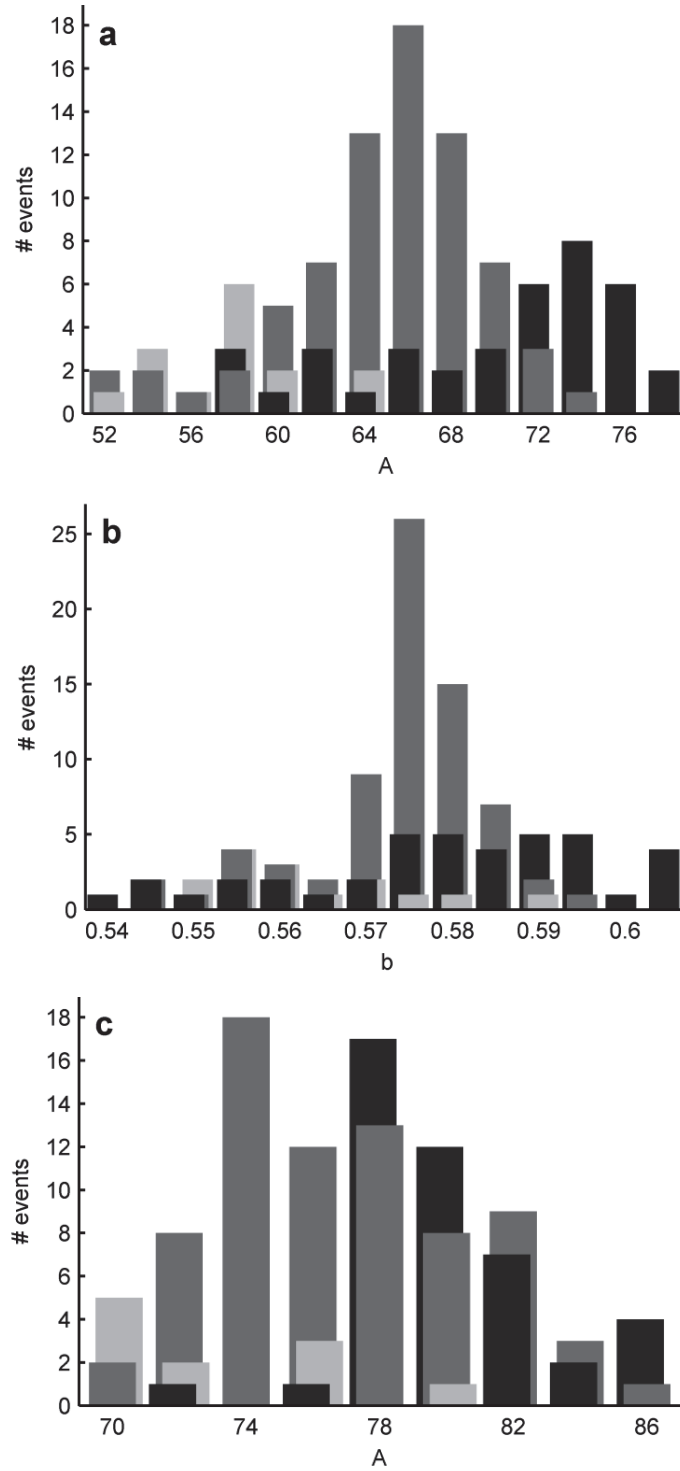


Figure 18. Distributions of (a) A , (b) b , and (c) A' fit parameters are shown for Full Charge (■), Charge 1 (▒), and Charge 2 (░). Parameters of similar magnitude are grouped into bins and the number of events per bin is shown. Bars for each class are slightly offset for visibility but correspond to the same bin values. The mean value of each fit parameter increases with increasing propellant mass.

Muzzle Plume

The shock front formed by expanding muzzle gases is characterized by strong discontinuities in both density and pressure. As the front expands, drag exerted by the atmosphere decelerates the gases sufficiently such that the pressure discontinuity detaches and propagates more quickly than the mass flow. Detachment results in two distinct quantities: (1) the blast wave characterized as a supersonic pressure wave whose amplitude and velocity decrease as it expands (because of cessation of the driving mass that formed it), and (2) a muzzle plume composed of gaseous and particulate propellant by-products whose expansion continues to decelerate due to drag by ambient atmosphere.

Whereas expansion of the blast wave can be expressed by Equation (10), expansion of the muzzle plume is represented by:

$$r(t) = r_m \left(1 - e^{-\kappa t}\right) \quad (17)$$

where the parameters:

r_m = stopping distance

κ = drag coefficient

define, respectively, the maximum distance muzzle flow travels before being completely decelerated by atmospheric drag and the rate of deceleration. Maximum plume radius as a function of time was measured for a subset of the firings. A representative sampling of radius-time points and the fit of Equation (17) to the data are shown in Figure 17 (a). RMS uncertainty in radius beyond the near-field is 0.55 m due to directional non-uniformity and drift due to wind and flow momentum. Differences in plume expansion for each configuration are not resolvable to within measurement uncertainty, and a

common set of drag model parameters, $r_m = 2.52 \pm 0.07$ and $\kappa = 221 \pm 20$, can be used to represent the plumes' expansion for all configurations.

The blast wave and muzzle plume are initially coincident, and detachment occurs when the gases' velocity falls below the blast wave's. Equation (15) defines the near-field limit [72] and identifies where the mass flow's influence on the blast wave can be neglected [66][69:97-199][70], which cannot be too greatly removed from when detachment occurs. Detachment times for each configuration are calculated via Equation (14) with the unconstrained fit parameters, A and b , and are provided in Table 5.

Discussion

Constant Breech Pressure Gun

Energy properties of the muzzle gas at shot exit are shown in Table 7. The gas heat of formation $(\Delta H_f^0)_g$ is calculated from the propellant combustion by-products at the muzzle using the JANAF tables [75], and enthalpy change ΔH is the difference in this value with the propellant's initial heat of formation $(\Delta H_f^0)_c$. Propellant energy loss ΔE is the total amount of energy removed from the propellant to perform work on the projectile or lost as heat Q to the gun system (by friction, barrel heating, etc.). Total gas energy E_g is the amount of energy remaining in the propellant gases in either kinetic or potential form. It is the energy that contributes to heating of the muzzle plume and expansion of muzzle gases against atmosphere external to the gun; the former is directly related to muzzle flash and the latter results in the blast wave.

The muzzle gas heat of formation, propellant energy loss, and specific heat capacity require knowledge of the muzzle gas' thermodynamic properties. A constant breech

Table 7. Properties of the muzzle gas at shot exit.

Quantity	Full Charge	Charge 1	Charge 2	Method
Gas heat of formation, $(\Delta H_f^0)_g$ [MJ]	-45.20	-38.31	-21.16	JANAF tables [75]
Enthalpy change, ΔH [MJ]	25.63	21.75	14.84	$\Delta H = (\Delta H_f^0)_c - (\Delta H_f^0)_g$
Propellant energy loss, ΔE [MJ]	9.85	8.37	6.09	CBP gun [45]
Inefficiency loss, Q [MJ]	0.99 (10.0%)	0.82 (9.8%)	0.50 (8.2%)	$Q = \Delta E - K_p$
Total gas energy, E_g [MJ]	15.78	13.38	8.76	$E_g = \Delta H - \Delta E$
Gas specific heat, c_p [J/kg-K]	1928	1918	2000	BLAKE [94]

pressure (CBP) gun model was used to estimate the thermodynamic state of the system from shot start to shot exit. It typically estimates efficiencies to within 5 – 10% of actual for well-designed guns [45]. The CBP model treats interior thermodynamics defined by constant pressure at the breech during propellant combustion, followed by isentropic pressure decay after the propellant has consumed all available oxygen [94]. It does not model energy loss due to heating of the gun tube, friction between the projectile and the barrel, or other inefficiencies that result in an overestimation of muzzle velocity. The CBP gun is presented in detail in Appendix B.

To account for inefficiencies, the CBP gun was first used with the properties of the test articles contained in Table 5; the difference between the work performed on the projectile from the model and the kinetic energy measured from radar data was assumed to be due to inefficiency loss, Q . The CBP gun was then re-run with an increased projectile mass (by 8 – 10% corresponding to the inefficiency energies provided in Table 7) such that the exit velocities agreed. The energy loss is artificially removed from the system (by treating it as projectile kinetic energy) so that the thermodynamic state of

gases at shot exit contains the correct total gas energy, E_g . Change in other thermodynamic state properties was minor, for example Full Charge observed a reduction in temperature by 62 K (3.4%), pressure by 3.48 MPa (3.9%), and major combustion by-products (CO, H₂, H₂O, N₂, and CO₂) by 1 – 4% due to a shift in chemical equilibrium.

Thermodynamic calculations were performed using the BLAKE equilibrium chemistry code [94]. This code handles non-ideal gas behavior via the Nobel-Able equation of state, which is necessary due to the extremely high pressures generated in the gun chamber where treatment of the interior flow-field by the ideal gas law is not valid. The reaction pathways typical of combusting muzzle plumes are detailed by Heimerl, et al. and Yousefian [50, 53]; however, a detailed study of these is not necessary since standard thermodynamic codes (such as BLAKE) incorporate the pertinent reactions and computes the pre- and post-combustion chemistries and thermodynamics [94]. Thermodynamic state estimates were improved by using Kotlar's implementation of the CBP gun which computes equilibrium product thermo-chemistry throughout the interior ballistics cycle rather than freezing it at the burnout state [45].

The kinetic, internal and total energies of the muzzle gas and its specific heat are obtained from the species composition of the propellant gas as muzzle exit. Simplifications in CBP gun calculations prevent accurate, highly-detailed predictions of the thermodynamic state of the muzzle gas. However, it is sufficient for macroscopic estimates of interior ballistics properties such as total energy release by the propellant and its partitioning between projectile and muzzle gases. The latter is used in interpreting the fit parameters obtained with the piecewise point blast model.

Blast Wave Energy

The total energy released into the blast wave described in Equation (13) can be re-expressed using the fit parameters, A and b , from Equations (11) and (12) as:

$$E_b(t) = \rho_0 \left(A / \xi \right)^{n+3} t^{b(n+3)-2} \quad (18)$$

This is the total energy deposited from shot exit to time t . After the time at which the shock detaches from the muzzle plume, $t = \tau$, the blast wave is no longer in contact with the muzzle flow and energy deposition ceases. Values of E_b (and E_b' for $b' = 3/5$) for each munitions configuration are given in Table 8. Because the unconstrained fit results yield values of b that do not correspond to integer values of s , the rate of energy deposition is neither instantaneous nor constant during the period of shock-plume interaction. Total energy deposition can be obtained from Equation (18), but it is useful to visualize what these values of b represent physically. The rate of energy deposition into the blast as a function of time is:

$$dE_b / dt = \rho_0 \left(A / \xi \right)^{n+3} (b(n+3) - 2) t^{b(n+3)-3} \quad (19)$$

Equations (18) and (19) are depicted in Figure 19 using the average values of the fit parameters for the Full Charge configuration and assumed spherical dimensionality ($n = 2$). As expected, curves for the constrained fit show that dE_b'/dt is constant with a value of approximately $E_0 = 3,600$ MJ/s, and E_b' increases linearly in time as $E_0 t$. When b is unconstrained, the mean of each configuration's rate exponent corresponds to $s \approx 0.9$. This is slightly on the instantaneous side of constant energy deposition and can be interpreted as an initially large transfer followed by a decay to near constant. This is observed in the figure where dE_b/dt is initially large but falls off quickly. The E_b curve

Table 8. Muzzle blast and flash quantities for spherical dimensionality ($n = 2$).

Model	Full Charge		Charge 1		Charge 2	
	$b = 0.58$	$b' = 0.6$	$b = 0.57$	$b' = 0.6$	$b = 0.56$	$b' = 0.6$
Energy deposition rate		3.58 ± 0.20		2.93 ± 0.25		2.32 ± 0.27
Energy deposited into blast						
	3.9 ± 0.8	3.4 ± 0.4	3.0 ± 0.6	2.7 ± 0.5	1.7 ± 0.3	1.6 ± 0.4
Efficiency						
	0.24 ± 0.06	0.22 ± 0.03	0.22 ± 0.05	0.20 ± 0.04	0.19 ± 0.04	0.18 ± 0.05
Energy remaining in plume						
	11.9 ± 1.27	12.4 ± 1.07	10.4 ± 1.02	10.7 ± 0.96	7.1 ± 0.58	7.2 ± 0.64
Plume temperature						
	979 ± 46	$1,003 \pm 26$	997 ± 38	$1,017 \pm 32$	$1,194 \pm 40$	$1,209 \pm 46$
% unsuppressed flashing plumes		50%		75%		84%
% flashing plumes		15%		28%		84%

provides similar evidence – energy deposited into the blast is nearly parallel to E_b' yet it is slightly larger owing to the greater initial rate. The unconstrained fit results in a greater total energy being deposited into the blast during the shock-plume interaction time.

The *efficiency* of transferring energy from the gaseous muzzle flow to the blast wave is the ratio of energy deposited into the blast to the gases' total energy:

$$f = E_b / E_g \quad (20)$$

The efficiencies for each munitions configuration are given in Table 8. Constraining $b' = 0.6$ results in similar but slightly lower efficiencies. On average 18 – 24% of energy contained in the muzzles gases was transferred to the blast wave. Efficiency did not change significantly with weapon configuration, although a slight decrease was observed as charge mass decreased. This trend includes when flash suppressant was removed and

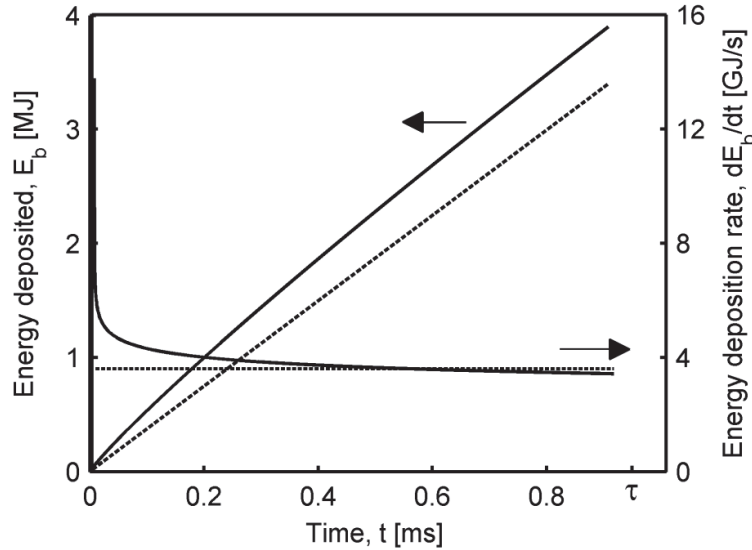


Figure 19. The rate of energy deposition into the blast is shown on the right axis for the Full Charge point blast model with b unconstrained (—) and constrained to a value of $b' = 3/5$ (---). The constrained rate is constant and the unconstrained case is initially large but drops quickly. The total energy deposited into the blast as a function of time is shown on the left axis. The unconstrained case is nearly parallel to the constrained case excepting that it has deposited more energy into the blast at very early times. Both sets of curves stop at $\tau = 0.95$ ms where the blast wave detaches from the plume and is no longer influenced by muzzle flow.

is characterized by a decrease in efficiency by an additional 1 – 2% without the suppressant mass. Decrease in efficiency is attributable to a combination of relatively greater energy transfer rates and later detachment times for larger masses, on a per mass basis. For example, increasing the propellant mass by ~18% from Charge 1 to Full Charge results in an increase in muzzle gas energy by a corresponding ~18%, but the rate of transfer to the blast wave increases by ~22% and interaction between the blast and flow is ~3% longer. The slightly increased rate and duration, relative to increase in mass, are likely due to greater momentum of the muzzle flow resulting from higher pressures internal to the gun.

Because efficiency does not change drastically with changes to charge mass, if it is assumed to be relatively constant regardless of weapon configuration, measured blast energy and efficiency provide a method of estimating total enthalpy change of the propellant: $\Delta H \approx E_b / f + K_p$, where K_p is the kinetic energy of the projectile. Recall that E_g was calculated using the CBP gun model by treating the inefficiency loss Q as an increase in projectile mass. Because this is only an approximate solution, heat loss was also propagated as an uncertainty and is accounted for in the calculated values of the efficiency f . The energy remaining in the muzzle plume after detachment of the blast wave is:

$$E_p = E_g - E_b \quad (21)$$

This partitioning of muzzle gas energy between the blast wave and the plume allows for an estimate of the plume's pre-combustion temperature. This is useful because it relies (experimentally) only on optical observation of gun firing and interior ballistics

rather than in-situ measurements or external flow modeling. Assuming negligible plume kinetic energy and non-reactive chemistry, the change in plume temperature is:

$$T_f - T_0 = \frac{E_p}{m_c c_p} = \frac{(1-f)E_b / f}{m_c c_p} \quad (22)$$

T_f is an estimate of the plume's temperature after detachment of the blast wave (and prior to combustion), T_0 is the initial temperature of the propellant *prior* to shot start (typically ambient), m_c is propellant mass, and c_p is the muzzle gases' average specific heat. Temperature changes reported in Table 8 are determined by assuming that nearly all gaseous energy contributes to temperature increase, which is only valid because turbulence and expansion of the plume account for a very small fraction of the total energy after the blast wave has separated. If charge mass and composition are known then the heat capacity can be easily estimated; and if efficiency is assumed to be fairly constant independent of munitions configuration, which is supported by the results in Table 8 where the range of efficiencies only varies by 6%, the plume temperature can be estimated solely in terms of observed blast wave energy.

Muzzle Flash

Plume temperature is one of the critical conditions that determine whether the muzzle plume is able to ignite and sustain combustion [32, 49, 50, 53]. Equation (13) estimates the pre-combustion temperature of the plume based simply on energy partitioning and bypasses the need for complicated models that treat the interior ballistics and development of muzzle gases external to the gun.

The percentage of plumes in which muzzle flash occurred is shown in Table 8. Because the muzzle brake splits the flow into three plumes, each plume is treated

separately. Reduced charge mass is more likely to result in combustion, with or without flash suppressant. This is counterintuitive – greater mass releases more energy which ostensibly supports higher plume temperatures and is more likely to induce muzzle flash. If the results of Table 8 can be used as evidence – supportive but not conclusive due to the approximations used in the models – the smaller propellant charges actually result in higher temperatures and is the cause of the greater likelihood of flash in those configurations. The Charge 2 configuration’s plume temperatures are the greatest and above the plumes’ required ignition temperature, the minimum of which is typically near 1,000 K independent of propellant [28].

Figure 20 shows the number of plumes that combust as a function of the various pre-combustion temperatures and projectile velocities. The plot can be interpreted as displaying the variance in the partitioning of an assumed constant total propellant energy. Greater temperature (lower blast energy via Equation (12)) and lower projectile energy imply greater energy remaining in the plume and an increased incidence of muzzle flash. This is confirmed on a large scale where the trend shows that as projectile velocity decreases the temperature is likely to be greater, and the fraction of plumes flashing increases on average. This is particularly evident when comparing Charge 2 to either Charge 1 or Full Charge: all of the Charge 2 firings show a minimum of two plume combusting whereas the likelihood is greatly reduced in the other configurations. Charge 1 also tends to show a greater number of plumes combusting than Full Charge, per firing. Note that the groupings of Full Charge and Charge 1 munitions with the greatest velocities are chemically suppressed, and lack of flash cannot be attributed to reduced energy in the plume.

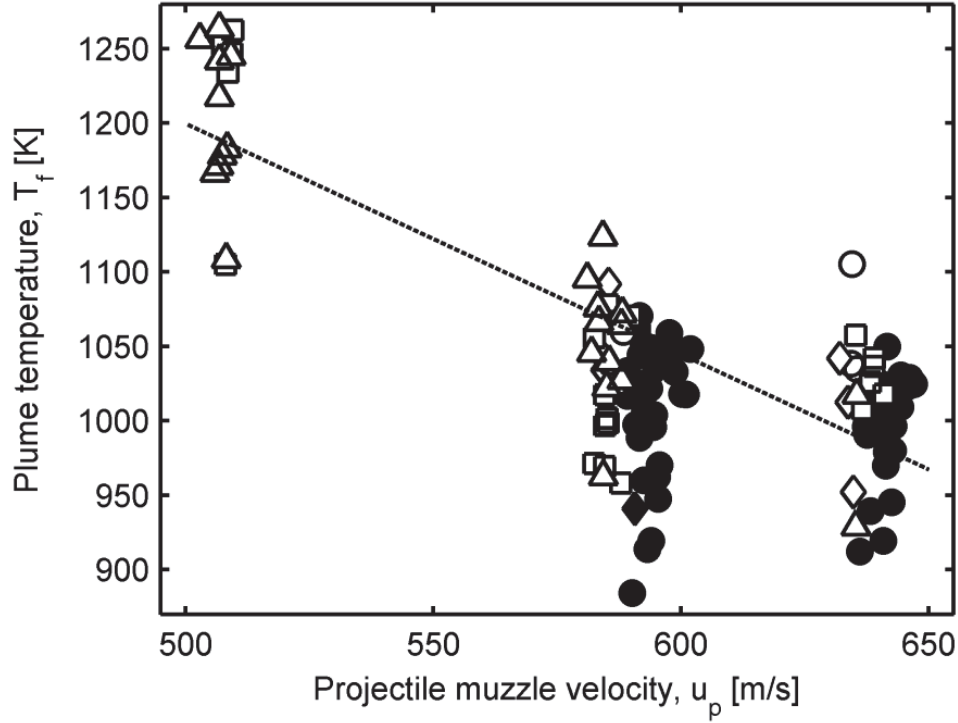


Figure 20. The number of plumes combusting is shown for each event as a function of estimated plume temperature and measured muzzle velocity of the projectile. Circles (\circ) indicate no flash; and diamonds (\diamond), squares (\square), and triangles (\triangle) represent 1, 2, and 3 plumes flashing. Configurations containing flash suppressant are shown with solid symbols and rarely flash. Three distinct groupings are observed corresponding to Full Charge, Charge 1, and Charge 2, from right to left.

The data do not show the same trend within a configuration. As projectile velocity and plume temperature vary, the number of plumes flashing is uncorrelated. The lack of correlation between energy and flash may result from stochastic effects in the flow field as well as measurement uncertainty. Measurement uncertainty is low enough that the differences in blast wave trajectory can be distinguished even between the similar munitions configurations, yet it is not low enough that very minor variations can be accurately detected within a single configuration. Additionally, whether the plume flashes is not completely deterministic – more energy remaining in the plume (which translates to higher temperatures) increases the likelihood of flash, but combustion is not

guaranteed. For combustion to occur requires that local regions in the plume have the necessary fuel and oxygen ratio, temperature, and dwell time for ignition, and that the turbulence in the flow field is sufficient to sustain combustion yet not too great to quench the flame. Thus greater energy in the plume – lower blast wave energy per propellant energy release – is a necessary but not necessarily predictive condition for muzzle flash.

Direct measurement by the Weibel radar provided significantly lower uncertainty in measurement of projectile energy ($< 2\%$) than fit parameter estimation of plume energy (9 – 10%) and reveals a relationship based on the partitioning of energy: lower projectile velocity may be weakly correlated with likelihood of flash, as is shown in Figure 21. The inverse relationship of projectile muzzle velocity and blast efficiency to the increase in plume temperature and propensity for combustion should be confirmed with more precise energy measurements. In-situ characterization of the thermodynamic state of the muzzle flow (temperature, flow velocity, etc.), properties of the blast (velocity, overpressure, etc.), and state of the weapon (projectile velocity, barrel heating, etc.) could be used to establish how energy is partitioned and correlated with plume ignition. The difficulty with which accurate measurements can be made in the non-laboratory field environment (which is necessitated for firings of large caliber guns) typically precludes experimental tests; however computational fluid dynamics (CFD) simulations are likely a satisfactory alternative. Previous CFD modeling of muzzle blast and flash have shown that the necessary quantities can be calculated to a high degree of fidelity [95, 96], and – although beyond the scope of this work – demonstrate CFD's potential for use in further investigation of energy partitioning and propellant mass' effect on projectile velocity, blast energy, plume temperature, and muzzle flash.

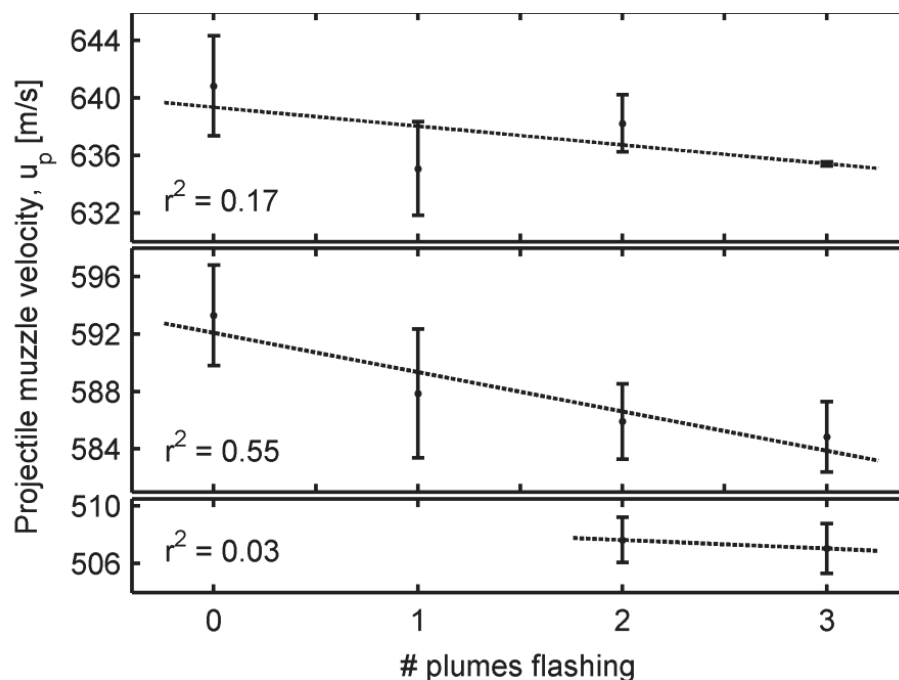


Figure 21. Mean and variance in projectile muzzle velocity is shown as a function of the number of plumes flashing for each configuration, from top to bottom: Full Charge, Charge 1, and Charge 2. The data indicate a weak correlation in which lower muzzle velocity increases the likelihood of flash.

Classification Potential

One of the practical reasons to observe a statistically significant number of gun firings is to identify which properties of the muzzle signatures show potential for the classification. Physical rather than empirical properties are preferred because they provide confidence, and understanding the properties may allow for extrapolation to unobserved systems. Such properties include several already examined: blast energy, plume temperature, projectile velocity, and muzzle flash. Those signatures that are correlated with munitions properties (mass, enthalpy, composition, etc.) and can be measured with sufficient precision have potential for classification.

The blast wave trajectory properties show potential. Arguably, if sufficient fidelity imagery is available to identify the blast wave then measurement of the projectile

velocity would instead provide the greatest ability to distinguish configurations. The variance in velocity is significantly less than the separation between configurations, as is evident in Figure 20 and Figure 21. Nonetheless, hypothesizing a situation in which blast wave trajectory data are the only available source for classification, Table 5 and Table 8 indicate that most properties can be used. Interpretation of parameters that are most pragmatic are those obtained from Equations (18) and (19): total energy in the blast and the rate of deposition. All other physically meaningful interpretations – while useful for interpreting phenomenology – are reformulations of the same information that may require too much *a priori* information to be pragmatic for classification. For example, temperature estimation requires knowledge of heat capacity and mass, whereas energy parameters can be obtained directly from the data.

Perhaps the best physical feature for distinguishing the three configurations is obtained by constraining $b' = 3/5$. This reduces the rate of deposition to a constant with respect to time, the distributions of which are shown in Figure 22. The distributions were obtained by summing area-normal Gaussians for all events of each configuration with the mean and width defined as the energy rate and fit uncertainty for each event. The curves were then normalized by the number of events per configuration to obtain probability distributions. Separation of the configurations, and consequently potential for differentiation, is quantified by the ratio of the sum of differences in means of the distributions to the sum of their variances. The ratio for the three configurations is 1.32, indicating approximately 32% greater between-class separation than within-class variability. The ability to distinguish configurations may be improved by reducing within-class variance. Some variance is inherent due to changes in atmospheric

conditions and munitions non-uniformities from shot-to-shot, but the remainder may be eliminated by improving measurement accuracy of the blast trajectory. Improved contrast of the blast (via optimization of imager configuration or control of scene background) would remove error associated with spatial uncertainty, and a faster imager would improve resolution of the mid-field curvature from which rate of energy release is derived.

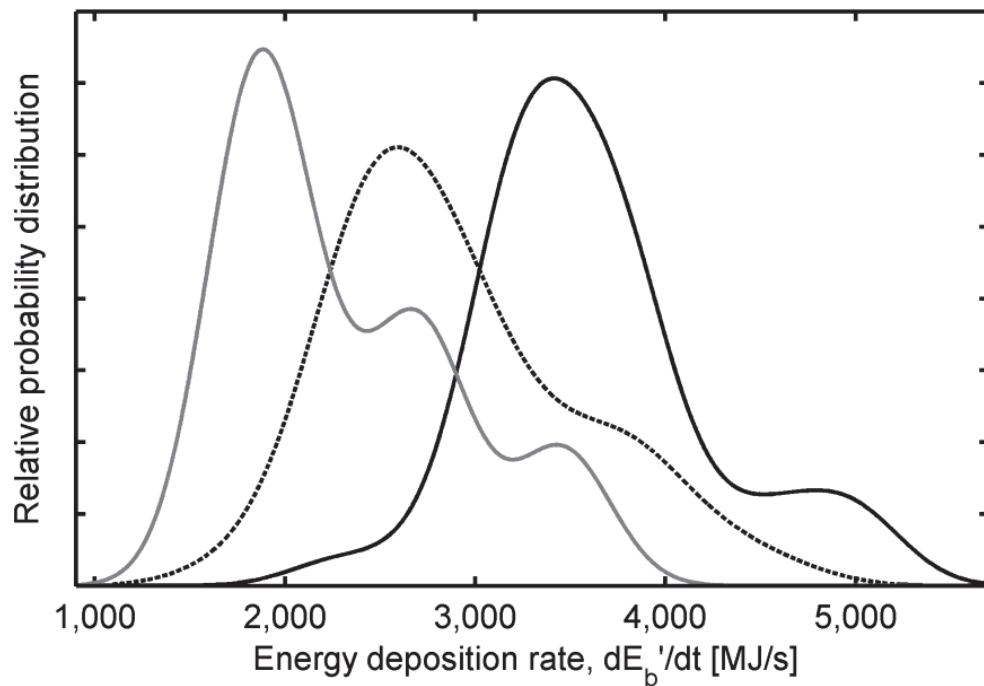


Figure 22. Distributions of the time-independent rate of energy deposition, corresponding to $b' = 3/5$, is shown for Full Charge (—), Charge 1 (···), and Charge 2 (—) munitions configurations. The configurations are clearly separated despite overlap due to variation from event to event.

Conclusions

The blast waves from a 152 mm howitzer are nearly spherical and exhibit a near constant rate of propellant energy release. The blast wave and muzzle plume expansions have initial velocities of Mach 3 – 4 and are coincident until the shock-front detaches

from the plume at about 0.8 – 0.9 ms. Beyond 5 ms the blast wave has decayed to near acoustic velocity and the plume has nearly stopped expanding. The efficiency of converting energy from the muzzle flow to the blast wave is 18 – 24% and does not change significantly with propellant configuration, although a trend proportional to mass was observed. A method for estimating the plume temperature based on the blast wave imagery and energy partitioning is developed. Temperatures of 980 ~ 1,210 K are derived, increase with reduced propellant weight, and are directly correlated with the probability of observing muzzle flash. The use of energy partitioning for temperature calculations should be verified, possibly using spectro-radiometric plume data or high-fidelity CFD simulations. The point blast model with extension to the far-field acoustic limit successfully reduces the trajectory data to a single parameter, the blast energy, with sufficient fidelity to partially distinguish between propellant masses of 4 – 9 kg.

V. Visible and Near-Infrared Spectra of the Secondary Combustion of a 152 mm Howitzer

Introduction

The firing of gun systems, to include both small-arms and large-caliber artillery, results in optical and acoustic signatures that may be remotely detected at great distances [28, 30]. However, in the engineering design of large-caliber gun-systems, often the weapons engineer's focus is to optimize the gun's ballistics performance and meet operational requirements, such as projectile range, firing cadence, barrel life, etc. Firing signatures are also considered but are primarily limited to (1) minimizing the muzzle blast because of its harmful effect on nearby structures and health risks to the firing team and (2) suppression of muzzle flash [28]. The latter is a practical concern because gun firing often results in emissions that are easily visible and pose risks for detection and localization by hostile forces [28].

The term *muzzle flash* can refer to a number of temporally and spatially distinct phenomena which have been characterized previously and are only summarized here [28, 30, 31, 39]. In typical fuel-rich gun systems, partially combusted propellant gases begin to flow out of the barrel immediately after the projectile and emit visible radiation because of their high temperatures. This is the *primary flash* and, because the gases cool quickly as they expand, it is localized to a very small spatial region at the muzzle. Expansion against atmosphere results in downstream shock structure that can reheat the expansion-cooled propellant gases and cause them to self-luminesce, forming the *intermediate flash*. The third region – and the one typically referred to as muzzle flash or *secondary combustion* – results from the combustion of propellant gases after mixing

with atmospheric oxygen. Of the three regions, only the occurrence of secondary combustion is not assured due to its dependence on re-ignition. When it does occur, secondary combustion is the greatest source of radiation in magnitude, size, and duration [28, 40].

Although there has been a significant amount of research into the occurrence and suppression of secondary combustion [23:241-260; 49, 53], the available literature on the spectral characteristics of muzzle flash is limited. Early studies commissioned by the U.S. Army found that less than 1% of radiated energy is in the visible and identified that the principal emissions in the visible result from electronic transitions from to atomic potassium, sodium, calcium, and copper; band emissions from calcium and copper oxides and hydroxide molecules; and continuum from particulates such as soot [30, 31]. Work by Klingenberg, et al. confirmed that line, band, and continuum emissions result from excitation due to shock heating and exothermicity in the combusting plume [23:397-412; 28, 39, 40]. Carbon monoxide and cyanide band emissions were also identified, and with the atomic and molecular emissions previously identified, account for nearly all of the non-continuum emissions [39].

No modern characterizations of the spectra resulting from gun firing could be found in the literature. Because of the increasing preponderance and fidelity of remote observation systems, a study of the visible spectral characteristics of the muzzle flash of a large-caliber gun is warranted. We focus on secondary combustion signatures for practical applications including monocular passive ranging and munitions discrimination.

Experimental

Visible through near-infrared emission spectra and visible imagery were observed for 201 firings of a 152 mm howitzer during 10 – 19 October 2007. Imagery of the gun firing and muzzle plumes were reported previously [93], and various flash geometries observed with the imager are shown in Figure 23. An Ocean Optics UV-NIR grating spectrometer collected spectra on 165 of the firings at 0.75 nm spectral resolution over a 200 – 1100 nm spectral range. The spectrometer's 5 μm entrance slit was fiber-coupled to a ~ 30 cm diameter, ~ 4.5 mrad full field of view, Cassegrain telescope. Instrumentation was located with a view perpendicular to the firing azimuth at a distance of 429 m, providing the telescope a full field of view of approximately 2 meters. The spectrometer acquired spectra at nearly 10 Hz with an integration time of 100 ms per spectra.

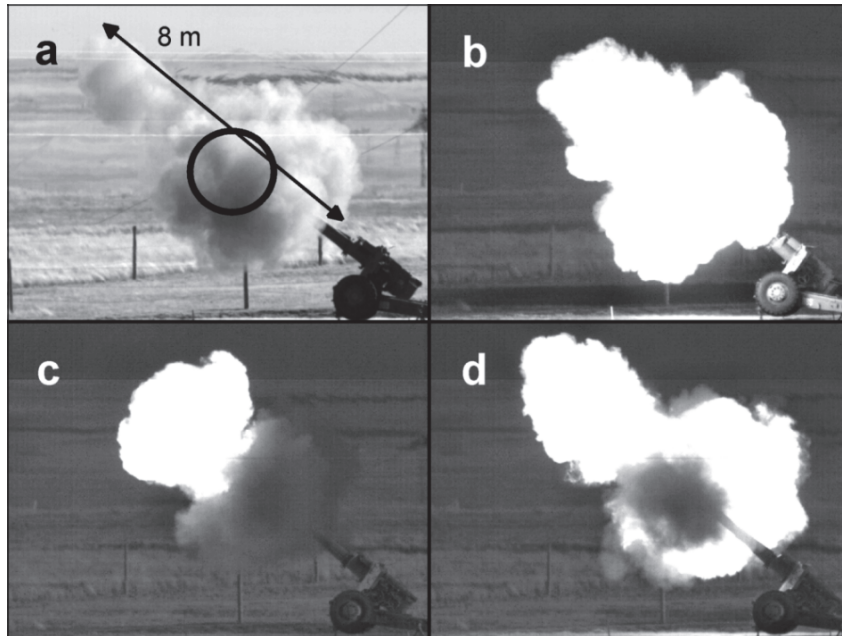


Figure 23. View of the gun, plumes, and flash from the instrumentation site. (a) The axial extent of the plumes is approximately 8 m at 27 ms after shot exit. The circle shows the approximate field of view of the spectrometer. Flash scenarios include (b) all plumes combusting and (c) one or more plumes do not combust. (d) When the left lateral plume does not combust the flash may be partially obscured by cooler, unburned soot and propellant gases.

Five munitions configurations were fired during the test. All munitions configurations consisted of a steel-cased, high-explosive warhead with a copper driving band, black powder igniter, and were distinguished only by composition and mass of propellant. Full Charge was 8.85 kg propellant composed of nitrocellulose and nitroglycerin, with minor amounts of dinitrotoluene, methylcentralite, and diethyl phthalate. Charge 1 was obtained by removing a fraction of the propellant mass resulting in 7.5 kg propelling charge and a minor alteration of the composition ratios. Both Full Charge and Charge 1 configurations were fired with optional chemical flash suppressant during a fraction of the firings. Secondary combustion was chemically inhibited in the majority of firings in which flash suppressant was included, and suppressed configurations are excluded in this analysis. The final configuration, Charge 2, contained the lowest propellant mass (4.24 kg) and used a different composition of high nitrogen content nitrocellulose with minor amounts of dinitrotoluene, diethyl phthalate, and black powder.

The 152 mm howitzer was fired at its maximum elevation of approximately 45 degrees to minimize interaction between the ground and muzzle plume. The barrel was equipped with a double-baffle muzzle brake that split the muzzle effluent into one forward and two lateral plumes. Combustion occurred in none, one, two, or three plumes with no apparent pattern or predictability. The plumes did not appear to interact, but the observation geometry resulted in the left lateral plume obscuring the right lateral plume. The limited field of view of the telescope prevented collection of flash spectra when it was bore-sighted on a non-combusting plume, and it resulted in reduced signal when only a portion of a combusting plume was within the field of view.

Atmospheric meteorological conditions were monitored using a WeatherHawk weather station collecting air temperature, relative humidity, and barometric pressure. Conditions were cool with temperatures 8 – 21 °C, relative humidity in the range 28 – 60%, and barometric pressure of 83.4 – 96.8 kPa.

Results and Discussion

Observed Spectra

Figure 24 shows several frames of combustion emission spectra for a firing in which the secondary flash strongly spanned consecutive samplings. Secondary combustion persisted for 50 – 100 ms and was typically observable only in a single frame. Primary and intermediate flash were always of sufficiently short duration and dim intensity that they were not measurable above the noise level in the spectra.

The spectral cube in Figure 24 represents raw instrument data from one event and is characterized by a maximum signal of $\sim 1.38 \times 10^4$ counts. Peak signal always occurred at the potassium $4^2P_{3/2,1/2} - 4^2S_{1/2}$ doublet near 767 nm and was often saturated when the signal was above the maximum instrument response of $\sim 4 \times 10^4$ counts. The frames prior to muzzle flash show solar spectra with a peak signal of ~ 1620 counts at ~ 520 nm, and after flash the peak is ~ 1750 likely due to additional plume-scattered solar radiation and emission from hot, unburned soot. Random fluctuations in signal (noise) have RMS magnitude of ~ 80 counts but were observed to vary between 20 ~ 100 counts from event to event. Spectra were superimposed on a 1160 ~ 1260 count instrument baseline signal.

Figure 25 shows representative secondary flash emission spectra (transitions labeled with #s are identified in Table 9). Emissions from all three configurations were similar.

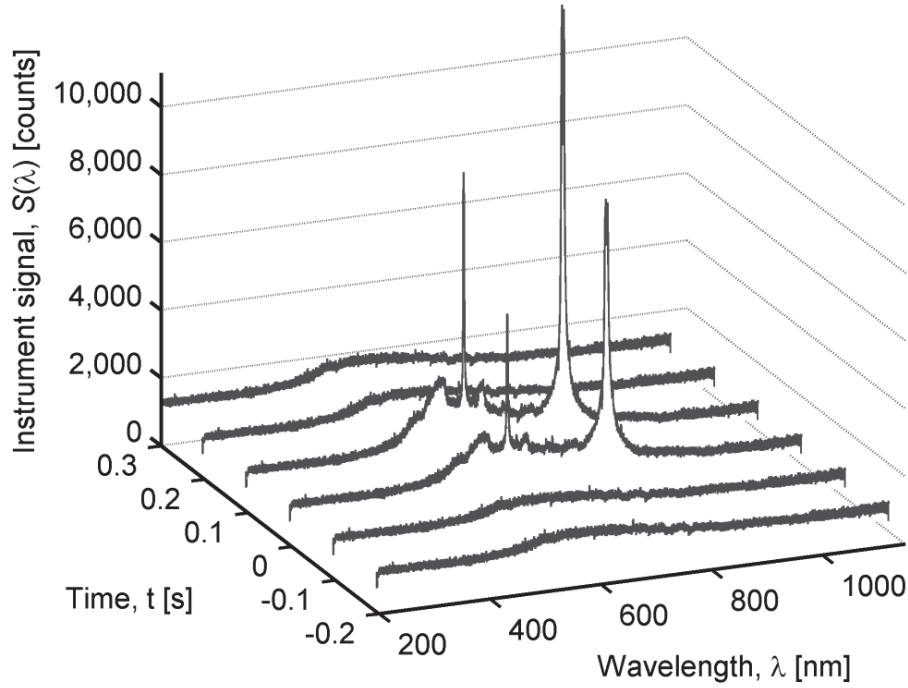


Figure 24. Uncalibrated response from the Ocean Optics grating spectrometer is shown for a single gun firing. The instrument collected 200 – 1100 nm spectral intensity data at 10 Hz.

Table 9. Potassium and sodium level and transition properties [100].

#	Emitter	Upper Level, k	Lower Level, j	λ_{kj} [nm]	A_{kj} [10^6 s^{-1}]	g_k	g_j	E_k [cm^{-1}]	E_j [cm^{-1}]
1	K	$7^2\text{S}_{1/2}$	$4^2\text{P}_{1/2}$	578.2	1.23	2	2	30274.25	12985.19
2	K	$7^2\text{S}_{1/2}$	$4^2\text{P}_{3/2}$	580.2	2.46	2	4	30274.25	13042.90
3	Na	$3^2\text{P}_{3/2}$	$3^2\text{S}_{1/2}$	589.0	61.6	4	2	16973.37	0
	Na	$3^2\text{P}_{1/2}$	$3^2\text{S}_{1/2}$	589.6	61.4	2	2	16956.17	0
4	K	$6^2\text{S}_{1/2}$	$4^2\text{P}_{1/2}$	691.1	2.72	2	2	27450.71	12985.19
5	K	$6^2\text{S}_{1/2}$	$4^2\text{P}_{3/2}$	693.9	3.90	2	4	27450.71	13042.90
6	K	$4^2\text{P}_{3/2}$	$4^2\text{S}_{1/2}$	766.5	38.0	4	2	13042.90	0
7	K	$4^2\text{P}_{1/2}$	$4^2\text{S}_{1/2}$	769.9	37.5	2	2	12985.19	0
8	Na	$3^2\text{D}_{3/2}$	$3^2\text{P}_{1/2}$	818.3	42.9	4	2	29172.89	16956.17
9	Na	$3^2\text{D}_{3/2}$	$3^2\text{P}_{3/2}$	819.5	8.57	4	4	29172.89	16973.37
	Na	$3^2\text{D}_{5/2}$	$3^2\text{P}_{3/2}$	819.5	51.4	6	4	29172.84	16973.37

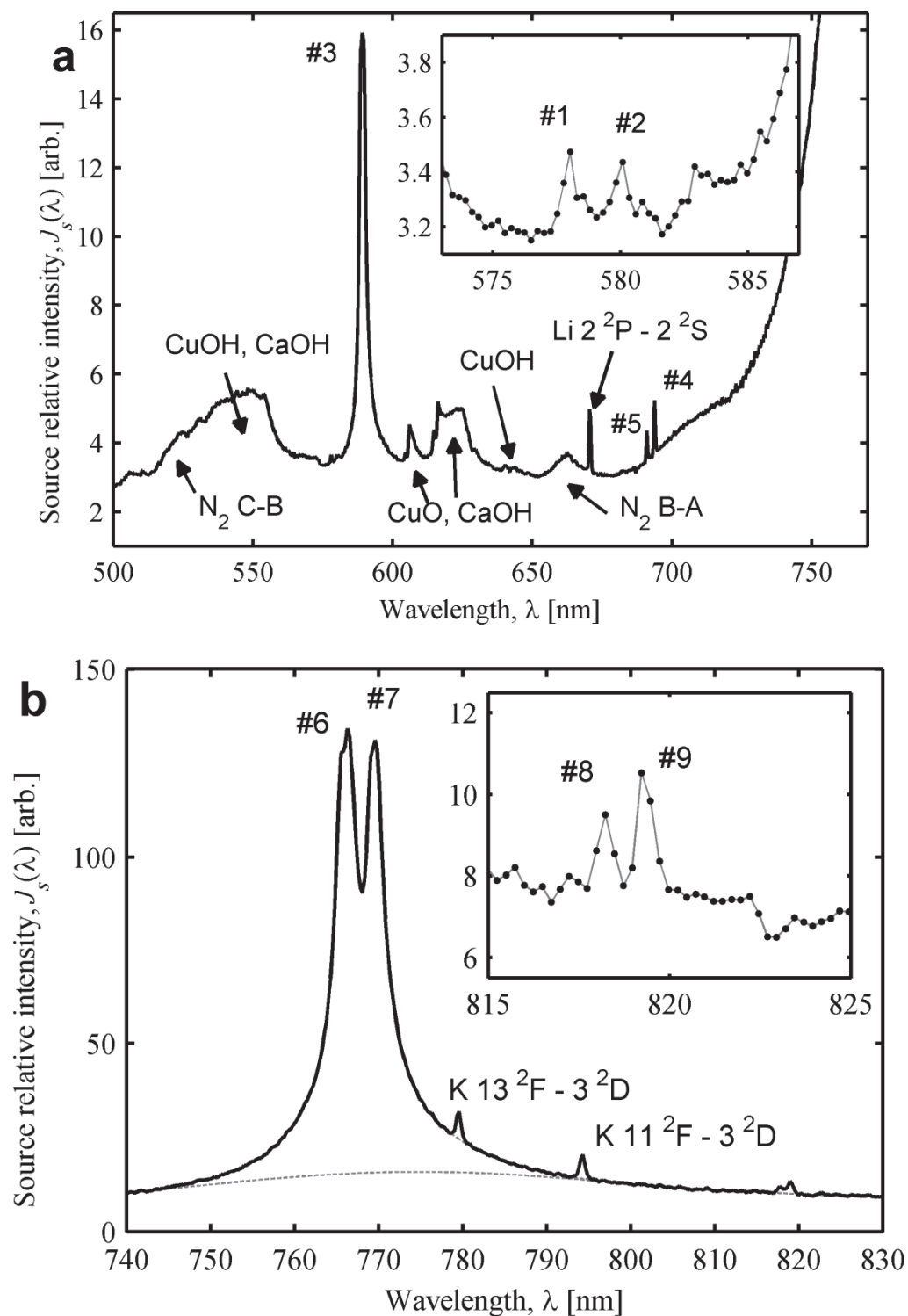


Figure 25. Atomic lines and molecular bands labeled are identified in Table 1. Relative source spectra (—) at (a) shorter wavelengths show that most emission features are due to species containing contaminants. (b) All atomic and molecular features are superimposed on a continuum baseline (····) from hot particulate emissions and plume-scattered solar radiation.

Nearly all emission features are due to electronic excitation of contaminant species. The propellant compositions are almost entirely carbon, hydrogen, nitrogen, and oxygen (CHNO) with potassium and sulfur in the < 1% (by mass) black powder included as the only non-CHNO species. Sodium, lithium, and calcium are contaminants that are likely present in the propellant, and the majority of copper is introduced by wear on the projectile's driving band as it traverses the gun barrel [31].

Atomic sodium lines are observed near 589 nm for the $3^2P_{3/2,1/2} - 3^2S_{1/2}$ doublet and also at 818.3 and 819.5 nm for the $3^2D_{5/2,3/2} - 3^2P_{3/2}$ and $3^2D_{1/2} - 3^2P_{1/2}$ transitions. The lithium $2^2P_{3/2,1/2} - 2^2S_{1/2}$ doublet is observed at 670.8 nm. Observed atomic potassium transitions include the $7^2S_{3/2,1/2} - 4^2P_{1/2}$ doublet at 578.2 and 580.2 nm, $6^2S_{3/2,1/2} - 4^2P_{1/2}$ doublet at 691.1 and 693.9 nm, and $4^2P_{3/2,1/2} - 4^2S_{1/2}$ doublet at 766.5 and 769.9 nm. The $4^2P_{3/2,1/2} - 4^2S_{1/2}$ transitions are very intense and often result in saturation. The strengths of the upper state $6^2S_{1/2}$ and $7^2S_{1/2}$ transitions are greater than would be expected for thermally excited populations and suggest non-equilibrium due to chemical interaction [31]. Collision with combustion molecules have been shown as a mechanism for excitation to $5^2S_{1/2}$ and $6^2S_{1/2}$ states [97], and is also likely the source for the $7^2S_{1/2}$ levels. Two other lines possibly result from potassium: $13^2F_{7/2} - 3^2D_{5/2}$ and $13^2F_{5/2} - 3^2D_{3/2}$ near 779.6 nm, and $11^2F_{7/2} - 3^2D_{5/2}$ and $11^2F_{5/2} - 3^2D_{3/2}$ near 795.6 nm. The selectiveness of the $13^2F_{7/2,5/2}$ and $11^2F_{7/2,5/2}$ upper states is not understood. We hypothesize that these highly excited states could result from one of several combustion reactions in which potassium participates [23:241-260; 53].

Atomic transitions account for a small fraction of the emitted radiation. A number of molecular bands, mostly resulting from molecules containing contaminant species, were

previously reported [23:397-412; 30, 31, 39]. These were observed in the collected spectra and include copper and calcium hydroxides near 550 nm, copper oxide and calcium hydroxide near 610 and 625 nm, and copper hydroxide near 640 nm. Additionally, N₂ C-B and B-A electronic transitions may account for structure near 510 and 660 nm, respectively. Plume-scattered solar radiation and hot particulate gray body emissions contribute continuum baseline on which the flash spectral structure is superimposed and have approximately 35 – 70% greater band-integrated intensity than background.

Variation in observed intensity from event to event spanned nearly two orders of magnitude as a result of a combination of factors: (1) emissive intensity scaled with number of plume combusting, (2) apparent intensity depended on the geometry of plume combustion due to obscuration by the left lateral plume, (3) telescope pointing uncertainty and limited field of view resulted in collection intensities that encompassed all, part, or none of one or more combusting plumes. When the telescope's field of view was centered on a combusting plume, the observed signal was often so intense that the potassium 4 ²P_{3/2,1/2} – 4 ²S_{1/2} transitions saturated the spectrometer's dynamic range. When only a small fraction of a combusting plume was observed, the signal was often dominated by noise.

Instrument Spectral Response and Lineshape

The signal reported by the spectrometer, $S(\lambda)$, is related to the source spectral emission intensity, $I_s(\lambda)$, by:

$$S(\lambda) = a \cdot R(\lambda) \cdot \int_{-\infty}^{\infty} \tau(\lambda') \cdot I_s(\lambda') \cdot F(\lambda - \lambda') d\lambda' + b \quad (23)$$

where:

a = scaling coefficient

$R(\lambda)$ = relative spectral response

$F(\lambda)$ = instrument lineshape

$\tau(\lambda)$ = atmospheric transmittance

b = instrument bias

Apparent intensity (source intensity attenuated by atmosphere) is convolved with the instrument lineshape (ILS), which limits maximum spectral resolution in the observed spectra. The relative spectral response (RSR), $R(\lambda)$, represents the wavelength-dependent efficiency of the instrument in converting intensity to electrical signal. The coefficient, a , scales the entire spectrum based on a combination of instrument gain and fraction of the emissive plume within the instrument's field of view, which is event-dependent. Wavelength-independent bias, b , is introduced into the signal by the instrument or constant background. The notation is adopted that I denotes quantities of radiometric intensity and J is used for quantities that are proportional to radiometric intensity by a scaling factor and convolution with the ILS:

$$J_o(\lambda) = \frac{S(\lambda) - b}{R(\lambda)} = a \cdot \int_{-\infty}^{\infty} I_o(\lambda') \cdot F(\lambda - \lambda') d\lambda' \quad (24)$$

The observed intensity includes both the source intensity and atmospheric transmission, $I_o(\lambda) = I_s(\lambda) \tau(\lambda)$.

The spectrometer system's RSR was estimated using a combination of high-temperature, 1200 °C blackbody measurements and ambient solar spectra (see Appendix C). Outside of a 450 – 850 nm spectral range the instrument response falls off

quickly, and collected signal becomes uncertain and noise-dominated. Because the instrument was not calibrated to a known radiometric standard in the field, a is unknown and observed intensities are only proportional to radiometric values.

The ILS was estimated using the lithium $2^2\text{P}_{3/2,1/2} - 2^2\text{S}_{1/2}$ line because it is sufficiently bright and isolated from other spectral features. The ILS is represented by a skewed Voigt profile:

$$F(\lambda - \lambda_0) = \frac{V(\lambda - \lambda_0; \Delta\lambda_L^F, \Delta\lambda_G^F)}{1 + e^{-\zeta \cdot (\lambda - \lambda_0)}} \quad (25)$$

$$V(\lambda - \lambda_0) = \int_{-\infty}^{\infty} G(\lambda'; \Delta\lambda_G^F) \cdot L(\lambda - \lambda_0 - \lambda'; \Delta\lambda_L^F) d\lambda' \quad (26)$$

where $G(\lambda)$ is the Gaussian function, $L(\lambda)$ is the Lorentzian function, $\lambda_0 = 670.8$ nm is the line center, $\Delta\lambda_L^F = 0.38$ nm is the instrumental Lorentzian width (full width at half maximum, FWHM), $\Delta\lambda_G^F = 0.27$ nm is the instrumental Gaussian width (FWHM), and $\zeta = 1.16$ is a skew factor. The ILS is shown in Figure 26 and has a FWHM of $\Delta\lambda_F = 0.52$ nm.

Atmospheric transmittance was convolved with the ILS to provide a transmission function for use in de-attenuation:

$$\tau_F(\lambda) = \int_{-\infty}^{\infty} \tau(\lambda') \cdot F(\lambda - \lambda') d\lambda' \quad (27)$$

Weather data (temperature, pressure, and relative humidity) were supplied to the Line-by-Line Radiative Transfer Model (LBLRTM) to estimate the horizontal atmospheric transmittance profile, $\tau(\lambda)$, for the 429 m path [98]. The model assumed standard constituents at the specified atmospheric conditions collected during the test. Equation (27) is only an approximation because $I_s(\lambda)$ cannot be removed from the convolution

integral in Equation (23). Nonetheless, dividing Equation (24) by Equation (27) provides an estimate of the relative source intensity that is proportional to radiometric source intensity by a scaling constant (and convolution with the ILS):

$$J_s(\lambda) = J_o(\lambda) / \tau_F(\lambda) \approx a \cdot \int_{-\infty}^{\infty} I_s(\lambda') \cdot F(\lambda - \lambda') d\lambda' \quad (28)$$

Optically Thick Conditions

The strongest observed emissions are due to the potassium $4^2P_{3/2} - 4^2S_{1/2}$ transition near 766.5 nm and $4^2P_{1/2} - 4^2S_{1/2}$ near 769.9 nm. The doublet's spectral profile has a FWHM $\Delta\lambda_K = 6.8$ nm that is much broader than the ILS, $\Delta\lambda_F = 0.52$ nm. The plume is optically thick. Photons near transition linecenter traverse a much shorter distance before being absorbed than those further into the wings of the atomic lineshape. Given sufficient optical path and absorber/emitter concentrations, the photon flux density in the wings begins to approach that at linecenter, which results in a broadening of the spectral distribution of photons emitted from the plume. The radiative transfer can be approximated as:

$$I_s(\lambda; s, T) = \int_0^s \kappa(\lambda) \cdot I_p(\lambda; T) e^{-\kappa(\lambda) \cdot s'} ds' \quad (29)$$

Equation (29) is the steady state radiative transfer equation for intensity, $I_s(\lambda)$, leaving a surface with boundary, s , where temperature and concentrations are independent of time and uniform along a path, s' , interior to the body. Time independence is easily satisfied because the time required for a photon to transit the plume is much less than typical combustion timescales; here $s/c \approx 10^{-8}$ sec $\ll t_c \approx 10^{-4} - 10^{-2}$ s, where c is the speed of light in air and t_c is a typical timescale for combustion [99]. Spatial uniformity along the path is a simplifying approximation that is not satisfied but is imposed. The quantity

$I_P(\lambda;T)$ is the spectral intensity for radiative equilibrium, e.g. the Planck function, and $\kappa(\lambda)$ is the spectral absorption coefficient.

Only the $4^2P_{3/2,1/2} - 4^2S_{1/2}$ doublet is considered, which simplifies the absorption coefficient to:

$$\kappa(\lambda) = \sum_k A_{kj} \frac{\lambda_{kj}^2}{8\pi} V(\lambda - \lambda_{kj}; \Delta\lambda_L, \Delta\lambda_D) \left(\frac{g_k}{g_j} N_j - N_k \right) \quad (30)$$

Emission and absorption are from the two upper levels, $k = 4^2P_{1/2}$ and $4^2P_{3/2}$, to the ground level, $j = 4^2S_{1/2}$. Table 9 provides NIST values of the center wavelengths, λ_{kj} ; spontaneous emission rates, A_{kj} ; and degeneracies, g_k and g_j , for the transitions [100]. The Voigt lineshape, $V(\lambda - \lambda_{kj})$, was defined in Equation (26). The linewidths are nearly equal for the two transitions, $\Delta\lambda_D(T) = 1.24 \times 10^{-4} \times T^{1/2}$ nm, and a pressure-broadened FWHM:

$$\Delta\lambda_L(N) = \Delta\lambda_n + \gamma N \quad (31)$$

The natural linewidth is $\Delta\lambda_n = 1.2 \times 10^{-5}$ nm; the pressure broadening coefficient, $\gamma = 3.70 \times 10^{18}$ nm-cm³/molecule, assumes a temperature independent collision cross-section and is obtained from the data of Pitz, et al. [101]; and N is the concentration of collision partners in molec/cm³. In combustion reactions involving fuel-rich propellant and atmosphere, N₂ is an abundant species due to its preponderance over oxygen, and it is the assumed collision partner for potassium with cross-section $\sigma = 120 \text{ \AA}^2$ [101].

The instrument's response to the potassium $4^2P_{3/2,1/2} - 4^2S_{1/2}$ doublet is approximated when Equations (23), (29), and (30) are used with the values of transitions #6 and #7 in Table 9. The resulting observed relative intensities are shown in Figure 26 for values of $s = 3.9$ m, $T = 2,232$ K, $N(4^2S_{1/2}) = 9.11 \times 10^{14} \text{ cm}^{-3}$, $N(4^2P_{1/2}) = N(4^2P_{3/2}) = 1.14 \times 10^{11} \text{ cm}^{-3}$, and $N = 5.1 \times 10^{18} \text{ cm}^{-3}$. The latter is an estimate of the concentration

of N_2 in the plume, $N = \chi P_0 / k_B T$, assuming the plume is at typical atmospheric pressure $P_0 \approx 90,200$ Pa, pre-combustion plume temperature $T \approx 1,000$ K, and atmospheric N_2 mole fraction $\chi = 0.78$. The resulting spectral intensity is compared with the data in Figure (26). By adjusting the potassium concentration and path length, an adequate fit, particularly in the core of the two lines, is achieved. The broad potassium D_1 and D_2 lineshapes are consistent with optical trapping in muzzle plumes. The lineshapes will depend on plume geometry, for example large caliber muzzle plumes (such as from artillery, tanks, etc.) will emit spectral features with broader lineshapes than small arms. To accurately model the radiative transfer in the plume would require knowledge of the temperature and concentration distributions which are highly complicated by turbulence and reactive chemistry during secondary combustion.

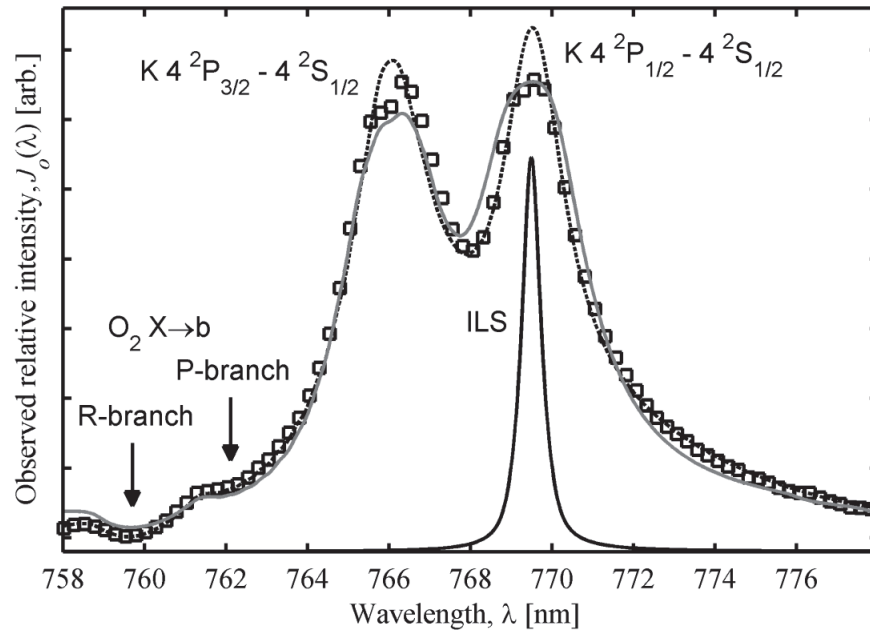


Figure 26. The potassium $4^2P - 4^2S$ doublet is significantly broader than the instrument lineshape (—) as a result of self-absorption. A simple radiative transfer model (—) approximates the phenomena, but an empirical function (···) provided a better fit to the data (□). O_2 $X \rightarrow b$ absorption is evident in the shortwave wing of the broadened potassium profile due to atmospheric oxygen along the observation path.

Passive Ranging

The O₂ X→b (0,0) absorption feature is contained entirely in the wing of the potassium 4 ²P_{3/2} – 4 ²S_{1/2} atomic line illustrated in Figure 26. The band is characterized by electronic excitation of an oxygen molecule from the ground state (X ³Σ_g⁻) to the second excited state (b ¹Σ_g⁺) by absorption near 758 – 765 nm. The magnetic dipole transition results in four rotational branches: ^{ΔK}ΔJ = ^PP, ^PQ, ^RR, and ^RQ [102]. Band-average absorption in these bands has been used to passively estimate range to source by comparing to modeled or historical data for oxygen along the observation path [6]. Obtaining the magnitude of absorption from observed spectra requires knowledge of the source spectra. In previous work this was accomplished by interpolation in the absorption band using out of band intensity measurements, which requires that the spectrum varies slowly across the band to obtain an accurate baseline [6:17-18]. Significantly broadening of the potassium doublet in the secondary combustion data precludes this technique.

The model of Equation (29) for radiation trapping could be employed to establish the baseline source emission. Such phenomenological models are not needed, and a pragmatic approach was instead used to estimate the source potassium 4 ²P_{3/2,1/2} – 4 ²S_{1/2} spectral intensity:

$$I_s(\lambda) = S_1 \left[P_1(\lambda - \lambda_1; \Delta\lambda_{L1}, \Delta\lambda_{G1}, f_1) + P_2(\lambda - \lambda_2; \Delta\lambda_{L2}, \Delta\lambda_{G2}, f_2) \right] + S_2 \cdot I_p(\lambda; T) + S_3 \quad (32)$$

where:

$$P(\lambda - \lambda_0; \Delta\lambda_L, \Delta\lambda_G, f) = f \cdot L(\lambda - \lambda_0; \Delta\lambda_L) + (1 - f) \cdot G(\lambda - \lambda_0; \Delta\lambda_G) \quad (33)$$

The pseudo-Voigt function, $P(\lambda)$, is defined as the sum of the fraction, f , of Lorentzian, $L(\lambda)$, and complementary fraction of Gaussian, $G(\lambda)$, functions. Each function has unit

area and is scaled by S_1 to adjust relative strength. $P_1(\lambda)$ and $P_2(\lambda)$ represent the $4^2P_{3/2} - 4^2S_{1/2}$ and $4^2P_{1/2} - 4^2S_{1/2}$ transitions, respectively; and continuum and baseline are represented by the Planck function having area-emissivity product (converted to signal counts), S_2 , and a constant background (in counts), S_3 . The model was fit to one (of six) unsaturated Charge 2 spectra; the resulting best-fit parameters (and 95% confidence interval for shape parameters) are reported in Table 10 and fit quality is shown in Figure 26. The fit widths are much broader than the atomic Doppler and pressure-broadened widths used in Equation (30) because Equation (32) is an empirical model that accounts for broadening due to self-absorption via broadening of the pseudo-Voigt functions rather than by integration along a path. The advantage to this empirical model is that it is analytic, and it does not require careful modeling of inhomogeneities or turbulence in the plume.

The profile obtained with Equation (32) was scaled to extrapolate the relative intensities of potassium $4^2P_{3/2,1/2} - 4^2S_{1/2}$ transitions for firings where the spectra were saturated. Figure 27 shows spectra from several firings that demonstrate the ranges of observed relative intensities and quality of extrapolation. The shape of the profile was

Table 10. Potassium profile line, scale, and continuum parameters

	λ_0 [nm]	$\Delta\lambda_L$ [nm]	$\Delta\lambda_G$ [nm]	f
Line 1	766.68 ± 0.10	1.899 ± 0.139	6.796 ± 2.036	0.703 ± 0.137
Line 2	770.23 ± 0.20	1.344 ± 0.388	5.633 ± 2.626	0.590 ± 0.109
	S_1 [counts]	S_2 [counts]	S_3 [counts]	T [K]
Scale	$1.52 \times 10^5 \pm 2.036$	5.96×10^{-6}	0.3834	1,449

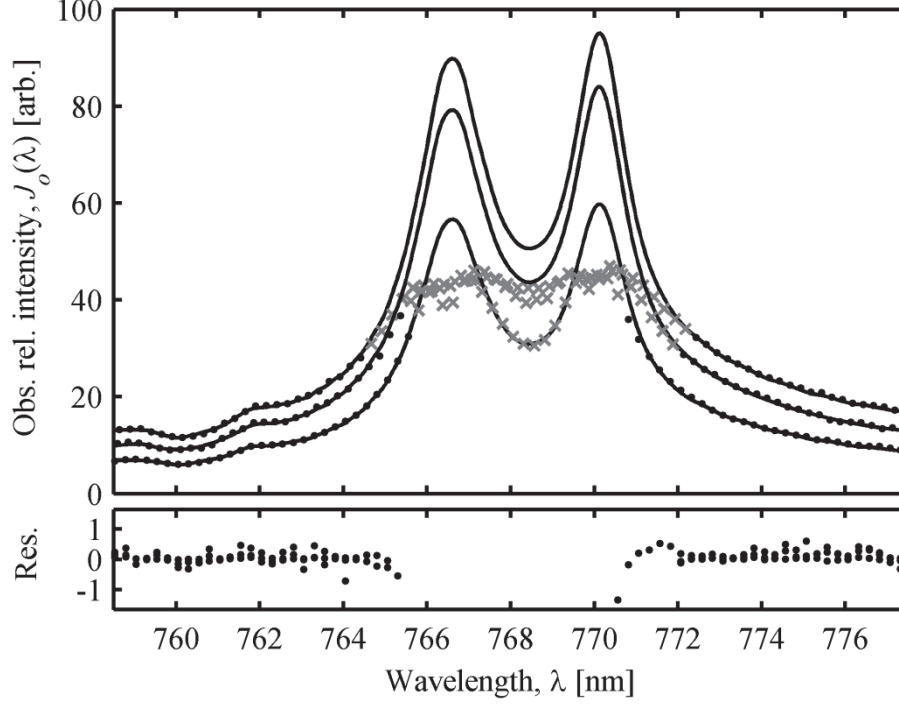


Figure 27. Intensity collected by the spectrometer varied significantly from event to event depending on the fraction of emissive plume in the instrument's field of view. An empirically determined potassium $4^2\text{P} - 4^2\text{S}$ profile (—) was scaled to the unsaturated data (\bullet) for each firing in order to extrapolate what the intensity should be in the saturated (\times) region of each spectrum. Residuals between the model and unsaturated data are shown, and in all cases average less than 3% error.

defined by the values of the fit parameters in Table 10, and only S_1 , S_2 , S_3 , T and b were allowed to vary to scale for observed signal strength, continuum, and bias. Scaling was performed by minimizing the residual between the profile and data in unsaturated regions, and in all cases the root-mean-square of the residuals for each event was less than 3%. The level of agreement provides confidence that the intensity profile is representative in saturated regions, and the extrapolated intensities were used in analysis.

The stability of the profile allowed it to be used as the prediction of source intensity for firings without assuming *a priori* knowledge of range. The relative source intensity profile, $J_s(\lambda)$, was obtained with Equations (32) and (33) using the values reported in Table 10 (from a single Charge 2 firing) and scaled to the observed spectrum (only

varying S_1 , S_2 , S_3 , T and b , as before). Observed spectral transmittance was calculated from the instrument response:

$$\tau_o(\lambda) = J_o(\lambda) / J_s(\lambda) \quad (34)$$

for Charge 2 firings from which the shape of the profile was *not* determined. Spectral transmittances, $\tau(\lambda; L)$, for standard atmospheric constituents were computed using the LBLRTM code with range to source, L , used as a free parameter. Range was adjusted to minimize the difference, $\Delta\alpha$, between the band-integrated observed and range-dependent absorptions:

$$\Delta\alpha = \left| \int_{\lambda_1}^{\lambda_2} (1 - \tau_o(\lambda)) d\lambda - \int_{\lambda_1}^{\lambda_2} (1 - \tau(\lambda; L)) d\lambda \right| \quad (35)$$

with the band limits $\lambda_1 = 758$ nm and $\lambda_2 = 763.5$ nm. The lower limit defines the shortwave extent of the absorption feature, but the upper limit is near the middle of the P-branch. The latter was chosen because at longer wavelengths saturation and line-reversal (likely due to a cooler outer layer at the surface of the plume) are observed in the potassium intensity data. These are not accounted for in the profile obtained with Equation (32) and they bias the solution of Equation (35) to longer ranges.

Typical observed and computed transmittances are shown in Figure 28. Ranges of 409.8 – 469.1 m were calculated for eight firings (four saturated and four un-saturated spectra). This yielded errors of 4.2 – 9.3% for the 429 ± 10 m distance from the observation site to the gun. Error was primarily introduced by noise, which had a significant effect when integrating transmittance ratios because of the scarcity of samples (~ 30) in the O₂ absorption band. An instrument designed specifically for ranging using

this feature should have much greater sampling – even if spectral resolution were not improved – so that noise effects would average out.

If multiple firings of a particular munitions configuration are treated as several instances of the same flash spectrum – which we have already assumed by using a single potassium profile as the relative source intensity profile – range estimates can be improved by averaging the spectra. The uncertainty-weighted range estimate was $L = 426.7 \pm 20.5$ m, yielding an error of only 0.5%. Multiple observations effectively increased sampling in the O_2 band, which is a practical alternative to increasing spectral sampling for a single observation. This is a viable solution considering that most battlefield applications of artillery provide ample opportunity to observe several firings, and each observed flash can be used to improve the range to source estimate.

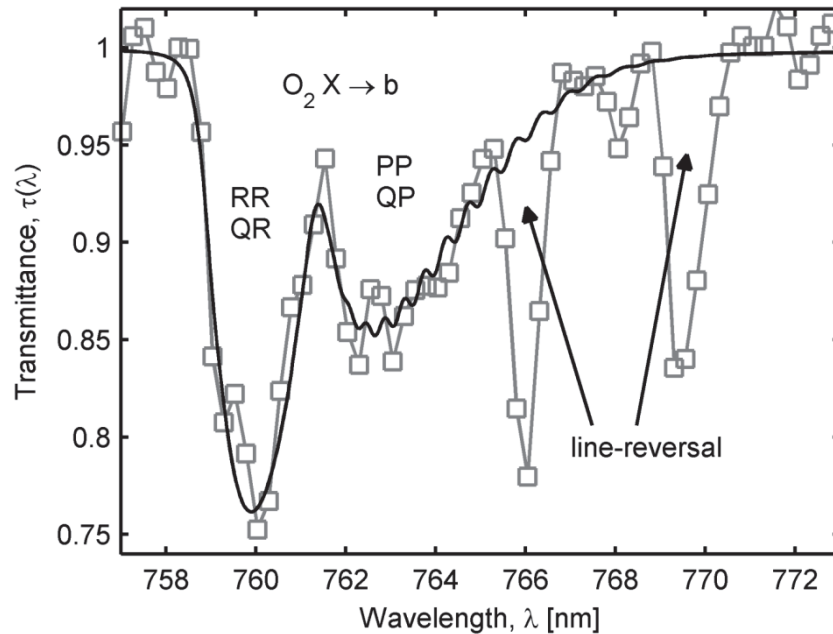


Figure 28. Spectral transmittance in the O_2 $X \rightarrow b$ absorption band is shown for observed data (\square) and as computed with the LBLRTM code (—) for a 429 m path with standard atmospheric constituents. Band-integrated absorption was calculated from $\lambda_1 = 758$ nm to $\lambda_2 = 763.5$ nm. Line reversal is observed near the potassium $4^2P - 4^2S$ doublet linecenters, likely due to a cooler outer layer at the surface of the plume.

Relative Line Intensity Ratios

The relative intensities of the atomic lines might be useful in classifying the munitions type. To assess the potential for event classification, we extract spectral features in two ways: (1) calculate the relative observed intensities for all pairs of atomic lines, and (2) reduce the dimensionality of the feature set by characterizing the intensity distributions with parametric temperatures.

Intensity ratios:

$$r_{uv} = \ln(J_u / J_v) \quad (36)$$

were calculated for all identified lines, u and v , regardless of emitter species. To minimize the effects of noise – which is particularly significant for the weakly observed K $7^2S - 4^2P$ and Na $3^2D - 3^2P$ transitions – intensities from separate lines resulting from fine structure splitting were averaged. For example, the K $7^2S - 4^2P$ to Na $3^2D - 3^2P$ intensity ratio was calculated rather than each K $7^2S_{1/2} - 4^2P_{3/2,1/2}$ to Na $3^2D_{5/2,3/2} - 3^2P_{3/2}$. This reduced the number of ratios from 66 to 28, but because spin-coupled line intensities are highly correlated, there was little loss of information and a corresponding reduction in noise-induced uncertainty by 3 – 14%.

For optically thin conditions, the observed peak intensities for each line provide a measure for the relative concentrations of the emitting states:

$$J_o(\lambda_{kj}) \propto \frac{hc}{\lambda_{kj}} A_{kj} N_k \quad (37)$$

where each photon contributes energy hc/λ_{kj} . Further assuming local thermodynamic equilibrium, a Boltzmann distribution of excited state populations:

$$\frac{N_k}{N_j} = \frac{g_k}{g_j} e^{-(E_k - E_j)/kT} \quad (38)$$

can be used to summarize the observed intensities with a single distribution parameter, the temperature, T . We have clearly demonstrated optically thick conditions for transitions terminating on the ground state, and the application of Equations (37) and (38) to characterize a temperature is not justified. However, the intensities can be adequately characterized by this distribution as shown below. Such a scheme may be useful in reducing the dimensionality of the classification features.

Because the signal strength varied significantly from event to event, the observed peak line intensities, $J_o(\lambda_{kj})$, above baseline are normalized to the emission from the lithium D₁ and D₂ ($2^2\text{P}_{3/2,1/2} - 2^2\text{S}_{1/2}$) lines.

The relative concentrations for the potassium lines from Table 9 are shown as a Boltzmann distribution in Figure 29. The distribution parameter, or temperature, and their standard errors for each munitions configuration are provided in Table 11. The values are considerably higher than expected combustion temperatures of 1,200 – 2,200 K.

Table 11. Excitation temperatures (Kelvin) for potassium and sodium transition ratios.

Levels:	All Potassium	K 7 ²S – 4 ²P K 6 ²S – 4 ²P	K 7 ²S – 4 ²P K 4 ²P – 4 ²S	K 6 ²S – 4 ²P K 4 ²P – 4 ²S	Na 3 ²P – 3 ²S Na 3 ²D – 3 ²P
Full Charge	8945 ±2840	2,943 ±377	7,816 ±589	11,589 ±440	7,424 ±513
Charge 1	8769 ±1947	3,682 ±607	8,457 ±503	11,773 ±1,419	8,971 ±911
Charge 2	7921 ±1130	4,390 ±1,068	7,601 ±580	9,083 ±653	14,233 ±3,605

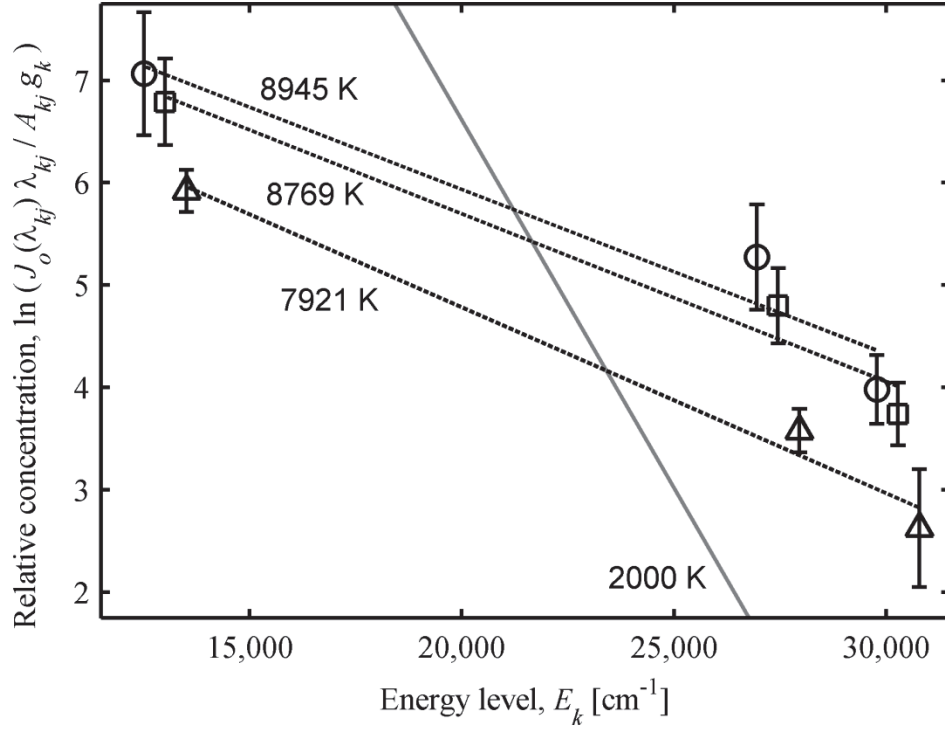


Figure 29. Relative concentrations of excited levels in potassium are shown for Full Charge (○), Charge 1 (□), and Charge 2 (△) munitions configurations. The slopes of the best-fit lines (---) for each configuration can be interpreted to provide temperature if a Boltzmann distribution is assumed. A 2,000 K line (—) is shown for reference.

Munitions Discrimination

That firing emissions can be used to detect and locate a gun is not novel [28]. However, firing signatures have the potential to reveal much more than a gun's location. Distinct spectral characteristics reveal type and relative amounts of contaminants – such as K, Na, or Li – and, with this information, it may be possible to identify the munitions fired from a gun. Intensity ratios and temperatures obtained with Equations (36) and (38) provide two sets of features that can be used for this classification objective.

First, multiple discriminant analysis (MDA) was applied as a method of feature selection to identify which of the $p = 28$ ratios of atomic lines can best distinguish between $n = 32$ firings of the munitions configurations. It projects n observations in a

p -dimensional space, $\mathbf{X} = \{\mathbf{X}_1 \dots \mathbf{X}_p\}$, to a subspace of $K - 1$ dimensions, $\mathbf{Y} = \{\mathbf{Y}_1 \dots \mathbf{Y}_{K-1}\}$, that best differentiates all observations, where $K < p$ is the number of distinct classes. MDA is a linear technique that solves an eigenvalue problem to maximize between-class variance while minimizing within-class variance. Each eigenvalue, λ_i , corresponds to an eigenvector, \mathbf{b}_i , defining a dimension of the subspace, \mathbf{Y}_i , where $i = 1 \dots K - 1$ are subspace dimensions with decreasing magnitude eigenvalues. The subspaces are linear combinations of the dimensions of the original space, $\mathbf{Y}_i = \mathbf{X}\mathbf{b}_i$, and one or more of the dimensions may be excluded if unimportant. To obtain a more comprehensive review of MDA, the literature should be referenced [64:121-124; 65:400-407]. Here each ratio is a dimension of the original space, each munitions configuration is a class, and each firing is an observation. MDA was also performed independently for the four temperature ratios in Table 11.

Figure 30 shows total class separation as a function of number of features (i.e. ratios and temperatures) used in MDA. Total class separation, $\Lambda = \lambda_1 + \dots \lambda_{K-1}$, is the sum of eigenvalues and is a measure of between-class to within-class variance of all dimensions \mathbf{Y}_i , $i = 1 \dots K - 1$, in the subspace. The plot does not indicate class separation obtained with each feature, rather it shows the class separation obtained by cumulatively including each feature up to the indicated feature number, and the features are sorted by their importance. Those features with the greatest correlation to the largest eigenvalued subspaces contribute most to separation of classes and are consequently the most important. The first four most important line ratios and temperatures are labeled, and their order of importance was independent of the number of features retained. Because larger values of Λ indicate greater separation of classes relative to variance in the classes,

it is apparent that the line ratios are significantly more important than temperatures: only a single ratio, potassium $6^2S - 4^2P$ to sodium $3^2D - 3^2P$, more effectively differentiates munitions configuration than all of the temperatures combined. The implication is that the relative concentration of emitter species is a superior discriminator than the relative concentration of excited levels within a species.

Figure 31 (a) and (b) show the distributions of Full Charge, Charge 1, and Charge 2 spectra in the first two most important subspaces, Y_1 and Y_2 , and two most important ratios. Y_1 and Y_2 are composed of the four most important line ratios (indicated in Figure 30). $\Lambda = 18.2$ indicates a factor of ~ 18 greater between-class separation than within-class variance, and all observations are within their class' distribution. Projection of physically

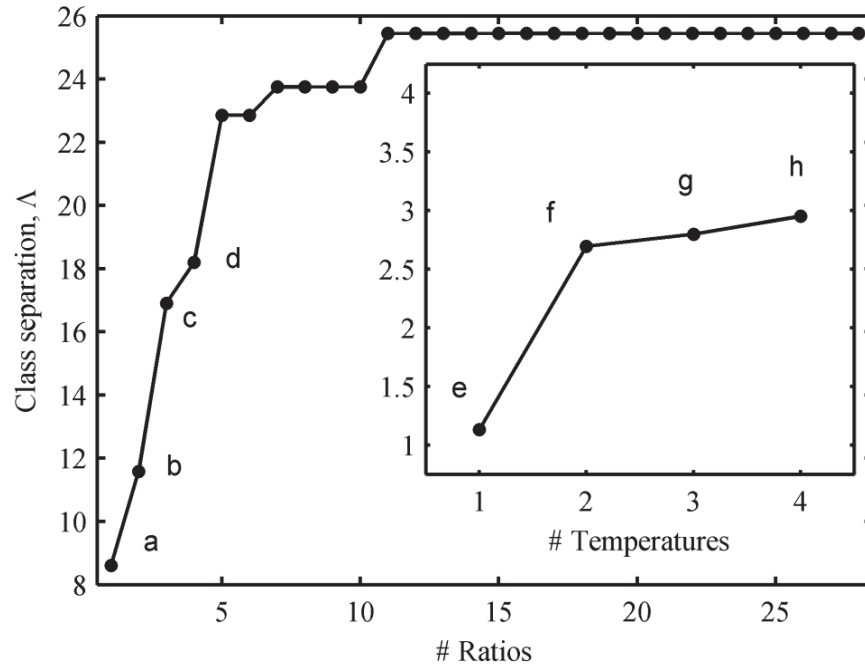


Figure 30. Cumulative between-class to within-class variance (class separation) is shown as a function of the number of features used in MDA. The features are sorted to show order of importance and indicate that the ratios of species (a) $K 6^2S - 4^2P / Na 3^2D - 3^2P$, (b) $K 4^2P - 4^2S / Na 3^2D - 3^2P$, (c) $K 6^2S - 4^2P / Li 2^2P - 2^2S$, and (d) $K 6^2S - 4^2P / K 13^2F - 3^2D$ are better discriminators than temperatures (e) $K 6^2S - 4^2P / K 4^2P - 4^2S$, (f) $Na 3^2P - 3^2S / Na 3^2D - 3^2P$, (g) $K 7^2S - 4^2P / K 4^2P - 4^2S$, and (h) $K 7^2S - 4^2P / K 6^2S - 4^2P$.

observable quantities into an abstract subspace, while useful, is not always intuitive. Examining the two most important intensity ratios, $K 6^2S - 4^2P / Na 3^2D - 3^2P$ and $K 4^2P - 4^2S / Na 3^2D - 3^2P$, provides good discrimination potential with $\Lambda = 11.6$. In this case, the distributions of Full Charge and Charge 1 overlap, likely because they are the two most similar propellant configurations. Projection of the two ratios into a 1-dimensional subspace further reduces ability to discriminate between classes to $\Lambda = 8.6$, with the Full Charge and Charge 1 distributions overlapping significantly.

Conclusions

Visible and near-infrared emission spectra of the secondary combustion from large caliber artillery show atomic and molecular emission features primarily involving K, Na, Li, Cu, and Ca contaminant species. Non-equilibrium excitation concentrations were observed, indicating probable collisional or reactive excitation during combustion of the plume. Distributions of excited levels were characterized by Boltzmann temperatures in the range 7,921 – 8,945 K using all available potassium upper levels. A radiative transfer model was used to demonstrate broadening in the potassium $4^2P - 4^2S$ doublet by self-absorption in an optically thick plume, and an empirical model was developed to represent the doublet with sufficient fidelity to extrapolate the profile's intensity for firings in which the spectra were saturated. Despite apparent limitations of the field data – e.g. varying signal magnitudes, saturation, and non-equilibrium excited state distributions – the spectra can be used for practical application including passive ranging and munitions discrimination. The $O_2 X \rightarrow b$ absorption feature was observed in the blue wing of the potassium doublet and used to estimate range to target to within 4 – 9% for

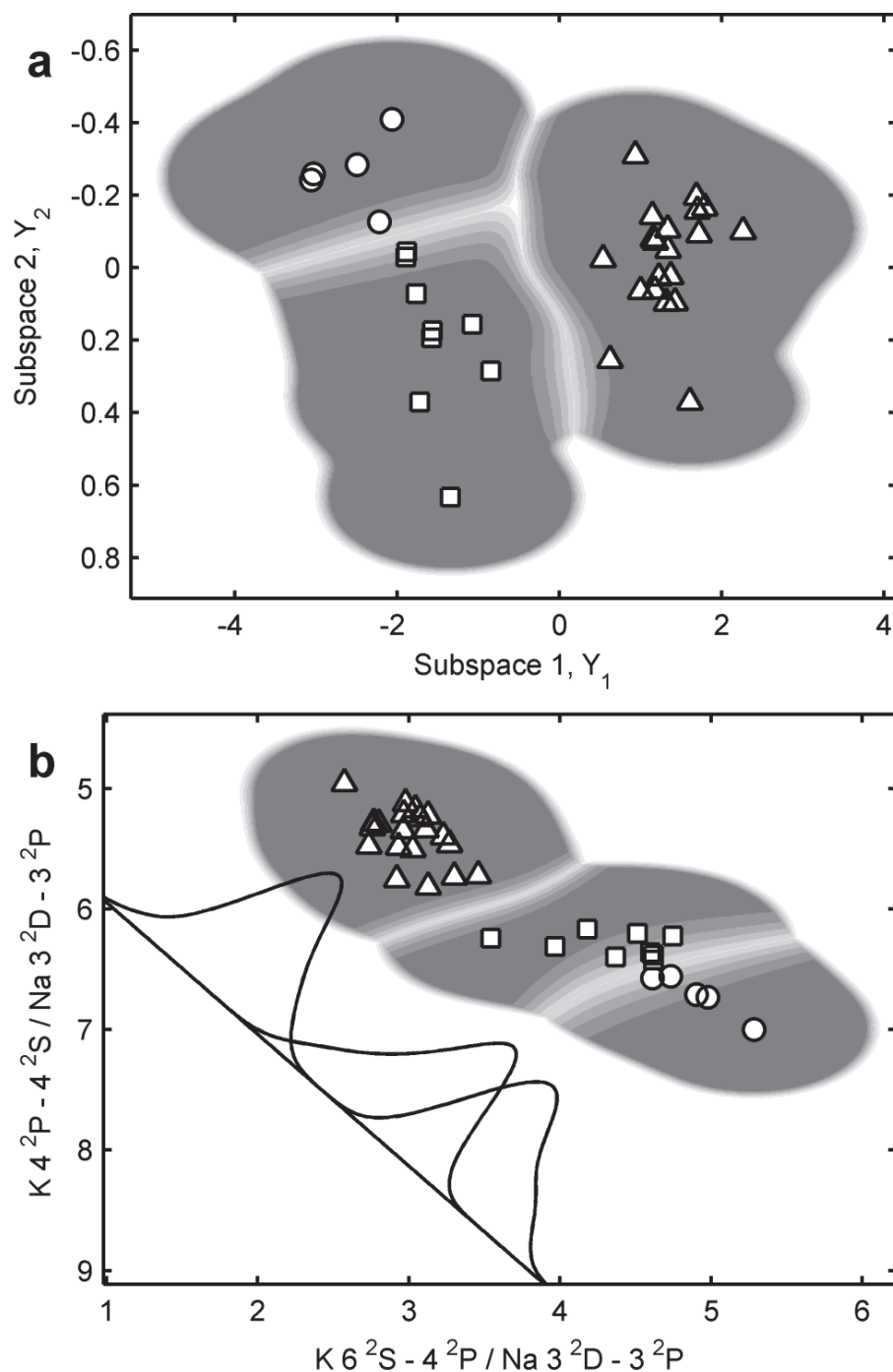


Figure 31. Features are projected into subspaces that maximize the between-class to within-class variance amongst the class. The gray-scale gradients indicate the relative probability of a particular configuration being present, and white gradients between distributions indicate overlap approaching equal probabilities. (a) Four line intensity ratios are projected to two subspace dimensions that completely separate the distributions of Full Charge (\circ), Charge 1 (\square), and Charge 2 (\triangle). (b) Two potassium to sodium line ratios discriminate the three configurations in two dimensions. Projection shows that the probability distributions for Full Charge and Charge 1 significantly overlap in a 1-dimensional subspace.

individual firings and to within $\sim 0.5\%$ with multiple observations. Classification was investigated with multiple discriminant analysis and revealed that relative concentrations of species are far more important than excitation concentration distributions. Observation of 32 Full Charge, Charge 1, and Charge 2 firings were fully differentiated with a between-class to within-class variance ratio of 18.2 using four intensity line ratios, and a ratio of 11.6 using only two ratios. The wealth of information obtained from the low spectral and temporal resolution field observations of muzzle flash foreshadows the fidelity with which passive ranging and remote discrimination of munitions may be accomplished with an instrument designed specifically for such practical applications.

VI. Modeling Midwave Infrared Muzzle Flash Spectra from Unsuppressed and Flash-Suppressed Large Caliber Munitions

Introduction

Muzzle blast and flash signatures are important for gun design operator safety and determining firing location [28, 50]. Despite the apparent utility of the signatures, study of muzzle flash has focused on its occurrence and suppression [28, 50, 53], and there are only a handful of works on the characteristics of flash signatures [23:397-412; 30, 31, 40]. No modern spectroscopic studies could be found in the literature. This is surprising considering that remote observation of signatures offers the potential for new academic and practical applications. Temporally-resolved spectral signatures may improve our understanding of the thermochemistry and fluid dynamics of muzzle plumes.

The most significant contributor to muzzle flash – both in terms of size and intensity – is *secondary combustion* [28]. This is the re-ignition of muzzle gases and particulate matter that have been expelled from the gun barrel. It can only occur after mixing with atmospheric oxygen [46, 50, 53]. After re-ignition, the flame front quickly envelops the entire muzzle plume, resulting in emissions throughout the visible and infrared. Nearly 99% of the energy radiated in muzzle flash is in the infrared, making it an ideal spectral region to characterize for practical use [30]. Even if re-ignition does not occur (such as with the use of flash suppressors) the plume that develops from the muzzle flow contains high concentrations of high-temperature particulate matter that emit continuum radiation throughout the infrared [46, 50].

Midwave infrared (MWIR, 1 – 5 μm) spectral features from high-explosive (HE) fireballs have recently been modeled to identify emitter species at specific temperatures

and concentrations [9, 15]. These models have not been applied or adapted for muzzle flash. Combusting muzzle plumes are similar to fireballs – gaseous fuel and particulate matter burn with entrained atmospheric oxygen in a hot, turbulent mixture – and the work presented here extends the application of the HE model to muzzle flash spectra.

The following presents a characterization of muzzle signatures (to include emissions from both secondary-combusting and non-combustion plumes) obtained during a test designed to develop an understanding of large caliber gun firing signatures. Results of application of the HE model to MWIR secondary combustion and non-combusting spectra are presented. Evolving flash temperatures, sizes, and emitter concentrations are estimated, and temperature dynamics are examined in terms of combustion heat release. A new implementation of the model is developed that relaxes the spatial uniformity assumptions of the HE fireball model. Observed emissions are treated as resulting from a distribution of temperatures and concentrations that account for the effects of turbulent mixing in the plume. Improved, low dimensionality muzzle flash models may be required to extract phenomenological features for event classification.

Experimental

Two hundred and one firings of a 152 mm howitzer were conducted during 10 – 19 October 2007. The test was instrumented with numerous spectrometers, radiometers, and high-speed imagers spanning the visible and infrared, and gun firings were observed from one of two locations. Only those details pertinent to this study are reported here, and additional details on test execution, instrumentation, and layout can be found in the reference [93].

The gun fired munitions with three different carbon, hydrogen, nitrogen, and oxygen (CHNO) double-base propellants designated Full Charge (8.85 kg), Charge 1 (7.52 kg), and Charge 2 (4.24 kg). All propellants were under-oxidized. Due to the length of the howitzer barrel, available oxygen is consumed and combustion ceases interior to the gun. Prior to exiting the 152 mm howitzer muzzle, the flow is shock heated when it passes through a brake that splits the flow into one forward and two later plumes [28, 46, 50]. When the hot muzzle effluent turbulently entrains atmospheric oxygen, the gases may re-ignite and combustion can continue to completion. To inhibit secondary combustion, Full Charge and Charge 1 both contained optional chemical flash suppressant (0.28 kg) that consume OH and H combustion radicals [50, 53].

Table 12 indicates the relative stoichiometry for each propellant. For complete combustion, all propellant is converted to H_2O , CO_2 , and N_2 . This neglects non-CHNO species, which account for less than 1% of the propellant composition. In this case, the quantity $R = 2 \cdot [\text{H}_2\text{O}] / ([\text{CO}_2] + [\text{CO}])$ is equivalent to the stoichiometric hydrogen-to-carbon (H:C) ratio. The brackets denote number density of the indicated species. If the muzzle plume does not re-ignite and secondary combustion does not occur, the under-oxidized propellant burns only with oxygen available interior to the gun. The products of incomplete combustion are preferentially H_2O and CO [54:22; 76:78]. Remaining hydrogen and carbon primarily produce H_2 and soot, and negligible CO_2 concentrations are assumed. In non-combusting plumes, $R_d \equiv R$ includes only the primary, oxidized hydrogen and carbon containing species (i.e. H_2 and soot are neglected). These incomplete combustion R_d values are also shown in Table 12.

Table 12. Propellant and observation details for each munition configuration. Stoichiometry is relative to carbon. R_d is the incomplete combustion H:C ratio. The numbers for each instrument resolution indicate the useable data out of the total observed.

Charge	Supp.	Stoichiometry	R_d	# Firings	32 cm ⁻¹	16 cm ⁻¹	4 cm ⁻¹
Full Charge	Yes *	C ₁ H _{1.25} N _{0.38} O _{1.37}	0.75	69	49 / 54	0 / 0	1 / 2
	No	C ₁ H _{1.25} N _{0.38} O _{1.36}	0.72	28	14 / 18	7 / 7	0 / 2
Charge 1	Yes	C ₁ H _{1.24} N _{0.38} O _{1.38}	0.75	53	35 / 42	5 / 9	0 / 1
	No	C ₁ H _{1.24} N _{0.38} O _{1.36}	0.72	28	14 / 15	11 / 11	0 / 0
Charge 2	No	C ₁ H _{1.14} N _{0.42} O _{1.55}	1.09	23	22 / 23	0 / 0	0 / 0

* two firings contained 1/2 bags of suppressant but did not flash

An ABB-Bomem MR-254 Fourier transform spectrometer (FTS) was located with a side-on view of the gun at a distance of 429 meters. The instrument has two channels that were equipped with InGaAs (5,800 – 10,000 cm⁻¹) and InSb (1,800 – 7,800 cm⁻¹) detectors. The detectors shared a common input aperture with a visible, bore-sight camera used for pointing and focus. Field of view (FOV) was limited by a 75 mrad telescope providing a radial FOV of approximately 16 meters at the gun, sufficient to contain the entire muzzle plume whose maximum dimension was 8 – 10 meters (oriented along the firing axis). The plumes' side-on projected area was typically a maximum of 35 – 40 m² (about 5% of the FOV). The bore-sighted visible camera was used to ensure that the plume was within and under-filled the instrument's FOV.

The MR-254 is a Michelson-type interferometer in which light is split between two optical paths then recombined to form a constructive and destructive interference pattern. The instrument samples the interference pattern, termed an interferogram. To correct for errors in sampling, each double-sided interferogram was phase corrected using Mertz's

technique with $n = 182$ points sampled to either side of the centerburst [103,104:85-88]. The corrected interferograms were then apodized with a Hanning function, $H(x) = \cos^2(\pi x/2x_m)$, and Fast-Fourier Transformed to yield raw spectral irradiances, $E_o(\nu)$. Complex gain and offset calibration coefficients were used to center and scale raw irradiance data to radiometrically accurate values. Blackbody measurements of six area-temperature pairs were taken several times per day, and the nearest (in time) was used to obtain the calibration coefficients for each firing. Details of this calibration procedure can be found in the references [9, 15]. Calibrated MWIR spectral irradiances were converted to apparent spectral intensities via the approximation $I_o(\nu) = r^2 E_o(\nu)$ where r is range to source and source area, A , represents a small angle (i.e. $r^2 \gg A$). A collection of spectral intensities obtained from successive interferograms form a spectral data cube. A representative spectral data cube is shown in Figure 32 for a Full Charge firing's secondary combustion plume.

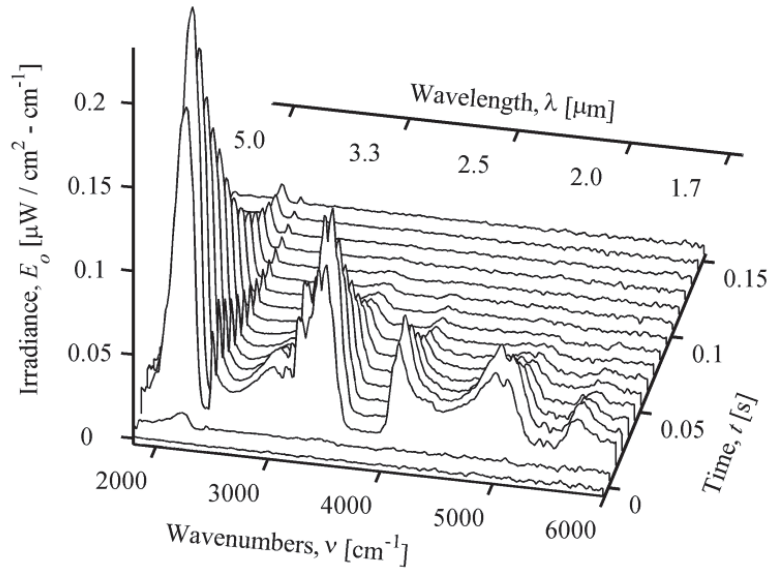


Figure 32. Spectral data cube of irradiance observed for an unsuppressed Full Charge firing. Spectra were collected at 100 Hz with 32 cm^{-1} resolution and show strong emissions until nearly 100 ms.

For each firing, the FTS acquired data at rates of 100 Hz, 82 Hz, and 35 Hz corresponding to nominal spectral resolutions of 32 cm^{-1} ($\Delta\nu = 15.43\text{ cm}^{-1}$, sampled with $n = 2048$ points), 16 cm^{-1} ($\Delta\nu = 7.71\text{ cm}^{-1}$, $n = 4096$), and 4 cm^{-1} ($\Delta\nu = 1.93\text{ cm}^{-1}$, $n = 16384$). The instrument's sampling period was moderately faster than the event duration. Corruption of the spectra by scene-change artifacts (SCAs) was assessed as negligible based on the lack of spectral structure in the imaginary component of the spectrum. While counter-intuitive, FTS has been successfully used to study other rapidly-evolving combustion systems and SCAs have been previously addressed [105, 106]. The total numbers of firings, firings acquired at each spectral resolution, and those resulting in useable spectra are indicated in Table 12 for each munitions configuration. The MR-254 did not observe all firings, which accounts for the difference between the total number of firings and those for which various resolution spectra were acquired. Throughout the test the instrument's signal was amplified or attenuated through a combination of electrical gain and neutral density filters placed in the input aperture in order to maximize the signal-to-noise ratio (SNR) and avoid saturation. In some cases, the collected data were not useable because excessive noise or saturation of the interferogram occurred.

Results

Observed Spectra

Peak spectra for both a combusting (unsuppressed) and non-combusting (suppressed) plume are shown in Figure 33. The spectra for all Full Charge, Charge 1, and Charge 2 munitions were not obviously different – likely because their propellant stoichiometries are similar – and are not distinguished in the work presented here. The plume filled at

most 5% of the FOV, and background emissions account for < 1% band-integrated intensity in combusting plumes and 5 – 15% in non-combusting. A background spectrum acquired at local, near-noon is included in Figure 33 for reference. The background was removed by subtracting the average of several spectra acquired prior to the gun firing.

The muzzle plume's emissions are detectable in the MWIR regardless of flash, but the magnitude and spectral characteristics are highly dependent on whether combustion occurs. Non-combusting plumes are dominated by continuum radiation throughout much of the MWIR, and visible imagery shows the plumes to be dark and opaque, consistent with large concentrations of soot resulting from under-oxidized propellant [30, 31, 40]. Prior studies have found that muzzle exhausts for fuel-rich propellants contain a high concentration of particulates ($10^5 - 10^8 \text{ cm}^{-3}$) that emit continuum radiation [28, 46].

If temperatures remain above 900 – 1000 K after atmospheric oxygen has been turbulently entrained into the muzzle flow, then the plume may re-ignite and propellant combustion by-products can continue to burn to completion [28, 50, 53]. Combustion consumes the particulate matter, which was previously found to vaporize near 1000 K [46]. Products of vaporization and continued combustion of muzzle gases are primarily H_2O , CO_2 , and N_2 with trace CO , NO_x , and species containing contaminants such as K, Na, Ca, Cu, etc. [54:22]. Consumption of the particulates eliminates most of the graybody emissions, and the observed MWIR spectra show highly structured features. This is also apparent in the visible imagery where the once sooty plume becomes transparent; for example, in Figure 33 the howitzer's barrel is clearly visible through the combusting plume whereas it was completely obscured in the non-combusting plume imagery.

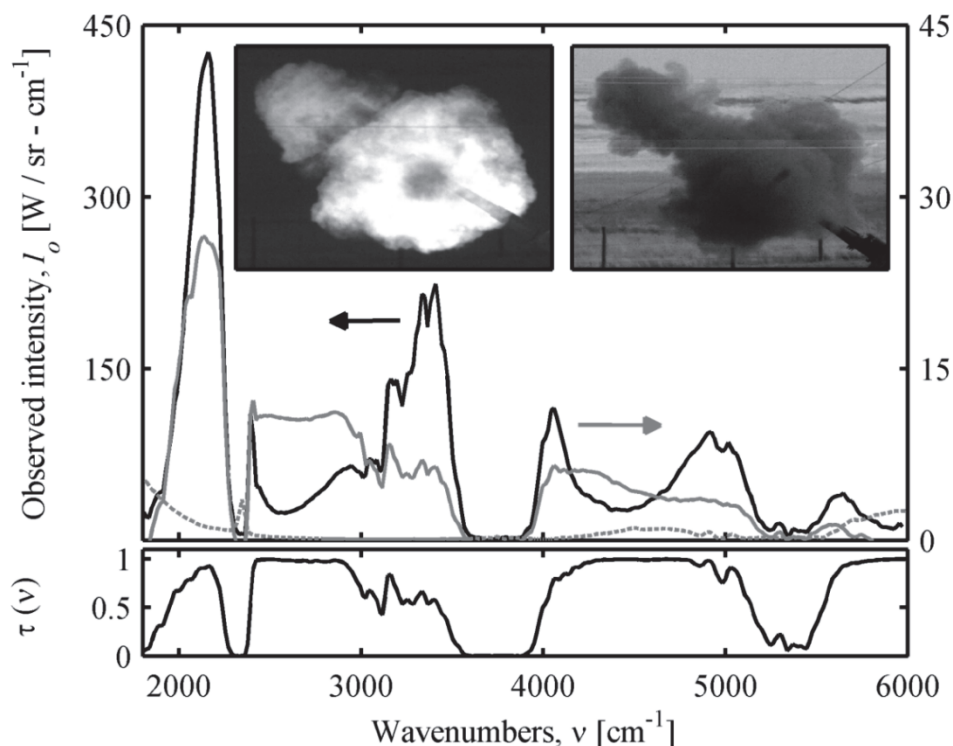


Figure 33. Peak observed spectra for combusting (—) and non-combusting (—) firings are shown. The left ordinate and image correspond to a combusting (unsuppressed) plume and show significant spectral structure. The right ordinate and image correspond to a non-combusting (suppressed), optically thick plume. Combustion results in band-integrated MWIR intensities a factor of ten greater than non-combusting. A near-local noon background spectrum (····) is also shown on the right ordinate. Atmospheric transmittance is shown in the lower panel.

Band-integrated total intensity is approximately ten times greater for combusting plumes, due to elevated temperatures and larger emissive areas. Hot H_2O and CO_2 are particularly emissive in the MWIR, and account for a significant fraction of the observed intensity. Previous studies of explosive detonations have demonstrated that MWIR spectra can be used to estimate the H_2O and CO_2 concentrations in combusting HE fireballs using a low-dimensional radiative transfer model [9, 15]. Although the timescales are different – Figure 32 showed muzzle plume combustion to be complete in less than 100 ms whereas HE fireballs may last 0.5 – 5 seconds or longer [9, 12] – the similarity in thermochemistry (if not kinetics), allows the HE model to be used to

estimate temperature and concentrations of H₂O and CO₂ from the muzzle flash spectra. In the case of non-combusting plumes, the model can also be used to estimate temperature for highly graybody emissions.

Spectral Model

The HE model extracts the evolving temperature, emissive area, particulate emissivity, and column densities for H₂O, CO₂, and CO. Spectra of fireballs resulting from the detonation of high explosive materials are modeled well in the 2500 – 7000 cm⁻¹ range, with typical residuals of less than 5 – 10% [9, 15]. The model is capable of estimating the H:C ratio, a key feature for event classification [15]. We now explore the validity of this model for characterizing muzzle flash spectra.

The model assumes local thermodynamic equilibrium (LTE), a constant optical path length, a uniform distribution of temperatures and concentrations in the image plane, negligible scattering, and no background transmission through the source. The source spectral intensity is described as:

$$I_s(\nu; T, \mu) = A \epsilon(\nu; T, \mu) B(\nu; T) \quad (39)$$

where:

A = projected source area

$\epsilon(\nu; T) = 1 - e^{-\alpha(\nu; T)}$ = source emissivity

$B(\nu; T)$ = blackbody (Planckian) spectral radiance

The absorbance, α , depends on the species-dependent absorption cross-sections, $\sigma_i(\nu)$, column densities, $\mu_i = n_i l$, and graybody, particulate component, α_s :

$$\alpha(\nu; T) = \alpha_s + \sum_i \sigma_i(\nu; T) n_i l \quad (40)$$

where:

l = optical path length

i = index for H₂O, CO₂, and CO species

n_i = concentration of species i

The particulate (soot) emissivity is assumed independent of frequency. The cross-sections are pressure and temperature dependent and computed using the Line-by-Line Radiative Transfer Model (LBLRTM) with high temperature extension (HITEMP) to the HITRAN spectroscopic database [98, 107]. The cross-sections include the Boltzmann factor for relative populations in each internal state, so that n_i represents the total concentration of the i th species. Details of the calculation are provided in references [9, 15]. The temperatures, areas, soot emissivity, and species concentrations are determined as a function of time from evolving spectra.

Intensities obtain via Equations (39) and (40) were sampled at $\Delta\nu = 0.0025 \text{ cm}^{-1}$, the resolution at which the cross-sections were calculated in LBLTRM. For comparison to the MR-254 spectra, instrument responses were calculated by propagating source intensities through atmosphere and convolving with the instrument lineshape (ILS):

$$I_m(\nu) = \int_{-\infty}^{\infty} \tau(\nu') I_s(\nu') \text{ILS}(\nu - \nu') d\nu' = F \left\{ F^{-1} \left\{ \tau(\nu) I_s(\nu) \right\} H(x) \right\} \quad (41)$$

Atmospheric attenuation, $\tau(\nu)$, for the 429 m horizontal path was calculated using LBLRTM with the HITRAN database at $\Delta\nu = 0.0025 \text{ cm}^{-1}$ resolution for the median atmospheric pressure (90,200 Pa), temperature (15.6 °C), and relative humidity (37%) recorded during the test. Because the MR-254 is an interferometer, the convolution was implemented as the right-hand side of Equation (41). The inverse Fast-Fourier

Transform, $F^{-1}\{\}$, converted the attenuated, high-resolution source intensity to an interferogram that was then apodized with the Hanning function and Fourier Transformed, $F\{\}$, back to a spectrum. Resolution in a FTS is defined by the maximum optical path difference (MOPD) between mirrors ($\Delta\nu = 1/x_m$). By truncating the interferogram at $x_m = 0.032$ cm, 0.065 cm, or 0.259 cm, model intensities were obtained at the nominal 32 cm^{-1} , 16 cm^{-1} , or 4 cm^{-1} spectral resolutions. x_m is based on actual MOPD recorded during the test and does not exactly match the nominal resolutions.

Plume Dynamics

The model was fit to each spectrum in a data cube to obtain the time-dependent fit parameters. Area, temperature, soot absorbance, and concentration of H_2O , CO_2 , and CO were varied to minimize root-mean-square (RMS) residuals between observed and simulated spectra. Fits were performed using a nonlinear optimization simplex search method [80]. Representative fits to the peak spectra of combusting and non-combusting plumes are shown in Figure 34. When significant soot is present, a strong Planckian component is observed and the fit parameters are weakly correlated. At later time in combusting plumes, soot is reduced and plume opacity decreases. In the optically-thin limit, plume area and column densities become highly correlated; temperature, however, remains a useful parameter as it is determined from the relative ro-vibrational distributions. Fits to combusting spectra result in highly uncertain area and column densities when the plumes become optically thin ($t > \sim 50$ ms). Previously fireball studies have seen similar effects, with uncertainties in emissive area exceeding 30 – 40% when temperature declines below 1000 K [15]. To extend the spectral fit for the combusting plumes to longer times, the constraint that area monotonically increases is imposed.

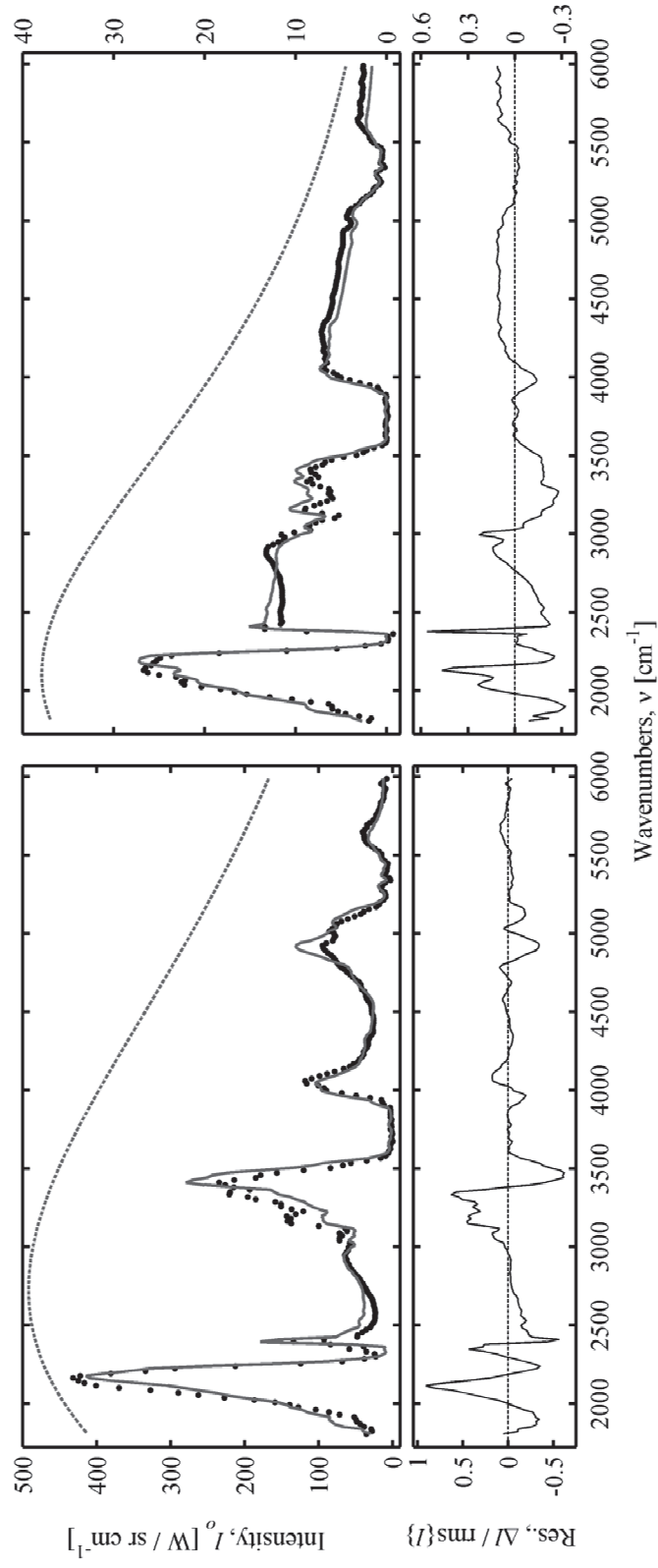


Figure 34. HE model (—) and observed (•) spectral intensities are shown for the peak band-integrated intensity of a combustor (left) and non-combustor (right) plume. Planckian emissions (---) at equivalent temperatures are shown for reference. Residuals between the model and data as a fraction of RMS intensity are indicated in the bottom panels.

The residuals shown in Figure 34 are significant and highly structured. Maximum residuals for combusting and non-combusting plumes are 22.5% and 18.3% relative to peak intensity. Relative errors for combusting ($e = 21.5\%$) and non-combusting ($e = 13.3\%$) plumes were calculated as the RMS of the residual, $\Delta I = I_o - I_m$, relative to RMS observed intensity. The largest residuals occur off-resonance of many spectral features – due in part to their width rather than amplitude – and this error metric gives equal weight to low intensity features. The figure shows that the basic structure of emissions from plumes that contain primarily selective emitters or particulate matter can be approximated using the HE fireball model.

Model parameters for fits to the peak spectra, and additional quantities derived from the parameters, are reported in Table 13. Decoupling of emitter concentration from column density is estimated assuming that the plume lateral dimension is the same as the optical path, $l = A^{1/2}$. The absolute emitter concentrations are plausible, as are combusting and non-combusting plume temperatures. In particular, the relative fraction of carbon-monoxide is consistent with equilibrium thermochemistry estimates for both plumes, i.e. nearly all CO is converted to CO₂ during combustion, but in non-combusting plumes CO is the primary product of burning a fuel-rich propellant [46, 54:22; 76:78].

The time-dependence of the spectral parameters are depicted in Figure 35. When a gun fires, fuel-rich propellant combustion by-products exit the barrel and develop into plumes composed largely of carbon-monoxide and soot with lesser concentration of other CHNO species [46, 54:22]. The under-oxidized plumes are initially ($t < 20$ ms) not burning and the relatively large soot emissivities indicate large concentrations of particulates. Re-ignition is probable when atmospheric oxygen is entrained if plume

temperature remains above 900 – 1000 K [28, 50, 53]. High-speed imagery of the howitzer firings showed re-ignition to occur near $t = 10 - 20$ ms, after which time the signatures of combusting and non-combusting plumes diverge.

Spectral modeling suggests non-combusting plume temperatures are initially near $T_0 = 850 \sim 1050$ K and quickly cool from expansion and continued entrainment of cold atmosphere. As temperature falls, emissions decrease rapidly and approach to within 5% of background by 30 – 40 ms after gun firing; model parameters beyond this time are unreliable due to lack of signal. A decrease in soot emissivity with time is observed but is consistently higher than in combusting plumes. Carbon-monoxide concentrations are also

Table 13. Model parameters for optimized fit to peak spectra from combusting and non-combusting plume. Derived quantities are indicated by italics. Gas mixing fraction indicates the percentage of each species relative to the concentrations of H₂O, CO₂, and CO

Fit Parameter	Combusting			Non-combusting		
Area, A [m ²]	32.3	±	4.5	5.4	±	0.7
<i>Optical path, $l = A^{1/2}$ [m]</i>	5.68	±	0.40	2.32	±	0.83
Temperature, T [K]	1389	±	67	1072	±	23
Soot absorbance, α_s	2.67	±	0.08	1.03	±	0.04
<i>Emissivity, $\epsilon_s = (1 - e^{-\alpha})$</i>	0.07	±	0.01	0.36	±	0.04
H ₂ O column density, μ [cm ⁻²]	2.5·10 ²⁰	±	6.0·10 ¹⁹	1.3·10 ²⁰	±	5.0·10 ¹⁹
<i>Concentration, $N = \mu / l$ [cm⁻³]</i>	4.4·10 ¹⁷	±	1.1·10 ¹⁷	5.6·10 ¹⁷	±	6.0·10 ¹⁷
<i>Gas mixing fraction</i>	13.3%	±	0.4%	44.4%	±	37.0%
CO ₂ column density, μ [cm ⁻²]	1.6·10 ²¹	±	3.9·10 ²⁰	2.5·10 ¹⁹	±	2.4·10 ¹⁹
<i>Concentration, $N = \mu / l$ [cm⁻³]</i>	2.8·10 ¹⁸	±	6.9·10 ¹⁷	1.1·10 ¹⁷	±	2.9·10 ¹⁷
<i>Gas mixing fraction</i>	84.0%	±	1.8%	8.7%	±	18.0%
CO column density, μ [cm ⁻²]	5.1·10 ¹⁹	±	5.5·10 ¹⁹	1.4·10 ²⁰	±	6.1·10 ¹⁹
<i>Concentration, $N = \mu / l$ [cm⁻³]</i>	9.0·10 ¹⁶	±	9.8·10 ¹⁶	5.9·10 ¹⁷	±	7.3·10 ¹⁷
<i>Gas mixing fraction</i>	2.7%	±	2.2%	46.9%	±	45.0%

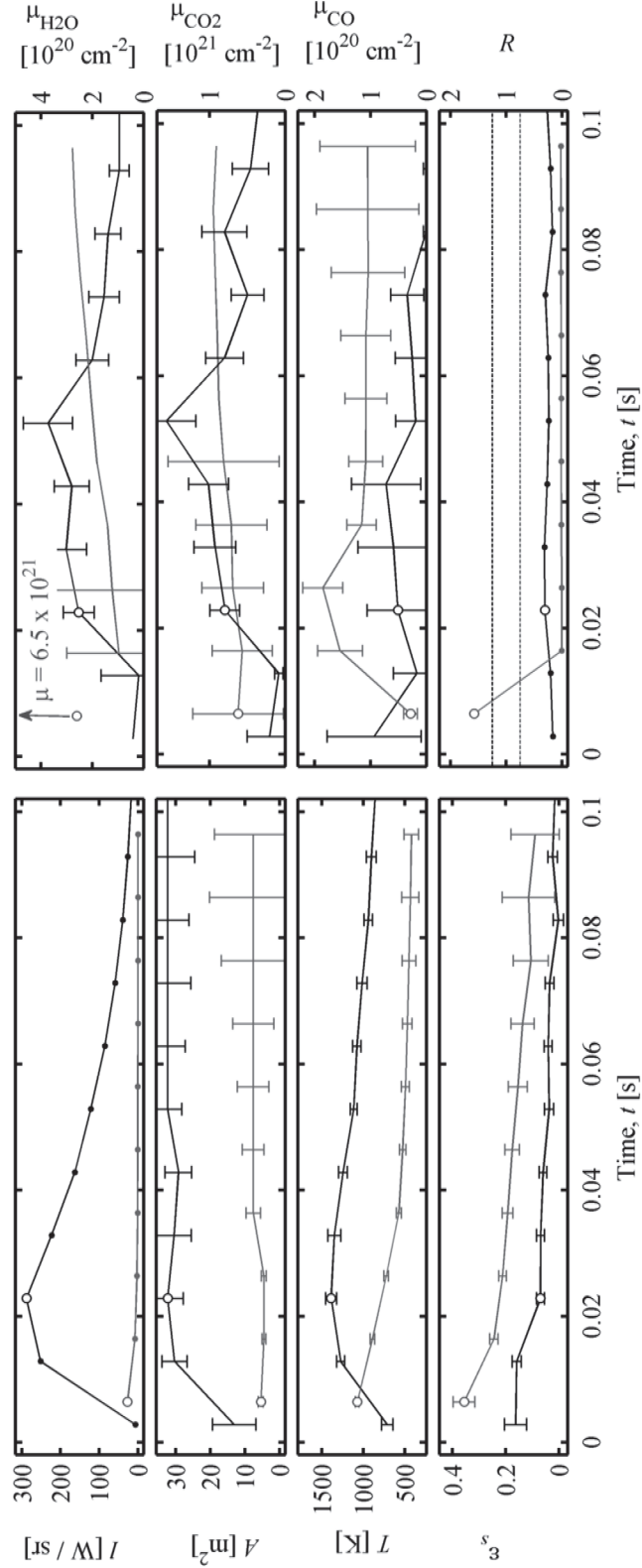


Figure 35. Temporal dependence of HE model parameters when fit to combustive (—) and non-combusting (—) plumes. The values corresponding to peak intensity are indicated (○) and $t = 0$ occurs at gun firing. *Left, top to bottom*: band-integrated intensity, area, temperature, and soot emissivity. *Right, top to bottom*: column densities of H_2O , CO_2 , and CO ; and H:C ratio. Theoretical H:C ratios for combustive (---) and non-combusting (---) plumes are shown. For depiction on the same scale, non-combusting column densities and uncertainties are multiplied as following: $\text{H}_2\text{O} \times 50$, $\text{CO}_2 \times 50$, and $\text{CO} \times 1/5$. Error bars are excluded when off the scale of the plots.

higher in non-combusting plumes, consistent with incomplete combustion of the fuel-rich propellant. Alternatively, if a plume re-ignites, combustion raises the average temperature to near $T_0 = 1200 \sim 1600$ K. Elevated temperatures vaporize soot particulates and provide reaction pathways responsible for large increases in concentrations of H_2O and CO_2 . Burning of soot is indicated by an abrupt decrease in soot emissivity immediately after re-ignition ($t \approx 10 - 20$ ms). Sustained burning maintains strong emissions beyond 100 ms even as temperature decreases while fuel is consumed and additional cold air is entrained.

Figure 35 also shows that the hydrogen-to-carbon ratios (derived from model parameter concentrations) for both plumes are lower than the theoretical values for complete combustion of the propellants. The model may overestimate CO_2 concentration and contribute to systematic bias of the H:C ratio. Observed spectral emissions in the $2000 - 2250 \text{ cm}^{-1}$ region are disproportionately more intense than allowed by a single temperature, equilibrium radiation distribution $B(\nu;T)$. This phenomenon was also observed in HE fireballs and has not yet been explained [15]. It may be the result of non-equilibrium emissions from CO_2 or CO – both of which emit due to fundamental vibrational modes in this region – or a distribution of temperatures across the fireball.

Similarly, both H_2O and CO_2 have a number of overlapping combination and resonance states that are thermally populated at combustion temperatures and emit strongly from $4500 - 5200 \text{ cm}^{-1}$. However, no single temperature mixture of H_2O and CO_2 reproduces the smooth, broad emissions from $4500 - 4850 \text{ cm}^{-1}$ (red shoulder) without overemphasizing the $4850 - 5200 \text{ cm}^{-1}$ region (blue shoulder) and introducing an unobserved spike near 4900 cm^{-1} . In fitting the model to data, the non-linear optimization

obtained an overall lower RMS error by increasing CO₂ concentration to reproduce emissions near 2000 – 2250 cm⁻¹ and 4500 – 4850 cm⁻¹. Consequences include overestimation of the amount of CO₂ (resulting in a lower H:C ratio) and introduction of systematic residuals throughout the spectrum.

These results indicate that the model does not completely treat phenomenology of the plume. Improvement of the model may require (1) generalizing to a distribution of temperatures and species concentrations across the plume; (2) treating radiative transfer through multiple non-uniform plume layers along the observation path; (3) modeling the frequency dependence of soot emissions rather than assuming graybody; (4) including additional species whose emissions are inadequately compensated for by H₂O, CO₂, and CO; or (5) allowing for ro-vibrational distributions of species that are not in equilibrium with the thermal temperature of the plume.

Discussion

Spectral Model with Spatial Variations

To explore one approach for increasing model fidelity, the uniformity assumption of Equation (39) was relaxed to allow for a distribution of temperatures and concentrations across the plume. The distributions are introduced in an attempt to account for the effects of turbulence-induced variations observed in muzzle plumes [28, 50, 53]. Radiative transfer is approximated as before, except Equation (39) is generalized to allow for a distribution of temperatures and concentrations:

$$\Phi(\nu) = \iint P(T - T_0, \mu / \mu_0) I_s(\nu; T, \mu) dT d\mu \quad (42)$$

Skewed normal and log-normal distribution functions are employed for the temperature and concentrations, respectively:

$$P(T, \mu) \equiv C \left(\frac{e^{-(T/\Delta_T)^2}}{1 + e^{\zeta_T T/\Delta_T}} \right) \left(\frac{e^{-\log_{10}^2(\mu)/\Delta_\mu^2}}{1 + e^{\zeta_\mu \log_{10}(\mu)/\Delta_\mu}} \right) \quad (43)$$

Equation (43) is separable in T and μ , and is unit-area normalized with constant C . The distributions for each species i are assumed to have the same spread and skew. The function was chosen because adjustment of the mean (T_0, μ_0), spread (Δ_T, Δ_μ), and skew (ζ_T, ζ_μ) parameters allows for a broad range of continuous and efficiently computable distributions. It should be evident that Equation (42) is a generalization of Equation (39), and the two become equivalent as the distribution function approaches a Dirac delta function, $P \rightarrow \delta$.

In the optically thin limit (or for species each from independent locations), the sum over species in Equation (40) can be replaced by a sum of the intensities:

$$\Phi(\nu) \cong \sum_i \iint P(T - T_0, \mu / \mu_i) I_s(\nu; T, \mu_i) dT d\mu_i \quad (44)$$

The approximation of Equation (44) is not satisfied for the plume's optically thick conditions, but rather employed for convenience in the computation.

Equations (43) and (44) and the spatially-uniform HE model were fit to the peak spectra of a combusting plume, and the results are compared in Figure 36. When distributions were permitted, residuals demonstrated a 40% reduction in maximum error and 21% reduction in RMS error ($e = 21.5\% \rightarrow e = 16.9\%$). For comparison, RMS residuals of the non-distribution, HE model when applied to explosive fireballs were typically 5 – 10%. This contrast suggests that there is a phenomenological difference

between HE fireballs and muzzle plumes that is not explained in the model of Equation (39) but may be partially mitigated by the use of non-uniformity in Equation (42).

The best-fit H₂O and temperature distribution functions are also depicted in Figure 36. CO₂ and CO follow the same distributions but have different concentrations, provided in Table 14 with all fit parameters. The concentration distribution is skewed by $\zeta_\mu \approx -18$ towards positive values of $\log_{10}(\mu/\mu_0)$, and it spans a range nearly equal to the spread $\Delta_\mu \approx 0.2$ (when measured by its full width at half maximum, FWHM). The temperature distribution is biased by $\zeta_T \approx 18$ to lower temperatures, and the FWHM is also nearly equal to the spread, $\Delta_T \approx 130$. Uncertainties in all fit parameters are increased by the use

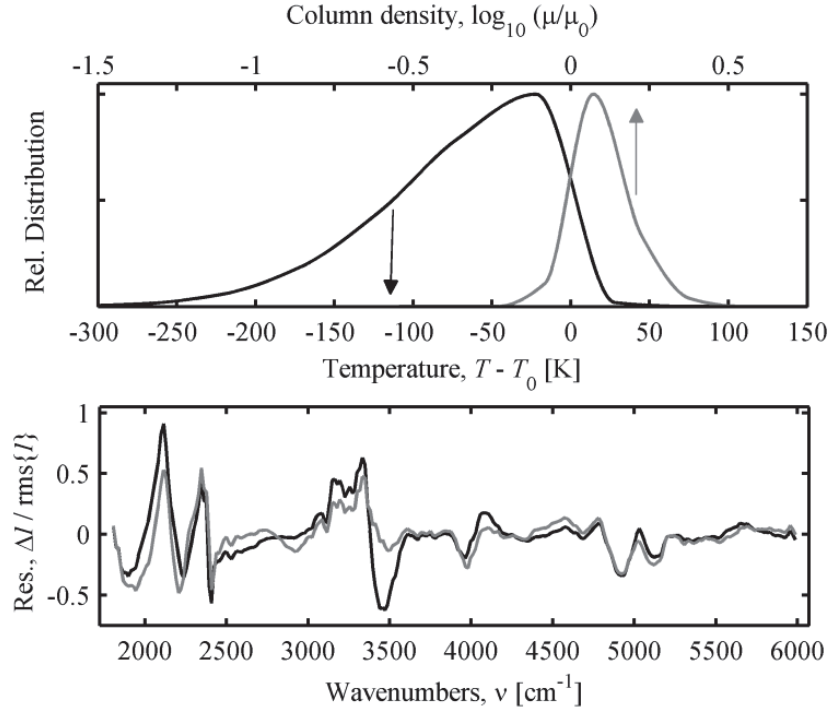


Figure 36. HE and distribution model fits to a combustng plume. *Upper panel:* distributions of temperature (—) and H₂O column density (---) centered at $T_0 = 1472$ K and $\mu_0 = \mu_{\text{H}_2\text{O}} = 4.7 \times 10^{20} \text{ cm}^{-2}$. CO₂ and CO have the same column density distribution centered at $\mu_{\text{CO}_2} = 1.6 \times 10^{21} \text{ cm}^{-2}$ and $\mu_{\text{CO}} = 8.9 \times 10^{19} \text{ cm}^{-2}$. *Lower panel:* Residuals between observed spectral intensity and distribution (—) and HE (---) models. RMS error is reduced from $e = 21.5\%$ to $e = 16.9\%$ when temperature and concentrations vary spatially.

Table 14. Model parameters and relative RMS error for the peak intensity spectrum of a combusting muzzle plume.

Parameter	HE	1-region	2-region	
			Core	Flame-front
$A \text{ [m}^2\text{]}$	32.3 ± 4.5	21.6 ± 5.0	20.7 ± 3.9	5.0 ± 2.7
$T_0 \text{ [K]}$	$1,389 \pm 67$	$1,472 \pm 98$	$1,548 \pm 151$	$2,552 \pm 243$
$\Delta T \text{ [K]}$		130 ± 197	104 ± 142	135 ± 157
ζ_T		18.4 ± 18.8	3.2 ± 4.0	-12.7 ± 9.8
$\mu_{\text{H}_2\text{O}} [10^{20} \text{ cm}^{-2}]$	2.52 ± 0.60	4.71 ± 1.54	4.52 ± 1.19	$(1.1 \pm 0.8) \times 10^{-2}$
$\mu_{\text{CO}_2} [10^{20} \text{ cm}^{-2}]$	15.97 ± 3.92	15.78 ± 5.03	10.55 ± 2.77	$(8.5 \pm 6.1) \times 10^{-5}$
$\mu_{\text{CO}} [10^{19} \text{ cm}^{-2}]$	5.13 ± 5.54	8.91 ± 8.28	0.57 ± 0.64	$(1.0 \pm 2.7) \times 10^{-9}$
$\Delta\mu$		0.21 ± 0.50	0.22 ± 0.34	1.69 ± 0.88
ζ_μ		-17.9 ± 22.6	-19.7 ± 23.6	17.6 ± 7.9
$\varepsilon_s [10^{-2}]$	6.90 ± 1.48	2.03 ± 2.81	2.30 ± 0.14	0.10 ± 0.01
R	0.31	0.57	0.85	
e	21.5%	16.9%	13.8%	

of the generalized model. This is likely due to increased parameterization (6 \rightarrow 10 fit parameters). Relative uncertainties indicate an insensitivity to skew and spread. This may indicate that simply using a distribution, regardless of it having a well-defined shape, provides improvement to the model.

The distribution model was also fit to the peak spectrum of a non-combusting plume. Negligible improvement (< 4%) was obtained. This is possibly because plumes are sooty and optically thick when they do not combust, and their Planckian-like emissions are insensitive to relatively small variations in concentrations and temperature. Because residuals are not significantly improved and distributions increase parameterization, the HE model is preferred when modeling non-combusting plumes.

Multiple Spatially Varying Regions

The 152 mm howitzer is equipped with a muzzle brake that splits the muzzle flow into forward and lateral plumes. This was shown in Figure 33, from which it is apparent that the plumes are composed of multiple distinct spatial regions. These may be characterized a number of ways. The forward and lateral plumes are two distinct spatial regions apparent to the observer. It may be possible that the each plume has sufficiently different temperatures or concentrations that a model with only a single region – even one containing distributions – cannot reproduce their spectral emissions. The flow may be further divided into sub-regions. For example, each plume consists of thin outer layers in contact with atmosphere, and these layers surround plume cores of ~3 meter depth [93, 108]. The outer layers may be significantly hotter than the core if burning occurs at the surface where atmospheric oxygen is turbulently entrained; likewise core regions may be under-oxidized and consequently have higher concentrations of carbon monoxide. The example is not given as the justification for multiple regions; rather it exemplifies the type of phenomenology that may require a multi-region model.

A multi-region model is obtained as the summation of several source intensities calculated from Equation (44). Total at-source intensity is composed of emissions from more than one distribution of spectral radiances, each weighted by its region's emissive area. Note that this formulation treats each region as spatially isolated from the perspective of the observer, e.g. forward and lateral plumes, or core and surface layers viewed at the plume's edge. Radiative transfer through multiple layers at increasing depths from the observer is not treated here.

Figure 37 depicts the distribution of a two-region model for a combusting plume that reduces RMS error to $e = 13.8\%$. Fit parameters that characterize the distributions of temperatures and concentrations in both regions are given in Table 14. The previous description of a plume comprised of a core and surface layer is a plausible explanation of the parameters. The *core* is similar to the one-region distribution model (e.g. $A \approx 21 \text{ m}^2$, $T_0 \approx 1500 \text{ K}$, etc.) and emissions from this region account for 70% of the observed intensity. These emissions compose the basic structure of the spectrum and include nearly all of the blackbody radiation. Non-distribution, HE model parameters are all located within the distributions of this core region. With the exception of CO column density and emissive area, the mean values of both models are nearly equivalent to within statistical uncertainty.

The second *surface layer* region is characterized by very low column densities of all species, indicating optical thinness. Mean temperature at $T_0 = 2552 \text{ K}$ is consistent with measured secondary combustion temperatures in excess of 2000 – 3000 K [46]. The high temperatures and low concentrations may be attributed to a flame-front at the edge of the plume's core region. The flame-front could be characterized by significant heat release as atmospheric oxygen interacts with the under-oxidized combustion by-products in a very thin surface layer.

Temperature Dynamics

Strong radiative emissions are observed from secondary combustion and suppressed muzzle plumes on timescales of $\sim 100 \text{ ms}$ and $\sim 20 \text{ ms}$, respectively. The timescale difference is evident in cooling rates. Figure 38 depicts the temperatures for a combusting and suppressed muzzle plume. Temperatures were extracted from the non-combusting

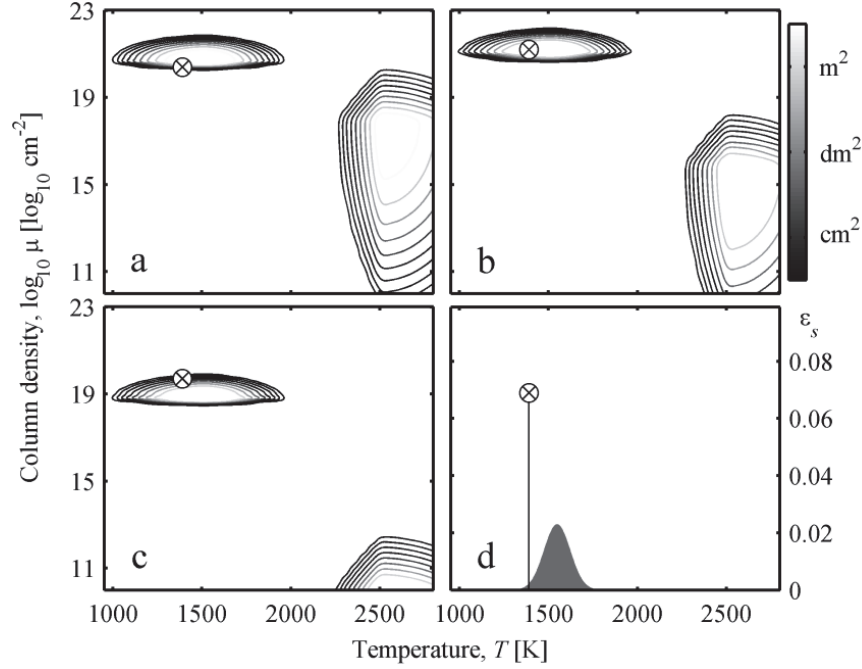


Figure 37. Distributions of a two-region model fit to the peak spectrum of a combusting muzzle plume. a) H_2O , b) CO_2 , and c) CO compose an optically thick core of temperature near $T \approx 1500$ K and thin flame-front near $T \approx 2550$ K. Contours indicate relative area-weighting of emissions for the range of temperatures and concentrations. d) Soot emissivity distribution shows that most Planckian-like emissions are near 1500 K. Parameters of the HE model (\otimes) are located within the core region's distributions.

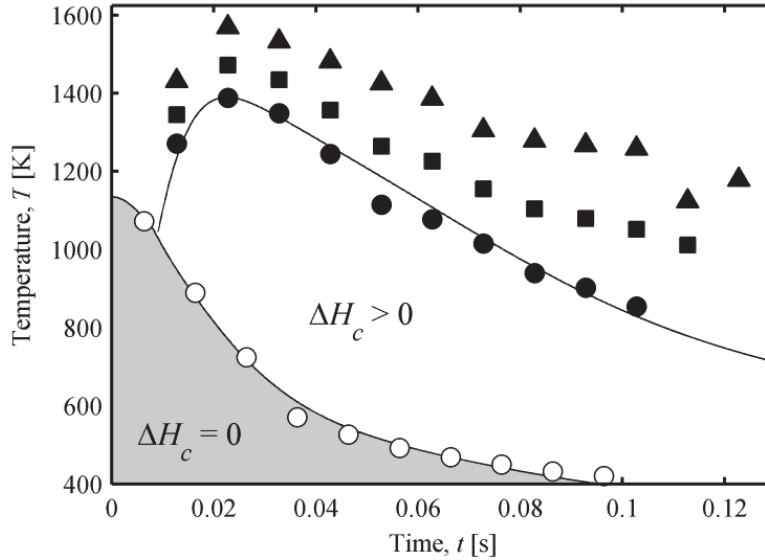


Figure 38. Temperatures extracted from a combusting muzzle plume using the HE model (●), one region distribution (■), and two region distribution (▲). The temperature of a suppressed, non-combusting plume (○) was estimated using the HE model. Curves through the data (—) represent empirically modeled temperature as a function of time.

plume using the HE model, and from the combusting plume using the HE and distribution models. Combustion temperatures all have similar temporal behavior but differ in magnitude by 200 ~ 300 K. All are plausible; however, the temperature derived from the HE model is more stable (due to fewer fit parameters) and may be preferable.

Rate of temperature change is a balance between multiple competing processes that contribute or dissipate energy. Temperature as a function time might be simply approximated as a decaying exponential, $T = T_0 e^{-\lambda t}$. Muzzle plume decay rates of $\lambda \approx 4 - 6 \text{ s}^{-1}$ (combusting) and $\lambda \approx 13 - 21 \text{ s}^{-1}$ (non-combusting) were estimated from the HE model temperatures. The difference in rates can be explained with the use of a recently developed HE model for temperature change [12]:

$$\frac{dT}{dt} = -a(T^4 - T_{am}^4) + b(e^{-ct} - e^{-dt}) \quad (45)$$

The first term accounts for radiative cooling, and the second term represents the rates of turbulent mixing and reduction in fuel concentration. The coefficients $a - d$ are empirically determined, and $b - d$ are related to thermodynamic quantities:

$$\Delta h_c \propto c_p b(1/c - 1/d) \quad (46)$$

where:

Δh_c = specific heat of combustion (J/kg)

c_p = specific heat capacity (J/kg-K)

Average heat capacity of the 152 mm howitzer propellant is approximately 1900 ~ 2000 J/kg-K [108]. Assuming stoichiometric mixing and ~1100 J/kg-K heat capacity of air (average over 300 – 1400 K), the total specific heat capacity of the plume is estimated to be $c_p = 1350 \sim 1450 \text{ J/kg-K}$.

Table 15 reports parameters for fits of Equation (45) to the HE temperatures in Figure 38. The results exemplify the principal difference between combusting and non-combusting plumes, i.e. additional energy is released in combustion as reactants are converted to products of lower internal energy. Specific heat values of 152 mm howitzer munitions were estimated as the heat release from gaseous propellant during combustion divided by the mass of the propellant and sufficient atmosphere for complete, stoichiometric combustion, i.e. $\Delta h_c = \Delta H_c / (m_c + m_a) \approx 2.54 - 2.72$ MJ/kg (see Appendix A). Heats of combustion from Equation (46) agree to within statistical uncertainty. Sustained heat release ($\Delta H_c > 0$) during combustion of the muzzle plume results in higher temperatures for longer durations, as is evident when comparing the combusting and non-combusting temperature profiles in Figure 38. The initial increase in temperature indicates dominance of combustive heating over all cooling effects. As the rate of heating slows (due to consumption of fuel) the plume begins to cool, yet at a slower rate than in non-combusting plumes whose temperature decays monotonically.

Table 15. Temperature rate parameters

Plume	a [$10^{-10} \text{ s}^{-1} \text{ K}^{-3}$]	b [10^4 K s^{-1}]	c [s^{-1}]	d [s^{-1}]	Δh_c [MJ/kg]
Combusting	189.0 ± 10.3	201.2 ± 43.4	54.7 ± 4.0	60.1 ± 45.3	4.9 ± 4.0
Non-combusting	103.3 ± 1.2	19.1 ± 19.8	74.0 ± 9.9	61.5 ± 34.1	$(-0.8 \pm -1.2) \approx 0$

For reference, HE fireballs with comparable heats of combustion have been observed with decay rates $\sim 0.7 \text{ s}^{-1}$ [12], almost an order of magnitude slower than the combusting muzzle plumes considered in this work. The disparity between these timescales may be due to the relationship between initial and combustion energy releases. In detonations,

explosive material is exothermically converted to gaseous products and energy release (heat of detonation) results in a sudden initial temperature increase [12]. This is quickly followed by combustion heat release as the products react with atmospheric oxygen. Detonation and combustion are spatially and temporally nearly coincident, but the ongoing rate of heat release depends on the rate at which oxygen is entrained. During a gun firing, propellant burning occurs interior to the gun and releases energy akin to the heat of detonation. Burning stops once all oxygen is consumed, typically prior to shot exit. Propellant gases cool as they flow from the muzzle and expand outside of the gun [50]. If combustion results, it is a separate process that occurs after the muzzle plume has developed and begun to mix with atmosphere. The temporal and spatial delay may allow sufficient pre-mixing that burning is not limited by the rate at which oxygen can be entrained, and heat is released much more quickly when the plume is ignited.

Summary

Muzzle plume emission spectra were collected in the midwave infrared (1800 – 6000 cm^{-1}) at 32 cm^{-1} spectral and 100 Hz temporal resolutions. They represent the highest fidelity spectra of large caliber firing signatures available in the published literature in several decades. Indeed, most prior studies were qualitative in nature, relying on photographic film with analog conversion to spectral intensity plots. The results presented here are the first reported spectra collected with digital instrumentation and amenable to spectral simulation and modeling.

Gun firings of a 152 mm howitzer were observed for unsuppressed and flash-suppressed munitions. Imagery of plumes from all munitions showed 35 – 40 m^2

projected areas from the perspective of the observation site. Plumes from unsuppressed munitions typically combust and are characterized by a maximum emissive area of $20 \sim 35 \text{ m}^2$, peak temperatures greater than 1200 K, and large concentrations of H_2O and CO_2 . Strong emissions last $\sim 100 \text{ ms}$ and are dominated by selective radiation. Most flash-suppressed munitions produce non-combusting plumes whose emissive area is $\sim 5 \text{ m}^2$ and that are composed primarily of particulate matter and CO at temperatures less than 1100 K. Suppressed spectra are one-tenth as intense, last less than $20 \sim 40 \text{ ms}$, and are predominantly continuum and CO emissions with lesser superimposed H_2O and CO_2 structure. Both plume types have peak spectral emissions in the $2000 - 2250 \text{ cm}^{-1}$ region that are 50% more intense than in any other region.

A low-dimensional radiative transfer model that characterizes emissions in terms of area, temperature, soot absorbance, and species concentrations of H_2O , CO_2 , and CO was assessed for muzzle flash spectra. The model was recently developed to simulate MWIR combustion emissions from HE detonation fireballs. Results for combusting plumes show temperatures that peak near $1200 - 1600 \text{ K}$ approximately $\sim 20 \text{ ms}$ after gun firing and cool with exponential decay rates of $4 - 6 \text{ s}^{-1}$. Non-combusting plume temperatures are $850 - 1050 \text{ K}$ and decay monotonically with a much faster $13 - 21 \text{ s}^{-1}$ rate. Plume ignition results in ~ 0.07 soot emissivity and substantial increases in H_2O and CO_2 , presumably as soot and CO are oxidized during secondary combustion. The non-combusting plume is characterized by ~ 0.36 soot emissivity and CO as the primary constituent. Direct application of the model results in $18 \sim 26\%$ RMS fit residuals. This limits the viability of the model for accurate prediction of muzzle flash spectral features;

however, the parameters are plausible of combustion conditions and may be used as classification features that characterize the spectra in low dimensionality.

These results are the first application of a radiative transfer model to MWIR muzzle flash. That spectral features are not adequately reproduced implies that pertinent phenomenology is not described. We investigated generalization of the model by using non-uniform distributions of temperature and species concentrations in the plane of observation. The use of distributions is one of several approaches to improving the model, and the additional degrees of freedom may account for, in an approximate way, the effects of spatially distinct regions and turbulent mixing. In particular, a plausible two-region interpretation of a combusting plume is a ~ 1500 K, optically thick core and ~ 2500 K, thin flame-front at the plume's surface. Fit residuals were reduced to 13 ~ 17% RMS error for combusting plumes but negligible improvement was obtained for non-combusting spectra.

The added complexity is not justified for the relatively minor reduction in residuals. Increased parameterization ($6 \rightarrow 10+$) result in larger parameter uncertainty and possible non-unique solutions. Simulation of muzzle spectra may require additional improvements. These could include a non-graybody treatment of soot emissions, inclusion of additional emitting species, non-equilibrium ro-vibrational distributions, or treating radiative transfer through non-uniformity along the path of observation. Improvements are desired because parameters that describe phenomenology of the plume in low dimensionality may be used to characterize the source of firing emissions. Without such parameters, distinguishing between different firing signatures relies on empirical features that are not always readily understood.

Modeling of temperature rate of change with time demonstrated greater success. Suppressed plume temperatures decay to 500 – 800 K within ~20 ms, whereas to reach the same temperature requires ~100 ms or longer in combusting plumes. The difference in timescale results from energy released during combustion. When combustion occurs, the temperature of the plume is initially increased and cooling is slowed. Heat of combustion near ~5 MJ/kg was estimated from the model and agrees to within a factor of two with predicted specific heat values for a stoichiometric plume and complete combustion. For comparison, detonation fireballs cool nearly an order of magnitude more quickly for comparable specific heats of combustion. Fireballs burn rate is dependent upon rate of oxygen entrainment, and spatial and temporal separation of initial propellant burning from plume combustion in muzzle plumes may allow pre-mixing that accounts for the difference in rates.

VII. Remote Discrimination of Large Caliber Gun Firing Signatures

Introduction

Remote sensing has proven effective in characterizing terrestrial combustion phenomena ranging from large-scale natural occurrences, such as forest fires [109, 110] to volcanic eruptions [111, 112], to man-caused events like the Kuwait oil field fires [113]. Detection of sources of limited spatial extent or relatively short duration, e.g. gas flares [114 – 116] or small fires [117], are more challenging and often require greater sensitivity in conjunction with pattern recognition techniques. For example, threshold-based rules have been used for automated forest fire and volcano identification [110, 111]; and both maximum likelihood estimators and adaptive neural networks have been used to identify landcover from multi-spectral imagery [118, 119]. Pattern recognition techniques are innumerable, and an overview of approaches applicable to this range of problems is summarized in the literature [64, 65].

The same improvements in sensor fidelity and pattern recognition that have advanced remote sensing for civil applications have also enabled new military uses, such as detection of buried ordnance and environmental damage assessments [118, 120]. In particular, technologies that have proven successful in detecting environmental combustion [109 – 117] are also ideally suited for use in battlespace characterization. Missile plumes, explosive fireballs, and muzzle flashes emit strongly in the visible and infrared and may be passively observed from the same types of airborne and space-based sensors used to characterize the environment. Different classes of sources (e.g. rocket exhaust, explosives, or muzzle flash) can be differentiated because their signatures are temporally and spatially very different [14].

Distinguishing between types within the same class is more challenging. Substantial study has gone into recognition of missiles for tactical and strategic warning systems [121 – 123]. In contrast, limited study has been performed for the classification of transient combustion events. Discrimination of conventional, novel, and improvised explosives has been demonstrated using a combination of multi-band imagery and infrared spectra [17, 18], and further reduction of spectra has yielded features effective for phenomenological interpretation [12, 15]. The work presented here extends discrimination of remotely observed optical and infrared signatures to a large caliber gun.

When a gun is fired, propellant gases flow from the muzzle and are responsible for several distinct firing signatures. A blast wave is formed as atmosphere is compressed by the supersonic expansion of the gases as they exit the muzzle [28]. Its strength and expansion trajectory are highly dependent on gun configuration, mass of propellant, and propellant energy content. Muzzle flash is a prominent firing signature and results from burning muzzle gases that strongly emit throughout the visible and infrared [30]. Relative strengths of spectral features are dependent on the chemical composition of the propellant. These blast and flash signatures may be remotely observed at large distances and their dependence on weapon properties suggests potential for discrimination. To assess this, firings signatures from three different munitions configurations were recently observed and characterized (see Chapters III – VI).

Since the ability to discriminate decreases as dimensionality increases [64:169-170], the vast number of observations required to define a discriminator would be intractable using the signatures themselves. Observation data were reduced to a set of empirical

features that characterize firing signatures in lower dimensionality. The current understanding of muzzle blast and flash phenomenology also allows for a number of physics-based features to be extracted. These can provide information about the signature that empirical features do not, e.g. combustion temperature or hydrogen-to-carbon ratio. Correlation amongst features of both types was assessed to identify those that provide redundant information.

Discrimination was restricted to multiple discriminant analysis (MDA), which is a robust, linear classification technique. MDA maximizes separation of classes in a multi-dimensional feature space [64:121-124; 65:400-407]. Classes of munitions were assigned based on Bayesian decision boundaries and classification accuracy was assessed using a leave-one-out evaluation scheme [64:20-26, 472-475]. All features were assessed for saliency and stability with a forward-selection method, and the minimal sets with the greatest ability to discriminate are reported. Classification accuracy was improved when a combination of features types were used, demonstrating further potential for classifying battlespace events if multiple remote sensors of different types are employed.

Successful discrimination of similar munitions from a single weapon predicts an even greater ability to differentiate weapons. A subset of the most important infrared flash features was used to demonstrate improved discrimination when applied to firings of two different weapons.

Feature Data

Features were recently extracted from signature data collected on five different munitions configurations fired from a 152 mm howitzer (see Chapters III – VI), and the

results are summarized below. Configurations included one of three propellants designated (in order of decreasing propellant mass) Full Charge, Charge 1, and Charge 2. Flash suppressant was an optional component in Full Charge and Charge 1 and inhibited combustion of the muzzle plume. Two hundred and one firings were observed using multiple sensors with a side-on view of the gun at approximately one-half kilometer distance. Although several instruments observed most firings, features could not always be extracted from the data due to poor signal-to-noise ratio (SNR), saturation, or other environmental conditions. The numbers of firings, and the number for which features were extracted from each data set, are shown in Table 16, per munitions configuration. The limited number of firings for which features were obtained with all sensors highlights the importance of identifying and correlating discrimination features; i.e. when a full feature space is not available (or unreliably so), knowledge of which reduced features may be used is necessary.

Visible, monochrome imagery was acquired at 1600 Hz and used to record the blast produced by the expansion of high pressure gases that flow from the muzzle after gun firing [108]. The blast's expansion was characterized as nearly spherical with radius

Table 16. Numbers of firings, successful collection of each signature type, and firings for which all signatures were available are indicated for each munitions configuration.

Configuration	Supp.	Firings	Blast Trajectory	VNIR Spectra	MWIR Spectra	All Signatures
Full Charge	Yes*	69	31	0	50	0
	No	28	13	7	14	4
Charge 1	Yes	53	47	0	35	0
	No	28	27	9	14	5
Charge 2	No	23	17	21	22	16

* two events contained 1/2 bags of suppressant but did not flash

approximated as $R = At^b$ at early times ($t = 1 - 4$ ms). A representative expansion trajectory for a single firing is shown in Figure 39; the parameter A scales with increasing propellant mass, and the inset plot shows that the data are nearly linear in the log-log plane with slope $b = 0.55 \sim 0.6$. Parameters A and b are related to the total energy in the blast E , and if propellant mass and heat capacity are known (or can be estimated) a pre-combustion plume temperature, T , can also be calculated [108]. Muzzle flow phenomenology allows the blast to be approximated as forming from a constant rate of energy deposition [29]. The rate, $\dot{E} \equiv dE'/dt = \text{constant}$, is characterized by $b' \equiv b = 0.6$ for an assumed spherical geometry [108]. The set of A , b , E , and T (and corresponding A' , b' , E' , T' , and \dot{E}) forms a feature space defined by the muzzle blast signature.

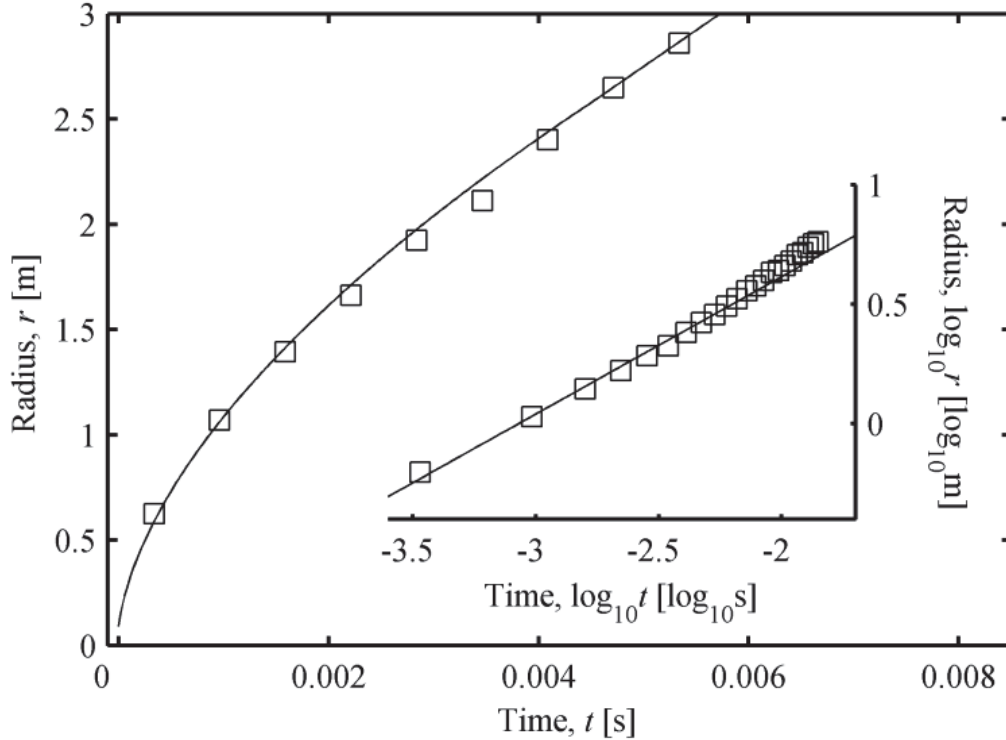


Figure 39. Observed 152 mm howitzer blast wave expansion (□) and trajectory model $R = At^b$ (—) at early times. The model is linear on a log-log plot where its slope is the temporal exponent b , and A is determined from the ordinate intercept at $\log_{10} t = 0$.

Visible through near infrared (VNIR, 450 – 850 nm) emissions from a combusting plume were acquired with a grating spectrometer and a representative spectrum is shown in Figure 40. Plumes that did not combust (e.g. suppressed munitions) did not result in a detectable VNIR signature. Each combusting spectrum is composed of line, band, and continuum emissions. The most prominent emissions are atomic lines produced by electronically excited contaminants (i.e. K, Na, and Li) [30]. Lines with signal-to-noise ratio (SNR) greater than one are indicated in the figure and their intensities were extracted as features. When different spin-orbit states were resolvable, their average amplitude (normalized by transition rates A and degeneracies g of the upper states) was used as the line intensity, I_u , of the u th line.

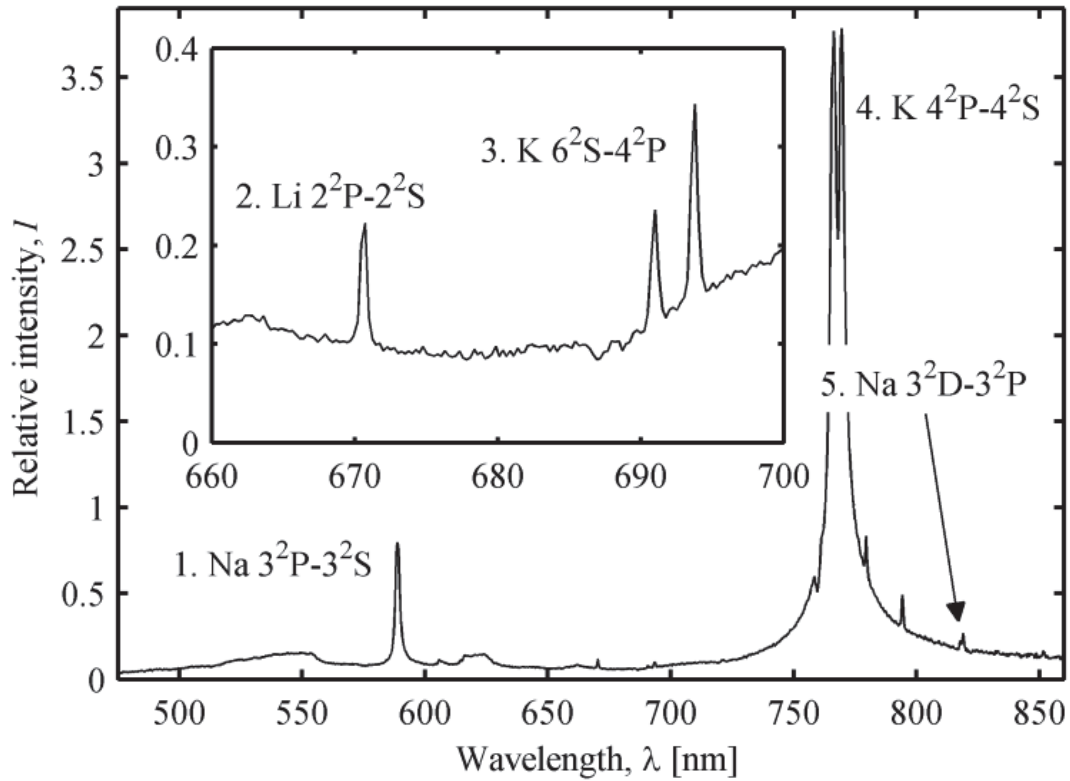


Figure 40. Peak intensity spectrum representative of combusting 152 mm howitzer visible and near-infrared flash signatures. The strongest (SNR > 1) identified lines emissions are labeled.

The ratio of line intensities, $r_{uv} = \log(I_u/I_v)$ for transitions u and v , are dependent on contaminant concentrations and vary by propellant type and manufacturing conditions. For conciseness, atomic lines are referenced by the numbers indicated in Figure 40, e.g. r_{15} corresponds to the ratio of $u = 1$ (Na $3^2\text{P} - 3^2\text{S}$) to $v = 5$ (Na $3^2\text{D} - 3^2\text{P}$). Ratios of line amplitude for transitions u and v were also used to estimate an electronic excitation temperature, T_{uv} , by assuming a Boltzmann distribution [124]. T_{uv} is only equivalent to a thermal temperature if the species are in radiative equilibrium. The features obtained from the most intense VNIR spectrum of each combusting plume form a space of line ratios and temperatures, r_{uv} and T_{uv} . Features could not be extracted from non-combusting plumes due to the dimness of their emissions.

Midwave infrared (MWIR, $1800 - 6000 \text{ cm}^{-1}$) spectra of the muzzle plume were collected at 32 cm^{-1} resolution using a Fourier transform spectrometer (FTS). Figure 41 illustrates a spectrum of a combusting muzzle plume representative of unsuppressed howitzer munitions. Non-combusting plume signatures are also detectable in the MWIR but are an order of magnitude dimmer and are unlikely to be detected with many remote sensors. A low dimensional radiative transfer model was previously developed to simulate MWIR combustion emissions in terms of equilibrium temperature, T_{eq} ; soot emissivity, ϵ_s ; and concentrations, μ_i , of species $i = \text{H}_2\text{O}$, CO_2 , and CO [9, 15]. The model was recently applied to muzzle plumes and model fit parameters obtained [125]. The set of parameters (T_{eq} , ϵ_s , and μ_i for $i = \text{H}_2\text{O}$, CO_2 , CO) for the peak intensity spectrum of each firing form a space of phenomenological MWIR features.

Firing signatures of the three unsuppressed munitions configurations for the 152 mm howitzer were the primary source of feature data. Although the munitions differed

(specifically the propellant), a certain level of consistency is imposed on their firing signatures because they are all fired from the same gun. To investigate how features compared when observing different weapons, limited data were obtained for a single firing of a 120 mm tank cannon. An ABB-Bomem MR-304 FTS was used to acquire MWIR spectra at nominal 16 cm^{-1} spectral resolution, shown in Figure 41 for reference. Firing signature features of the 120 mm cannon were obtained in the same manner as the 152 mm howitzer. Differences in viewing conditions were mitigated by multiplying by a spectral correction to produce similar atmospheric attenuation. The correction, modeled with LBLRTM [98], removed the cannon's 332 m observation path and replaced it with a 429 m attenuation similar to that of the howitzer.

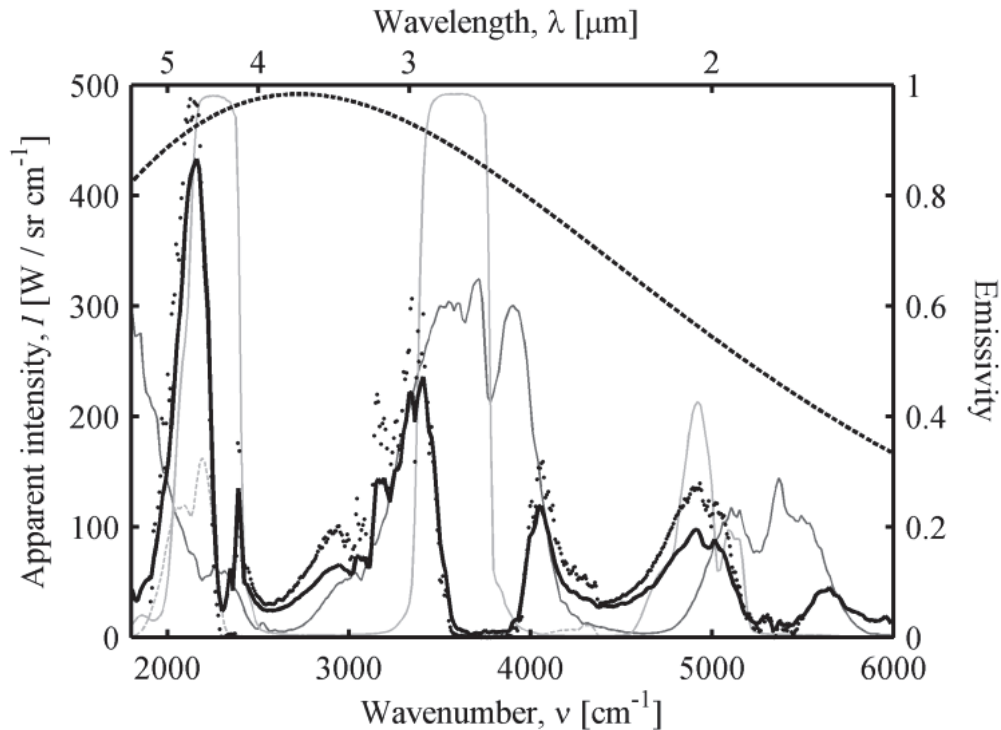


Figure 41. *Left ordinate:* Apparent midwave infrared spectra are shown for a combusting 152 mm howitzer plume (—) and a 120 mm tank cannon plume (••). Also shown is the Planckian distribution (•••) for the howitzer's model-estimated temperature $T = 1389 \text{ K}$. *Right ordinate:* Source spectral emissivity of H_2O (—), CO_2 (—), and CO (•••) as estimated from fit of the model to the howitzer data.

Results

Feature Sets

Blast, VNIR, and MWIR signatures for each firing are similar enough that when viewed collectively (as in Figure 39, Figure 40, and Figure 41) little difference is discernible. However, the set of extracted features reduced the signatures to a space into which differences were apparent. The space is composed of both empirical and phenomenological features. Interpretations of fit parameters that provide insight into the physics of the target are phenomenological features, and their mean and standard deviations are shown in Table 17, per configuration. The mean values show differences in firing signatures between configurations and the standard deviations represent variability within a configuration.

Empirical features are those without direct physical significance. Their mean values are in Table 18 and include several empirical features not yet discussed. The new features, designated F1 – F7 and E1 – E10, were obtained from band-integrated intensity of MWIR spectra. Because many sensor systems integrate spectral intensity in regions of finite bandwidth, these features represent a set of bands that could be collected with real-world sensors. The advantage of bands is that sensor data are directly used as features, which is especially beneficial in real-time applications where time constraints may not allow for computationally intensive fits of models to the data, e. g. as has been studied for missile typing [121 – 123].

Figure 42 depicts filter response curves for the bands from which F1 – F7 were obtained. These curves represent several filters that were used with instruments deployed during the howitzer firings. Superimposed on the response curves are normalized peak

Table 17. Mean phenomenological blast, VNIR, and MWIR features for each munitions configuration. Variability is indicated by the standard deviation of each feature, expressed as a percent of the mean value, per configuration.

Feature		Full Charge		Charge 1		Charge 2		120 mm
Blast	E [MJ]	3.69	(12%)	3.02	(38%)	1.73	(24%)	
	T [K]	1,006	(2%)	1,008	(8%)	1,194	(4%)	
	E' [MJ]	3.68	(17%)	3.12	(18%)	1.74	(31%)	
	T' [K]	1,006	(4%)	1,001	(4%)	1,192	(5%)	
	\dot{E} [GJ/s]	3.88	(17%)	3.39	(18%)	2.53	(31%)	
VNIR	T_{34} [K]	11,017	(7%)	11,869	(11%)	8,864	(9%)	
	T_{15} [K]	7,385	(9%)	8,810	(10%)	13,628	(28%)	
MWIR	T_{eq} [K]	1,302	(6%)	1,262	(2%)	1,358	(7%)	1,204
	$\varepsilon = 1 - e^{-\alpha}$	0.04	(2%)	0.03	(0%)	0.06	(3%)	0.08
	μ_{H_2O} [cm ⁻²]	4.03×10^{20}	(62%)	6.03×10^{20}	(19%)	5.20×10^{20}	(56%)	1.13×10^{21}
	μ_{CO_2} [cm ⁻²]	2.25×10^{21}	(50%)	2.15×10^{21}	(29%)	1.69×10^{21}	(33%)	8.57×10^{21}
	μ_{CO} [cm ⁻²]	1.36×10^{19}	(101%)	6.01×10^{19}	(76%)	3.52×10^{19}	(99%)	2.61×10^{15}

spectra of both 152 mm howitzer and 120 mm tank firings. Each spectrum was normalized by the standard deviation of its spectral intensity across the 1800 – 6000 cm⁻¹ band. Normalization is pragmatic because radiometric intensity is highly affected by atmosphere, aspect angle, and range to target; and if magnitude of intensity is not removed, band-integrated intensities may depend more on observation conditions than munitions characteristics. Standard deviation of intensity was used as the normalization factor because it puts all spectra on the same variance scale. Effects of atmosphere on spectral structure are also not insignificant, but the same observation geometry for all firings mitigated its effect. In general, atmosphere can be compensated for with various methods established in the literature [126].

Table 18. Mean empirical blast, VNIR, and MWIR features for each munitions configuration. Variability is indicated by the standard deviation of each feature, expressed as a percent of the mean value, per configuration.

Munitions	F1	F2	F3	F4	F5	F6	F7	$\log_{10} A$	b	$\log_{10} A'$
Full Charge	8.1 (35%)	5.4 (0%)	2.2 (82%)	-10.6 (90%)	-23.4 (44%)	3.2 (39%)	3.4 (117%)	1.86 (2%)	0.58 (2%)	1.91 (1%)
Charge 1	-2.6 (107%)	0.3 (0%)	-2.7 (54%)	-0.8 (867%)	37.3 (59%)	-6.1 (41%)	2.2 (93%)	1.83 (2%)	0.58 (3%)	1.90 (1%)
Charge 2	-5.5 (103%)	-6.6 (0%)	0.9 (347%)	13.8 (93%)	-12.8 (152%)	4.6 (182%)	-4.2 (115%)	1.76 (1%)	0.57 (2%)	1.87 (1%)
120 mm	11	-30	10	35	-131	30	-10			
Munitions	E1	E2	E3	E4	E5	E6	E7	E8	E9	E10
Full Charge	-1.0 (1110%)	14.5 (19%)	15.5 (72%)	7.2 (78%)	-2.0 (604%)	-65.4 (37%)	-5.9 (33%)	2.5 (560%)	-1.0 (1181%)	16.8 (122%)
Charge 1	5.5 (97%)	-3.2 (98%)	-10.5 (79%)	-0.2 (2808%)	-13.3 (78%)	37.0 (67%)	7.9 (44%)	-12.5 (64%)	-5.9 (220%)	-5.8 (185%)
Charge 2	-10.1 (89%)	-12.7 (98%)	-6.1 (187%)	-9.1 (79%)	24.6 (65%)	22.7 (166%)	-3.1 (124%)	16.1 (114%)	19.8 (128%)	-18.8 (96%)
120 mm	-66	26	-49	-43	123	-117	-25	102	135	-38
Munitions	r_{12}	r_{13}	r_{14}	r_{15}	r_{23}	r_{24}	r_{25}	r_{34}	r_{35}	r_{45}
Full Charge	2.5 (22%)	-2.5 (4%)	-4.4 (2%)	2.4 (8%)	-4.9 (12%)	-6.8 (9%)	-0.1 (1092%)	-1.9 (7%)	4.9 (3%)	6.7 (2%)
Charge 1	2.3 (21%)	-2.6 (10%)	-4.3 (2%)	2.0 (9%)	-4.8 (8%)	-6.6 (6%)	-0.3 (109%)	-1.8 (10%)	4.6 (5%)	6.3 (2%)
Charge 2	1.9 (18%)	-1.6 (24%)	-4.0 (5%)	1.4 (26%)	-3.5 (6%)	-5.9 (4%)	-0.5 (33%)	-2.4 (9%)	3.0 (7%)	5.4 (4%)

Figure 42 also shows the residual differences between the average of all spectra for each munitions relative to the average of all 152 mm howitzer firing spectra. The band features F1 – F7 were calculated as the integral over the residual in each band, weighted by the relative response of each filter:

$$Fi = \int (I_z(\nu) - I_m(\nu)) \cdot w_i(\nu) d\nu \quad (47)$$

where:

I_z = normalized spectrum of an individual firing, $I_z(\nu) = I(\nu) / \text{std}\{I(\nu)\}$

I_m = mean of all n normalized 152 mm spectra, $I_m(\nu) = \frac{1}{n} \sum_{i=1}^n I_{zi}(\nu)$

w_i = relative spectral response of the i th filter

Integrating over broad bands allowed signatures acquired at different spectral resolutions (e.g., 32 cm^{-1} for 152 mm vs. 16 cm^{-1} for 120 mm) to be compared. This assumes that resolution does not impact in-band intensity, which is generally valid. Subtraction of I_m from all observations makes differences in feature more readily apparent.

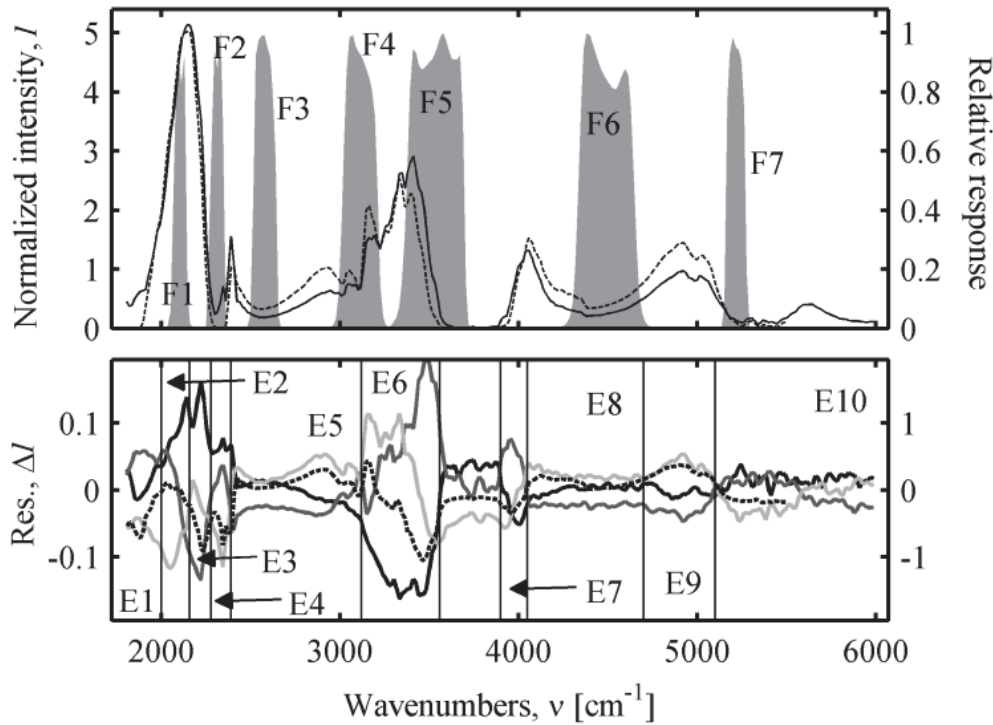


Figure 42. *Upper panel:* Normalized 152 mm howitzer (—) and 120 mm cannon (···) midwave infrared spectra are superimposed on the relative response curves for the F1 – F7 band filters. The howitzer spectrum is the mean of all normalized firing spectra. *Lower panel:* Residuals between the mean normalized howitzer spectrum and the mean normalized Full Charge (—), Charge 1 (—), and Charge 2 (—) spectra are shown on the left ordinate. Residuals between the mean normalized howitzer and normalized cannon spectra (···) are an order of magnitude larger, indicated on the right ordinate. Band edges are shown for E1 – E10 and, except for the near-zero atmospheric transmission region from $3560 - 3900 \text{ cm}^{-1}$, span the spectrum. Each band defines a region where spectral residuals show distinct differences between configurations.

Several ideal, square-band filters are also indicated (E1 – E10). The bands span the observed spectral range (with the exception of the region of near-zero atmospheric transmission, 3560 – 3900 cm^{-1}) and are possible alternatives to F1 – F7. Features based on these square bands were calculated in Equation (47) with zero filter response outside of the band, unity inside, and band edges as shown in Figure 42 (provided in Appendix D). Such bands have previously been used to discriminate explosives and, in that application, were chosen based on a combination of known emission features and a brute-force search that maximized discrimination of two explosive types [18]. The band edges of E1 – E10 were selected where distinct differences between configurations were evident in the residuals.

Feature Correlations

Correlation amongst features indicates redundancy in information. For example, r_{15} , r_{35} , and r_{45} are highly correlated (look ahead to Figure 43), presumably due their dependence on K and Na where a change in one species affects all line ratios. If feature correlations are strong across sensor types, it may be possible to exclude one or more sensors yet still obtain all information conveyed by the features. The square of Pearson's correlation coefficient, r^2 , was calculated between features for which firing signatures were obtained with all instruments. Only features from Charge 2 were assessed in order to ensure that results represented correlation amongst features rather than a potential bias due to changes in feature values across configurations.

A subset of the strongest correlations of the empirical features from different instrument data sets is shown in Figure 43 (upper triangle). Although there were a number of weak correlations ($r^2 = 0.2 - 0.5$), the large number of moderate to strong

correlations suggests that many properties of firing signatures are consistent with respect to one another, despite variations inherent in firing phenomenology. Strong correlations (typical $r^2 = 0.6 - 0.9$) were observed between features from a single sensor, as well as between radiometric emission features from different sensors, e.g. VNIR line ratios and MWIR band-intensities ($r^2 = 0.6 - 0.8$). Correlations between the blast wave model A parameter, VNIR intensity ratios ($r^2 = 0.5 - 0.8$), and MWIR bands (F2, F4, and E5; $r^2 = 0.6 - 0.7$) were moderate. This may indicate a relationship between blast trajectory and radiometric emissions, which is significant because the blast is directly related to thermodynamic flow properties.

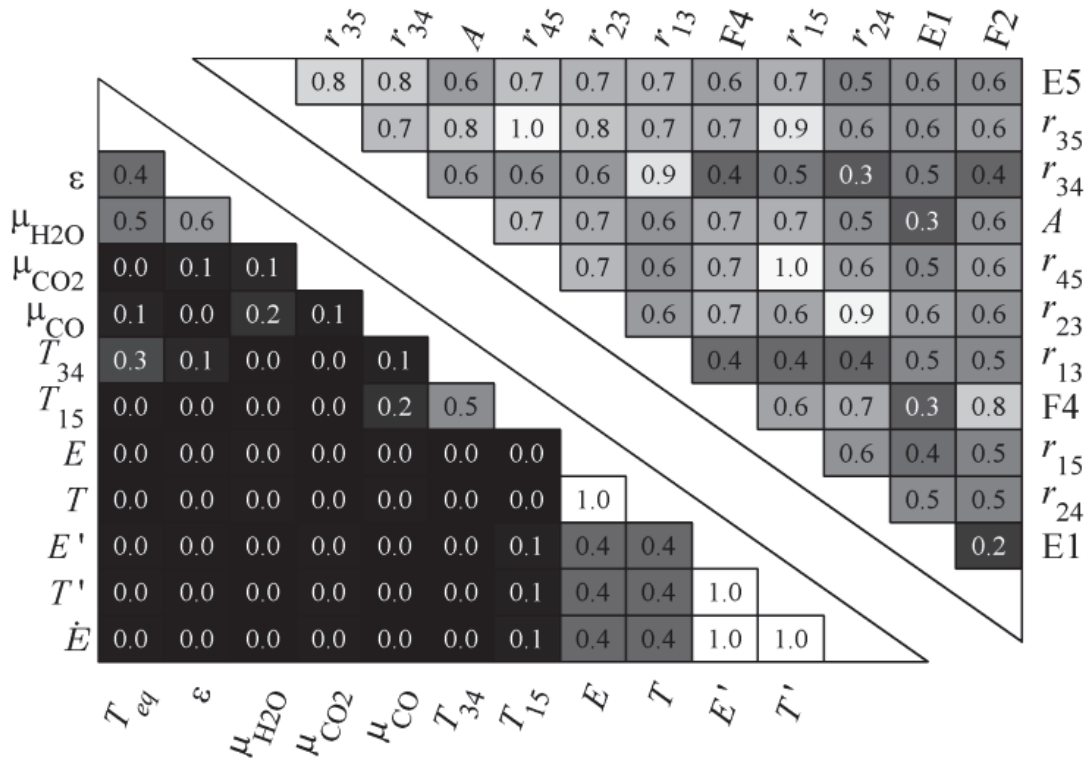


Figure 43. *Upper right:* Correlation matrix containing the twelve empirical features with the largest r^2 values. Strong correlations are evident for features within and across instrument data sets. *Lower left:* Correlation matrix for all phenomenological features. Very few strong correlations are observed, with the exception of blast parameters.

The lower triangle of Figure 43 shows that there were few strong phenomenological correlations ($r^2 > 0.6$), even amongst features from the same instrument. Blast features show the strongest correlation; however, they are all different interpretations of the same fit parameters [108]. Most inter-sensor phenomenological correlations were non-existent and only a very few weak ($r^2 = 0.2 - 0.3$) correlations were observed. Lack of correlation has the potential to be beneficial in that features may provide unique information that can contribute to discrimination, or it can indicate uncertainty or variability that provides no new information. Application of discrimination techniques (to be discussed later) indicates the former, that is, phenomenological features from different sensors provide independent, complementary information.

Figure 44 shows the correlation matrix of empirical and phenomenological features, sorted such that larger correlations are in the lower-left corner, on average. Although empirical and phenomenological features were obtained from the same data, they were derived in different, non-linearly ways; and correlation of the two sets can reveal non-linear relationships that would otherwise not be apparent. Most of the matrix demonstrates a lack of correlation, and those features that are correlated are often from the same sensor data. When correlations are strong, it may be possible to use the phenomenological and empirical features interchangeably; or more significantly, it may be possible to infer phenomenological properties from empirical observation. Strong correlations are observed for blast ($A' \sim T', E', \dot{E}$) and VNIR ($T_{34} \sim r_{34}$) features. Low correlation between MWIR phenomenological features and band-integrated intensities implies additional (orthogonal) information content in the two feature sets which may aid in discrimination.

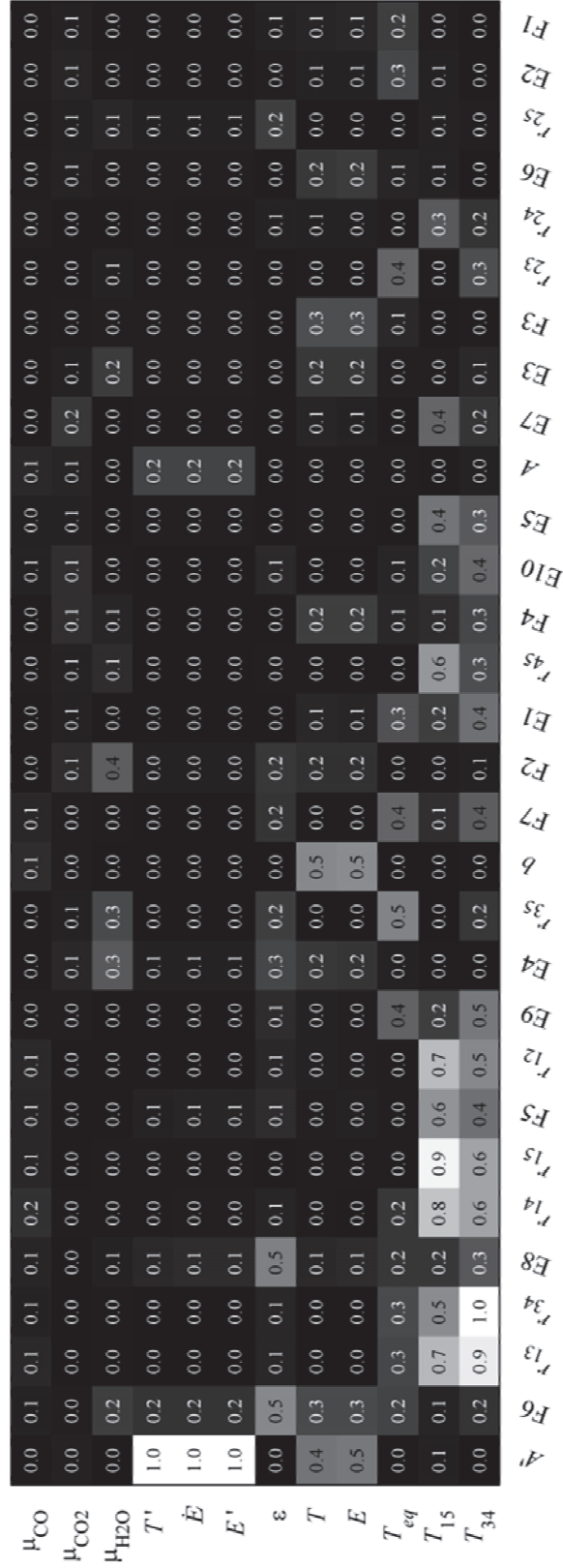


Figure 44. Correlation matrix of all phenomenological and empirical features.

Discussion

The full set of blast, VNIR, and MWIR features was assessed for its ability to discriminate munitions configurations. Because sensor availability and resolution are limited in real-world applications, it is not always possible to obtain all features, and our objectives were: (1) identify the minimum number of features that maximize discrimination potential; (2) determine the feature saliency (importance) and stability of the features; and (3) assess classification accuracy for a subset of the features. Discriminant analysis and forward-selection were used to determine feature saliency and stability [65:238-239], and Bayesian decision theory with Parzen-windows was used for classification [64:20-26, 164-172].

Feature Selection

First, the notation adopted is that there are K distinct classes of munitions or weapons configuration, and that the k th class is observed n_k times. The i th observation $\mathbf{X}_i = [X_{i1} \dots X_{ip}]^T$ is composed of p features (such as those from Table 17 and Table 18). The set of all observations form an $(n = n_1 \dots + n_K) \times p$ sample matrix $\mathbf{X} = [\mathbf{X}_1 \dots \mathbf{X}_n]^T$ whose columns specify the values of a single feature for all observations and each row contains all features of a single observation. In multiple discriminant analysis (MDA), the observations are projected into a subspace $\mathbf{Y} = [\mathbf{Y}_1 \dots \mathbf{Y}_n]^T$ of $\min(p, K - 1)$ dimensions in which classes are optimally separated [64:121-124; 65:400-407]. Projection into the j th dimension of the subspace $\mathbf{Y}_j = \mathbf{X}\mathbf{b}_j$ is a linear combinations of the original p features weighted by $\mathbf{b}_j = [b_{j1} \dots b_{jp}]^T$. Weight vectors are found by maximizing the quantity:

$$\lambda = \frac{\mathbf{b}^T \mathbf{B} \mathbf{b}}{\mathbf{b}^T \mathbf{W} \mathbf{b}} \quad (48)$$

where \mathbf{B} is the between-class sums-of-squares (SS) matrix and \mathbf{W} is the within-class SS matrix. $\mathbf{W} = \mathbf{W}_1 + \dots \mathbf{W}_K$ is a quantification of the variance in the K classes and the within-class SS matrix for the k th individual class is:

$$\mathbf{W}_k = \sum_{i=1}^{n_k} (\mathbf{X}_{ki} - \underline{\mathbf{x}}_k)(\mathbf{X}_{ki} - \underline{\mathbf{x}}_k)^T \quad (49)$$

having class centroid $\underline{\mathbf{x}}_k = [\underline{x}_1 \dots \underline{x}_p]^T$. $\mathbf{B} = \mathbf{T} - \mathbf{W}$ is the difference between within-class variance and total variance:

$$\mathbf{T} = \sum_{k=1}^K \sum_{i=1}^{n_k} (\mathbf{X}_{ki} - \underline{\mathbf{x}})(\mathbf{X}_{ki} - \underline{\mathbf{x}})^T \quad (50)$$

where $\underline{\mathbf{x}}$ is the grand centroid of the p features for all n observations.

It should be apparent from the definitions of \mathbf{W} and \mathbf{B} that Equation (48) is a ratio of between-class to within-class variance of the projections. Its maximum is obtained by taking the derivative with respect to \mathbf{b} and rearranging to the form:

$$(\mathbf{W}^{-1}\mathbf{B} - \lambda\mathbf{I})\mathbf{b} = 0 \quad (51)$$

This is an eigenvalue problem where λ is the eigenvalue corresponding to eigenvector \mathbf{b} and \mathbf{I} is the identity matrix. There are p eigenvalue-eigenvector pairs (because \mathbf{W} and \mathbf{B} are both $p \times p$), but there are only $\min(p, K - 1)$ non-zero eigenvalues. Because λ is also the ratio of the between-class to within-class variance, the relative separation of classes obtained by the j th projection $\mathbf{Y}_j = \mathbf{X}\mathbf{b}_j$ is proportional to λ_j ; the eigenvectors corresponding to $\lambda = 0$ do not contribute to class separation and may be discarded. The sum $\Lambda = \lambda_1 + \dots \lambda_{\min(p, K - 1)}$ is a metric that describes the total between-class to within-class separation across all dimensions of the subspace \mathbf{Y} .

In this context, each howitzer munition was a class, and there were $K = 3$ classes with $p = 42$ features (from Table 17 and Table 18). Suppressed munitions were excluded because of the dimness of their radiometric emissions. Of the $n = 25$ observed firings, there were $n_0 = 4$ Full Charge, $n_1 = 5$ Charge 1, and $n_2 = 16$ Charge 2. These yield $K - 1 = 2$ discrimination dimensions and a maximum separation of $\Lambda = \lambda_1 + \lambda_2$ between classes.

Empirical and phenomenological features were initially examined separately to determine if either was preferential for munitions discrimination. The phenomenological and empirical sets contained $p = 12$ and $p = 30$ features, respectively. Saliency was determined with a forward-selection procedure. Equations (48 – 51) were solved for each individual feature and the one with the largest value of Λ was identified. Additional features were included, one at a time, such that class separation was maximized. This required iteratively solving Equations (48 – 51) for the addition of each individual feature and identifying which increased Λ the most. The order in which features maximized Λ identified their saliencies, i.e. the first $q \leq p$ features are the most salient individual features for maximizing between-class to within-class separation.

Stability of the features is defined as the fraction of the iterations in which a given feature had the specified saliency or better. It is a characterization of how consistently a feature contributes to class separation. Note that if $q \leq 2$ features are used then MDA is not necessary because \mathbf{Y} is merely a rotation of \mathbf{X} . As the number of features increases, the subspace is defined by linear combinations of the q features. This improves class separation but often introduces instability, especially if features are correlated.

Classification

Classification accuracy for the most salient features was determined by testing with a leave-one-out procedure [64:472-475]. The discriminant weights \mathbf{b} and subspace \mathbf{Y} were trained according to Equations (48 – 51) using only $n - 1$ of n observations. The left-out observation was then projected into the subspace (using the weights determined in training) and assigned to the class with the largest posterior probability. The procedure was repeated until all n observations were left-out once, and the class assignment of each left-out observation was compared to its true class to determine the fraction that were correct, termed classification accuracy (CA). The procedure was first performed using only the single most salient feature, and then repeated by iteratively adding the next most salient feature until CA was determined for all dimensionalities from $q = 1$ to $q = p$. CA characterizes how well discrimination performs on a new (untrained) observation and Λ quantizes the separation of classes for all trained observations.

Classification followed Bayes' formula for the posterior probability that an observation belongs to the k th class [64:20-26]:

$$P(k | z) = \frac{p(z | k)P(k)}{p(z)} \quad (52)$$

where $p(z | k)$ is the class-conditional probability density, $p(z)$ is the unconditional probability density (i.e. sum over all class-conditional probability densities), and z is any continuous feature dimension or space. $P(k)$ is the prior probability of an observation belonging to the k th class and was assumed to be equal for each class. Discrimination of 152 mm howitzer munitions occurred in a subspace of $K - 1 = 2$ and the posterior probability is a function of multi-dimensional class-conditional probabilities, $p(\mathbf{z} | k)$.

Class-conditional probability densities are unknown but were estimated from observations using the Parzen-window method [64:164-172]. A multivariate normal distribution (kernel) was centered on each observation in the multi-dimensional space, \mathbf{z} . Kernel width is a heuristic parameter; in this work the width in each dimension was set equal to the standard deviation of feature values (in the dimension) for all observations of an individual class. The multi-dimensional class-conditional probability densities for each class, $p(\mathbf{z} | k)$, were obtained by summing the kernels of all observations of the k th class ($k = 1,2,3$) and normalizing by the number of kernels. This maintained unit total probability. Figure 45 and Figure 46 depict $p(\mathbf{z} | k)$ for each 152 mm howitzer class where the $q = 4$ most salient features were projected into the discriminant subspace $\mathbf{z} = \mathbf{Y}$ for both phenomenological and empirical features sets. Given a new observation, its location in \mathbf{z} determines for which class $P(k | \mathbf{z})$ is largest and to which class it is assigned.

Munitions Discrimination

Figure 47 and Figure 48 depict the saliency and stability of the most important phenomenological and empirical features for discriminating amongst 152 mm howitzer munitions. T and T' were identified as the most salient phenomenological features and subsequently excluded because their derivation included knowledge of propellant mass. The three next most salient (and stable) phenomenological features were T_{34} , E , and T_{eq} . Each feature is from a different sensor, indicating that they provide complementary information for discrimination, which may explain their lack of correlation. High stability implies that the features were consistently important discriminators and were relatively insensitive to random effects in the data (such as noise or signature variability).

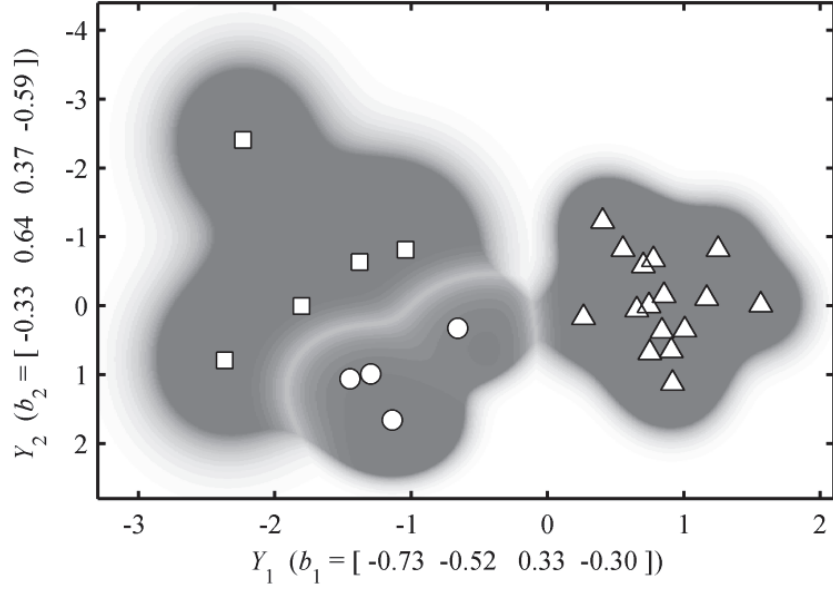


Figure 45. Class-conditional probability densities are shown for a discriminant subspace composed of the four most salient phenomenological features (T_{34} , E , T_{eq} , and μ_{CO}). Class probabilities are indicated by shading from gray (100%) through white (probabilities approach zero or equal values for two or more classes). Observations of Full Charge (\circ), Charge 1 (\square), and Charge 2 (Δ) projected into the subspace have class separation $\Lambda = 10.9$.

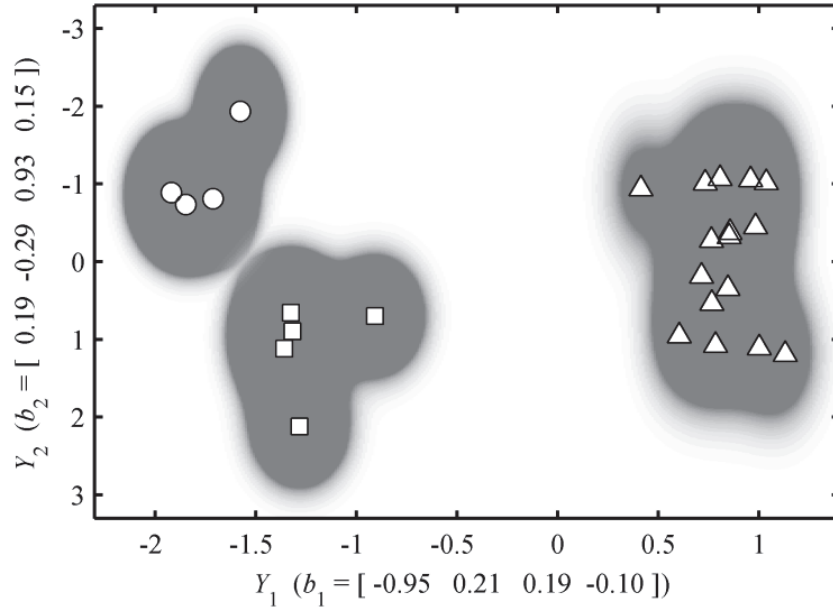


Figure 46. Class-conditional probability densities are shown for a discriminant subspace composed of the four most salient empirical features (R_{35} , F6, E6, and A'). Class probabilities are indicated by shading from gray (100%) through white (probabilities approach zero or equal values for two or more classes). Observations of Full Charge (\circ), Charge 1 (\square), and Charge 2 (Δ) projected into the subspace have class separation $\Lambda = 48.3$.

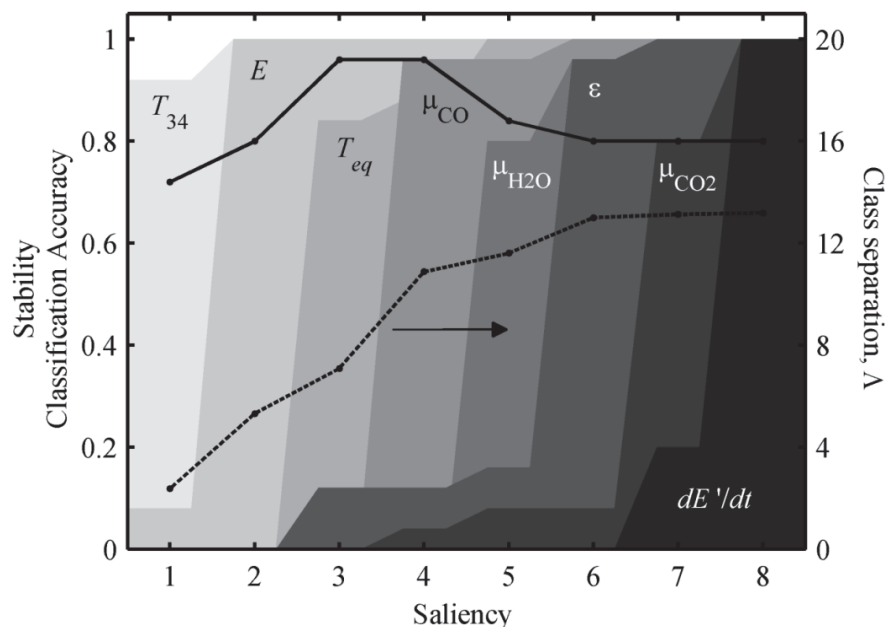


Figure 47. The most salient phenomenological features are indicated. Shading depicts stability (left ordinate) and shows the fraction of times each feature has the indicated saliency or better. Classification accuracy (—) for each number of discrimination features is also shown on the left ordinate. Class separation (···) is shown on the right ordinate and increases as dimensionality increases.

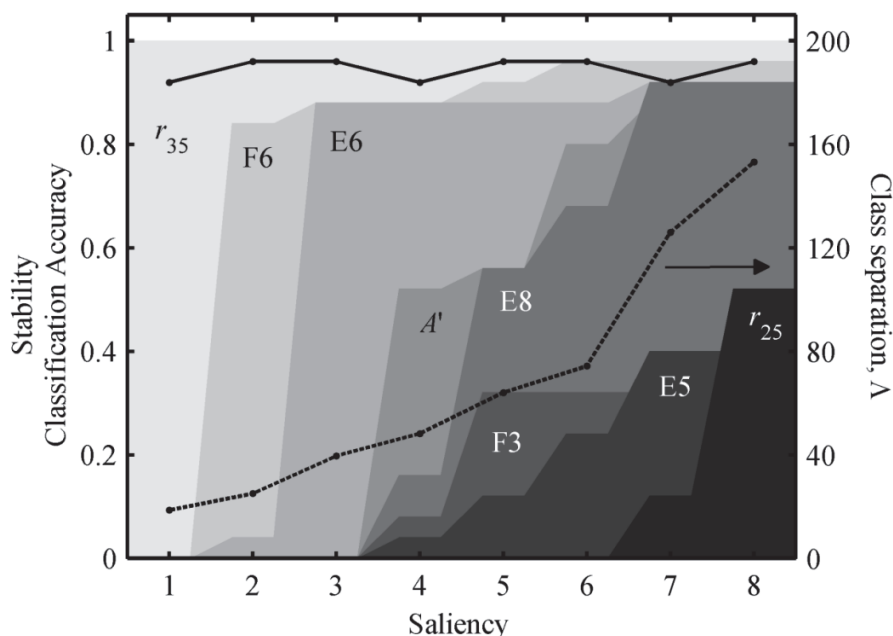


Figure 48. The most salient empirical features are indicated. Shading depicts stability (left ordinate) and shows the fraction of times each feature has the indicated saliency or better. Classification accuracy (—) for each number of discrimination features is also shown on the left ordinate. Class separation (···) is shown on the right ordinate and increases as dimensionality increases.

The most salient empirical feature is the potassium to sodium intensity ratio, followed almost exclusively by MWIR band features. Blast features are not unimportant, but they do not contribute as significantly as VNIR and MWIR emissions. Stability decreases quickly after the first $q = 3$ features, likely because the features are correlated and were substituted for one another during the MDA iterations in feature selection.

Classification accuracy and class separation as a function of number of features (from most to least salient) are also shown in Figure 47 and Figure 48. Class separations are an order of magnitude greater with empirical than phenomenological features. This is illustrated by the class distributions in Figure 45 and Figure 46 for the $q = 4$ most salient features. Phenomenological CA increased from 80% to 96% as up to four features were included but then decreased, likely due to overtraining of the discriminant subspace for small class separations. For empirical features, class separation continued to increase as features were added, resulting in a consistent 92% – 96% CA regardless of dimensionality. Both CA and Λ metrics indicate that the empirical features were superior discriminators.

As stated previously, correlated features provide redundant information and it may be possible to use them interchangeably. This was not explored thoroughly, but a few cases were examined. The three most salient phenomenological features (T_{34} , E , T_{eq}) demonstrated a 96% CA and $\Lambda = 7.1$. Substituting the three most correlated empirical features from the same sensor (r_{34} , b , F7) results in reduced CA (68%) and Λ (5.5). Correlation between T_{34} and r_{34} is nearly complete ($r^2 = 0.995$); however, lower correlation of E with b ($r^2 = 0.53$) and T_{eq} with F7 ($r^2 = 0.39$) implies loss of information that may be responsible for the reduced performance.

When additional correlated, empirical features are included in the substitution ($E \sim A'$ with $r^2 = 0.45$; and $T_{eq} \sim E9$ with $r^2 = 0.36$), separation of training observations is restored ($\Lambda = 7.1$) but discrimination of leave-one-out test observations remains inferior (72% CA). However, when only r_{34} is substituted for T_{34} , CA remains at 96% and separation is only slightly reduced ($\Lambda = 6.3$). The results suggest that only strongly correlated features may be substituted, but a single case is not conclusive and further study is needed.

For completeness, the combined set of phenomenological and empirical features were trained and tested. The most salient features were a combination of phenomenological and empirical, and more importantly, the two most salient features (r_{35} and T_{eq}) were found to be complementary. This is evident in that for $q = 2$, $\Lambda = 27.6$ for the combination versus $\Lambda = 25.1$ for purely empirical or $\Lambda = 5.3$ for purely phenomenological features. However, as the number of features was increased above $q = 3$, separation and classification accuracy was consistently highest when using only empirical features. Phenomenological features introduce an instability as dimensionality increases, indicating that empirical features should be used.

Weapons Discrimination

High classification accuracies and class separations were obtained when discriminating munitions from the 152 mm howitzer. Because the munitions are very similar, discrimination between different weapons has a high likelihood of success. The basis for this statement is that discriminating munitions from a single weapon relies on differences between the munitions (typically the propellant), whereas firing signatures from different guns are affected by both munitions and weapon properties. This is

observable in Figure 41 and Figure 42 where the differences in spectral structure between the 152 mm howitzer and 120 mm cannon are apparent. Because only a single firing of the 120 mm cannon was observed, leave-one-out training and testing could not be performed. However, separation between classes is also an indicator of how well classification is likely to perform. The cannon's observation \mathbf{X}_t was used to test discriminators trained using $n = 25$ howitzer observations for several sets of MWIR features.

The value of Λ describes the separation of howitzer munition classes that were used to train the discriminator. Mahalanobis distance D is used to quantify the separation between weapons in discriminant space. Its square is analogous to Λ in that it is a measure of difference normalized by variance, except that it normalizes by unequal covariance across multiple dimensions [65:367]. Due to the way subspaces are constructed in MDA, the grand centroid of training data is located at the subspace origin in any projection. Thus the mean separation between training (howitzer) and test (cannon) observations in the discriminant subspace is the location of the test observation after projection into the subspace. The covariance matrix \mathbf{S} is estimated from the training data, and the resulting separation between weapons is $D^2 = (\mathbf{X}_t \mathbf{b}) \mathbf{S}^{-1} (\mathbf{X}_t \mathbf{b})^T$.

Figure 49 shows the location of the cannon observation and class-conditional probabilities for howitzer munitions in a subspace trained using all howitzer observation band features (F1 – F7 and E1 – E10). The 120 mm observation is significantly separated from the 152 mm munitions ($D^2 = 46.6$), which are themselves well separated from one another ($\Lambda = 76.4$). It may be counterintuitive that $D^2 < \Lambda$ even though the weapons are separated more than the munitions; this results because Λ is normalized by within-class

variance (which is minimized with large number of features), whereas D^2 is normalized by total variance (which increases with large numbers of features). The results observed in the figure confirm that different weapons are more easily distinguished than munitions from a single weapon.

The two most salient square-band features (E7 and E2) result in a reduced, yet still significant, ability to differentiate munitions and weapons ($\Lambda = 3.7$ and $D^2 = 14.3$). Separation is improved with the use of phenomenological features (ϵ_s and μ_{H_2O} , $\Lambda = 7.2$ and $D^2 = 26.6$), which may imply phenomenological differences in the firing signatures for the two guns. Class separation did not increase significantly with more than two phenomenological features, yet it continued to increase when additional band features

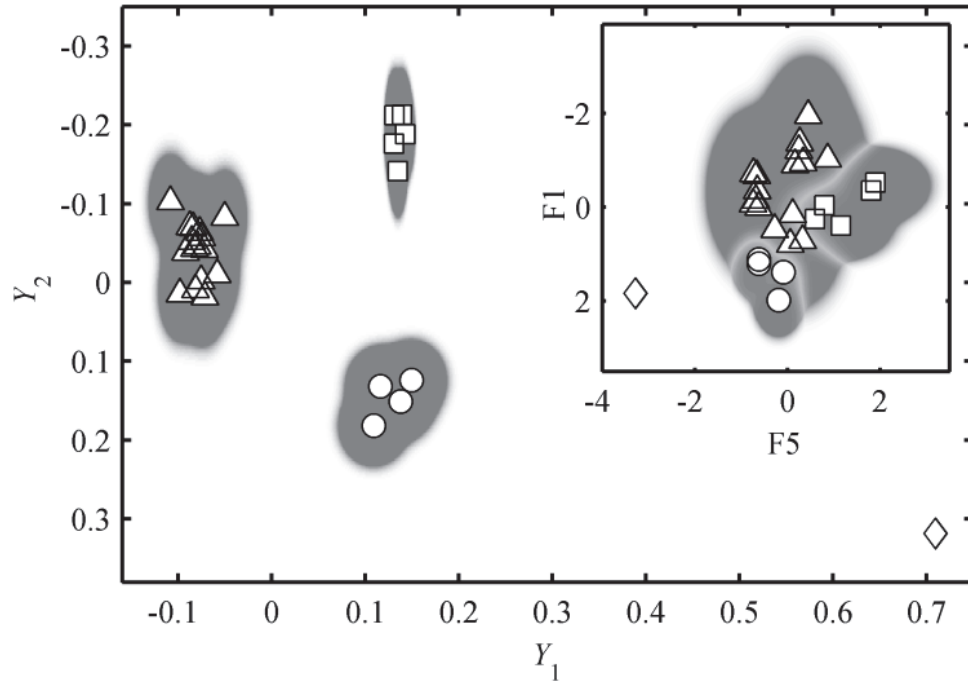


Figure 49. Class-conditional probability densities are indicated by shading from gray (100%) through white (probabilities approach zero or equal values for two or more classes). Observations of 152 mm howitzer Full Charge (○), Charge 1 (□), Charge 2 (Δ), and 120 mm cannon (◇) are overlaid. Y_1 and Y_2 are the dimensions of a subspace composed of all MWIR band features, characterized by $\Lambda = 76.4$ and $D^2 = 46.6$. *Inset:* Feature space of filter bands F5 and F1.

were projected into discriminant space. When all phenomenological and empirical MWIR features were used together, bands were the most salient (E7, E3, F3, E3 ...) and phenomenological features did not become important until more than ten bands had been included.

The inset in Figure 49 depicts the distributions in a subspace of the two most salient filter features (F1 and F5). These show that the two weapons can be easily discriminated using only a single feature (F5), but if a second feature (F2) is also used, class separation is improved ($D^2 = 15.7$). Howitzer munitions are separated to a lesser degree ($\Lambda = 2.8$). The significance of both cases is that F1 and F5 represent real-world filters, suggesting significant potential for classification using realistic, demonstrated sensor designs.

Summary

Gun firing signatures, to include muzzle blast and combustion emissions spanning the visible and infrared, have demonstrated a definite ability to discriminate between weapon configurations. Different guns (152 mm howitzer and 120 mm cannon) were well separated in low-dimensional MWIR features spaces and could be distinguished using a single filter band near 3500 cm^{-1} (F5). Separation was improved with a second band near 2100 cm^{-1} (F1, $D^2 = 15.7$). Guns were also well-separated with square-band filters from $2000 - 2160\text{ cm}^{-1}$ and $3900 - 4050\text{ cm}^{-1}$ (E7 and E2, $D^2 = 14.3$), or physics-based soot emissivity and water concentration model parameters ($D^2 = 26.6$).

Despite their similarity, munitions from a single gun were discriminated with 96% leave-one-out classification accuracy using only three phenomenological (atomic potassium excitation temperature, blast wave energy, and equilibrium combustion

temperature) or empirical (atomic potassium to sodium excitation ratios, filter near 4500 cm^{-1} , and square-band from 3120 – 3560 cm^{-1}) features. Empirical features demonstrated stable classification accuracy (92 – 96%) for any number of discrimination features, and class separations ($\Lambda = 18.6 - 153.2$) were consistently an order of magnitude greater than with phenomenological features ($\Lambda = 2.4 - 13.2$). VNIR and MWIR emissions consistently provided the most salient discrimination features.

In real-world applications, all firing signatures may not be available when large numbers of sensors are impractical due to logistics or resources. This is particularly true of those that require a high-degree of temporal, spatial or spectral resolution. However, a considerable amount of the information content in the observed features was found to be redundant, and the existence of correlations may allow information on unobserved features to be inferred from those that can be obtained. Potassium and sodium intensity ratios were nearly perfectly correlated ($r^2 = 0.9 - 1.0$), and they also exhibited strong correlations ($r^2 = 0.6 - 0.8$) with MWIR band features. Blast features were moderately correlated ($r^2 = 0.5 - 0.8$) to VNIR and MWIR features. Examination of a single case found that very strongly correlated features could be substituted without reducing classification accuracy. Additional study is necessary before identifying whether the correlation relationships are causal, dependent on underlying phenomena or properties of the munitions, or simply coincidental.

The phenomenological interpretation of signatures used was not optimal, and other interpretations may improve discrimination. The advantage of phenomenological features is that they provide information on the munitions that empirical features do not (such as temperature, hydrogen-to-carbon ratio, soot content, etc.) and can be used to further

characterize a firing signature after discrimination. As the phenomenology of firing signatures is further studied and understood, it will become increasingly possible to distinguish weapons from one another, and perhaps even infer phenomenological information from correlated, more easily obtained empirical features.

VIII. Conclusion

The face of warfare was markedly changed in the 20th century with technological advancements to both weapon systems and remote sensing platforms. Innovations to gun weapons have allowed for increased range, improved accuracy, and faster rates of fire. Initially, guns served strictly as offensive instruments, and aside from acoustic signatures (or flash at night) that alerted combatants of enemy presence, gun firing did little to help develop defensive strategies or provide intelligence. Advances in sensing technology have begun to change that. Several systems have been developed to localize weapon fire using their acoustic or broadband flash signature, and use of the remaining signature content (such as spectroscopic) shows potential to provide an even greater characterization of the battlespace.

Prior to this work, many aspects of gun firing signatures were poorly understood. This is particularly true of large caliber guns, due to the impracticality of firing such weapons in a laboratory environment and the difficulty associated with experimental characterization in the field. Battlespace classification is one obvious application that benefits from an improved understanding of gun firing blast and flash signatures. Advances in data collection, characterization, and differentiation of signatures from various types of high explosives have recently been demonstrated by the AFIT RSG. The work presented here is the successful culmination of the next step in extending classification efforts beyond explosives and to a new class of previously uncharacterized battlespace events, i.e. gun firing.

The prominent, remotely detectable firing signature that results from muzzle flow is the muzzle blast. Flow phenomenology has been extensively studied but has primarily relied on measurement of small arms firing in a laboratory environment. Properties of the blast are often extrapolated to large caliber guns. The few studies of muzzle blast that include large caliber gun firings have reported only one or a handful of observations. These have served to verify scaling of average properties, but they lack a characterization of variation in the blast properties. This has hitherto precluded assessment of blast signatures for battlespace classification and is addressed in the work presented here.

Muzzle flash spectral signatures have received even less attention. Occurrence of muzzle flash has been studied and research has focused on flash suppression, but characterization of the signatures themselves is lacking. The most recent published spectra are from the mid-1970s and were collected with photographic film and manually converted to spectral intensity plots. Hence, spectral characterization has been highly qualitative and not amenable to simulation, modeling, or classification. More recent characterization of flash has used broadband visible and infrared imagery to successfully locate the source of weapon fire. The spectral content of flash signatures is far richer than band-integrated radiometry and has the potential to reveal far more than just the gun's location, yet only now has this been studied.

Muzzle Flash

Foremost, this work represents the first modern characterization of muzzle flash spectra. Visible and near infrared (VNIR, 450 – 850 nm) spectra are reported at ~0.75 nm resolution, sufficient to identify fine structure of many atomic lines. Strong secondary

combustion emissions have 50 – 100 ms duration and consist of atomic and molecular emission features involving K, Na, Li, Cu, and Ca superimposed on continuum. Non-equilibrium potassium excitation concentrations are characterized by Boltzmann temperatures in the range 7,921 – 8,945 K and imply collisional or reactive excitation.

The potassium D1 and D2 lines are the most prominent features in the VNIR, exhibiting extreme broadening such that the entire O₂ (X→b) absorption band is evident in the blue wing. A radiative transfer model was used to demonstrate that broadening likely results from self-absorption, characterized by realistic values of $5.1 \times 10^{18} \text{ cm}^{-3}$ potassium concentration, ~2200 K temperature, and 3.9 m plume depth. The O₂ and K profiles are improved with an empirical model, with which range to target can be estimated to within 4 – 9% for individual firings and to within ~0.5% with multiple observations. The ability to use muzzle flash spectra for monocular passive ranging was unexpected, yet it is a welcome potential battlespace application.

Time-resolved, midwave infrared (MWIR, 1800 – 6000 cm⁻¹) spectra were collected at 32 cm⁻¹ spectral and 100 Hz temporal resolutions for both secondary combustion and flash-suppressed muzzle plumes. Flow from the gun muzzle is initially non-combusting, and post-expansion plumes are characterized by initial temperatures in the range 1000 ~ 1200 K. The blackbody distribution peaks in the MWIR at these temperatures. While not muzzle flash by the conventional definition, emissions from thermally excited selective emitters (primarily H₂O and CO) and particulate matter comprise an infrared signature that may be remotely detected for ~20 ms after gun firing.

Muzzle plumes typically re-ignite if temperatures are above 900 – 1000 K for unsuppressed munitions or 1100 – 1200 K for propellants containing chemical flash-

suppressant. Combustion often occurs in unsuppressed plumes ~10 ms after gun firing and raises the average temperature to near ~1400 K. Median spectral emissions are a factor of ten more intense than in non-combusting plumes. Radiation is dominated by ro-vibrational H₂O and CO₂ band emissions that persist upwards of 100 ms after gun firing. Peak spectral emissions occur in the 2200 – 2250 cm⁻¹ band and are 50% more intense than any other region.

Plume emissions are quantified using low dimensional empirical and phenomenological models. Model parameters indicate that non-combusting plumes have a strong graybody component (~0.36 emissivity) and 850 – 1050 K temperatures that rapidly decay with 13 – 21 s⁻¹ rates. Soot and particulates are quickly consumed in combusting plumes, lowering emissivity to ~0.07 within 20 ms after gun firing. Maximum model temperatures are 1200 – 1600 K, coincident with peak band-integrated intensity approximately ~20 ms after gun firing. Cooling occurs more slowly than in non-combusting plumes with 4 – 6 s⁻¹ decay rates. The difference in rates is attributable to 2.5 ~ 5 MJ/kg heat released in combustion which can be estimated from the plumes' temperature dynamics.

Muzzle Blast

This work has also quantified the properties and variability of muzzle blasts from a large caliber gun and demonstrated its potential as a firing signature. High-speed, 1600 Hz imagery was used to observe the expansion of the blast front. Muzzle blasts initially expand with Mach 3 – 4 velocities and detach from the flow at approximately 0.7 – 0.95 ms after gun firing. The blast approaches to within 95% spherical geometry in the same

timeframe (0.77 – 0.91 ms) with a corresponding radius of 0.98 – 1.25 m and Mach velocity 2.3 ~ 2.5. Its velocity approaches near-acoustic after propagating 2.6 – 3.3 m from the gun. The decay to acoustic is 30 – 50% sooner than the thermochemistry theoretical maximum. Blast expansion trajectories may be approximated by several models of 1 – 4 parameters in the mid-field or 3 – 4 parameters through the far-field. Drag model stopping distance of 1.5 ~ 2.3 m is correlated with the maximum muzzle plume expansion and projected area of 35 – 40 m².

The trajectory can be best represented (average error less than 10 cm) by a spherical geometry, modified point blast model. Point blast rate exponent ($b \approx 3/5$, $s \approx 1$) indicates nearly constant rate of energy deposition into the blast, consistent with continual muzzle flow during the blast-flow interaction timeframe. A method for estimating the rate of energy deposition by partitioning energy between the projectile, blast, and muzzle gases was developed. Deposition rates of 2300 ~ 3600 MJ/s were observed and scale with propellant mass. Total blast energies are 1.6 – 3.9 MJ, dependent on charge mass. A blast efficiency term was defined as the fraction of energy in the blast relative to that in the flow. Efficiencies of 18 – 24% were calculated, and larger masses were found to have the largest efficiency (22 – 24%). The remaining energy resides in the muzzle gases and contributes to plume heating. Pre-combustion temperatures of 980 – 1210 K were estimated and class-average temperatures were correlated with likelihood of secondary combustion. The link between the blast trajectory and thermodynamic properties of the gun firing emphasize the blast's potential to provide information about a weapon.

Variability in the blast trajectory was assessed using 147 firings, representing the largest set of large caliber firing observations in the published literature. Properties are

reproducible for distinct munitions configurations and only appear to trend with propellant mass or energy. At early times (less than 1 – 3 ms) blast expansion velocities are fairly uniform, characterized by ≤ 20 cm variance. At later times, the variation is ± 50 cm from the mean trajectory of each configuration. In context of the point blast trajectory model parameters, standard variation is less than 5%. The differences between configurations are $\sim 32\%$ greater than variation for firings of each configuration type, suggesting moderate ability to distinguish amongst similar firings from a single weapon.

Battlespace Classification

The capstone of this work is the demonstration of the ability to apply battlefield classification to gun firing signatures. Not only can different weapons be differentiated (120 mm cannon and 152 mm howitzer), but even Full Charge, Charge 1, and Charge 2 munitions fired from the 152 mm howitzer can be classified with 96% accuracy using only 2 – 3 relevant features.

Reduction of blast and flash signatures resulted in thirty empirical features comprised of blast trajectory model parameters, atomic line ratios, and band-integrated intensities. Multiple discriminant analysis identified that the atomic K to Na intensity ratio is the most salient empirical feature, providing a 92% classification accuracy (CA) and 18.6 class separation (between-class to within-class variance ratio). Including the next two most salient empirical features (filter band-integrated intensity near 4500 cm^{-1} and square-band from $3120 - 3560\text{ cm}^{-1}$) yielded a consistent 96% CA and improved 39.6 class separation. Such features are obtained directly from observed radiometry, which simplifies feature extraction for battlespace classification.

Interpretation of signature data provides additional, orthogonal information content such as blast energetics, plume temperature and emissivity, excitation ratios, and species concentrations. Of twelve phenomenological features, at least three are required to achieve 96% CA. These were identified as the atomic K excitation temperature, blast wave energy, and equilibrium combustion temperature. The features span signature data that includes blast trajectory and visible through MWIR spectra, yet produce only 7.1 class separation. The relatively lower class separation and need for features from all three sensors suggests that the features are not optimal for classification. However, after classification has been performed with other more salient features, these features can be used for characterization of weapon properties (such as estimating plume temperature, species concentrations, etc.).

The most relevant objective of battlespace classification is discriminating amongst different weapons. Limited MWIR data were available on a firing of a 120 mm cannon and were used to assess how well the extracted features could differentiate it from the 152 mm howitzer. Only two band-integrated intensity features, F1 and F5 (centered near 2100 cm^{-1} and 4000 cm^{-1}), were needed to significantly separate the two guns, characterized by a 15.7 class separation. That the two weapons are well-separated by a discriminator based only on howitzer data indicates that there are distinct differences in firing signatures between the two weapons (and likely other weapons too). That the discriminating features are based on real-world radiometric filters suggests that implementation in a battlespace characterization system is not only feasible, but may be possible in the near-term.

Future Efforts

While this work provides the most complete description of 152 mm howitzer firing signatures available to date, the results are not exhaustive. The quantity of data collected from the 152 mm howitzer firings was sufficiently large to allow only approximately one-third of the data to be analyzed within the scope of this research. Ostensibly, the most relevant and highest fidelity one-third was used, however, two other instrumentation teams also deployed on the field test to observe firing signatures and data from their spectrometers, radiometers, and imagers may reveal additional firings features that were not apparent from the AFIT observation location. Specifically, correlating their high speed, 200 – 2000 Hz MWIR radiometer data with infrared imagery and the ~100 Hz MWIR spectra presented in Chapter VI may provide additional insight into the radiometric and temperature dynamics of combusting muzzle plumes.

It is also likely that the results of this work are the most complete, general description of artillery signatures available, and the data presented here may serve as approximations for similar large caliber guns whose signatures are not available. However, there are differences between firing signatures for different weapons, as confirmed by the class separation between 120 mm cannon and 152 mm howitzer munitions. These differences should be investigated to develop an understanding of which aspects of gun firing can be effectively used for battlespace classification. Additional field tests are needed to collect firing signatures from a wider range of gun weapons, and the tests should include a sufficient number of firings such that signature variability can be established and robust classification methods can be applied. Ideally, at

least 30 firings for which all sensors acquire good data should be observed, per weapon and munitions configuration.

The focus of this work was characterization of gun firing signatures with the objective of battlespace classification, not phenomenological modeling. However, models were used and deficiencies identified. The lesser saliency of phenomenological features suggests that signature data is not optimally interpreted, and improving the models to accurately represent gun firing signatures should provide improved features for classification. In particular, a model that was recently developed for high explosives was used to simulate the muzzle flash MWIR spectrum, with marginal results. A modest attempt was made to improve the results by generalizing the model, but greater gains may be made by exploring other approaches. Similarly, potassium broadening was demonstrated by self-absorption but an empirical model was used for passive ranging. If self-absorption can instead be modeled to a high degree of fidelity, it may be possible to obtain both range to target and a quantification of potassium content. The latter is dependent on munitions properties and may provide additional information on the weapon type or origin.

Finally, while the results presented here are significant in that they fill a gap in the existing knowledge of muzzle flash spectra and blast variability, they also importantly identify which features may be the most relevant and easily identifiable for battlespace characterization of gun weapons. This work foreshadows the fidelity with which classification of battlespace events may be accomplished, particularly with an instrument designed for such a purpose, and the results should be considered in any future sensor designs aimed at improving battlespace awareness.

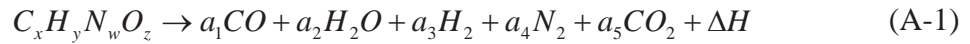
Appendix A. Propellant, Muzzle Gas, and Plume Thermochemistry

Propellants, muzzle gas, and plume chemical and thermodynamic properties were provided throughout Chapters III – VI. These are consolidated here and presented with limited explanation. Properties of the solid (unburned) propellant are given in Table 19.

Table 19. Propellant properties

Property (per kilogram propellant)			Full Charge Supp.		Charge 1 Supp.		Charge 2
Mass	m_c	[kg]	9.14	8.85	7.80	7.52	4.24
Specific enthalpy	Δh_f^0	[MJ/kg]	-2.23	-2.13	-2.22	-2.11	-2.01
Heat of formation	ΔH_f^0	[MJ]	-20.4	-18.9	-17.3	-15.9	-8.5
H:C Ratio	R		1.25	1.25	1.24	1.24	1.14
Oxygen balance			-47.3%	-48.9%	-46.8%	-48.7%	-34.3%
Atomic composition [mol/kg]							
Carbon	C		24.28	24.63	24.19	24.59	22.55
Hydrogen	H		30.24	30.66	30.08	30.57	25.74
Nitrogen	N		9.21	9.35	9.18	9.34	9.39
Oxygen	O		33.37	33.50	33.32	33.46	34.87
Sulfur	S		0.13	0.05	0.15	0.06	0.12
Potassium	K		0.28	0.12	0.33	0.15	0.26

Burning of propellant is complex but may be simply expressed for carbon, hydrogen, nitrogen, and oxygen (CHNO) by the stoichiometry reaction:



Propellant is converted to molecules of lower internal energy accompanied by an exothermic release of energy equal to the change in enthalpy from reactant to products.

The 152 mm howitzer propellants are fuel-rich and under-oxidized. All available oxygen is consumed prior to shot exit and burning stops interior to the gun. Kistiakowsky and Wilson developed a set of rules (K-W rules) describing the hierarchy of under-oxidized combustion products [76:78]:

1. Carbon is converted to carbon monoxide ($C \rightarrow CO$)
2. Hydrogen is converted to water ($H \rightarrow H_2O$)
3. Carbon monoxide is oxidized to carbon dioxide ($CO \rightarrow CO_2$)
4. Nitrogen forms nitrogen gas ($N \rightarrow N_2$)

The rules typically apply to explosives with oxygen balance greater than -40%. A modified set of rules in which water is preferentially produced over carbon monoxide should be used when oxygen is more deficient [54:22; 76:78-81]; however, equilibrium chemistry calculations (look ahead to Table 21) are in better agreement with the unmodified rules.

Properties of an ideal firing in which the propellant burns interior to the gun and according to the K-W rules are shown in Table 20. Species containing sulfur or potassium account for less than 1% (by mole) of the products and are neglected in Reaction (A-1). The energy released in deflagration of the propellant:

$$\Delta H_d = \Delta H_f^0 - \Delta H_f^d = m_c (\Delta h_f^0 - \Delta h_f^d) \quad (A-2)$$

is equal to the change in enthalpies from propellant to gaseous propellant combustion products. Specific enthalpies were calculated using values of heats of formation at 300 K from the JANAF tables [75]. For example, unsuppressed Full Charge deflagration enthalpy per kilogram of propellant is:

$$\begin{aligned}
\Delta h_f^d &= a_1 (\Delta H_f^0)_{CO} + a_2 (\Delta H_f^0)_{H_2O} + a_3 (\Delta H_f^0)_{H_2} + a_4 (\Delta H_f^0)_{N_2} + a_5 (\Delta H_f^0)_{CO_2} \\
&= \left(24.63 \frac{\text{mol}}{\text{kg}} \right) \left(-110.5 \frac{\text{kJ}}{\text{mol}} \right) + \left(8.87 \frac{\text{mol}}{\text{kg}} \right) \left(-241.8 \frac{\text{kJ}}{\text{mol}} \right) \\
&\quad + \left(6.03 \frac{\text{mol}}{\text{kg}} \right) \left(0 \frac{\text{kJ}}{\text{mol}} \right) + \left(4.60 \frac{\text{mol}}{\text{kg}} \right) \left(0 \frac{\text{kJ}}{\text{mol}} \right) + \left(0 \frac{\text{mol}}{\text{kg}} \right) \left(-393.5 \frac{\text{kJ}}{\text{mol}} \right) \\
&= -4.87 \text{ MJ / kg}
\end{aligned}$$

A fraction of this energy performs mechanical work to accelerate the projectile and the remainder is heat that raises the temperature of the propellant gases and gun.

Equilibrium product species can also be calculated. The properties shown in Table 21 were obtained for propellant gases at muzzle conditions (temperature, pressure, etc.) calculated using a CBP gun (see Appendix B) and the BLAKE thermodynamic equilibrium chemistry code [94]. Energy release is similar to ideal deflagration; however, quantities of H₂O and CO are reduced; and CO₂, H₂, and trace species are produced.

Table 20. Properties of ideal propellant deflagration interior to the gun

Property (per kilogram propellant)		Full Charge Supp.		Charge 1 Supp.		Charge 2
Specific enthalpy	Δh_f^d [MJ/kg]	-4.88	-4.87	-4.88	-4.86	-5.47
Specific heat release	Δh_d [MJ/kg]	2.66	2.74	2.67	2.76	3.46
$R_d = 2 [\text{H}_2\text{O}] / ([\text{CO}_2] + [\text{CO}])$		0.75	0.72	0.75	0.72	1.09
Gas composition [mol/kg]						
CO	a_1	24.28	24.63	24.19	24.59	22.55
H ₂ O	a_2	9.09	8.87	9.13	8.87	12.32
H ₂	a_3	6.03	6.46	5.91	6.41	0.55
N ₂	a_4	4.60	4.67	4.59	4.67	4.70
CO ₂	a_5	0.00	0.00	0.00	0.00	0.00
Total	[mol/kg]	44.01	44.63	43.82	44.55	40.12

Table 21. Equilibrium muzzle gas properties from BLAKE

Property (per kilogram propellant)	Full Charge Supp.	Charge 1 Supp.	Charge 2
Specific enthalpy Δh_f^m [MJ/kg]	-5.02 -5.06	-4.99 -5.03	-5.67
Specific heat release Δh_m [MJ/kg]	2.80 2.93	2.77 2.93	3.66
$R_m = 2 [\text{H}_2\text{O}] / ([\text{CO}_2] + [\text{CO}])$	0.48 0.47	0.48 0.47	0.65
Gas composition [mol/kg]			
CO a_1	20.49 20.89	20.54 20.97	17.74
H ₂ O a_2	5.74 5.73	5.68 5.67	7.34
H ₂ a_3	8.63 8.88	8.77 9.04	5.28
N ₂ a_4	4.57 4.65	4.57 4.65	4.69
CO ₂ a_5	3.38 3.36	3.32 3.33	4.77
Total (all species) [mol/kg]	44.32 44.96	44.33 45.04	41.20
Fraction CO, H ₂ O, H ₂ , N ₂ , CO ₂	96.6% 96.8%	96.7% 96.9%	96.7%

Muzzle gases develop into plumes composed of a mixture of products from incomplete propellant combustion and air that has been turbulently entrained. Propellant gases may continue to combust with the atmospheric oxygen. Table 22 shows properties of a stoichiometric muzzle plume and complete combustion (i.e. all CHNO species are converted to the products H₂O, CO₂, and N₂).

Enthalpy of combustion products, and specific heat of combustion (Δh_c), and product species are per kilogram of propellant. Each mole of entrained oxygen is accompanied by 3.76 moles nitrogen gas. Entrained air increases the mass of the plume; the absolute masses of air and plume corresponding to each propellant configuration are indicated. Plume specific heat of combustion (Δh_u) is also shown and is reduced because of the added mass of air. Total plume heat of combustion is constant: $\Delta H_u = m_c \Delta h_c = m_u \Delta h_u$.

Table 22. Plume properties for stoichiometric mixing and complete combustion

Property (per kilogram propellant)			Full Charge Supp.		Charge 1 Supp.		Charge 2
Specific enthalpy	Δh_f^c	[MJ/kg]	-13.21	-13.40	-13.16	-13.37	-11.99
Specific heat release	Δh_c	[MJ/kg]	8.33	8.53	8.27	8.51	6.52
Plume composition [mol/kg]							
CO	a_1		0.00	0.00	0.00	0.00	0.00
H ₂ O	a_2		15.12	15.33	15.04	15.29	12.87
H ₂	a_3		0.00	0.00	0.00	0.00	0.00
N ₂	a_4		61.59	63.12	61.17	62.95	48.14
CO ₂	a_5		24.28	24.63	24.19	24.59	22.55
Total		[mol/kg]	101.0	103.0	100.4	102.8	83.56
Entrained air [mol/kg]							
Oxygen	O ₂		15.16	15.54	15.05	15.50	11.55
Nitrogen	N ₂		56.99	58.44	56.58	58.28	43.44
Air mass	m_a	[kg]	19.01	18.89	16.11	15.99	6.73
Plume mass	m_u	[kg]	28.14	27.74	23.90	23.51	10.97
Heat of formation	ΔH_f^u	[MJ]	-120.7	-118.6	-102.6	-100.5	-50.83
Heat release	ΔH_u	[MJ]	76.09	75.52	64.51	63.94	27.63
Specific heat release (per kg plume)	Δh_u	[MJ/kg]	2.70	2.72	2.70	2.72	2.52

Appendix B. Constant Breech Pressure Gun

The constant breech pressure (CBP) gun is a thermodynamic simulation of the interior ballistic properties that occur during gun firing. It models the limiting case of maximum gun efficiency and predicts projectile muzzle velocities accurate to within 5 – 10% for well-designed guns [45, 127]. An overview of the model is provided from the U.S. Army Research Laboratory technical reports that detail its computational implementation and an improvement that includes chemical reactions throughout the entire ballistics cycle [45, 94, 127]. An example calculation specific to the 152 mm howitzer follows.

Model Overview

The CBP gun simulates interior ballistic thermodynamics by treating the propellant as adiabatically combusting within the fixed volume of the gun chamber until the gas pressure rises to a specified maximum value. This value is the maximum chamber (breech) pressure and is different for each gun. It is typically equal to the pressure at which force exerted on the base of the projectile is sufficient to overcome friction between the projectile and its casing. After this point, the projectile begins to accelerate, increasing volume available to propellant gases. The rate of propellant burning is considered equal to the rate at which the available volume is expanding and the chamber pressure remains constant at its maximum value; hence constant breech pressure. Burning of the propellant stops when all oxygen is consumed. In many guns, this occurs prior to shot exit and the expansion of propellant gases follows isentropic pressure decay as the projectile travels down the barrel.

There are four well-defined states to consider: pre-firing, shot start, burn-out, and muzzle exit. These are depicted in Figure 50 in terms of axial position along the barrel, x , where:

x_0 = rear of chamber (breech)

x_p = base of projectile

x_c = front of chamber (coincides with base of projectile at shot start)

x_b = propellant burn-out

x_m = muzzle (coincides with base of projectile at shot exit)

All thermodynamic properties and chemical species for each state can be calculated from the known design parameters of the gun.

Prior to propellant ignition the thermodynamic state is equivalent to ambient conditions (i.e. $T_0 \sim 300$ K, $P_0 \sim 1$ atm, etc.). For condensed-phase propellants the internal energy U is nearly equal to the enthalpy of formation, ΔH_f^0 , and the two are assumed to be equal [128]. Thus the internal energy of the propellant prior to ignition can be calculated:

$$U_0 \approx \sum_i n_i (\Delta H_f^0)_i \quad (\text{B-1})$$

as the sum of the heats of formation for molar quantities, n_i , of each of the i th components. The base of the projectile is located at axial position $x_p = x_c$ in the initial, pre-firing state.

When the propellant is ignited, it is converted to gaseous combustion products that expand to fill the chamber between x_0 and x_c . No work is performed in this free expansion

and all energy liberated in burning is converted to heating of the products gases. Chamber pressure continues to rise as solid propellant is converted to additional product gas.

The second well-defined thermodynamic state is shot start. It occurs when the product gases reach the maximum breech pressure of the gun, P_c , and the projectile begins to accelerate as the force of the propellant gases overcomes frictional resistance. At the instant acceleration begins, the projectile's base is still located at $x_p = x_c$, and the gases occupy the volume of the chamber, V_c . The remaining thermodynamic properties can be calculated using an appropriate equation of state. Due to the extremely high temperatures in the gun chamber, Nobel-Abel or virial equations of state are typically used [94, 127]. Product species are determined assuming chemical equilibrium, often with the use of a standard thermochemical code [94, 129].

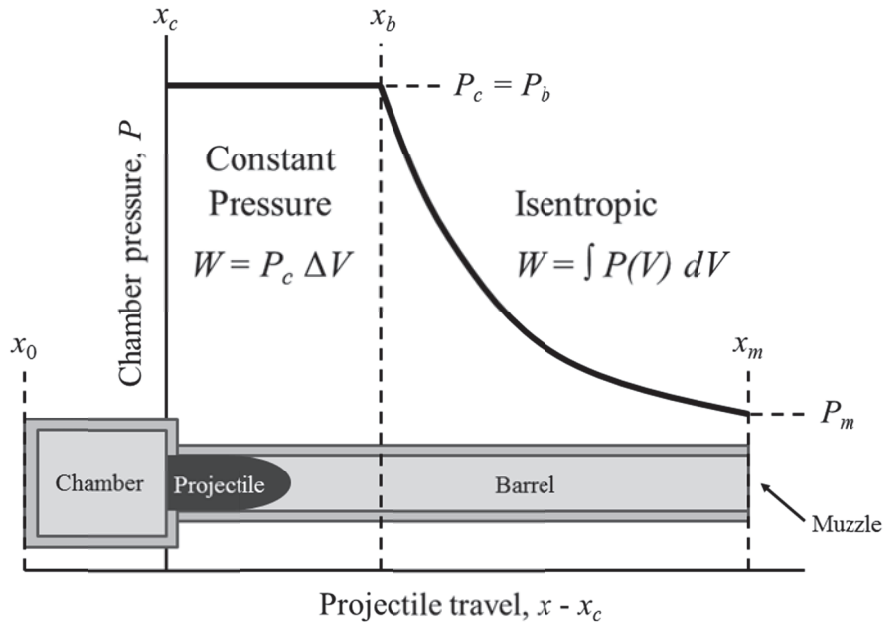


Figure 50. Pressure as a function of projectile travel. Gases generated during burning of the propellant expand to fill the chamber. Upon reaching maximum pressure, the projectile accelerates at a constant rate from its initial position, x_c , to where the propellant burns out, x_b . Propellant gases continue to expand isentropically, providing continued acceleration until the projectile has reached the muzzle exit, x_m .

After shot start the burn rate of the propellant is assumed to be balanced to the expansion of product gases such that the maximum breech pressure of the gun is maintained. A continuous axial gradient exists between the breech pressure, $P(x_0)$, and the pressure at the base of the traveling projectile, $P(x_p)$. The gradient accounts for the small fraction of force exerted by the gas that goes into accelerating propellant away from the chamber. If the ratio of propellant charge mass m_c to projectile mass m_p is near or less than unity, the pressure exerted on the projectile is given by the Lagrange correction [42, 130:134]:

$$P(x_p) = P(x_0) \left(1 + m_c / 2m_p\right)^{-1} \quad (\text{B-2})$$

The correction factor comes from the use of a Lagrange approximation, which assumes the density of gaseous propellant byproducts is uniform throughout the available volume; the velocity distribution of propellant gases increases linearly from zero at the breech to projectile velocity at the projectile's base; and the chamber, projectile base, and space-mean pressure all remain constant while the propellant burns [130:339-347; 131].

The space-mean pressure:

$$\underline{P}(x_p) = \frac{1}{x_p - x_0} \int_{x_0}^{x_p} P(x) dx = P(x_0) \frac{1 + m_c / 3m_p}{1 + m_c / 2m_p} \quad (\text{B-3})$$

is used to find the total work performed during propellant burning:

$$W(x_p) = \underline{P}(x_p) \Delta V(x_p) \quad (\text{B-4})$$

where:

$$\Delta V(x_p) = A(x_p - x_c) = \text{change in volume as a function of projectile position}$$

A = cross-sectional area of the gun barrel

Work produces a constant acceleration of the projectile (and propellant gases) as long as the propellant is combusting.

Propellant burn-out is the third CBP state. It occurs when all oxygen is consumed and propellant combustion burns out. Most ballistics simulations assume a $\rho = 0.2 \text{ g/cm}^3$ loading density (propellant mass per initial free volume in the chamber) which only approximately establishes the burn-out position, x_b [132]. A more sophisticated treatment by Kotlar solves for the burn-out enthalpy from known quantities [45]:

$$H_b = U_0 + \underline{P}(x_b)V_c \quad (\text{B-5})$$

Because burn-out pressure is known, the remaining thermodynamic properties and equilibrium chemical composition can be determined using the equation of state.

The final interior ballistics state is at shot exit. It may be estimated by assuming an adiabatic expansion from the completely defined burn-out state. The entropy is held constant, and the volume of the product gases is reversibly increased from burn-out to the total volume (chamber plus barrel) at muzzle exit V_m . During this expansion the space-mean pressure is no longer constant and depends on the volume available to propellant gases. The adiabatic expansion of a polytropic gas follows [133:154]:

$$\underline{P}(x)(V(x) - \eta m_c)^\gamma = C \quad (\text{B-6})$$

where:

γ = adiabatic exponent (typically near ~ 1.2 for most propellants)

η = propellant co-volume

C = constant

Using the burn-out state to define γ , η , and C , the thermodynamic state of the muzzle can be determined from P_m and V_m with the equation of state.

The total work performed is the sum of the work performed until burn-out plus the contribution from the adiabatic expansion between x_b and x_m :

$$W = W(x_b) + A \int_{x_b}^{x_m} \underline{P}(x) dx \quad (\text{B-7})$$

The work is equivalent to the change in internal energy of the propellant and propellant gases, $W = U_0 - U_m$. The internal energy lost by the propellant gas is converted to the kinetic energy gained by the gas and projectile:

$$W = K_g + K_p = K_p \left(1 + m_c / 3m_p \right) \quad (\text{B-8})$$

where kinetic energy is partitioned between the projectile, K_p , and propellant gas, K_g , by the Lagrange assumption.

When the predicted muzzle velocity:

$$v_p = \sqrt{2K_p / m_c} \quad (\text{B-9})$$

exceeds experimental observation the difference in kinetic energies, ΔK_p , may be attributed to inefficiencies in the gun, such as heating of the barrel or projectile. The final thermodynamic state of the CBP simulation may be improved by treating the inefficiency as energy lost from the system, $\Delta H_m' = \Delta H_m - Q$, where $Q = \Delta K_p (1 + m_c / 3m_p)$ uses the Lagrange correction to account for the total energy difference. The thermodynamic state and equilibrium chemical composition may then be re-calculated at the new muzzle state enthalpy. The results provide a realistic estimate of the properties of the propellant gases at muzzle exit.

Example Calculation

The CBP gun was used to estimate the thermodynamic state at shot exit for the 152 mm howitzer munitions. A CBP gun simulation for an unsuppressed Full Charge is provided as an example. The BLAKE thermodynamic code was used to compute the thermodynamic and chemical equilibrium properties. It was chosen because it uses non-ideal equations of state and can handle the extremely high in-barrel pressures. Specifically, a virial equation of state was used with second coefficient derived from a spherical Lennard-Jones 6-12 intermolecular model and the third from a hard-sphere model [94]. Results of the calculations at each well-defined state are reported in Table 23.

The munitions configuration is defined by propellant charge mass $m_c = 8.85$ kg and heat of formation $\Delta H_f^0 = -18.8$ MJ. The 152 mm howitzer's chamber volume is $V_c \sim 0.0149$ m³ with axial length $x_c \sim 0.8$ m, and the gun barrel length measured from the breech is $x_m \sim 4.25$ m. The projectile has a mass $m_p = 43.5$ kg and base area $A \approx 181.5$ cm² corresponding to the caliber of the gun, $d = 2(A/\pi)^{1/2} \approx 152$ mm. Median atmospheric conditions, $P_0 = 90.2$ kPa and $T_0 = 288.8$ K, are assumed. These properties describe the initial state of the CBP gun simulation.

Shot start is defined by a maximum breech pressure of $P_c \sim 235$ MPa. The distribution is uniform throughout the chamber because the projectile has not yet begun to travel down the barrel. The full thermodynamic state was obtained by specifying the propellant chemical composition in BLAKE and calling the code to simulate constant volume combustion at the chamber volume. The reported product gas enthalpy is at elevated temperature because all energy released by propellant burning is converted to an increase in temperature to $T \sim 2600$ K.

The burn-out state is then determined. First, the space-mean pressure is obtained for constant breech pressure using Equation (B-3):

$$\underline{P}(x_b) = P(x_0) \frac{1 + m_c / 3m_p}{1 + m_c / 2m_p} = 235 \text{ MPa} \frac{1 + 8.85 \text{ kg} / (3 \times 43.51 \text{ kg})}{1 + 8.85 \text{ kg} / (2 \times 43.51 \text{ kg})} = 227.8 \text{ MPa}$$

The burn-out state enthalpy can then be calculated using Equation (B-5):

$$H_b = U_0 + \underline{P}(x_b)V_c = -18.8 \text{ MJ} + (227.8 \text{ MPa})(0.0149 \text{ m}^3) = -15.4 \text{ MJ}$$

These two quantities, with an equation of state, completely define the equilibrium thermodynamic properties, which are again computed using BLAKE. The total work performed to this point is obtained using the total gas volume (from BLAKE), $V(x_b) = 0.041 \text{ m}^3$, and Equation (B-4):

$$W(x_p) = \underline{P}(x_p)\Delta V(x_p) = (227.8 \text{ MPa})(0.041 \text{ m}^3 - 0.0149 \text{ m}^3) = 5.95 \text{ MJ}$$

The fraction that is projectile kinetic energy is obtained with Equation (B-8):

$$K_p = W / (1 + m_c / 3m_p) = 5.95 \text{ MJ} / (1 + 8.85 \text{ kg} / (3 \times 43.51 \text{ kg})) = 5.57 \text{ MJ}$$

from which the projectile velocity at burn-out is obtained, $v_p = (2 K_p / m_p)^{1/2} \approx 506 \text{ m/s}$.

The muzzle state can be obtained using Equation (B-6). However, BLAKE was used in the actual implementation. The burn-out thermodynamic state was input as the initial condition and the total gun volume (chamber plus barrel) was specified to define the final state. The code incrementally increases volume at constant entropy and reports the final thermodynamic state. The work performed by expansion of the gases cannot be calculated as before because the pressure is not constant between burn-out and muzzle states. However, the work is equal to the difference in initial and muzzle state internal energy:

$$W(x_m) = U_0 - U_m = (-18.8 \text{ MJ}) - (-29.5 \text{ MJ}) = 10.7 \text{ MJ}$$

and projectile kinetic energy, $K_g \approx 10.0 \text{ MJ}$, is calculated as before.

CBP simulated muzzle velocity is $v_p = (2 K_p / m_p)^{1/2} \approx 679 \text{ m/s}$. The average muzzle velocity for an unsuppressed Full Charge that was measured during the field test was $v_p \approx 638 \text{ m/s}$. The difference in simulated and measured kinetic energy is attributed to losses from inefficiencies in the gun, $Q \approx 1.2 \text{ MJ}$. The gas enthalpy is reduced by this amount, $H_m = -22.7 \text{ MJ} \rightarrow -23.9 \text{ MJ}$. Muzzle state pressure is assumed not to be affected by inefficiency loss, and it is used with the new enthalpy to define the corrected thermodynamic state. BLAKE is run a final time to compute the remaining thermodynamic properties and chemical equilibrium species of the propellant gases.

Table 23. Thermodynamic and interior ballistic properties at well-defined CBP states.

Property			Initial	Shot start	Burn-out	Muzzle	Corrected
Projectile travel	$x = x_p - x_c$	[m]	0.00	0.00	1.43	3.44	3.44
Gas volume	V^*	[m x cm ²]	149	149	410	776	776
Enthalpy	ΔH_f	[MJ]	-18.8	-15.4	-15.4	-22.7	-23.9
Internal energy	U	[MJ]	-18.8	-18.8	-24.7	-29.5	-28.3
Temperature	T	[K]	289	2639	2198	1833	1833
Breech pressure	$P(x_0)$	[Mpa]	0.1	235.0	235.0	96.9	96.9
Base pressure	$P(x_p)$	[Mpa]	0.1	235.0	213.3	88.0	88.0
Mean pressure	$\underline{P}(x_p)$	[Mpa]	0.1	235.0	227.8	93.9	93.9
Work	W	[MJ]	0.00	0.00	5.95	10.71	9.46
Projectile energy	K_p	[MJ]	0.00	0.00	5.57	10.03	8.86
Projectile velocity	v_p	[m/s]	0.0	0.0	505.9	678.9	638.0

* volume is in the natural units of barrel length (m) times cross-sectional area (cm²)

Appendix C. Calibration of VNIR Spectra

The visible and near infrared spectra presented in Chapter V were collected with an Ocean Optics HR4000CG UV-NIR spectrometer. It is a grating spectrometer (GS) of Czerny-Turner design that is responsive over 200 – 1100 nm. A 5 μm entrance slit is imaged onto ~3 pixels of a 3648 element CCD detector array, and combined with a blazed grating with approximately 0.25 nm/pixel dispersion, spectral resolution is approximately 0.75 nm full width at half maximum (FWHM). Calibration sources were not available during the field test, and wavelength and relative spectral response were calibrated post-test.

Wavelength Calibration

The spectrometer's acquisition software applies a factory-default conversion from detector array pixel location to wavelength. Because the wavelength conversion has the potential to drift as a function of time and environmental conditions, periodic recalibration is necessary. Conversion from unitless pixel index, p , to wavelength follows the relationship [134]:

$$\lambda_p = \lambda_0 + C_1 p + C_2 p^2 + C_3 p^3 \quad (\text{C-1})$$

Alkali lines in the muzzle flash spectra served as calibration sources. Table 24 identifies six groupings of identified lines that span most of the spectral range of interest.

Figure 51 shows the pixel on which each alkali line was centered and the corresponding transition wavelength obtained from NIST [100]. Also shown is Equation (C-1) fit to the data. The resulting best-fit calibration coefficients are:

$$\lambda_0 = 200.05 \text{ nm}$$

$$C_1 = 0.261 \text{ nm}$$

$$C_2 = -8.754 \times 10^{-9} \text{ nm}$$

$$C_3 = -7.445 \times 10^{-10} \text{ nm}$$

Figure 52 shows the residuals between the data and calibration function. Wavelength uncertainty is approximately ± 0.12 nm over the 575 ~ 825 nm spectral range. Equation (C-1) is not constrained outside of this range and uncertainty in absolute wavelength increases to greater than ± 1.0 nm below 450 nm and above 945 nm.

Table 24. Location of alkali lines present in muzzle flash spectra.

Transition	Pixel Index p	NIST Wavelength λ [nm]	Calibration Wavelength λ_p [nm]	Residual $\Delta\lambda$ [nm]
K $7^2S_{1/2} \rightarrow 4^2P_{1/2}$	1456	578.24	578.22	0.02
K $7^2S_{1/2} \rightarrow 4^2P_{3/2}$	1464	580.18	580.28	-0.10
Na $3^2P_{3/2} \rightarrow 3^2S_{1/2}$	1498	589.00	589.00	0.00
Na $3^2P_{1/2} \rightarrow 3^2S_{1/2}$	1500	589.59	589.51	0.08
Li $2^2P_{3/2,1/2} \rightarrow 2^2S_{1/2}$	1818	670.78	670.67	0.11
K $6^2S_{1/2} \rightarrow 4^2P_{1/2}$	1899	691.11	691.21	-0.10
K $6^2S_{1/2} \rightarrow 4^2P_{3/2}$	1910	693.88	694.00	-0.12
K $4^2P_{3/2} \rightarrow 4^2S_{1/2}$	2198	766.49	766.53	-0.04
K $4^2P_{1/2} \rightarrow 4^2S_{1/2}$	2211	769.90	769.79	0.11
Na $3^2D_{3/2} \rightarrow 3^2P_{1/2}$	2406	818.33	818.42	-0.09
Na $3^2D_{5/2,3/2} \rightarrow 3^2P_{3/2}$	2410	819.48	819.42	0.06

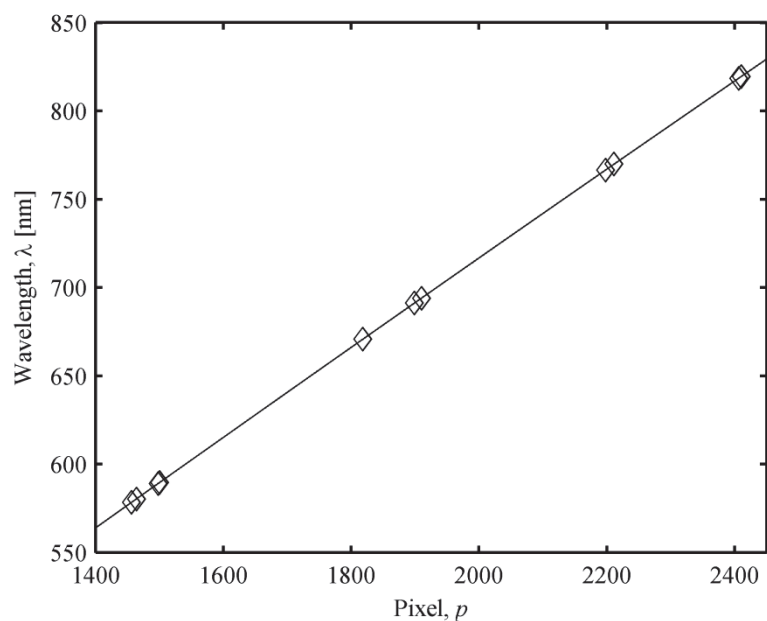


Figure 51. Relationship between pixel number and wavelength over the 550 – 850 nm spectral range. The 3rd order polynomial conversion function (—) was obtained by fitting to alkali lines (◇) present in the muzzle flash spectra.

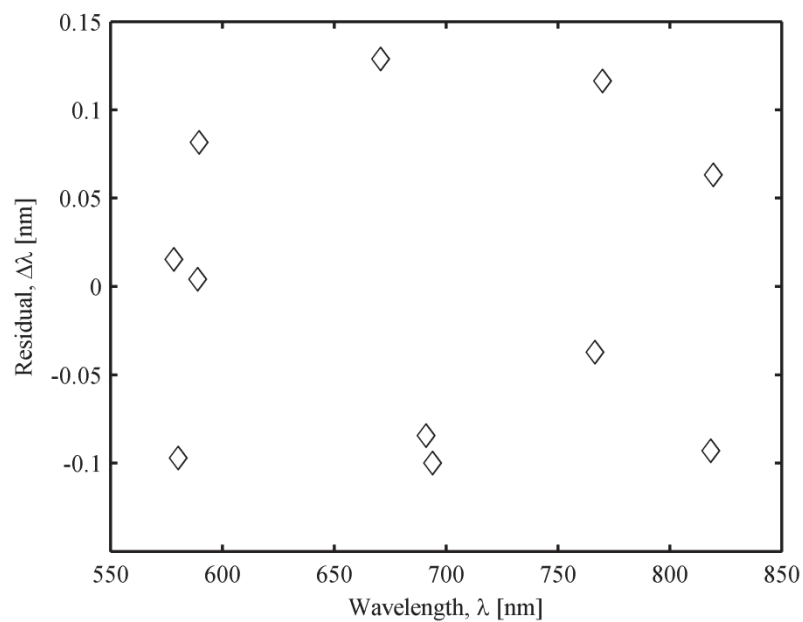


Figure 52. Residual difference between NIST reported wavelengths and those obtained with the 3rd order polynomial conversion function.

Relative Spectral Response Calibration

The relative spectral response (RSR) of the spectrometer system is the efficiency – as a function of wavelength – with which photons incident at the system’s entrance aperture are converted to signal counts. It may be calculated as the combined effects of all components of the system. Responsivity of the CCD array and grating reflection efficiency are reported [135, 136]. However, muzzle flash was observed using a reflective Meade telescope coupled to the Ocean Optics GS via a trifurcated fiber optic cable (trifurcation allowed the telescope to be used with three instruments). The telescope reflectivity, fiber transmissivity, and fiber trifurcation spectral dependencies are unknown. The system RSR can also be measured as:

$$R(\lambda) = \frac{S(\lambda) - b}{I(\lambda)} \quad (\text{C-2})$$

where:

$S(\lambda)$ = signal counts as a function of wavelength [counts]

b = signal bias [counts]

$I(\lambda)$ = apparent spectral intensity [W/sr-nm]

The signal bias accounts for a wavelength-independent offset likely introduced by the system’s electronics, and typically $I(\lambda)$ is a known calibration source. Because VNIR calibration sources were not available during the test, calibration was performed post-test using a combination of high-temperature blackbody spectra collected in the laboratory and ambient solar spectra collected during the test. The latter was a pragmatic solution because no other truth sources were available and solar spectra are well-characterized.

Figure 53 shows instrument response, calibration spectrum, and derived RSR for a 1200 °C blackbody over the 450 – 850 nm range that muzzle flash spectra were analyzed. The radiation distribution from the blackbody was sufficient to characterize the system response over most of this range. Blackbody spectra were collected using the same experimental setup that was used during the field test (i.e. Meade telescope and trifurcated fiber optic cable). Instrument response $S(\lambda)$ was obtained from an average of ~800 frames and had an offset $b = 60.5$ counts, and the calibration spectral intensity $I(\lambda)$ was calculated from Planck's radiation distribution in units of W/sr-nm. Equation (C-2) converts these quantities to a blackbody-based RSR, $R_b(\lambda)$, that peaks near 550 nm. Its response decreases as wavelength increases, falling below 20% at wavelengths $\lambda \geq 820$ nm. Conversely, apparent blackbody intensity fell to within the instrument noise level at shorter wavelengths ($\lambda \leq 575$ nm) and the RSR is uncertain in this region.

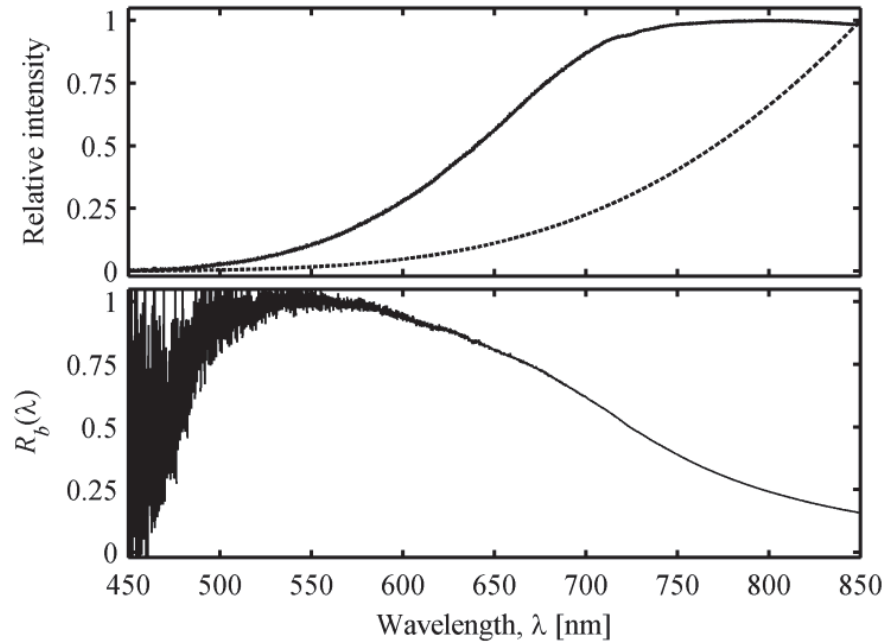


Figure 53. *Upper panel:* instrument response (—) to a 1200 °C blackbody distribution (---). Curves are normalized for depiction on the same scale. *Lower panel:* estimated blackbody-based RSR (—).

The ambient solar spectra that were collected during the muzzle flash field test and used to estimate the RSR at shorter wavelengths are shown in Figure 54. Event #32 was chosen because it coincided with solar noon, which occurred at 15:25 local time on October 15, 2007. Sky-scattered solar radiation and atmospheric radiance incident on the spectrometer's collection optics (Meade telescope), termed *skyshine*, were simulated using the Air Force Research Laboratories (AFRL) atmospheric modeling software PLEXUS [137]. The software was used to compute skyshine based on sensor location and solar position for the date and time specified. The spectrometer's latitude, longitude, and pointing azimuth were specified according to actual observation geometry. Clear, northern latitude atmospheric conditions were assumed and are consistent with the environment of the test.

The average of twenty background spectra from Event #32 is the instrument response used in calibration. Because significant noise remains, the spectrum was smoothed to ~10 nm FWHM resolution with a 21-point moving average. Skyshine is superimposed and is dominated by solar spectral features. Instrument bias, $b = 811$ counts, was obtained from the offset of the smoothed spectrum and a skyshine-based system RSR, $R_s(\lambda)$, was estimated with Equation (C-2). Above 575 nm the general shape of the RSR is similar to that obtained with the blackbody, albeit there are relatively significant residuals in atmospheric absorption regions. The latter may imply that the simulated skyshine spectrum does not precisely match the spectral radiance incident at the instrument or there is a mismatch in spectral resolutions.

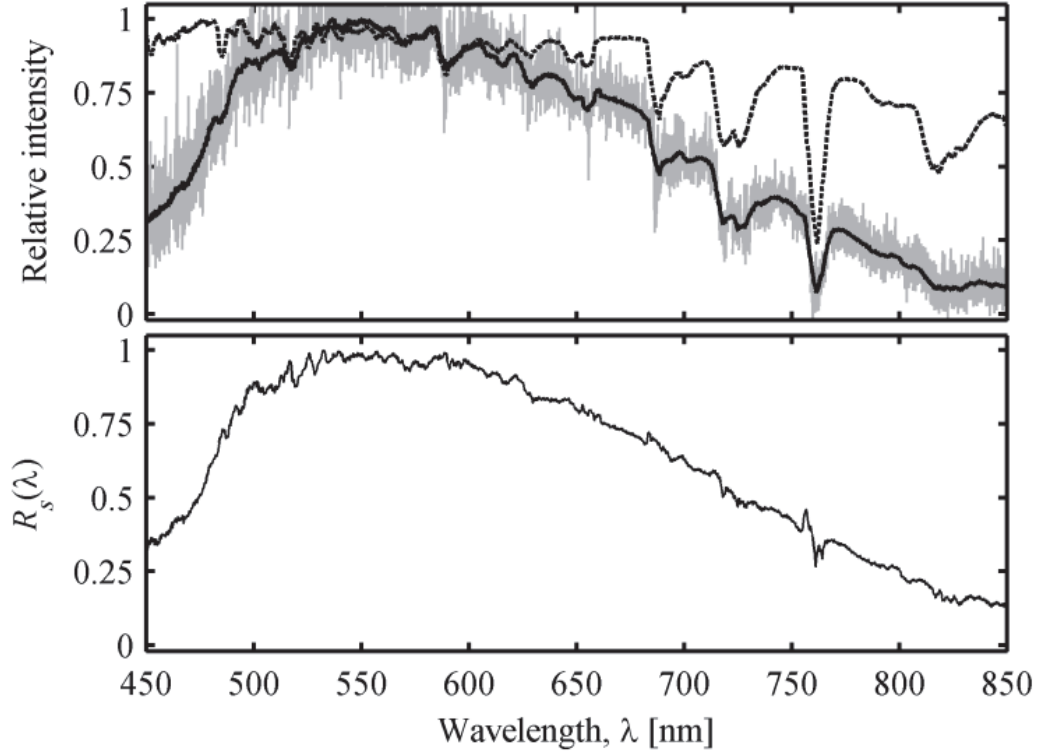


Figure 54. *Upper panel:* original (—) and smoothed (—) instrument responses from Event #32 background spectra are shown relative to simulated skyshine (···) at solar noon. Curves are normalized for depiction on the same scale. *Lower panel:* estimated skyshine-based RSR (—).

Both RSR curves are depicted in Figure 55 and show good agreement above 575 nm, characterized by an RMS difference in relative response of only 1.83% and a maximum difference (in spectral absorption regions) that is less than 10%. The overall level of agreement provides confidence that the use of skyshine as a calibration source is not unreasonable. Skyshine spectra collected during the test allow approximation of the RSR in the blackbody's low signal-to-noise region ($\lambda < 575$ nm). The system RSR that was used in the analysis of muzzle flash spectra is thus a combination of the blackbody and skyshine RSR curves:

$$R(\lambda) = \begin{cases} R_s(\lambda) & \lambda < 575 \text{ nm} \\ R_b(\lambda) & \lambda \geq 575 \text{ nm} \end{cases} \quad (\text{C-3})$$

In effect, the two calibration sources were both used to estimate the system's spectral response, and in each region the higher fidelity of the two was used.

The RSR is used to convert instrument response to a signal proportional to radiometric intensity:

$$I(\lambda) \propto (S(\lambda) - b) / R(\lambda) \quad (\text{C-4})$$

Although the Ocean Optics spectrometer is a photon-counter (it responds to the number of incident photons regardless of their individual energies) the proportionality is to radiometric intensity *not* photon flux. This results from the use of radiometric spectra for calibration sources, i.e. conversion from photon counts to energy units is incorporated into the RSR. The relationship is a proportionality rather than an equality because $R(\lambda)$ only accounts for the relative wavelength-dependent response of the instrument, not its absolute efficiency in converting photons to signal counts.

An example of a muzzle flash spectrum corrected using the combined system RSR is shown in Figure 55. The obvious difference between instrument response and relatively calibrated intensity is an upward scaling that increases with the difference in wavelength from the RSR's peak location near 525 – 575 nm. Spectral structure of up to 10% intensity is introduced into the muzzle flash spectrum by variations in the skyshine component of the RSR. This does not affect quantitative analysis of the spectral features in Chapter V (i.e. the alkali lines listed in Table 24) because these features are in the 575 – 850 nm region that is smoothly scaled by the blackbody component of the RSR. Overall uncertainty in relative intensity is estimated from a combination of noise and spectral structure in calibration measurements. It is less than 6% above 575 nm, less than 10% from 490 – 575 nm, and upwards of 40% below 490 nm.

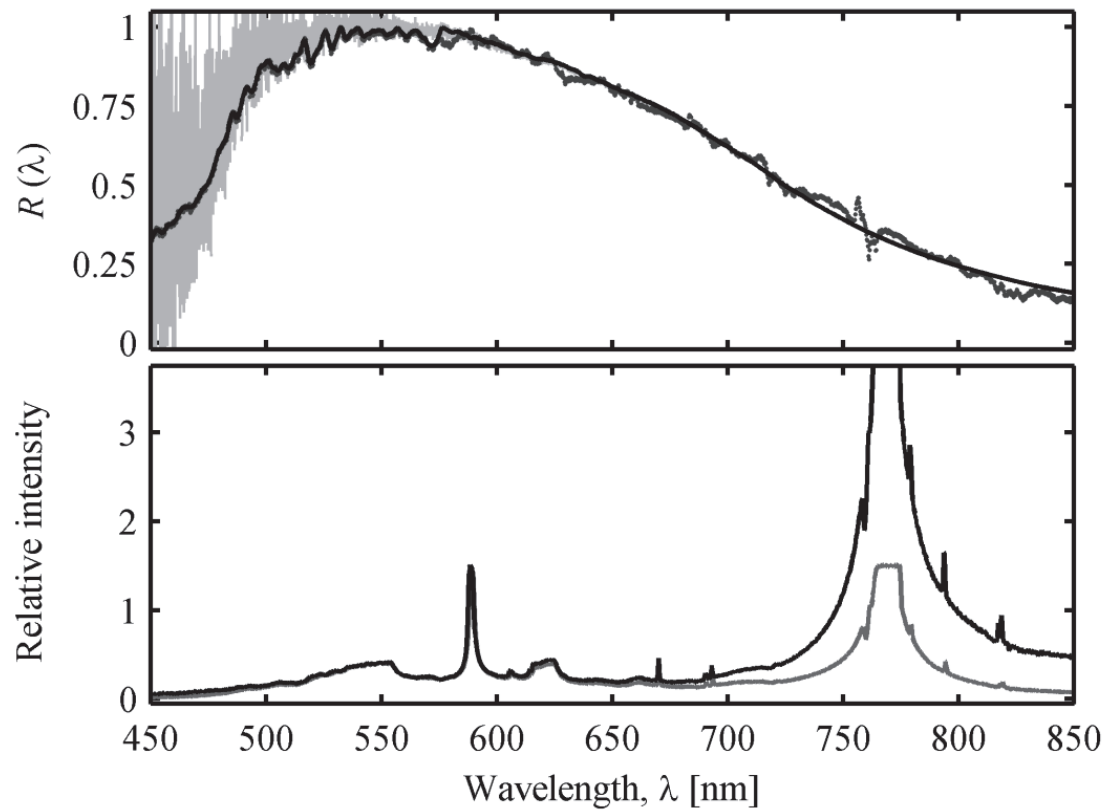


Figure 55. *Upper panel:* estimated system RSR (—) is shown relative to response curves derived from blackbody (—) and skyshine (•) spectra. *Lower panel:* muzzle flash instrument response (—) and relatively calibrated intensity spectrum (—).

Appendix D. Feature Tables

Mean values of features for the events used in classification were indicated in Chapter VII, per munitions configuration. Feature values of the individual firings are provided in the following tables.

Table 25. Blast features

Event	Charge	$\log_{10} A$	b	E [MJ]	T [K]	$\log_{10} A'$	E' [MJ]	T' [K]	\dot{E} [GJ/s]
39	Full	1.86	0.58	3.88	996	1.91	3.59	1013	3.78
40	Full	1.90	0.60	3.83	998	1.93	4.61	952	4.85
44	Full	1.83	0.57	4.00	987	1.90	3.34	1026	3.52
46	Full	1.85	0.58	3.06	1041	1.90	3.20	1033	3.37
115	1	1.86	0.61	1.59	1106	1.88	2.55	1040	2.77
121	1	1.81	0.58	2.66	1032	1.89	2.77	1024	3.01
125	1	1.86	0.58	3.47	977	1.91	3.67	963	3.99
157	1	1.84	0.58	2.69	1033	1.89	2.84	1022	3.09
158	1	1.80	0.55	4.69	894	1.92	3.77	958	4.10
15	2	1.74	0.56	1.53	1218	1.84	1.16	1263	1.68
16	2	1.77	0.57	1.70	1199	1.90	2.51	1103	3.64
18	2	1.77	0.58	1.13	1266	1.84	1.15	1264	1.67
19	2	1.76	0.57	1.31	1245	1.84	1.21	1257	1.75
20	2	1.77	0.56	1.98	1166	1.90	2.46	1109	3.57
21	2	1.75	0.56	1.80	1187	1.88	1.93	1171	2.80
22	2	1.76	0.56	2.33	1124	1.88	1.97	1167	2.86
63	2	1.76	0.57	1.26	1248	1.84	1.22	1253	1.77
64	2	1.80	0.59	1.04	1273	1.85	1.31	1242	1.89
65	2	1.76	0.57	1.58	1209	1.86	1.52	1217	2.20
67	2	1.81	0.58	1.75	1190	1.91	2.64	1085	3.83
68	2	1.72	0.55	1.91	1172	1.85	1.29	1245	1.87
70	2	1.76	0.56	2.06	1154	1.88	1.82	1183	2.63
72	2	1.73	0.56	1.81	1183	1.85	1.38	1234	2.00
73	2	1.78	0.56	2.57	1094	1.90	2.48	1105	3.60
74	2	1.76	0.56	1.95	1168	1.88	1.86	1178	2.70

Table 26. VNIR features

Event	Charge	T_{15} [K]	T_{34} [K]	r_{12}	r_{13}	r_{14}	r_{15}	r_{23}	r_{24}	r_{25}	r_{34}	r_{35}	r_{45}
39	Full	7152	11806	2.0	-2.5	-4.3	2.5	-4.5	-6.3	0.4	-1.8	5.0	6.7
40	Full	7269	11465	2.6	-2.5	-4.3	2.4	-5.1	-6.9	-0.2	-1.8	4.9	6.7
44	Full	6795	10264	2.0	-2.3	-4.4	2.6	-4.4	-6.4	0.5	-2.0	4.9	6.9
46	Full	8324	10534	3.1	-2.5	-4.5	2.1	-5.7	-7.6	-1.0	-2.0	4.6	6.6
115	1	10008	14024	1.7	-3.0	-4.5	1.8	-4.7	-6.2	0.1	-1.5	4.7	6.2
121	1	8411	11457	2.5	-2.5	-4.4	2.1	-5.0	-6.8	-0.4	-1.8	4.6	6.4
125	1	8022	11698	2.9	-2.4	-4.2	2.2	-5.3	-7.1	-0.7	-1.8	4.6	6.4
157	1	9424	10420	2.0	-2.3	-4.3	1.9	-4.3	-6.3	-0.1	-2.0	4.2	6.2
158	1	8184	11746	2.4	-2.5	-4.2	2.1	-4.8	-6.6	-0.2	-1.8	4.6	6.4
15	2	12536	9421	1.5	-1.9	-4.1	1.4	-3.4	-5.6	-0.1	-2.2	3.3	5.5
16	2	19525	9224	1.2	-2.1	-4.3	0.9	-3.3	-5.5	-0.3	-2.3	3.0	5.2
18	2	17071	9888	1.5	-2.1	-4.2	1.0	-3.6	-5.7	-0.5	-2.1	3.1	5.2
19	2	15693	8711	1.8	-1.5	-3.8	1.1	-3.3	-5.7	-0.7	-2.4	2.6	5.0
20	2	19763	9663	1.7	-2.1	-4.2	0.9	-3.8	-5.9	-0.8	-2.1	3.0	5.1
21	2	20757	9740	1.5	-2.2	-4.3	0.8	-3.7	-5.9	-0.7	-2.1	3.0	5.2
22	2	15061	9558	1.8	-1.9	-4.1	1.2	-3.7	-5.9	-0.6	-2.2	3.1	5.3
63	2	9796	8468	2.3	-1.5	-4.0	1.8	-3.8	-6.3	-0.5	-2.5	3.3	5.8
64	2	11106	8119	2.1	-1.4	-3.9	1.6	-3.5	-6.1	-0.6	-2.6	2.9	5.5
65	2	10437	8075	2.2	-1.1	-3.7	1.7	-3.3	-5.9	-0.5	-2.6	2.8	5.3
67	2	11737	8679	2.2	-1.5	-3.9	1.5	-3.7	-6.1	-0.7	-2.4	3.0	5.4
68	2	11818	9531	2.1	-1.7	-3.9	1.5	-3.8	-6.0	-0.6	-2.2	3.2	5.4
70	2	12122	9296	2.1	-1.7	-3.9	1.4	-3.8	-6.0	-0.6	-2.2	3.1	5.3
72	2	10219	7549	2.2	-1.0	-3.8	1.7	-3.2	-6.0	-0.5	-2.8	2.7	5.5
73	2	8389	7670	2.5	-1.0	-3.7	2.1	-3.5	-6.2	-0.4	-2.7	3.1	5.8
74	2	12018	8227	2.0	-1.3	-3.8	1.5	-3.3	-5.8	-0.5	-2.5	2.8	5.3

$$1 = \text{Na } 3^2\text{P} - 3^2\text{S}$$

$$2 = \text{Li } 2^2\text{P} - 2^2\text{S}$$

$$3 = \text{K } 6^2\text{S} - 4^2\text{P}$$

$$4 = \text{K } 4^2\text{P} - 4^2\text{S}$$

$$5 = \text{Na } 3^2\text{D} - 3^2\text{P}$$

Table 27. MWIR filter features

Event	Charge	F1	F2	F3	F4	F5	F6	F7
39	Full	12.1	7.6	1.3	-14.7	-16.5	1.6	6.6
40	Full	7.8	6.3	1.3	-11.2	-12.7	2.8	4.5
44	Full	6.5	-0.5	1.3	2.8	-32.3	4.3	-2.3
46	Full	5.8	8.0	4.9	-19.4	-32.2	4.3	4.7
115	1	-2.5	-2.6	-3.8	5.5	20.3	-5.8	-0.2
121	1	0.6	7.6	-1.0	-8.8	33.6	-5.0	4.3
125	1	-0.4	-2.2	-2.3	4.9	12.9	-2.8	0.2
157	1	-6.0	1.7	-1.8	-7.0	61.4	-7.6	3.3
158	1	-4.8	-2.8	-4.5	1.6	58.1	-9.4	3.4
15	2	-7.4	-9.4	-1.1	27.8	-36.6	11.6	-9.9
16	2	-7.1	-4.2	0.6	21.1	-33.9	10.9	-7.7
18	2	-2.2	-2.7	1.7	12.6	-32.5	7.4	-3.9
19	2	3.5	-17.8	4.4	18.7	-6.8	-18.8	2.3
20	2	-4.8	-5.4	2.0	16.1	-33.4	15.4	-8.2
21	2	-3.3	-10.0	0.4	21.9	-34.6	7.2	-8.6
22	2	-2.8	-5.1	4.3	9.3	-37.0	14.6	-5.9
63	2	-9.7	-4.9	-3.0	9.8	23.0	-0.6	-7.2
64	2	-16.4	-8.8	-2.0	23.5	7.6	-2.6	-7.1
65	2	-12.2	-9.2	-4.0	28.8	0.7	-3.0	-5.8
67	2	-11.0	-10.2	-3.1	23.4	0.1	0.6	-0.2
68	2	-9.1	-7.5	-0.5	17.8	3.3	3.9	-5.5
70	2	-8.9	-6.6	-0.2	15.4	-3.2	7.5	-4.3
72	2	2.9	1.1	4.0	-16.3	3.0	3.1	8.5
73	2	-1.1	0.1	7.3	-11.5	-5.0	6.8	0.1
74	2	1.2	-4.4	4.4	2.2	-19.5	9.7	-3.0
Alternate designator:		M6	M2	M7	S5	S2	S7	S1

Table 28. MWIR square-band features

Event	Charge	E1	E2	E3	E4	E5	E6	E7	E8	E9	E10
39	Full	-9.5	17.3	11.1	10.3	-14.6	-59.1	-6.7	-10.0	-2.7	37.9
40	Full	-9.4	10.8	15.0	8.4	-9.8	-54.0	-8.3	-5.5	1.9	19.1
44	Full	0.8	14.5	5.0	-1.0	12.0	-47.6	-3.6	22.1	12.2	-11.2
46	Full	14.1	15.2	31.1	10.9	4.2	-101.0	-5.2	3.6	-15.3	21.3
115	1	10.1	-2.5	-14.6	-3.7	-10.8	41.3	9.6	-9.8	0.6	-14.6
121	1	-1.3	-1.8	1.4	10.9	-21.0	18.2	4.5	-19.4	-17.5	11.6
125	1	3.5	0.1	-13.0	-2.7	-4.6	27.5	6.3	-5.2	5.9	-11.9
157	1	3.5	-3.7	-6.1	-0.5	-3.1	19.9	5.9	-5.7	3.7	-11.8
158	1	11.8	-8.3	-20.2	-5.1	-26.8	78.0	13.3	-22.5	-21.9	-2.4
15	2	-11.9	-10.0	-20.2	-12.7	40.0	28.7	-5.0	43.2	51.1	-50.8
16	2	-15.5	-15.7	-5.3	-4.4	38.0	9.0	-6.2	30.8	41.6	-35.5
18	2	-15.9	-8.6	3.4	-3.8	29.9	-13.1	-6.5	21.0	30.9	-17.2
19	2	-16.6	6.9	-8.1	-29.3	47.1	5.3	-11.8	-24.8	-16.6	-16.5
20	2	-16.1	-9.5	-8.9	-5.9	35.7	13.8	-6.9	39.8	38.6	-27.0
21	2	-12.9	-7.2	-16.3	-13.5	37.8	12.8	-4.3	26.5	47.2	-32.8
22	2	-17.7	-11.5	3.8	-6.5	40.6	-15.2	-4.5	32.1	24.5	-18.8
63	2	-11.3	-25.1	-8.5	-8.4	-9.1	69.8	-3.4	-8.7	15.2	3.4
64	2	-13.9	-36.1	-10.0	-11.8	15.4	76.8	1.0	3.9	26.1	-16.7
65	2	-14.1	-26.5	-23.8	-12.5	16.5	78.7	1.3	10.0	39.6	-27.8
67	2	-11.5	-24.0	-14.6	-14.9	15.3	63.5	-0.4	10.5	31.9	-20.0
68	2	-15.6	-22.7	-12.5	-9.9	21.7	56.5	-1.1	13.6	26.7	-21.7
70	2	-7.8	-18.5	-7.5	-9.1	17.7	46.1	0.3	24.1	15.1	-23.8
72	2	13.6	7.3	10.2	1.4	-5.9	-23.1	-4.3	-0.3	-35.9	26.8
73	2	-1.7	-6.7	20.1	0.5	23.2	-29.4	0.0	6.1	-17.0	4.1
74	2	7.2	4.6	0.8	-5.2	30.1	-16.8	2.5	29.7	-2.6	-26.4
Lower edge, v [cm⁻¹]:		1800	2000	2160	2280	2390	3120	3900	4050	4700	5100
Upper edge, v [cm⁻¹]:		2000	2160	2280	2390	3120	3560	4050	4700	5100	6000

Table 29. MWIR phenomenological features

Event	Charge	T_{eq} [K]	$\varepsilon = 1 - e^{-\alpha}$	μ_{H_2O} [10^{20} cm^{-2}]	μ_{CO_2} [10^{21} cm^{-2}]	μ_{CO} [10^{19} cm^{-2}]
39	Full	1365	0.04	2.80	1.55	1.15
40	Full	1266	0.05	2.78	2.42	0.17
44	Full	1202	0.02	7.80	3.77	0.80
46	Full	1376	0.06	2.74	1.25	3.31
115	1	1271	0.03	6.77	2.00	11.96
121	1	1230	0.02	6.09	2.28	2.84
125	1	1239	0.03	7.06	2.77	2.17
157	1	1279	0.03	4.07	1.14	9.88
158	1	1292	0.02	6.15	2.54	3.23
15	2	1418	0.10	4.19	0.90	2.69
16	2	1397	0.09	3.26	1.95	1.12
18	2	1427	0.08	2.89	1.53	4.03
19	2	1203	0.01	8.19	1.75	4.23
20	2	1535	0.09	3.16	0.91	3.95
21	2	1264	0.01	14.32	2.00	0.07
22	2	1399	0.08	3.02	1.67	3.21
63	2	1459	0.05	3.21	1.17	3.00
64	2	1328	0.06	5.42	1.84	4.66
65	2	1327	0.05	7.28	2.67	2.25
67	2	1392	0.05	6.10	2.00	15.63
68	2	1450	0.06	4.00	1.82	3.59
70	2	1338	0.08	3.93	1.95	0.55
72	2	1189	0.05	5.39	0.70	3.22
73	2	1353	0.06	2.97	1.52	2.56
74	2	1255	0.06	5.80	2.65	1.51

Appendix E. Selected Data

To report all data from the two hundred and one observed 152 mm howitzer firings would be too voluminous. Selected signatures for each of the five munitions configurations are shown in the following figures.

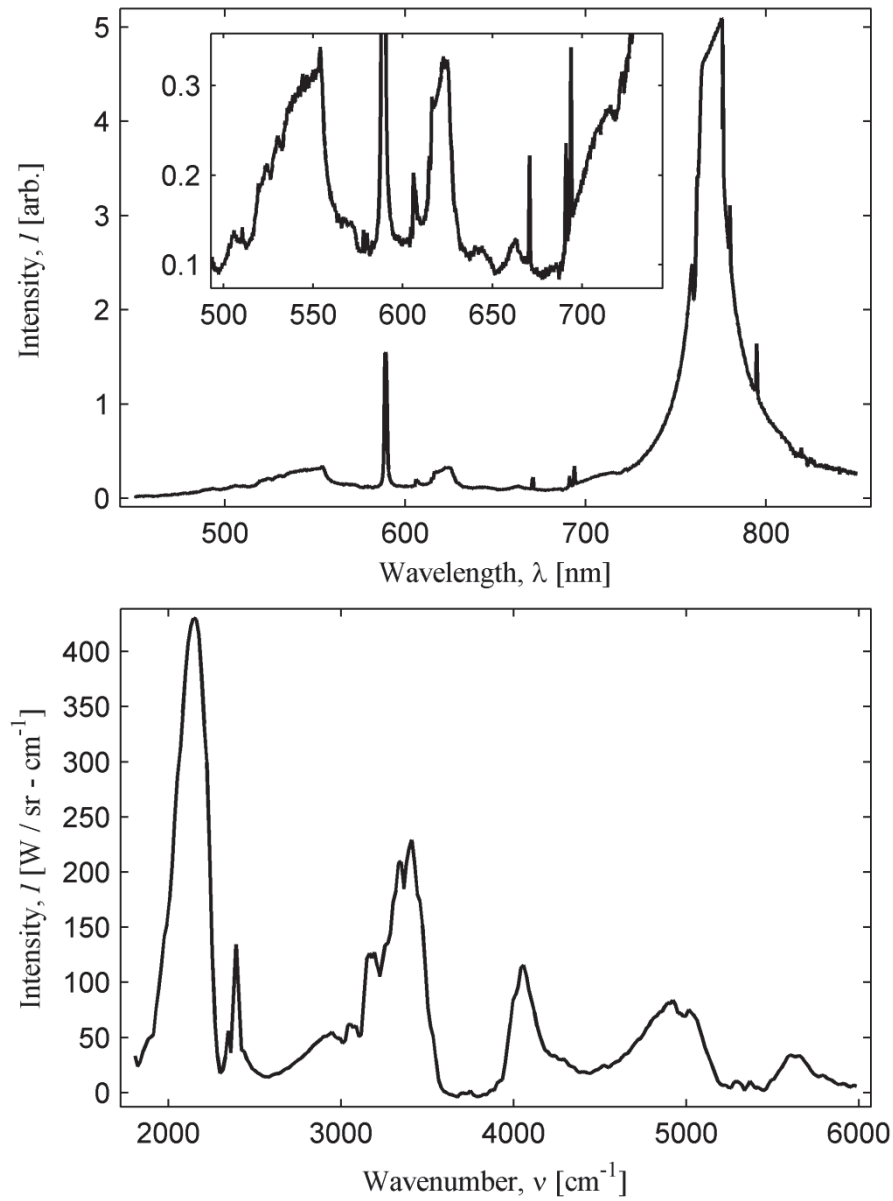


Figure 56. Event 44, unsuppressed Full Charge peak intensity VNIR and MWIR muzzle flash spectra.

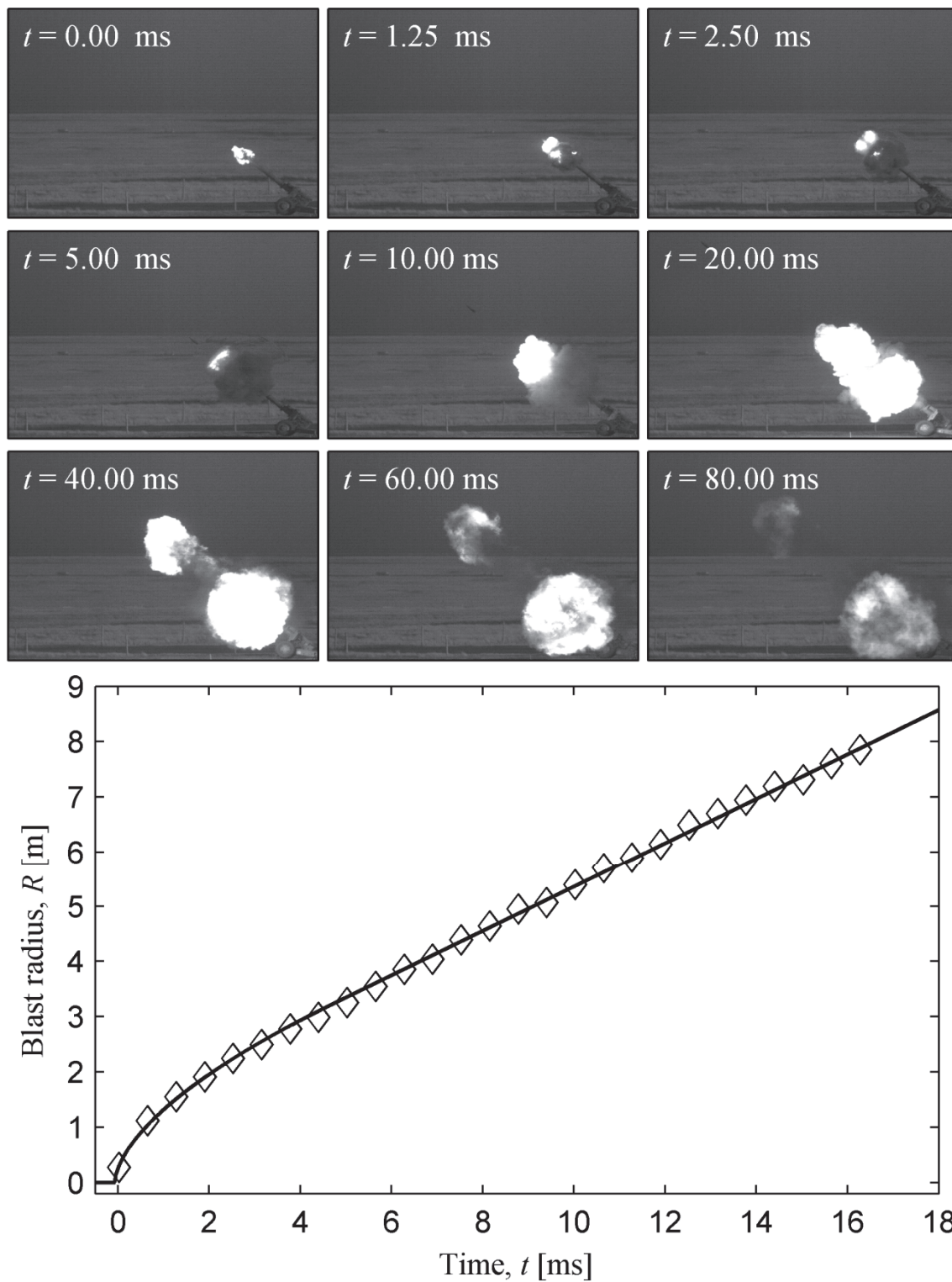


Figure 57. Event 44, unsuppressed Full Charge flow imagery and blast trajectory.

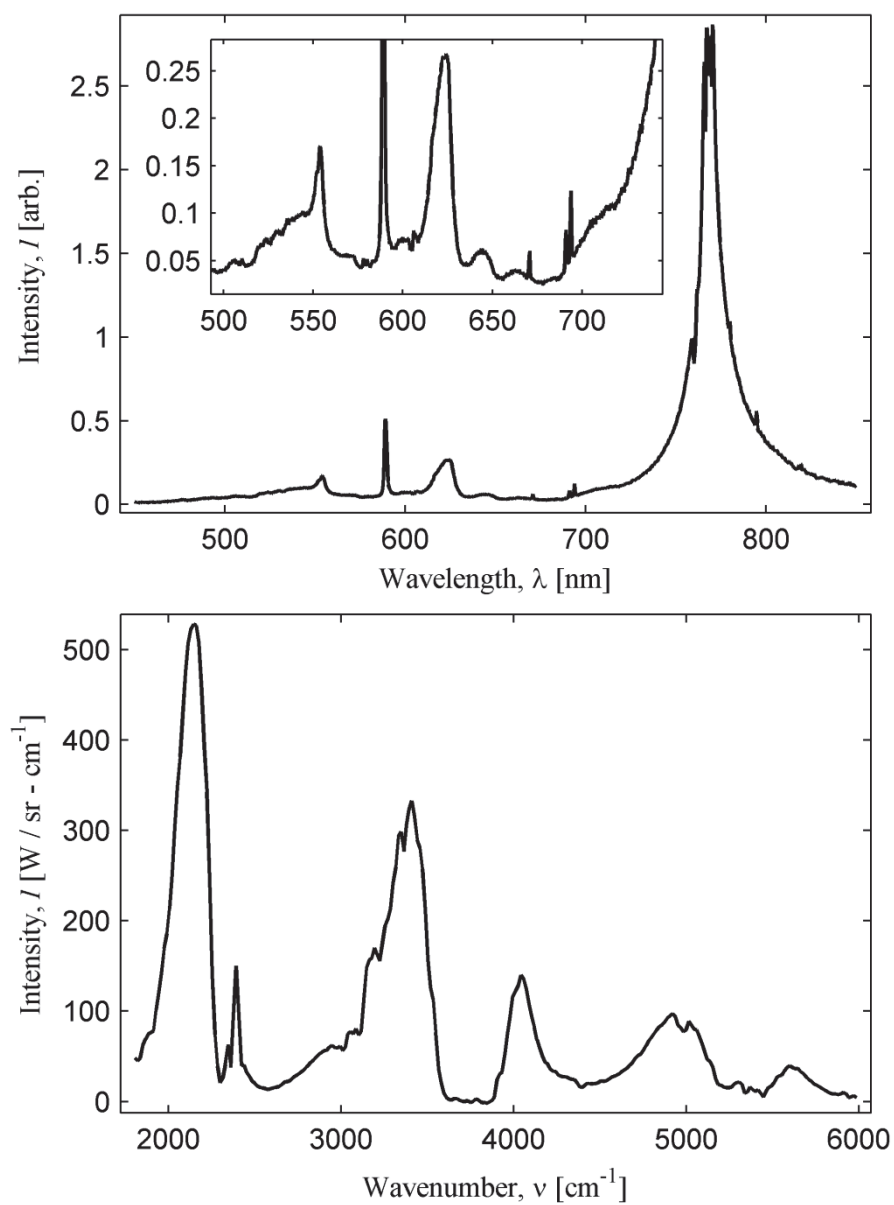


Figure 58. Event 158, unsuppressed Charge 1 peak intensity VNIR and MWIR muzzle flash spectra.

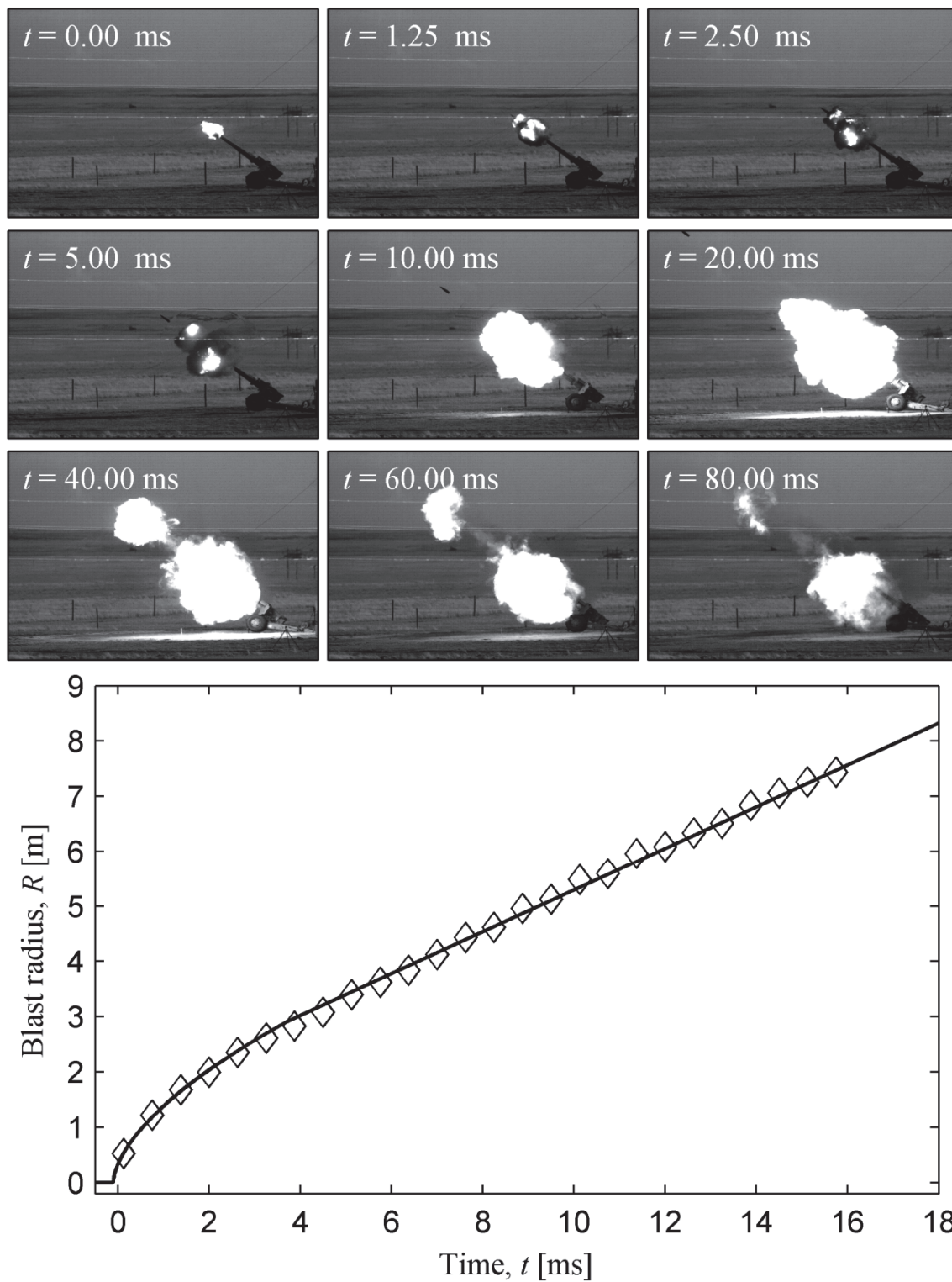


Figure 59. Event 158, unsuppressed Charge 1 flow imagery and blast trajectory.

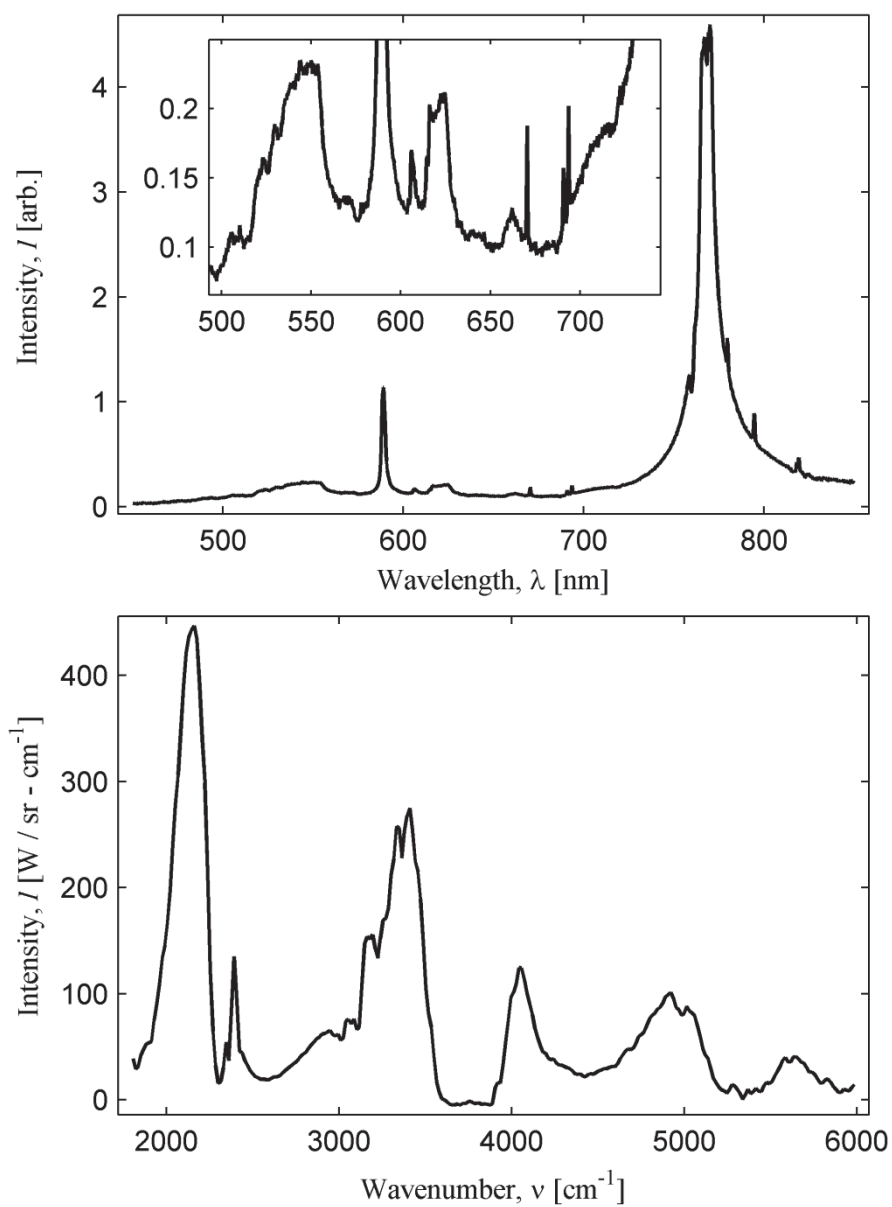


Figure 60. Event 68, unsuppressed Charge 2 peak intensity VNIR and MWIR muzzle flash spectra.

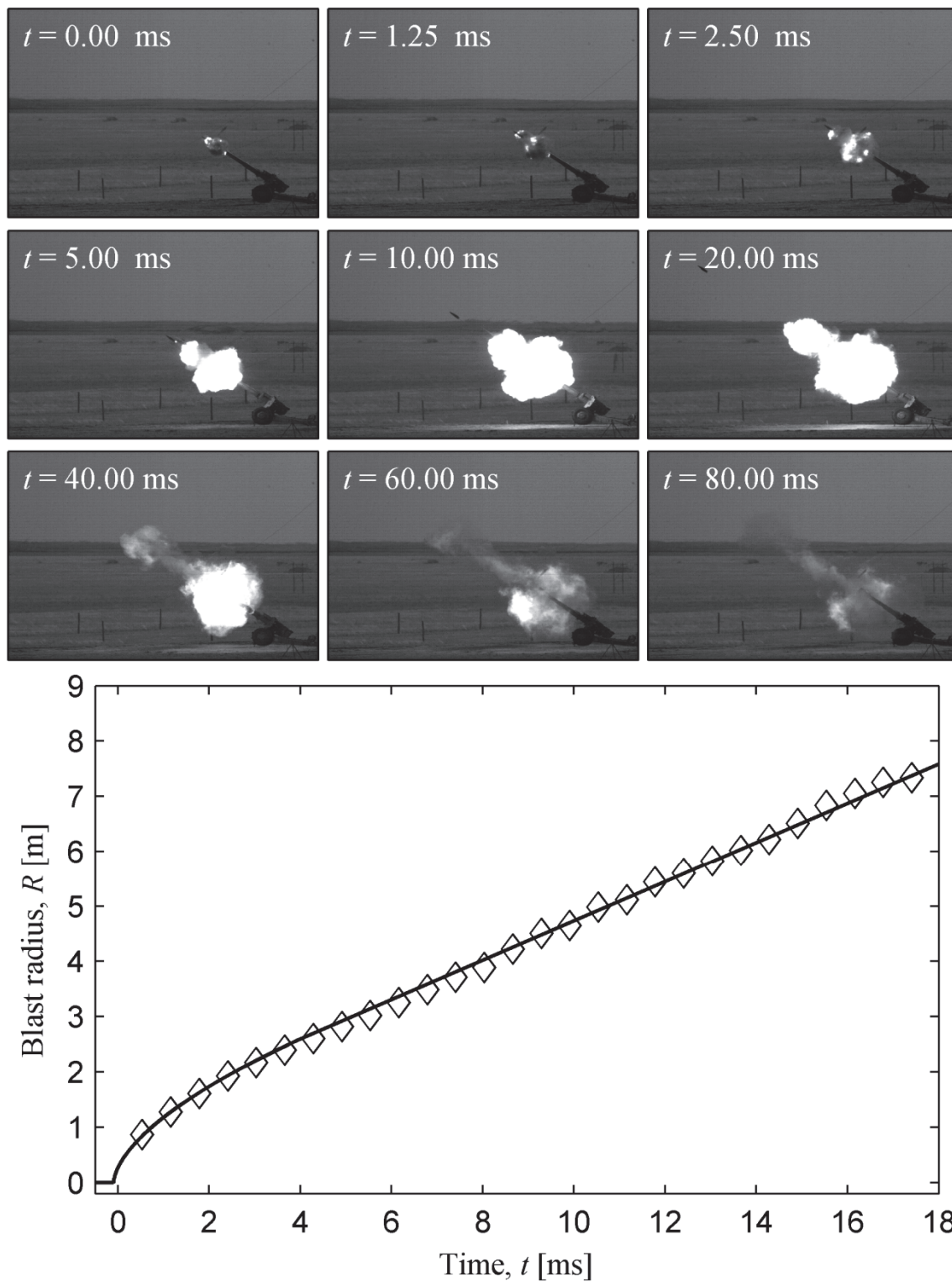


Figure 61. Event 68, unsuppressed Charge 2 flow imagery and blast trajectory.

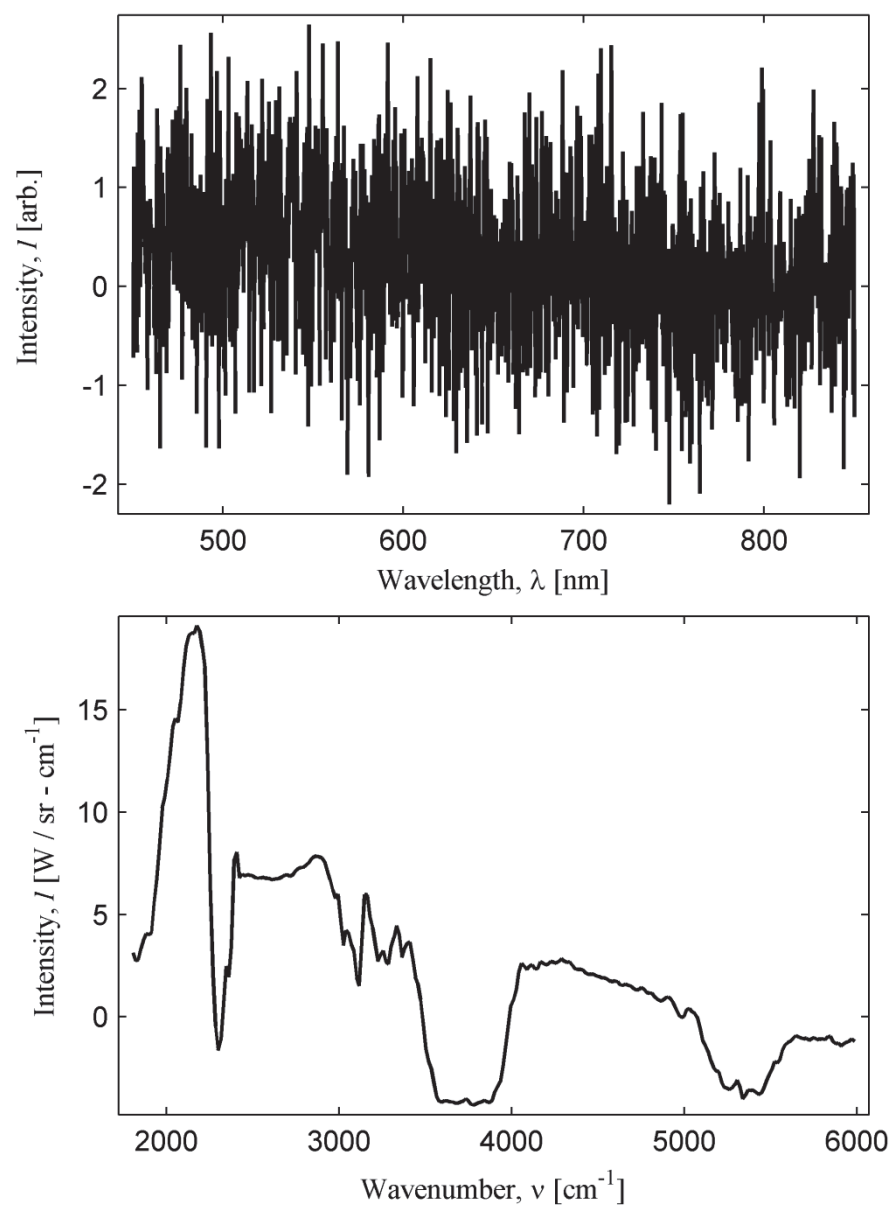


Figure 62. Event 98, suppressed Full Charge VNIR and MWIR muzzle plume spectra. Flash did not occur and the VNIR spectrum is representative of background.

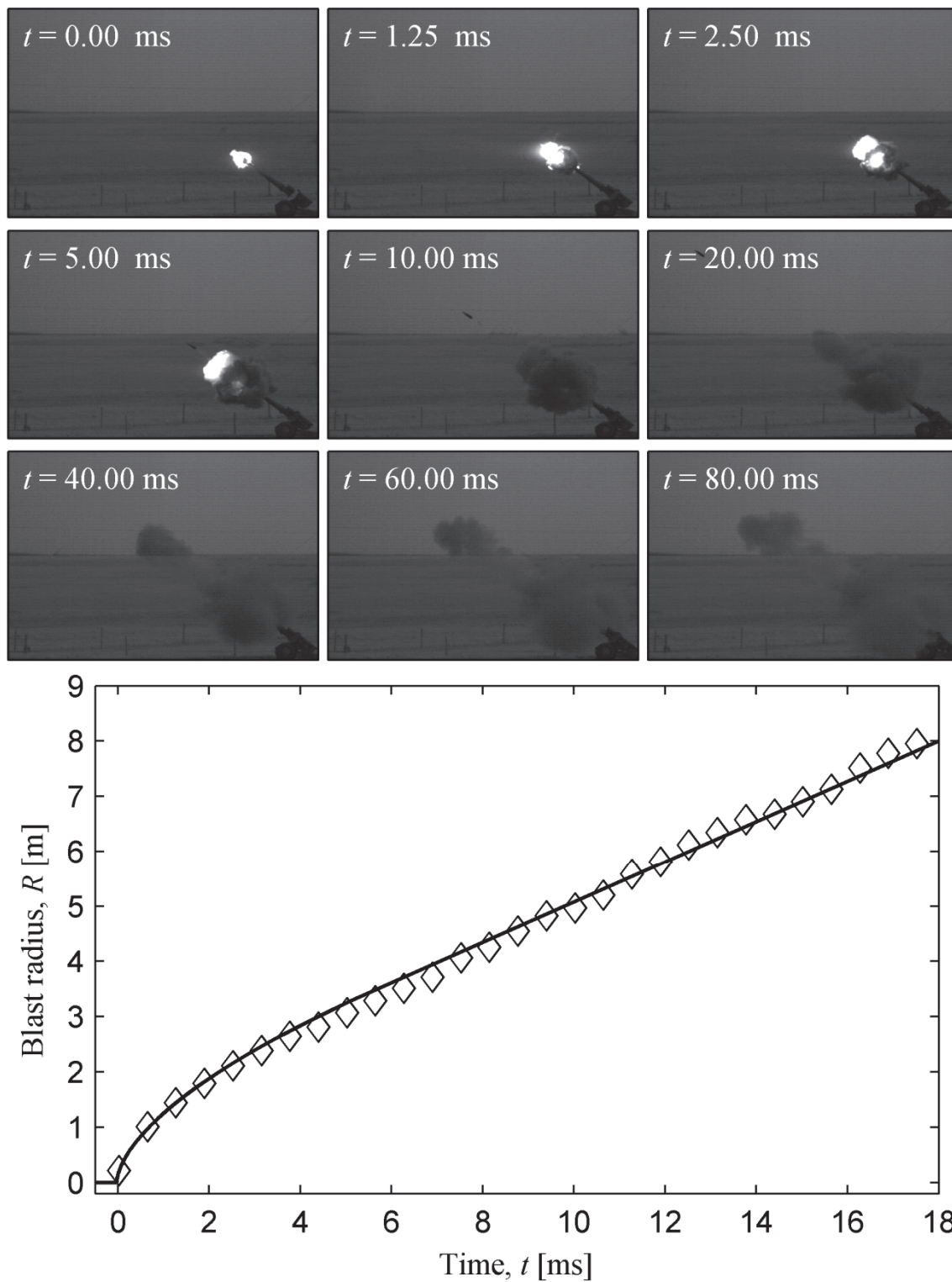


Figure 63. Event 98, suppressed Full Charge flow imagery and blast trajectory.

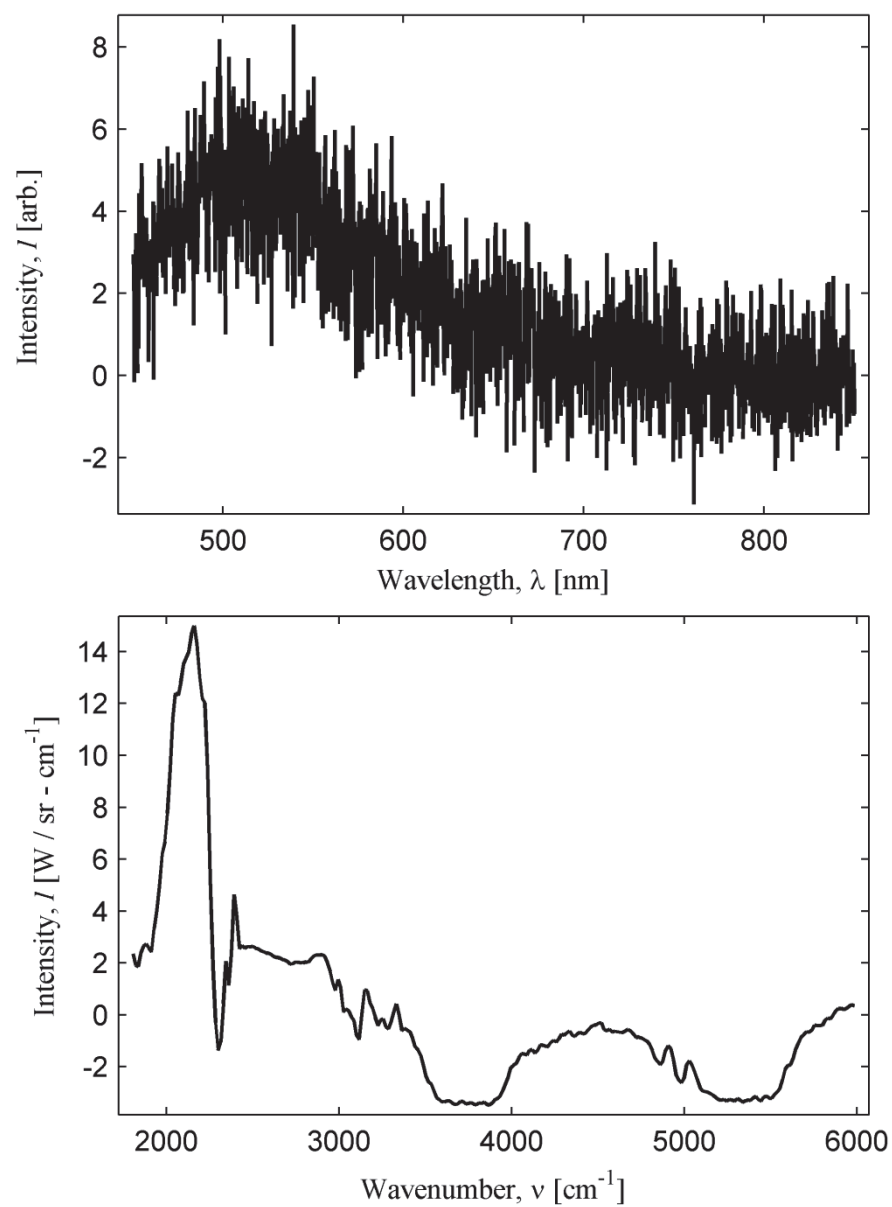


Figure 64. Event 127, suppressed Charge 1 VNIR and MWIR muzzle plume spectra. Flash did not occur and the VNIR spectrum is representative of background.

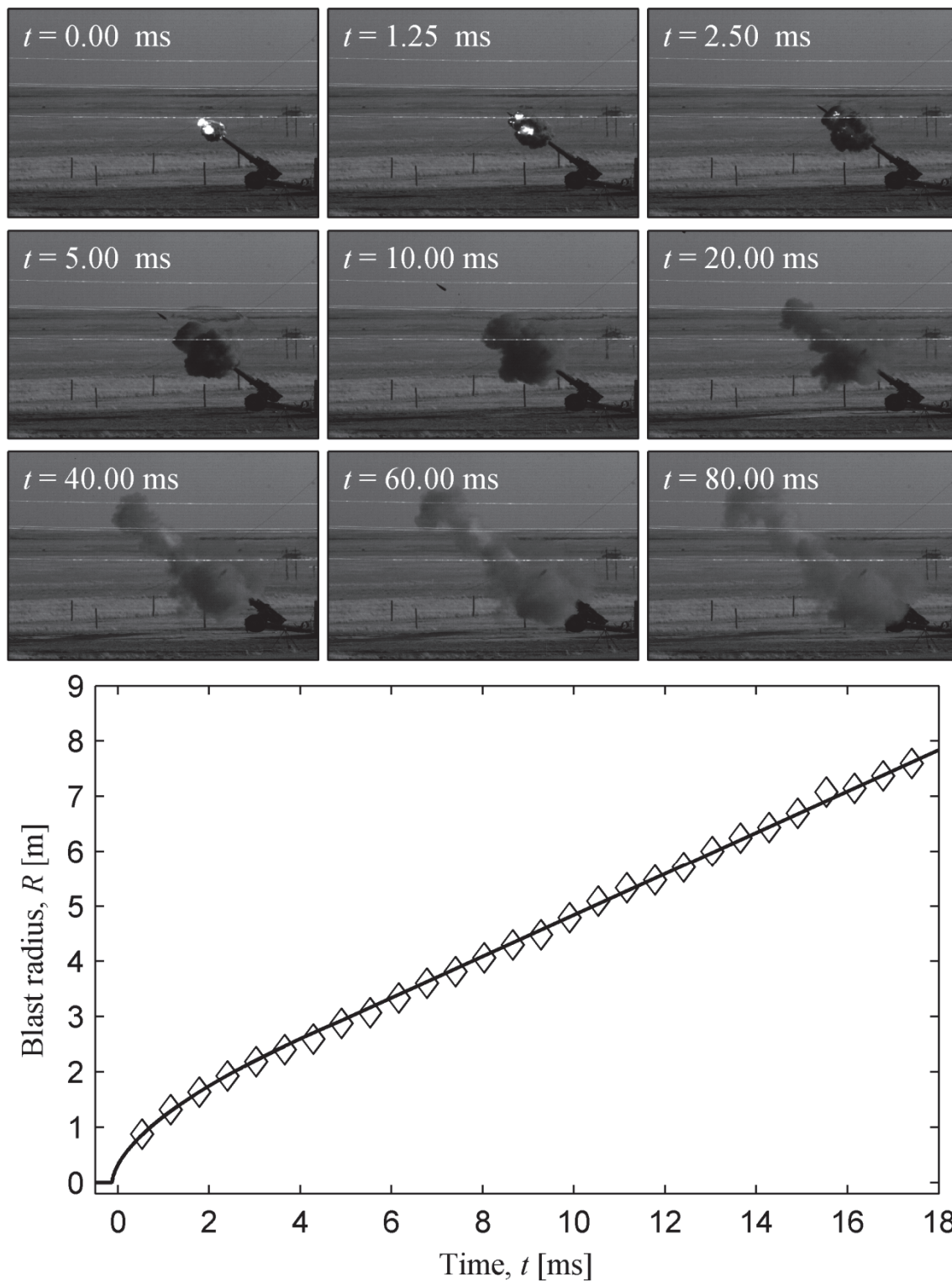


Figure 65. Event 127, suppressed Charge 1 flow imagery and blast trajectory.

Bibliography

1. Baril, M. *Tarnak Farm Board of Inquiry – Final Report*. Ottawa, 2002.
2. Rasmussen, R. E. *The Wrong Target*. MS thesis, JFSC 25789. Joint Advanced Warfighting School, Joint Forces Staff College, Norfolk, VA, June 2007.
3. Department of Defense. *Hyperspectral Classification for Muzzle Flash Recognition from the Silver Fox UAV*. Small Business Innovation Research Award. Award ID 74998, Tracking number N043-253-1109. 4 September 2011
<http://sba-sbir-qa.reisys.com/sbirsearch/detail/73664>.
4. Bradley, K. C. *Midwave Infrared Imaging Fourier Transform Spectrometry of Combustion Plumes*. Air Force Institute of Technology (AU), Wright-Patterson AFB OH, September 2009.
5. Steward, B. J. "Dual Thrust Smokey SAMs: NIR Quick-look." Report, Air Force Institute of Technology (AU), Wright-Patterson AFB OH, November 2005.
6. Hawks, M. R. *Passive Ranging Using Atmospheric Oxygen Absorption Spectra*. Air Force Institute of Technology (AU), Wright-Patterson AFB OH, January 2006.
7. Warren, T. *Characterization of Detonation Phenomena Observed in High-speed, Visible Imagery*. MS thesis, AFIT/GAP/ENP/06-20. Graduate School of Engineering and Management, Air Force Institute of Technology (AU), Wright-Patterson AFB OH, March 2006.
8. Orson, J. A., W. F. Bagby, and G. P. Perram. "Infrared Signatures from Bomb Detonations," *Infrared Physics & Technology*, 44: 101-107 (April 2003).
9. Gross, K. C., J. Wayman, and G. P. Perram. "Phenomenological Fireball Model for Remote Identification of High-Explosives," *Proceedings of SPIE*. 6566, 656613. Orlando, FL, 9-13 April 2007.
10. Gross, K. C., G. P. Perram, and R. F. Tuttle. "Modeling Infrared Spectral Intensity Data from Bomb Detonations," *Proceedings of SPIE*. 5811, 100. Orlando, FL, 28 March-1 April 2005.
11. Orson, J. A. *Collection of Detonation Signatures and Characterization of Spectral Features*. MS thesis, AFIT/GSO/ENP/00M-01. Graduate School of Engineering and Management, Air Force Institute of Technology (AU), Wright-Patterson AFB OH, March 2000.
12. Gordon, J. M., K. C. Gross, and G. P. Perram. "Empirical Model for the Temporally Resolved Temperatures of Post-detonation Fireballs for Aluminized High Explosives," *Proceedings of SPIE*. 8018, 80181M. Orlando, FL, 25-29 March 2011.

13. Bagby, W. F. *Spectral and Temporal Characterization of High-Temperature Events*. MS Thesis, AFIT/GAP/ENP/01M-01. Graduate School of Engineering and Management, Air Force Institute of Technology (AU), Wright-Patterson AFB OH, March 2001.
14. Steward, B. J. *Reproducibility, Distinguishability, and Correlation of Fireball and Shockwave Dynamics in Explosive Munitions Detonations*. MS thesis, AFIT/GAP/ENP/06-19. Graduate School of Engineering and Management, Air Force Institute of Technology (AU), Wright-Patterson AFB OH, March 2006.
15. Gross, K. C. *Phenomenological Model for Infrared Emissions from High-Explosive Detonation Fireballs*. Air Force Institute of Technology (AU), Wright-Patterson AFB OH, September 2007.
16. Gordon, J. M. *Shock Wave Dynamics of Novel Aluminized Detonations and Empirical Model for Temperature Evolution from Post-Detonation Combustion Fireballs*. Air Force Institute of Technology (AU), Wright-Patterson AFB OH, March 2011.
17. Dills, A. N. *Classification of Battlespace Detonations from Temporally Resolved Multi-Band Imagery and Mid-Infrared Spectra*. Air Force Institute of Technology (AU), Wright-Patterson AFB OH, March 2005.
18. Slagle, S. E. *Advanced Radiometry for High Explosive Fireball Discrimination*. MS thesis, AFIT/GEO/ENP/09-M02. Graduate School of Engineering and Management, Air Force Institute of Technology (AU), Wright-Patterson AFB OH, March 2009.
19. Steward, B. J. "Muzzle Flash Test: NIR Quick-look." Report, Air Force Institute of Technology (AU), Wright-Patterson AFB OH, December 2005.
20. Gross, K. C., B. J. Steward, T. Warren, and G. P. Perram. "Conventional and Q30 Flashless Gunpowder Preliminary Test Report." Report, Air Force Institute of Technology (AU), Wright-Patterson AFB OH, January 2006.
21. Klingenberg, G. "Investigation of Combustion Phenomena Associated with the Flow of Hot Propellant Gases. III: Experimental Survey of the Formation and Decay of Muzzle Flow Fields and of Pressure Measurements," *Combustion and Flame*, 29: 289-309 (1977).
22. Schmidt, E. M. and D. D. Shear. "Optical Measurements of Muzzle Blast," *AIAA Journal*, 13: 1086-1091 (1975).
23. Klingenberg, G. and J. M. Heimerl. *Gun Muzzle Blast and Flash*. Washington DC: AIAA, 1992.

24. Merlen, A. "Generalization of the Muzzle Wave Similarity Rules," *Shock Waves*, 9: 341-352 (October 1999).
25. Westine, P. "The Blast Field About the Muzzle of Guns," *Shock and Vibration Bulletin*, 39: 139-149 (1969).
26. Horst, A. W. "Pressure Wave Phenomena in Large-Caliber Guns," in *Gun Propulsion Technology*. Ed. Ludwig Stiefel. Washington DC: AIAA, 1988.
27. Schmidt, E. M. "Muzzle Flow Gasdynamics," in *Gun Propulsion Technology*. Ed. Ludwig Stiefel. Washington DC: AIAA, 1988.
28. Klingenberg, G. "Gun Muzzle Blast and Flash," *Propellants, Explosives, Pyrotechnics*, 14: 57-68 (April 1989).
29. Fansler, K. S. "Description of Muzzle Blast by Modified Ideal Scaling Models," *Shock and Vibration*, 5: 1-12 (Winter 1998).
30. Department of the Army. *Engineering Design Handbook: Spectral Characteristics of Muzzle Flash*. AMCP-706-255, HQ Army Materiel Command, Washington DC, June 1967 (AD818532).
31. Agnew, J. T. *Basic and Technical Work on Military Propellants*. The Franklin Institute, Philadelphia, PA, December 1949 (ADB803102).
32. Klingenberg, G. and J. M. Heimerl. "Combustion Following Turbulent Mixing in Muzzle Flows," *Combustion and Flame*, 68: 167-175 (May 1987).
33. Smith, M., S. Buscemi, and D. J. Xu. "Gunshot Detection System for JTRS Radios," *Proceedings of the 2010 Military Communications Conference*. 266-271. San Jose, CA, 31 October-3 November 2010.
34. Mazurek, J. A. and others. *Boomerang mobile counter shooter detection system*. BBN Technologies White Papers. 4 September 2011
http://www.bbn.com/docs/whitepapers/Boomerang_2005_Approved.pdf
35. Page, E. "The SECURES Gunshot Detection and Localization System, and Its Demonstration in the City of Dallas," *Proceedings of the 5th Battlefield Acoustics Symposium*. 693-716. Ft. Meade, MD, 23-25 September 1997.
36. Pauli, M., and others. *Infrared Detection and Geolocation of Gunfire and Ordnance Events from Ground and Air Platforms*. RTO-MP-SCI-158, Naval Research Laboratory, Washington DC, October 2004.

37. Ertem, M. C., E. Heidhausen, M. and Pauli. "Quick Response Airborne Deployment of Viper Muzzle Flash Detection and Location System During DC Sniper Attacks," *Proceedings of the 32nd Applied Imagery Pattern Recognition Workshop*. 221-225. Washington DC, 15-17 October 2003.
38. Goldberg, A. *Infrared Signatures of the Muzzle Flash of a 120 mm Tank Gun and their Implications for the Kinetic Energy Active Protection System (KEAPS)*. ARL-TR-909, Army Research Laboratory, Adelphi, MD, October 2001.
39. Klingenberg, G. and H. Mach. "Investigation of Combustion Phenomena Associated with the Flow of Hot Propellant Gases – I: Spectroscopic Temperature Measurements Inside the Muzzle Flash of a Rifle," *Combustion and Flame*, 27: 163-176 (August-December 1976).
40. Ladenberg, R. *Report on Muzzle Flash*. Report No. 426, Army Research Laboratory, Aberdeen Proving Ground, MD, November 1943.
41. Hughes, G. "On the Mean Accuracy of Statistical Pattern Recognizers," *IEEE Transactions on Information Theory*, 14: 55-63 (January 1968).
42. Drysdale, W. H. and B. P. Burns. "Structural Design of Projectiles," in *Gun Propulsion Technology*. Ed. Ludwig Stiefel. Washington DC: AIAA, 1988.
43. Stiefel, L. "Pressure-Time-Velocity-Travel Relationship in Typical Gun Systems," in *Gun Propulsion Technology*. Ed. Ludwig Stiefel. Washington DC: AIAA, 1988.
44. Baer, P. G. and J. M. Frankle. *The Simulation of Interior Ballistic Performance of Guns by Digital Computer Program*. Report No. 1183, Army Research Laboratory, Aberdeen Proving Ground, MD, December 1962 (AD299980).
45. Kotlar, A. J. "The Effect of Variable Composition Equilibrium Thermochemistry In Constant Breech Pressure (CBP) Gun Simulations," *15th International Symposium on Ballistics*. 119-126. Jerusalem, Israel, May 1995.
46. Klingenberg, G. "Experimental Diagnostics in Reacting Muzzle Flows," in *Gun Propulsion Technology*. Ed. Ludwig Stiefel. Washington DC: AIAA, 1988.
47. Wilson, D. E., K. Kim, and L. L. Raja. "Theoretical Analysis of an External Pulsed Plasma Jet," *IEEE Transactions on Magnetics*, 35: 228-233 (January 1999).
48. Schmidt, E. M. *Secondary Combustion in Gun Exhaust Flows*. ADA107312, Army Research Laboratory, Aberdeen Proving Ground, MD, October 1981.
49. Carfagno, S. P. *Handbook on Gun Flash*. The Franklin Institute, Philadelphia, PA, 1961 (AD327051).

50. Heimerl, J. M., G. E. Keller, and G. Klingenberg. "Muzzle Flash Kinetics and Modeling," in *Gun Propulsion Technology*. Ed. Ludwig Stiefel. Washington DC: AIAA, 1988.
51. Crist, S., P.M. Sherman, and D.R. Glass. "Study of the Highly Underexpanded Sonic Jet," *AIAA Journal*, 4: 68-71 (1966).
52. Sinha, N. Vice President, Combustion Research and Flow Technology, Inc., Pipersville, PA. Personal Correspondence. 30 April 2008.
53. Yousefian, V., I. W. May, and J. M. Heimerl. "Modeling the Occurrence of Muzzle Flash in Guns," *Proceedings of the 17th JANNAF Combustion Meeting*. 124-140. Hampton, VA, 22-26 September 1980.
54. Cooper, P. W. *Explosives Engineering*. New York: Wiley-VCH, 1997.
55. May, I. W. and S. I. Einstein. *Prediction of Gun Muzzle Flash*. ARBRL-TR-02229, Army Research Laboratory, Aberdeen Proving Ground, MD, March 1980 (ADA083888).
56. Yousefian, V. *Muzzle Flash*. ARI-RR-236, Aerodyne Research, Inc., Billerica, MA, November 1980.
57. Yousefian, V. *Muzzle Flash Onset: An Algebraic Criterion and Further Validation of the Muzzle Exhaust Flow Field Model*. ARBRL-CR-00506, Aerodyne Research, Inc., Billerica, MA, March 1983 (ADA126103).
58. Klett, K. K., Jr. "Signal-to-Solar Clutter Calculations of AK-47 Muzzle Flash at Various Spectral Bandpass Near the Potassium D1/D2 Doublet," *Proceedings of SPIE*, 7697: 76971I-1-76971I-8 (April 2010).
59. Vanderhoff, J. A., A. J. Kotlar, and R. B. Peterson. *CARS Temperature Measurements in the Muzzle Flash Region of a 7.62 mm Rifle*. BRL-TR-2873, Army Research Laboratory, Aberdeen Proving Ground, MD, November 1987 (AD-A190786).
60. Joint Staff. *Department of Defense Dictionary of Military and Associated Terms*. Joint Publication 1-02. 8 November 2010
http://www.dtic.mil/doctrine/dod_dictionary
61. Orloff, S. M., S. M. Hsu, and H. K. Burke. "Exploitation of Landsat Imagery and Ancillary Data for Battlespace Characterization," *Proceedings of the Fifth International Conference on Information Fusion*, 2: 994-998 (2002).

62. Dills, A. N., G. P. Perram, and S. C. Gustafson. "Detonation Discrimination Techniques Using a Near-Infrared Focal Plane Array Camera," *Proceedings of SPIE*, 5431: 77-86 (2004).
63. Dills, A. N., S. C. Gustafson, and G. P. Perram. "Detonation Discrimination and Feature Saliency Using a Near-Infrared Focal Plane Array and a Visible CCD Camera," *Proceedings of SPIE*, 5811: 123-132 (2005).
64. Duda, R., P. Hart, and D. Stork. *Pattern Classification* (2nd Edition). New York: John Wiley & Sons, Inc., 2001.
65. Dillon, W. R. and M. Goldstein. *Multivariate Analysis*. New York: John Wiley & Sons, Inc., 1984.
66. Sakurai, A. *Blast Wave Theory*. Report #498, Mathematics Research Center, University of Wisconsin, Madison, WI, December 1964 (AD608861).
67. Baker, W. E. *Explosions in Air*. Austin: University of Texas Press, 1973.
68. Korobeinikov, V. P. *Problems of Point-Blast Theory*. New York: American Institute of Physics, 1991.
69. Zel'dovich, Y. B. and Y. P. Raizer. *Physics of Shock Waves and High-Temperature Hydrodynamic Phenomena*. Mineola: Dover Publications, 2002.
70. Taylor, G. I. "The Formation of a Blast Wave by a Very Intense Explosion I. Theoretical Discussion," *Proceedings of the Royal Society of London. Series A, Mathematical and Physical Sciences*, 201: 159-174 (March 1950).
71. Freiwald, D. A. and R. A. Axford. "Approximate Spherical Blast Theory Including Source Mass," *Journal of Applied Physics*, 46: 1171-1174 (March 1975).
72. Phelps, C., C. J. Druffner, G. P. Perram, and R. R. Biggers. "Shock Front Dynamics in the Pulsed Laser Deposition of YBa₂Cu₃O_{7-x}," *Journal of Physics, D: Applied Physics*, 40: 4447-4453 (July 2007).
73. Sedov, L. I. *Similarity and Dimensional Methods in Mechanics* (10th Edition). New York: CRC Press, 1993.
74. Landau, L. D. and E. M. Lifshitz. *Fluid Mechanics*. New York: Pergamon Press, 1959.
75. Chase, M. W. and others. "JANAF Thermochemical Tables, 3rd Edition," *Journal of Physical and Chemical Reference Data*, 14: Supp. 1, 1985.

76. Akhavan, J. *The Chemistry of Explosives*. Cambridge: Royal Society of Chemistry, 1998.
77. Celmins, A. *Theoretical Basis of the Recoilless Rifle Interior Ballistics Code RECRIF*. BRL Report 1931, Army Research Laboratory, Aberdeen Proving Ground, MD, September 1976 (AD11B0138.12L).
78. Smith, F. "A Theoretical Model of the Blast from Stationary and Moving Guns," *1st International Symposium on Ballistics*, Orlando, FL, 13-15 November 1974.
79. Merlen, A. and A. Dymont. "Anisotropic Blast Waves and Explosions in a Moving Gas," *European Journal of Mechanics B, Fluids*, 11: 161-198 (1992).
80. Lagarias, J. C., J. A. Reeds, M. H. Wright, and P. E. Wright. "Convergence Properties of the Nelder-Mead Simplex Method in Low Dimensions," *SIAM Journal of Optimization*, 9: 112-147 (1998).
81. Ismail, M. M. and S. G. Murray. "Study of the Blast Wave Parameters from Small Scale Explosions," *Propellants, Explosives, Pyrotechnics*, 18: 11-17 (February 1993).
82. Courtney, M. "Acoustic Methods for Measuring Bullet Velocity," *Applied Acoustics*, 68: 925-928 (December 2008).
83. Held, M. "Blast Waves in Free Air," *Propellants, Explosives, Pyrotechnics*, 8: 1-7 (February 1983).
84. Rasmussen, P., G. Flamme, M. Stewart, D. Meinke, and J. Lankford. "Measuring Recreational Firearm Noise," *Journal of the Acoustical Society of America*, 127: 1794 (2010).
85. Oved, Y., S. Eidelman, and A. Burcat, "The Propagation of Blasts from Solid Explosives to Two-Phase Media," *Propellants, Explosives, Pyrotechnics*, 3: 109-115 (August 1978).
86. Hargather, M. J. and G. S. Settles, "Optical Measurements and Scaling of Blasts from Gram-range Explosive Charges," *Shock Waves*, 17: 215-223 (December 2007).
87. Settles, G. S. *Schlieren and Shadowgraph Techniques*. New York: Springer-Verlag, 2001.
88. Hooke, R. *Micrographia*. London: J. Martyn & J. Allestry, 1665.
89. Weinstein, L. M. *An Optical Technique for Examining Aircraft Shock Wave Structures in Flight*. NASA CP 3279, NASA Langley Research Center, Hampton, VA, October 1994.

90. Taylor, G. I. "The Formation of a Blast Wave by a Very Intense Explosion II. The Atomic Explosion of 1945," *Proceedings of the Royal Society of London. Series A, Mathematical and Physical Sciences*, 201: 175-186 (March 1950).
91. Rogers, M. H. "Similarity Flows Behind Strong Shock Waves," *The Quarterly Journal of Mechanics and Applied Mathematics*, 11: 411-422 (Winter 1958).
92. Glasstone, S. and P. J. Dolan. *The Effects of Nuclear Weapons*. Washington DC: United States Government Printing, 1983.
93. Steward, B. J., K. C. Gross, and G. P. Perram. "Reduction of Optically Observed Artillery Blast Wave Trajectories using Low Dimensionality Models," *Proceedings of SPIE*. 8020, 80200D. Orlando, FL, 25-29 April 2011.
94. Freedman, E. *BLAKE - A Thermodynamics Code Based on Tiger - User's Guide and Manual*. ARL-CR-422, Army Research Laboratory, Aberdeen Proving Ground, MD, July 1998.
95. Cler, D., N. Chevaugnon, M. S. Shephard, J. E. Flaherty, and J. Remacle. "CFD Application to Gun Muzzle Blast – A Validation Case Study," *Proceedings of the 41st Aerospace Science Meeting and Exhibit*. 2003-1142. Reno, NV, 6-9 January 2003.
96. DeMagistris, M. C., N. Sinha, and B. J. Steward. "3-D Modeling of a Large Caliber Gun Muzzle Flash," *Proceedings of the 31st JANNAF Exhaust Plume Technology Subcommittee Meeting*. Wright-Patterson AFB, OH, 2009.
97. Kempter, V., B. Kübler, P. LeBreton, J. Lorek, and W. Mecklenbrauk. "Excitation of Alkali Atoms in Collisions with Molecules. Population of the States $K(6^2S)$ and $K(5^2-P)$," *Chemical Physics Letters*, 21: 164-166 (August 1973).
98. Clough, S. A., M. W. Shephard, E. J. Mlawer, J. S. Delamere, and M. J. Iacono. "Atmospheric Radiative Transfer Modeling: A Summary of the AER Codes," *Journal of Quantitative Spectroscopy and Radiative Transfer*, 91: 233-244 (March 2005).
99. Correa, S. M. "Turbulence-Chemistry Interactions in the Intermediate Regime of Premixed Combustion," *Combustion and Flame*, 93: 41-60 (April 1993).
100. Ralchenko, Y., A. E. Kramida, J. Reader, and NIST ASD Team. *NIST Atomic Spectra Database* (Version 4.1.0). National Institute of Standards and Technology, Gaithersburg, MD. 10 June 2011 <http://physics.nist.gov/asd>

101. Pitz, G. A., C. D. Fox, and G. P. Perram. "Pressure Broadening and Shift of the Cesium D₂ Transition by the Noble Gases and N₂, H₂, HD, D₂, CH₄, C₂H₆, CF₄, and ³He with Comparison to the D₁ Transition," *Physical Review A*, 82: 042502 (October 2010).
102. Babcock, H. D. and L. Herzberg, "Fine Structure of the Red System of Atmospheric Oxygen Bands," *Astrophysical Journal*, 108: 167-190 (September 1948).
103. Mertz, L., "On the Phase Spectra of Interferograms," *Journal de Physique Colloques*, 28: C2-11-C2-13 (March 1967).
104. Griffiths, P. R. and J. A. de Haseth. *Fourier Transform Infrared Spectroscopy*. New York: Wiley-Interscience, 2007.
105. Kick, H., V. Tank, and E. Lindermeir. "Impact of Scene Changes During Data Acquisition in Fourier Spectroscopy," *Journal of Quantitative Spectroscopy & Radiative Transfer*, 92: 447-455 (June 2005).
106. Gross, K. C., A. M. Young, C. Borel, B. J. Steward, and G. P. Perram. "Simulating Systematic Scene-change Artifacts in Fourier-transform Spectroscopy," *Proceedings of SPIE*. 7695, 76951Y. Orlando, FL, 5-8 April 2010.
107. Rothman, L. S., I. E. Gordon, R. J. Barber, H. Dothe, R. R. Gamache, A. Goldman, V. I. Perevalov, T. A. Tashkun, and J. Tennyson. "HITEMP, the High-temperature Molecular Spectroscopic Database," *Journal of Quantitative Spectroscopy & Radiative Transfer*, 111: 2139-2150 (October 2010).
108. Steward, B. J., K. C. Gross, and G. P. Perram. "Optical Characterization of Large Caliber Muzzle Blast Waves," *Propellants, Explosives, Pyrotechnics*, 37: in press (December 2011).
109. Tralli, D. M., R. G. Blom, V. Zlotnicki, A. Donnellan, and D. L. Evans. "Satellite Remote Sensing of Earthquake, Volcano, Flood, Landslide and Coastal Inundation Hazards," *ISPRS Journal of Photogrammetry and Remote Sensing*, 59: 185-198 (June 2005).
110. Pozo, D., F. J. Olrno, and L. Alados-Arboledas. "Fire Detection and Growth Monitoring using a Multitemporal Technique on AVHRR Mid-Infrared and Thermal Channels," *Remote Sensing of Environment*, 60: 111-120 (May 1997).
111. Wright, R., L. P. Flynn, H. Garbeil, A. Harris, and E. Pilger. "Automated Volcanic Eruption Detection using MODIS," *Remote Sensing of Environment*, 82: 135-155 (2002).

112. Patrick, M., K. Dean, and J. Dehn. "Active mud volcanism observed with Landsat 7 ETM+," *Journal of Volcanology and Geothermal Research*, 131: 307-320 (March 2004).
113. McQueen, J. T. and R. R. Draxler. "Evaluation of Model Back Trajectories of the Kuwait Oil Fires Smoke Plume using Digital Satellite Data," *Atmospheric Environment*, 28: 2159-2174 (July 1994).
114. Casadio, S., O. Arino, and D. Serpe. "Gas Flaring Monitoring from Space using the ATSR Instrument Series," *Remote Sensing of Environment*, in press, 2011.
115. Muirhead, K. and A. P. Cracknell. "Identification of Gas Flares in the North Sea using Satellite Data," *International Journal of Remote Sensing*, 5: 199-212 (1984).
116. Haus, R., R. Wilkinson, J. Heland, and K. Schäfer. "Remote Sensing of Gas Emissions on Natural Gas Flares," *Pure and Applied Optics*, 7: 853-862 (July 1998).
117. Wang, W., J. J. Qu, X. Hao, Y. Liu, and W. T. Sommers. "An Improved Algorithm for Small and Cool Fire Detection using MODIS Data: A Preliminary Study in the Southeastern United States," *Remote Sensing of Environment*, 108: 163-170 (May 2007).
118. Abuelgasim, A. A., W. D. Ross, S. Gopal, and C. E. Woodcock, "Change Detection Using Adaptive Fuzzy Neural Networks: Environmental Damage Assessment after the Gulf War," *Remote Sensing of Environment*, 70: 208-223 (November 1999).
119. Maselli, F., C. Conese, T. D. Filippis, and M. Romani. "Integration of Ancillary Data into a Maximum-Likelihood Classifier with Nonparametric Priors," *ISPRS Journal of Photogrammetry and Remote Sensing*, 50: 2-11 (April 1995).
120. Schaber, G. G. "SAR Studies in the Yuma Desert, Arizona: Sand Penetration, Geology, and the Detection of Military Ordnance Debris," *Remote Sensing of Environment*, 67: 320-347 (March 1999).
121. Breiter, R., W. A. Cabanski, K. Mauk, W. Rode, J. Ziegler, H. Schneider, and M. Walther. "Multicolor and Dual-band IR Camera for Missile Warning and Automatic Target Recognition," *Proceedings of SPIE*. 4718: 280-288 (August 2002).
122. McDermott, D. J., R. S. Johnson, J. B. Montgomery, R. B. Sanderson, J. F. McCalmont, and M. J. Taylor. "Near Infrared Missile Warning Testbed Sensor," *Proceedings of SPIE*. 6946, 694608. Orlando, FL, 17-21 March 2008.
123. Karlholm, J. and I. Renhorn. "Wavelength Band Selection Method for Multispectral Target Detection," *Applied Optics*, 41: 6786-6795 (2002).

124. Steward, B. J., G. P. Perram, and K. C. Gross. "Visible and Near-Infrared Spectra of the Secondary Combustion of a 152 mm Howitzer," *Applied Spectroscopy*, 65: in press (December 2011).
125. Steward, B. J., K. C. Gross, and G. P. Perram. "Modeling Midwave Infrared Muzzle Flash Spectra from Unsuppressed and Flash-Suppressed Large Caliber Munitions," *Infrared Physics and Technology*, submitted (2011).
126. Kondratev, K. Y., V. V. Kozoderov, and O. I. Smotky. *Remote Sensing of the Earth from Space: Atmospheric Correction*. New York: Springer-Verlag, 1992.
127. Oberle, W. F. *Constant Pressure Interior Ballistics Code CONPRESS: Theory and Users Manual*. ARL-TR-199, Army Research Laboratory, Aberdeen Proving Ground, September 1993 (ADA275491).
128. Kotlar, A. J. *The Proper Interpretation of the Internal Energy of Formation Used in Thermodynamic Equilibrium Calculation*. BRL-MR-3985, Army Research Laboratory, Aberdeen Proving Ground, 1992.
129. Wibenson, W. B., Jr., W. H. Zwisler, L. B. Seely, and S. R. Brinkley Jr. *TIGER Computer Program Documentation*. Stanford Research Institute, Menlo Park, CA, March 1974 (ADA002791).
130. Corner, J. *Theory of the Internal Ballistics of Guns*. New York: John Wiley & Sons, 1950.
131. Nusca, M. J. "Computational Simulation of the RAM Accelerator Using a Coupled CFD/Interior-Ballistics Approach," *33rd AIAA/ASME/SAE/ASEE Joint Propulsion Conference and Exhibit*, Seattle, WA, 6-9 July 1997.
132. Freedman, E. "Thermodynamic Properties of Military Gun Propellants," in *Gun Propulsion Technology*. Ed. Ludwig Stiefel. Washington DC: AIAA, 1988.
133. Whitham, G. B. *Linear and Nonlinear Waves*. New York: Wiley Series of Pure and Applied Mathematics, 1974.
134. *HR4000 and HR4000CG-UV-NIR Series High-Resolution Fiber Optic Spectrometers Installation and Operation Manual*. Document Number 210-00000-000-02-0908. Dunedin, FL: Ocean Optics, Inc., 2008.
135. *Grating Efficiency Curves: HCl Composite Grating*. Dunedin, FL: Ocean Optics, Inc. 11 June 2010
http://www.oceanoptics.com/Products/bench_gratingcharts_hcl.asp.
136. *Toshiba CCD Linear Image Sensor*. TCD1304AP datasheet. Toshiba Corporation, 15 October 2001.

137. *PLEXUS Release 3.0*. Version 3.0 Beta 1, Windows XP. Computer software. Air Force Research Laboratories, Hanscom AFB, MA, 2006.

Vita

Bryan J. Steward graduated from Mountain Ridge High School located in Glendale, Arizona in 2000. He then entered undergraduate studies at the University of Arizona in Tucson where, in 2004, he graduated Summa Cum Laude with Honors with a Bachelor of Science degree in Optical Sciences and Engineering. Later that same year, he received a National Defense Science and Engineering Graduate Fellowship to study Applied Physics at the Air Force Institute of Technology (AFIT). After graduating Distinguished Graduate in 2006, he continued on the fellowship to pursue a Doctoral Degree in Optical Science. Concurrently, he went to work as an intelligence analysis engineer at the National Air and Space Intelligence Center (NASIC). In 2008, the fellowship period was complete and he continued doctoral research on a Dayton Area Graduate Studies Institute scholarship. In 2010, he was competitively selected for a long-term training program to return to AFIT full-time to complete his degree. Upon graduation, he will continue his work in Advanced Infrared at NASIC.

REPORT DOCUMENTATION PAGE				Form Approved OMB No. 074-0188	
<p>The public reporting burden for this collection of information is estimated to average 1 hour per response, including the time for reviewing instructions, searching existing data sources, gathering and maintaining the data needed, and completing and reviewing the collection of information. Send comments regarding this burden estimate or any other aspect of the collection of information, including suggestions for reducing this burden to Department of Defense, Washington Headquarters Services, Directorate for Information Operations and Reports (0704-0188), 1215 Jefferson Davis Highway, Suite 1204, Arlington, VA 22202-4302. Respondents should be aware that notwithstanding any other provision of law, no person shall be subject to any penalty for failing to comply with a collection of information if it does not display a currently valid OMB control number.</p> <p>PLEASE DO NOT RETURN YOUR FORM TO THE ABOVE ADDRESS.</p>					
1. REPORT DATE (DD-MM-YYYY) 22 Dec 2011		2. REPORT TYPE Doctoral Dissertation		3. DATES COVERED (From – To) 21 Nov 2005 – 22 Dec 2011	
4. TITLE AND SUBTITLE Characterization and Discrimination of Large Caliber Gun Blast and Flash Signatures				5a. CONTRACT NUMBER	
				5b. GRANT NUMBER	
				5c. PROGRAM ELEMENT NUMBER	
6. AUTHOR(S) Steward, Bryan J., Civilian				5d. PROJECT NUMBER N/A	
				5e. TASK NUMBER	
				5f. WORK UNIT NUMBER	
7. PERFORMING ORGANIZATION NAMES(S) AND ADDRESS(S) Air Force Institute of Technology Graduate School of Engineering and Management (AFIT/ENP) 2950 Hobson Way, Building 640 WPAFB OH 45433-8865				8. PERFORMING ORGANIZATION REPORT NUMBER AFIT/DS/ENP/11-D01	
9. SPONSORING/MONITORING AGENCY NAME(S) AND ADDRESS(ES) National Air and Space Intelligence Center Ms. Korin Elder, NASIC/DAIE 4180 Watson Way WPAFB OH 45433-8865 (937) 656-0423, (DSN 986-0423) korin.elder@wpafb.af.mil				10. SPONSOR/MONITOR'S ACRONYM(S) NASIC	
				11. SPONSOR/MONITOR'S REPORT NUMBER(S)	
12. DISTRIBUTION/AVAILABILITY STATEMENT Distribution Statement A. Approved for Public Release; Distribution is Unlimited					
13. SUPPLEMENTARY NOTES					
14. ABSTRACT Two hundred and one firings of three 152 mm howitzer munitions were observed to characterize firing signatures of a large caliber gun. Muzzle blast expansion was observed with high-speed (1600 Hz) optical imagery. The trajectory of the blast front was well approximated by a modified point-blast model described by constant rate of energy deposition. Visible and near-infrared (450 – 850 nm) spectra of secondary combustion were acquired at ~0.75 nm spectral resolution and depict strong contaminant emissions including Li, Na, K, Cu, and Ca. The O ₂ (X→b) absorption band is evident in the blue wing of the potassium D lines and was used for monocular passive ranging accurate to within 4 – 9%. Time-resolved midwave infrared (1800 – 6000 cm ⁻¹) spectra were collected at 100 Hz and 32 cm ⁻¹ resolution. A low dimensional radiative transfer model was used to characterize plume emissions in terms of area, temperature, soot emissivity, and species concentrations. Combustion emissions have ~100 ms duration, 1200 – 1600 K temperature, and are dominated by H ₂ O and CO ₂ . Non-combusting plume emissions last ~20 ms, are 850 – 1050 K, and show significant continuum (emissivity ~0.36) and CO structure. Munitions were discriminated with 92 – 96% classification accuracy using only 1 – 3 firing signature features.					
15. SUBJECT TERMS muzzle blast, muzzle flash, artillery, gun firing, battlespace characterization, discriminant analysis					
16. SECURITY CLASSIFICATION OF:			17. LIMITATION OF ABSTRACT	18. NUMBER OF PAGES	19a. NAME OF RESPONSIBLE PERSON
a. REPORT	b. ABSTRACT	c. THIS PAGE			Glen P. Perram, PhD, USAF
U	U	U	UU	254	19b. TELEPHONE NUMBER (Include area code) (937) 255-3636, x 4504 (glen.perram@afit.edu)